

K A D A

Journal of Physics

Vol. 2 (2) December, 2019 ISSN: 2579-1168

A Publication of
Department of Physics,
Faculty of Science,
Kaduna State University, Kaduna.

KADA JOURNAL OF PHYSICS

Vol. 2 (2) December, 2019 ISSN: 2579-1168

December, 2019

All rights reserved: No part of this publication may be reproduced
or transmitted in any way or form by any means without the
permission and express acknowledgment of the source.

Published By
DEPARTMENT OF PHYSICS, FACULTY OF SCIENCE,
KADUNA STATE UNIVERSITY,
P. M. B 2339, KADUNA - NIGERIA.
Email: kadajournphys@gmail.com
kadajournphys@kasu.edu.ng

**DEPARTMENT OF PHYSICS,
FACULTY OF SCIENCE,
KADUNA STATE UNIVERSITY, KADUNA - NIGERIA**

Editor-in-Chief

Dr. I. H. Daniel, MNIP, MIEEE, MIEEECS

Deputy Editor

Dr. C. G. Afuwai, MNIP, MNMGS, MAGS

Journal Editorial Committee

Dr. M. D. Dogara, MNIP

Dr. P. M. Gyuk, MNIP

Dr. S. G. Abdu, MNIP

Business Editor

Mr. Jerry Aba

Editorial Board Members

Prof B. J. Kwaha, FNIP

Department of Physics,
University of Jos.

Prof S. B. Elegba, FNIP

Department of Physics,
University of Abuja.

Prof K. M. Lawal, MNIP

Department of Physics,
Ahmadu Bello University, Zaria.

Prof I. Okunade, MNIP

Centre for Energy Research and Training,
Ahmadu Bello University, Zaria.

Prof G. Babaji, MNIP

Department of Physics,
Bayero University Kano

Dr. A. Mayere

University of Nottingham,
University Park, Nottingham,
United Kingdom.

Introduction:

Kada Journal of Physics (KJP) is published bi-annually by the Department of Physics, Kaduna State University, Nigeria. The KJP is a peer-review on-line international journal which is aimed at fast but standard publication of cutting edge research in all areas of physics and their applications.

AUTHOR'S GUIDELINE

Authors are expected to adhere to the following while submitting their manuscripts for assessment for possible publication in the Kada Journal of Physics.

FORMAT

All headings are flush left. The beginning of every paragraph must flush to the left margin. All paragraphs must be blocked and separated with an extra line space between them. All pages must be numbered.

ARRANGEMENTS

The contents of the articles must be presented in the following sequence: Title Names(s) of author(s), Abstract, Keywords, Introduction, Materials and Methods, Results, Discussions, Acknowledgments, and References.

TITLE

This should be on a separate page and contain the name(s) of the author(s), their addresses and e-mail addresses. In case of more than one author, indicate who correspondences should be addressed to. The title of the paper should, if possible, be short, but must contain enough information to reflect what is contained in the text.

ABSTRACT

This should be in on the same page with the title of the work. The abstract should convey the essential account concisely, in not more than 200 words all in one paragraph.

INTRODUCTION

It is the background information and therefore should include the theory behind the work. The goals of the research or hypothesis explaining clearly what you are investigating and why you choose to investigate it should be comprehensively addressed. The introduction should be motivation for the work.

MATERIALS AND METHODS

Procedures and materials used should be

described in sufficient detail to allow repetition of the work. Protocols already described elsewhere can be quoted.

RESULTS

Describe the data generated from the experiments using statements, tables and figures. Any data already presented in a table should not be repeated in a figure and vice versa. Also results described in the text must not be repeated in tables and figures again. Present the statistics you calculated, the sample size for the statistical test, and the P-value for the statistics. All tables and figures must be numbered in the order in which they are cited in the text.

DISCUSSIONS

Discuss and refer to the results obtained in the experiments and link the results to your original goal or idea. Compare the results obtained to other published studies. Since the objective is to make a contribution to the literature on this particular topic, you are expected to relate your work to the studies already done in this field. If your results are not what you expected, try to explain why they differ.

ACKNOWLEDGMENT

Where applicable, acknowledgment(s) should be concise.

CITATION OF REFERENCES IN THE TEXT

References by different authors should be arranged chronologically, e.g. (Ado 1965; James 1973; Kelvin 1977). No comma between name and year. References from the same year should be listed alphabetically, e.g. (Ali 1966; Chukwu 1966; Jude 1966) without comma between name and year. When the name of the author and the year of publication do not form part of a sentence, they should be written in parentheses and separated only by a single space without comma, e.g. (Gambo 1931). However, an author's name, and sometimes the year of publication, may form part of a sentence as follows: "Gambo (1931) showed that..." or "In 1931 Gambo published this report..." . In the case of two authors the two names should be linked by an ampersand

(&), E.g. Hassan & Umma (2005). For more than two authors, quote only the name of the first author followed by et al., Typed in italics, e.g. (Aboh, Smith & James (1931) become (Aboh et al. 1931). The quotation of multiple papers published by one author in the same year should be distinguished by the suffixes a, b, c, etc., inserted after the year of publication. For a series of papers, their arrangements should obey ascendant chronological order with each paper separated from the next by a semicolon (Garba 2005; Daniel 2006). If the papers are published the same year, use alphabetical orders (e.g. Daniel 2006; Garba 2006; Haruna 2006). Quotation of papers that are still in the press should be done only for those papers that have actually gone to the press by inserting the words “in press” in the text instead of the year of publication. When an unseen paper is being quoted from another publication, only the latter should be included in the reference list. The example only Garba (2000) would be included in the reference list. Authors must check to ensure accuracy that all references mentions in the text are listed at the end of the paper and vice versa.

LISTING REFERENCES AT THE END OF THE PAPER

References must be listed out according to the Harvard reference method. When one author has several publications they must be listed out chronologically. When two or more papers have the same author and published in the same year, the letters a, b, c, should be added after the year. When the publication carries the name of an editor and not the author of the article, insert “(Eds.)” between the name and the date of publication. If there is more than one editor, use the abbreviation “(Eds)”. When the reference includes both authors and editors, insert the phrase “edited by” after the title of the book. The title of a journal must be given in full and italicized, using Arabic numerals to indicate the volume number, e.g. *Geophysics*, 7:4-32. When the reference consists of a single page only, just insert a colon before the page number. Papers that are still in press should carry the word “in press”

after the name of the journal, the correct volume and page numbers. Titles of books must be italicized. Use the abbreviation “ed.” for edition and only an Arabic numeral to indicate the volume(s) cited. No page numbers are given for books, e.g. Godwin, A.S. 2006. *Concepts in Physics*, 3rd ed. 1. London; Churchill. When it is only the abstract of an article that had been seen, indicate this as follows: Jonah, T. N. 2005. Rural water development in Nigeria. *Nigerian Journal of Physics*, 2:200-210. Articles and book chapters should be written as follows: King, O. D. 1963. *Briquette making in: Small scale business*, edited by F. Smith & B. Timothy. Kaduna: Nura, B.A. 2003. Groundwater contamination of Narayi village. *Proceedings of the 30th Summit of Science Association of Nigeria*, Abuja, Nigeria 2013: 423-459. Individual articles from Annual Reports should be listed as follows: Esther, S A. A. 2003. Radiation Report of the Nigeria Nuclear Regulatory Agency, Nigeria, for 1999:62. Publications without the name of the author or editor should carry the name of the organization issuing the work, e.g. NNRA 1999. NNRA Year book for 1999. Unpublished theses and dissertations should be listed as follows: Halima, T. H. 2016. *Solar Radiation Effects in Kachia town*, Nigeria. B.Sc. Thesis, Kaduna State University, Kaduna 45 pp. Note that the title of an unpublished work is not italicized. For citations of journals from the web, follow the example below: Abu, M.S. 2005. A new method of digitization. *Science World Journal [on line]* 32-40. Available in <http://www.scienceworldjournal.com> (date and time retrieved).

For articles accessed in the net authors and the date of publication, use the example below: Solar flux over the Equatorial Axis. Retrieved 2nd January, 2016 from www.cc.geosci.edu

Other relevant information

TABLES

Each table must be typed using table menu for easy retrieval and editing. It should contain a brief heading with enough information to enable the reader to understand the table

without consulting the text. The approximate positions of all tables must be indicated in the main text. Duplication in the text of information given in the tables must be avoided. They are to be numbered with Roman numerals.

FIGURES

Illustrations are referred to as figures (abbreviated as “Fig.”). The approximate position of all figures must be indicated in the main text. Repetition in the text of information given in the figures must be avoided. They are to be numbered with Arabic numerals. Authors are encouraged to supply the original spreadsheet data used to produce the graph to enable us maintain a uniform look for all graphs in the journal.

PHOTOGRAPHS AND DIAGRAMS

Production of colour figures are free. They should be saved in JPEG format

PAGE CHARGES

Twenty Thousand Nigerian Naira (N20,000:00) or US \$100.00 will be charged per article after the paper might have been accepted for publication, while Five thousand

naira (N5,000.00) will be charged for Assessment fee.

Manuscripts that do not comply with the editorial requirements will be returned for amendment before they are considered by the Editorial Committee.

BANKER:

FCMB

Kada Journal of Physics

Acct. No. 4358627011

FONT SIZE:

All text must be in Times Roman with Text Size of 10 and Numbers of pages must not exceed 15 pages per article.

All Correspondence to:

Dr. I. H. Daniel, MNIP, MIEEE, MIEEECS

Editor-in-Chief

Department of Physics, Kaduna State University, P.M.B. 2339, Kaduna, Kaduna State, Nigeria.

✉ : kadajournphys@gmail.com

copy: kadajournphys@kasu.edu.ng

☎ : +234 706 853 2484, +234 817 060 4455

Insight into the Kwoi Tremor of September 2016 and other Seismic Events in Nigeria – A Review

Dogara, M. D.¹ and Joseph, I. A.²

¹Department of Physics, Kaduna State University, Kaduna State, Nigeria

²Department of Physics, Kaduna State College of Education, Gidan Waya

Corresponding author's e-mail: dogaramatoh@yahoo.com

ABSTRACT

Kwoi is the Headquarters of Jaba Local Government Area of Kaduna State, it falls around latitude $9^{\circ} 27' 22.6''$ N and longitude $8^{\circ} 00' 29.0''$ E with elevation ranging from 760 to 790m. From the geological map of Nigeria, it is evident that Kwoi and immediate environs is underlain by the crystalline basement complex rocks and they include both igneous and metamorphic rock types. Seismic events in Nigeria had been recorded instrumentally and historically from 1933 to date. There have been pockets of tremors felt in different parts of the country with the South-Western Nigeria recording the highest number of events and moderate magnitudes of 4.0 to 4.5. It is held, the existence of a major fault, the Ifewara-Zungeru fault, in the South Western Nigeria is the most probable mechanism responsible for the most observed and recorded events in that part of Nigeria and probably controls the general geology and the structural tectonic setting of that region. The tremor that occurred on the 11th and 12th of September 2016 with magnitude ranging from 2.6 to 3.0 was of great threat to the people and economy of Kwoi and environs, resulting to damages on man-made structures such as roads, bridges and buildings. The aftermath of the event resulted to psychological, psychosocial and economic trauma. Even though, there is no known geological possibility of an earthquake or even tremor around Kwoi, but what happened has instilled a new trend of research in the geosciences hence the need of this review article.

Keywords: Earth Tremor, Seismic Events, Tremors, Geosciences, Landslide, Volcanic Activities

Introduction

Earthquake is a shaking of the ground caused by the sudden release of energy stored in the rocks beneath the earth's surface. This may be due to tectonic forces acting deep in the earth and may exert stress on the rock, which may bend or change in shape. When a rock breaks, waves of energy are released and send out through the earth as seismic waves. The sudden release of energy when rock breaks may cause one huge mass of rock to slide past another mass of rock at a different relative position. This movement may be vertical, horizontal or even both.

The Nigerian landmass is geologically located in stable pre-Cambrian-Paleozoic age basement terrain which is believed to be seismically safe. However, over time, records have shown that earth tremors (minor earthquakes) have occurred in Nigeria from 1933 – 2016. The areas which have

experienced the vibrations resulting from past tremors include., Warri in 1933, Lagos, Ibadan and Ile-Ife in 1939, Ibadan in 1948, Ohafia in 1961, Ijebu-Ode in 1963, Kundunu in 1981, Jalingo and Gembu in 1982, Ijebu-Ode, Ibadan, Shagamu, Yola, Abeokuta, and Ijebu-Remo in 1984, Kombani Yaya in 1985, Obi in 1986, Gembu Akko and Kurba in 1987, Lagos in 1988, Ibadan and Jerre in 1990, Ojebu-Ode in 1994, Okitipupa in 1997, Jush-Kwari, Benin, Ibadan, Akure, Abeokuta, Ijebu-Ode, and Oyo in 2000, Lagos in 2001 and 2002, Yola in 2005, Lupma in 2006, Abomey-calari in 2009, Abeokuta in 2011 and Kwoi in 2016. These tremors bring to question the age long belief that Nigeria is seismically safe. The possible causes of tremor may include: Mining activities, fluid injection, large artificial water bodies (dams), oil & gas explorations, landslides, volcanic activity, and nuclear tests among others. The possible mechanisms for

these intraplate tremors could be due to the regional stress created by the West African Craton (Adepelumi et al. 2008). Also, two theories were considered as the origin of the seismicity in the country, the possible faults systems were inferred based on the spatial distribution of the earth tremors Yola–dambata, Akka–Jush and Warri–Ijebu Remo systems (Afegbua et al. 2011), and the theory which revealed that the tremors occurred in the inland extension of the north east – south west originally from the Atlantic ocean and that possibly causes the activities along the Ojebu-Ode and Ibadan axis which is inferred to be associated with the Ifewara-Zungeru fracture systems (Adepelumi et al. 2008).

The most recent event occurred on the 11th and 12th of September 2016 in Kwoi, Jaba Local Government Area of Kaduna State and the vibrations were felt in neighbouring villages of Samban-daji, Nok and Chori. At the time of occurrence of this event, the seismographic station of the centre for Geodesy and

Geodynamics at Kujama, Kaduna State recorded the event with magnitude ranging from 2.6 -3.0. Kwoi is the headquarters of Jaba Local Government area of Kaduna State, it falls around latitude $9^{\circ}27'N$ and longitude $8^{\circ}00'29.07'E$ with elevation ranging from 760-790m. From the geological map of Nigeria, it is evident that Kwoi and immediate environs is underlain by the crystalline basement complex rocks and they include both igneous and metamorphic types. The three divisions of the basement rocks generally recognized in the area are the migmatite-gneiss complex, the meta sedimentary rocks and the older (or Pan African) granites. These rock units have been affected by many periods of orogenic movements resulting in extensive deformation and migmatization. Studies of the Nigerian basement complex subscribe to the view that the rocks of migmatite-gneiss-quartzite complex comprise largely of sedimentary series, with associated minor igneous rocks which have been variably altered by metamorphic and granitic processes.

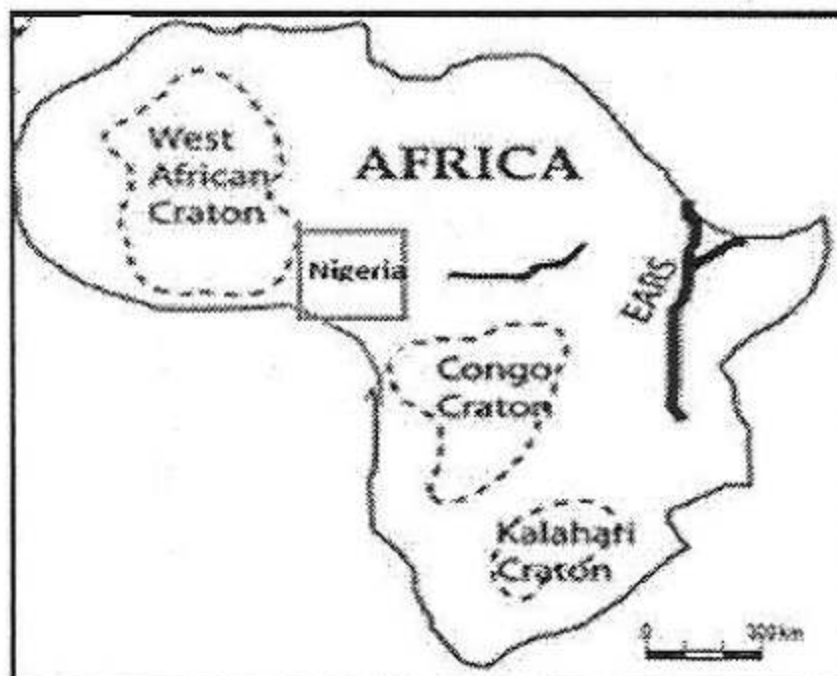


Fig. 1Location of Nigeria (in square) with respect to the Craton (Mohammed 2015)

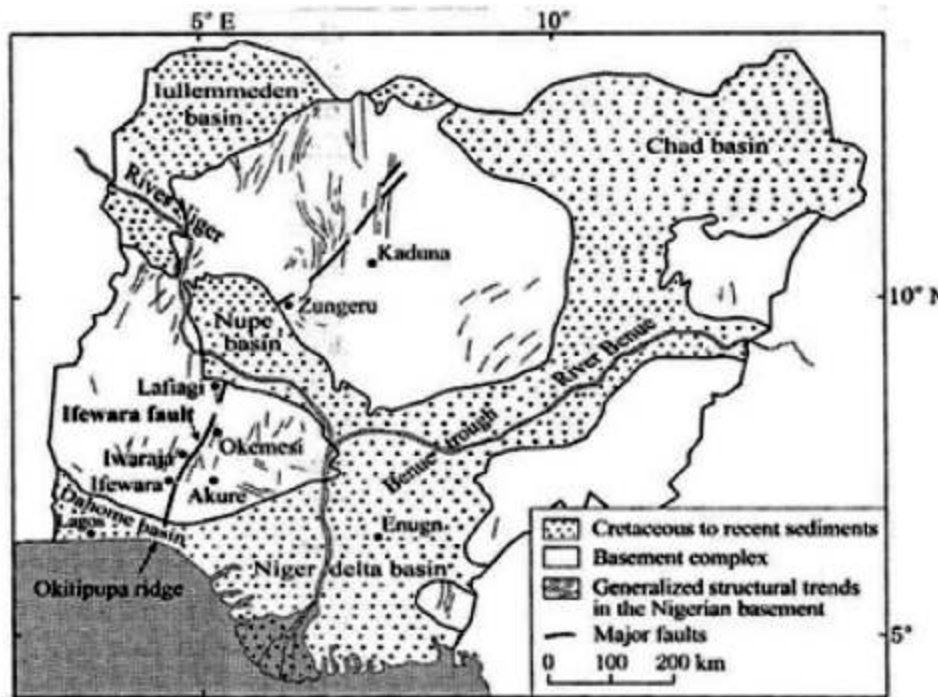


Fig. 2 Map of Nigeria showing the Zungeru-Ifewara fault (Odeyemi 2006; Akpan and Yakubu 2010)



Fig. 3 A map of Kaduna State showing Jaba and other Local Government Areas.

Probable Causes of Earth Tremor in Nigeria

The possible mechanism for the Nigeria Earth tremors has been attributed to the locations of Earth movements associated with NE – SW trending fracture and zones of weakness extending from the Atlantic Ocean into the country (Ajakaiye et al. 1986; Ajakaiye et al. 1987). In 1969, Burke et al. also suggested possible relationship between the epicenters of

some of the West African earthquakes and continental-ward extensions of oceanic fracture zones. Onuoha et al. in 2010 attributed the tremors to partial reactivation of fossil plate boundaries. The tremors have mostly likely been caused by regional stress and zones of weakness in the crust or transfer of stress from within plate boundaries.

Table 1 Historical/instrumental earthquakes felt in Nigeria (updated from Mohammed 2015)

S/N	Year-Month-Day	Origin Time	Felt Areas	Intensity/Magnitude	Probable Epicenter	Coordinates	
1	1933	-	Warri	-	-	05°45'23"E	05°31'42"N
2	1939-06-22	19:19:28	Lagos, Ibadan, Ile-Ife	6.5 (MI)	Akwapin fault in Ghana	03°23'00"E	06°30'11"N
3	1948-07-28	-	Ibadan	-	Close to Ibadan	-	-
4	1961-07-02	15:42	Ohafia	-	Close Ohafia area	07°47'21"E	05°37'15"N
5	1963-12-21	18:30	Ijebu-Ode	V	Close to Ijebu-Ode	-	-
6	1981-04-23	12:00	Kundunu	III	At Kundunu Village	-	-
7	1982-10-16	-	Jalingo, Gembu	III	Close to Cameroun Volcanic Line	-	-
8	1984-07-28	12:10	Ijebu-Ode, Ibadan, Shagamu, Abeokuta	VI	Close to Ijebu-Ode	-	-
9	1984-07-12	-	Ijebu Remo	IV	Close to Ijebu-Ode	03°22'00"E	07°11'45"N
10	1984-08-02	10:20	Ijebu-Ode, Ibadan, Shagamu, Abeokuta	V	Close to Ijebu-Ode	-	-
11	1984-12-08	-	Yola	III	Close to Cameroun Volcanic Line	-	-
12	1985-06-18	21:00	Kombaniyaya	IV	Kombaniyaya	-	-
13	1986-07-15	10:45	Obi	III	Close to Obi town	08°46'E	08°22'N
14	1987-01-27	-	Gembu	V	Close to Cameroun Volcanic Line	11°15'E	06°42'N
15	1987-03-19	-	Akko	IV	Close to Akko	10°12'E	10°17'N
16	1987-05-24	-	Kurba	III	Close to Kurba Village	10°12'E	11°29'E
17	1988-05-14	12:17	Lagos	V	Close to Lagos	-	-
18	1990-06-27	-	Ibadan	3.7 (ML)	Close to Ijebu-Ode	03°58'E	07°22'N
19	1990-04-05	-	Jerre	V	Close to Jerre Village	-	-
20	1994-11-07	05:07:51	Ojebu-Ode	4.2 (ML)	Dan Gulbi	-	-
21	1997	-	Okitipupa	IV	Close to Jushi-Kwari Village	-	-
22	2000-08-15	-	Jushi-Kwari	III	Benin City (55km from Benin)	07°42'E	14°03'N
23	2000-03-13	-	Benin	IV	Close to Okitipupa Ridge	-	-
24	2000-03-07	15:53:54	Ibadan, Akure, Abeokuta, Ijebu-Ode, Oyo	4.7 (ML)	Close to Lagos city	-	-
25	2000-05-07	11:00	Akure	IV	Lagos city	-	-
26	2000-05-19	-	Lagos	IV	-	-	-
27	2002-08-08	-	Lagos	IV	Close to Cameroon	-	-
28	2005-03	-	Yola	III	Volcanic Line	-	-
29	2006-03-25	11:20	Lupma	III	Close to Ifewara Zungeru Fault	-	-
30	2009-09-11	-	Abomey-Calavi	II	Close to Binin	-	-
31	2011-11-05	-	Abeokuta	4.4	Close to Abeokuta	-	-
32	2016	-	Kwoi	2.6 – 3.0	Jaba	8°00'29.0"N	9° 27' 22.6"N

Historical Tremors and Earthquakes felt in Nigeria

Records available indicates that some communities in Nigeria have experienced tremors and earthquakes in the past (see figure 4 and table 1), despite the fact that Nigeria lies far from the world's active plate boundaries. Most of these occurrences were not instrumentally recorded because there were no functional seismological observatories in Nigeria, but those of 1984 at Ijebu-Ode, 1990 at Ibadan, 2000 at Jushi Kwari and 2016 in Kwoi were recorded. The events of the past and

recent findings have shown that Nigeria may not be completely free from earthquake (Adepelumi et al. 2008, Akpan et al. 2010). With the recorded past tremors in Nigeria, any future events of Earth tremors in the country are most likely going to occur along the Zungeru – Ifewara fault zones (see figure 2). Already examined possible mechanisms for these intra-plate tremor include regional stresses created by Nigeria's position between two Cratons and zone of weakness resulting from magmatic intrusions and other tectonic activities in the sediments (Eze et al. 2011).



Fig. 4 Map of Nigeria showing some areas where earth tremors were felt (diameter of the solid dot denotes intensity of the events, after Akpan and Yakubu 2010). Not to scale.

Historical and recent seismic data indicate that catastrophic earthquakes have occurred in other parts of Africa far away from the Atlas mountain region and also in the areas far from the rift valley system (Onuoha et al. 1988). This is indicative that Nigeria and indeed some West African countries are likely to witness devastating earthquakes in future. This is in accordance with recent review of earthquake occurrences and observations in Nigeria which shows that several minor tremors were experienced in some parts of the country in 1933, 1939, 1948, 1961, 1963, 1981, 1982, 1984, 1985, 1986, 1987, 1988, 1990, 1994, 1997, 2000, 2001, 2002, 2005, 2006, 2009 and

2011 (Afegbua et al. 2011). The intensities of these events ranged from III to VI based on the Modified Mercalli Intensity Scale. Only events of 1984, 1990, 1994 and 2000 were instrumentally recorded. They had magnitudes ranging from 4.3 to 4.5 (Akpan et al. 2010). Another vibration of 2009 event with magnitude of 4.4 occurred and was felt in parts of Ibadan and Ogun state, South-Western Nigeria. Lately on September 11th and 12th, 2016 an earth tremor occurred in Kwoi, Jaba L.G.A of Kaduna State with magnitude ranging from 2.6-3.0, this tremor was felt in many villages around Kwoi.

Impact of Tremor and/or Earthquakes on Mankind and Property

For anyone who has experienced an earthquake or tremor, the experience can be frightening and traumatic. More so, earthquakes are unpredictable and even when one is anticipated, the intensity with which it strikes is only measurable after its occurrence has left a devastating mark of huge human and infrastructural damage. Population growth and increasing urbanization in earthquake prone areas suggest that earthquake impacts on human population will increase in the coming decades. Large earthquakes affecting large population in Japan, Haiti, Chile and New Zealand are evidence of this trend and also illustrate significant variations in outcomes of such damage and mortality levels (EM-DAT The International Disaster Database 2008). When an earthquake hits, it shakes the ground and causes structures to shake as well. When a structure is old or has not been properly built to withstand the force of an earthquake, it collapses, causing damage to surrounding buildings as well as people. Building collapses are the main cause of fatalities during and after earthquake as the shaking ground rarely causes any deaths in and of itself. Earthquakes can also cause the movement of unstable hills and mountains causing landslides. These landslides can also damage property and hurt people as the mobile earth moves down a sloped surface. The earth can be made of sand rock or other material capable of moving a long distance due to gravitational pull and the loose properties. The shaking can also cause liquefaction and sand blows that damage property and cover large areas with sand. Tsunamis are the result of earthquakes and can be one of the deadliest results of such a geological disturbance. Tsunamis are large waves that are created when an earthquake occurs at sea. The plates shift and the motion causes a huge wave that builds up momentum and size as it reaches land masses. These huge waves as high as 100 feet can take out buildings, structures and cause destruction for miles. Many people have become homeless or

have lost family and friends in furious flood of tsunami. Fires often associated with broken electrical and gas lines are one of the common side effects of tremors/earthquakes. Gas is set free as gas lines are broken and a spark will generate into “inferno”. Most often is complicated as water lines are broken and so there is no water to extinguish the fire. The San Francisco earthquake of 1906 caused 90% of damage by fire. Flooding can come from many sources such as broken water main pipes, dams that fail due to earthquake. When an earthquake breaks a dam or leave along a river, the water from the river or the reservoir floods the area, damaging buildings and maybe sweeping away or drowning people. People are affected in different ways by tremors/earthquakes. Even when no one is hurt, a tremor can have lasting effects on the human psyche. When the tremor/earthquake occurs, most people seek open air so that the building they are in does not crush them while others freeze due to shock. Tremor/earthquakes have resulted to many people been homeless and unable to rebuild their lives afterwards. In addition to the death toll, tremors/earthquakes can cost billions of dollars in damage to repair. The 2011 Japanese earthquake was estimated to cost \$232 billion dollars to repair and the damage of the 2004 Indonesian earthquake worth is estimated at \$8.4 billion dollars (United States Geological Survey 2007). In addition to physical damage, the destroyed infrastructure may the cause economies of the affected areas to suffer. Again, areas with poor building standards suffer most, although as evidenced by the case of Japan, earthquake can devastate developed economies as well. Table 2 shows that recent earthquakes of the first decade of the 21st century have resulted in near humanitarian and environmental catastrophe. Tremors/earthquakes have contributed on the average the highest human death toll besides material damage to both rich and poor countries across the world over the past decade. It is reported that earthquakes killed the most people over the period from 2000 to

2008 – an average of 50,184 people a year (theguardian.com: A decade of disasters – get the key data). With the recent catastrophe in Japan, comparison have emerged with that of January 2010 earthquake in Haiti. While the final human cost of the Japan disaster is still unknown, it is still likely to compare with 222,570 – strong death toll from Haiti earthquake.

Nigeria, like many other developing countries with tropical climate and unstable land forms, coupled with increasing population growth, illiteracy, poverty and lack of well-developed infrastructure is more vulnerable to suffer from the damaging potential of such disasters. Accordingly, various researches have shown that Nigeria is likely to experience major earthquakes in the future (Adepelumi et al. 2008, 2009, Onuoha et al. 1988).

Table 2 List of some recent Earthquakes (Shiwua 2012)

Name	Date of event	Type of hazard	Main cities affected	Total number of deaths	Total number of affected	Total damages US \$bn
Japan earthquake	11 th March 2011	Earthquake and tsunami	Sendai, Ichihera, Fukushima, Minamisanriku, Onagawa, Rikuzentakata, Ofunato, Kesennuma	5178 (as of 17:08:11)	Not yet known	Not yet known
Haiti earthquake	12 th January 2010	Earthquake	Port-au-Prince	222570	3400000	n/a
Sichuan earthquake	12 May 2008	Earthquake	Beichuan, Dujiangyan, Shifang, Mianzhu, Juyuan, Chengdu, Diongai, Deyang	87476	45976596	85
Java earthquake	26 th May 2006	Earthquake	Yogyakarta	5778	3177923	3.1
Kashmir earthquake	8 th October 2005	Earthquake	Muzaffarabad	73338	5128000	5.2
South Asian tsunami	26 th December 2004	Earthquake and tsunami	Bandu Acch, Chennai (some damages)	226408	2321700	9.2
Bam earthquake	26 th December 2004	Earthquake	Bam	26796	267628	0.5
Gurjarat earthquake	26 th January 2001	Earthquake	Bhuj, Ahmedabad	20005	6328112	2.6

Other problems associated with earthquake include: -

Deforestation, soil erosion, depletion & pollution of water resources, unhygienic conditions and precarious sanitation due to scarcity of safe drinking water, lack of latrines and showers, psychosocial and economic welfare of local communities during prolonged residency of the affected population in temporary settlements. These have impact on the physical and mental health which can alter the social context and habits of the people on short and long term bases.

Proactiveness and the mitigation of earthquakes

A natural disaster could occur in a few decades, in a year, tomorrow, or this very minute. Currently, there is no technology that can prevent extreme natural catastrophes. The precise time that tremors/earthquakes occur

cannot be changed, however, the impact on humans and the environment can be changed. The results obtained by Adepelumi et al. in 2008 offer useful information regarding earthquake potential and seismicity of the study areas, to the effect that most possibly, a large earthquake of magnitude M 5 may occur in the next 30 years in Nigeria, particularly areas within the Ifewara-Zungeru fault zone (see figure 2) which has been shown to be linked with the Atlantic fracture system (Adepelumi 2009; Anifowose 2010; Olujide 1989; Olurunfemi 1986). Some of the other important fault systems in Nigeria are the Anka and Kalangai fault systems. Anka and Kalangai fault systems are interpreted to have resulted from transcurrent movements and particularly, the 250km long NE – SW trending Ifewara fault zone which has a link with the Atlantic fracture system (Adepelumi et al. 2009). The dynamics of the Atlantic fracture

zones have been suggested to be responsible for the seismic activities experienced in the areas (Akpan et al. 2010). Tremors/Earthquakes are of great threat to Mankind and many of these effects must be taken into consideration when developing effective and proactive measures against the catastrophic impact of an earthquake. The energy released from the earthquake can be up to 10,000 times more than the first atomic bomb (Ajakaiye et al. 1986). Earthquakes also trigger tsunamis, fires, and landslides and each often destroys infrastructure. Avalanches, slumps and rock slides are all triggered by ground shaking. An example would be the April 2015 Nepal Earthquake, it triggered an avalanche on the Mount Everest, killing 21 people and then it also triggered an avalanche in the Langtang valley where more than 250 people were reported missing (Ajakaiye et al. 1984).

The severity of damage to manmade structures, such as bridges, dams and buildings varies from the intensity of the earthquake and from the quality of construction of the buildings. Seismologists believe that earthquakes do not kill people, the building do. Early warning systems are been developed, and possibly could detect earthquakes. However, earthquake prediction is momentarily still inaccurate and it lacks precision. Further measures to be taken and developed include warning systems, as well as proper medical aid after the occurrence of the earthquake. Keeping the effect of earthquake in mind, it is certain that the most important measure to take is to construct stable buildings and infrastructure to prevent collapses. In many cases, collapsing buildings and facilities cause many human deaths. Building infrastructure with stable material, such as steel and wood, would be a significant step to prevent collapses. People must be aware of what natural disasters they are likely to encounter. For instance, the media has become much more prevalent in the past few years making it ideal to spread awareness and information. Television, social media

platforms and radios must be prepared to respond speedily and effectively to catastrophes. Early warning systems can alarm the people through messages over phones and computers, which enable evacuation to a safer environment. As prominent as early warning systems are, education, a rather unexpected measure is certainly to be considered. Educational materials about preparedness, warnings, and protection should be implemented in school curricula, in order for children to receive the information they need to protect themselves before, during and after the occurrence of an earthquake, as well as any other natural catastrophe. Indonesia and Romania are among countries that have now adjusted its school curricula to include classes concerning disaster risk reduction and preparedness. Nigeria and other Less Economically Developed Countries (LEDCs) can take a clue into that for an effective risk reduction management against all natural disasters.

Conclusion

The aftermath of the Kwoi tremor of 11th and 12th September 2016 of magnitude 2.6-3.0 resulted to damages on roads, bridges and buildings. Since this event was unexpected and unpopular around this settlement and the State in general, there was psychological, psychosocial and economic trauma among the dwellers of Kwoi and immediate environs of Samban-daji, Nok, and Chori. Just like any other seismic events in Nigeria, there is always the fear of whether there would be a repeat of the event. This event shows the lack of awareness of majority of people within the locality as to what could be the cause of the tremor, because the dwellers have a misconception that a “traditional tree” was cut down by the Youths and that the tremor was the consequence of their actions. There should be an increasing awareness on the kind of human activities that could trigger such an event, Government should promulgate laws that will check and limit such human activities such as illegal mining, indiscriminate construction of

boreholes and bad farming practices among others. People should be encouraged to construct stable buildings and infrastructures to prevent collapses in the event of a future occurrence by using stable building materials such as steel and wood. Even though there is still no known geological possibility of an earthquake or even a tremor beyond the Ifeware-Zungeru fault zone, however, previous and recent happenings within Nigeria has re-awaken our consciousness on the need to develop and put in place early warning signal mechanisms, increased funding on research, and equipping existing seismographic stations with world class technology to march the growing concern and challenges that comes with seismic events in Nigeria.

References

- Afegbua, K. U., Yakubu, T. A., Akpan, O. U., Duncan, D. and Usifoh, E. S. (2011). Towards an Integrated Seismic Hazard Monitoring in Nigeria using Geophysical and Geodetic Techniques. *International Journal of the Physical Sciences*, 6(28): 6385-6393.
- Akpan, O. U., and Yakubu, T. A. (2010). A Review of Earthquake Occurrences and Observations in Nigeria, *Earthquake Science* 23(3): 289-294.
- Anifowose, A. Y. B., Oladapo, M. I., Akpan, O. U., Ologun, C. O., Adeoye-Oladapo, O. O., Tsebeje, S. Y. and Yakubu T. A. (2010). Systematic Multi-technique Mapping of the Southern Flank of Iwaraja Fault, Nigeria. *Journal of Applied Science and Technology*, 15(1-2): 70-76.
- Adepelumi, A. A. (2009). Short-term probabilistic forecasting of earthquakes occurrences in South-Western Nigeria, Technical Report Submitted to the centre for Geodesy and Geodynamics, Toro, Nigeria.
- Adepelumi, A. A., Ako, B. D., Ajayi, T. R., Olorunfemi, A. O., Awoyemi, M. O. and Falebita, D. E. (2008). Integrated Geophysical Mapping of the Ifewara Transcurrent Fault system, Nigeria. *Journal of African Earth Sciences*, 52(4-5): 161-166.
- Ajakaiye, D. E., Danuyan, M. A., Ojo, S. B., and Onuoha, K. M. (1987). July 28, 1984 South-western Nigeria Earthquake and its Implications for Tectonics and Evolution of Nigeria". *Journal of Geodynamics*, 7: 205-214.
- Ajakaiye, D. E., Hall, D. H., Millar, T. W., Verheijen, P. J., Awad, M. B., and Ojo, S. B. (1986). Aeromagnetic Anomalies and Tectonic Trends in and around the Benue Trough. *Nigeria Nature*, 319: 582-584.
- Berlin Model United Nations. (2016). Ending Human Suffering: Reassessing the UN's Role in a Globalized World.
- Burke, K. (1969). Seismic Areas of the Guinea Coast where Atlantic Fracture zones reach Africa. *Nature*, 222 (5194): 655-657.
- EM-DAT The International Disaster Database. (2011). Retrieved march 3, 2011 and July 28, 2011 from www.endat.be/.
- Eze, C. L., Sunday, V. N., Ugwu, S. A., Uko E. D. and Ngah S. A. (2011). Mechanical Model for Nigerian Inter-plate earth Tremors. <http://www.earthzine.org/2011/05/17/mechanical-model-for-nigerian-intraplate-earth-tremors>
- Ige, E. A., Ike, E. C., and Woakes, M. (1985). Some Geological Aspects of Nigerian Seismicity: Paper presented at the National Seminar on Earthquake in Nigeria, Ahmadu Bello University, Zaria, Nigeria, Abstract volume 10.
- Mohammed, S. T., Lar, U. A., Yakubu, T. A., Umar, A. K. and Dauda D. (2015). The Review of the Historical and Recent Seismic Activity in Nigeria. *IOSR Journal of Applied Geology and Geophysics*: 48-56.
- National Geographic. (2016). N.P., n.d web.06 June 2016. Nepal's Earthquake: One year later. The Atlantic Media Company.
- Olujide, P. O., Udoh, A. N. (1989). Preliminary comments on the fracture system of Nigeria, proceedings of the National Seminar on Earthquake in Nigeria: 97-109.
- Olorunfemi, M. O., Olarewaju, V. O., Awei, M. (1986). Geophysical investigation of a fault zone – Case history from Ile-Ife, Southwest

Nigeria, Geophysical prospecting, 34(8): 1277-1284.

Onuoha, K.M. (2010). Nigeria's Seismicity: past, present and future, presented at the workshop on Global Trend of Earthquake Occurrence: Nigeria's Monitoring Capabilities Abuja.

Onuoha, K.M. (1988). Earthquake hazard prevention and mitigation in the West African sub-region, Natural and Man-made Hazard: 787-797.

Osagie, E. O. (2008). Seismic activity in Nigeria. *Pacific Journal of Science Technology*, 9(2): 1-6.

Shiwua, A. J. (2012). Seismicity in Nigeria: The Need for Earthquake –Resistant Structures.

United States Geological Survey: Earthquake Facts and Statistics. Sydney morning Herald. Tsunami Death Toll passes 283: 300.

Wisner, B., Blaikie, P., Cannon, T. And Davis, I., (2008). At Risk: Natural hazards, people's vulnerability and disasters. 2nd Edition. New York: Routledge, 275.

Determination of Radioactivity Levels of ^{222}Ra , ^{40}K and ^{232}Th using Gamma Ray Spectrometry within Kaduna North Local Government Area of Kaduna State, Nigeria

Sarki, S. H¹, Kassimu, A. A.², Daniel. H. I.³ and Kure, N.⁴

¹Department of Science and Laboratory Technology, Nuhu Bamalli Polytechnic Zaria, Nigeria

²Air Force Research and Development Centre, Kaduna

^{3,4}Department of Physics, Faculty of Sciences, Kaduna State University, Kaduna State, Nigeria

Corresponding author's e-mail: Sundaysarki@yahoo.com

ABSTRACT

This paper presents the determination of radioactivity levels of ^{222}Ra , ^{40}K and ^{232}Th using Gamma Ray Spectrometry within Kaduna North Local Government Area of Kaduna State, Nigeria. Radioactivity levels of nine samples taken from three different locations within Kaduna North Local Government Area of Kaduna State, Nigeria were measured by means of gamma-ray spectrometry with NaI (Tl) detector to determine activity concentration of ^{40}K , ^{226}Ra and ^{232}Th . Results obtained indicate highest activity concentration of ^{40}K , ^{226}Ra and ^{232}Th from soil samples collected from UR1 (502.4883 Bqkg⁻¹), UK2 (74.6234 Bqkg⁻¹) and MA1 (195.0969 Bqkg⁻¹). The mean activity of ^{40}K (192.4486 Bqkg⁻¹) was found to be lower than the world average of 420 Bqkg⁻¹, while the mean activity concentrations of ^{232}Th (96.8200 Bqkg⁻¹) and ^{226}Ra (45.2556 Bqkg⁻¹) were found to be above the world average of 50 Bqkg⁻¹ and lower than the world average of 370 Bqkg⁻¹ respectively.

Keywords: Radionuclides, soil samples, radioactivity level, activity concentration, Gamma Ray spectrometry.

Introduction

The human environment is composed largely of soil, water, gases and in all probability microorganisms. Man uses soil or land for various purposes ranging from citing of industries, agriculture and erecting permanent structures for dwelling purposes. The environmentalists have studied for decades the impact of man's activities on his environment and vice-versa. Soil is a product of weathering and contains fossils, organic and inorganic matter, gases and physical contaminants called radionuclides or radioisotopes (Ayodele 2017).

Radionuclides occur naturally in the soil in the form of the Uranium and Thorium decay series (^{226}Ra and ^{232}Th) and natural potassium ^{40}K . The activity concentrations of these primordial radionuclides vary from one location to another and the distribution has been found to be largely dependent on geological and geographical conditions, and appear at

different levels in the soils of each region of the world (UNCEAR 2000). Hence Nuclear Scientists and or radiologists are working to characterize each environment based on the activity concentration and distribution of these radionuclides. Several studies have been carried out to assess the activity concentrations of these radionuclides around the world (McAulay and Morgan, 1988; Jibrin et al. 2009; Boukenfouf and Boucenna, 2011; Alaamer, 2008; Ayodele et al. 2017).

This research work is aimed at determining the levels of primordial radionuclides ^{226}Ra , ^{232}Th , and ^{40}K in selected sampling sites within Kaduna North Local Government Area of Kaduna state, Nigeria using a 76x76mm NaI(Tl) detector crystal device used primarily for monitoring, rapid identification and assessment of radioactivity and absorbed dose rates in the air.

Materials and Methods

In this research, a Rados meter was used (*RDS 120*) for background mapping. The Rados is a versatile gamma radiation detector designed for wide range of applications involving the detection of abnormal or elevated radiation levels. It could also be used to determine background radiation of a place. Its performance and its user-friendly interface make it the perfectly suitable devices for monitoring land detections of radiological hazards.

Monitoring of any release of radioactivity to the environment is important for environmental protection against ionizing radiation. Rapid and accurate methods for the measurements are essential. Many important isotopes in the naturally occurring radioactive materials (NORM) and technology enhance natural occurring radioactive materials (TENORM) have some suitable gamma rays, allowing qualitative and quantitative determination of the radionuclides by high-resolution gamma spectrometry.

Measurements of radiation levels and the concentrations of radionuclides in the environment are accomplished employing appropriate nuclear instruments. The radioactivity level in this study was detected and analyzed employing $76 \times 76 \text{ mm NaI(Tl)}$ detector crystal optically coupled to a photomultiplier tube (PMT) to determine the radioactivity level of each of the three radionuclides having spectral energy window and energy calibration.

Sample Collection

The samples were collected within Kaduna North Local Government Area (LGA) of Kaduna State, Nigeria, one of 774 Local Government Areas (LGAs) in Nigeria.

A total of nine soil samples were collected from three different locations namely Ungwan Rimi, Malali and Ungwan Kanawa respectively. Figure 1, presents a Google map of the sample locations within Kaduna North Local Government Area, Kaduna State, Nigeria.



Fig. 1 Google map of the sample locations within Kaduna North Local Government Area, Kaduna State, Nigeria

Soil Sample Preparation

Each of the soil samples collected was dried and crushed to a fine powder with the use of pulveriser. The packaging of the samples into radon-impermeable cylindrical plastic

containers which were selected based on the space allocation of the detector vessel which measures $76 \times 76 \text{ mm}$ in dimension (geometry) was also carried out to prevent ^{222}Ra from escaping; the packaging in each case was triple

sealed.

The sealing process includes smearing of the inner rim of each container lid with Vaseline jelly, filling the lid assembly gap with candle wax to block the gaps between lid and container, and tight- sealing lid-container with masking adhesive tape. After the samples were prepared the empty container were weighed to know the weight of the empty container and when the sample was sealed into the container it was then weighed again to know the weight of empty container and soil sample, then the weight of empty container and sample was subtracted from the weight of empty container to get the weight of soil samples. Radon and its short-lived progenies were allowed to reach secular radioactive equilibrium by storing the samples for 30 days at ambient temperature prior to gamma spectroscopy measurements.

Evaluation of Radioactivity of Samples

The major nuclear technique employed in the analysis of samples for background activity is the Gamma Spectrometry using a $76 \times 76\text{mm}$ NaI(Tl) detector (Ibrahim et al. 2013). The assembly has a preamble incorporated into it and a 1kilovolt external source. The detector is enclosed in a 6cm lead shield with cadmium and copper sheets. This arrangement is aimed at minimizing the effects of background and scattered radiation.

Dose calculation

To assess any radiological hazard, the

absorbed dose rate (nGy h^{-1}) in air at 1m above the ground surface due to the mean specific activities of ^{226}Ra , ^{232}Th , and ^{40}K (Bq kg^{-1}) in the collected samples, can be computed using,

$$D(\text{nGy h}^{-1}) = DCF_{\text{Ra}}C_{\text{Ra}} + DCF_{\text{Th}}C_{\text{Th}} + DCF_{\text{K}}C_{\text{K}} \quad (1)$$

Where D is the air absorbed dose rate, DCF_{K} (0.0417), DCF_{Ra} (0.462) and DCF_{Th} (0.0604) are the dose rate conversion factors and C_{Ra} , C_{Th} and C_{K} are the concentration of ^{226}Ra , ^{232}Th , and ^{40}K in the respective ^{226}Ra , ^{232}Th , and ^{40}K materials (Ibrahim et al. 2013).

Calibration and Efficiency Determinations

Calibration of the system for energy and efficiency were done using two calibration point source; $C_s - 137$ and $C_o - 60$. These were done with the amplifier gain that gives 72% energy resolution for 66.16 keV of $C_s - 137$ and counted for 30 minutes.

Background measurement

Generally, the background count rate is not constant but keeps fluctuating. This is because radioactive decay is a random process. The background count rate was done for 29000 seconds (10hrs 50mins). Table 1 show the spectral energy window used in the analysis in the subsequent section, while the energy calibration for quantitative spectral analysis is given in Table 2.

Table 1 Spectral Energy Window Used in the Analysis.

Isotope	Gamma Energy (KeV)	Energy Window (KeV)
Ra – 226	1764.000	1620 – 1820
Th – 232	2614.500	2480 – 2820
K – 40	1460	1380 – 1550

Table 2 Energy Calibration for quantitative Spectral Analysis.

Isotope	Calibration Factors		Conversion Factors (Bq kg^{-1})	Detection Limits	
	ppm	ppm	ppm	ppm	Bq kg^{-1}
K – 40	0.026	6.431	0.032	454.54	14.54
Ra – 226	10.500	8.632	12.200	0.32	3.84
Th – 232	3.612	8.768	4.120	2.27	9.08

Spectra Analysis

The computer based multi-channel analyzer system with emulsion software (MAESTRO-32) was used for spectra acquisition. Based on two-point energy calibration as set for the operation, the prominent peaks were identified in a bench-mark spectrum and the appropriate regions of interest were set up. These peaks which are characteristic of typical environment spectral are:

- The 295, 352, 607, 1120 and 1765 keV peaks in the Uranium series,
- The 238, 510. 583, 911, 965 and 2615 keV peaks in the Thorium series,
- The 1460 keV peak of potassium.

The set energy bands define the peaks of where the left and right channel markers are representative of the Compton continuum. Detector's specific calibration factors (efficiency) were applied to convert from net count rate to concentration. Only peaks with reasonable g- ray emission probability were considered.

Calculation of Activity Concentration

Following spectrum analysis, calculation of count rates for each detected photo peaks and radiological concentration (activities per unit mass or specific activities) of detected radio nuclides depends on the establishment of secular equilibrium reached between ^{232}Th , ^{238}U and their decay products. The concentration of ^{232}Th was determined from the average concentration of ^{208}Tl and ^{238}Ac and that of ^{238}U was determined from the average concentration ^{214}Pb and ^{214}Bi decay products. Thus, accurate radionuclide concentrations of

^{232}Th and ^{238}U were determined, whereas a true measurement of ^{40}K concentration was made.

The specific activity ($Bqkg^{-1}$) A_{Ei} of a nuclide and for a peak at energy E , is given by

$$A_{Ei} = \frac{N_{Ei}}{\epsilon_E t_d M_s} \quad (2)$$

Where, N_{Ei} is the net peak area of a peak energy E , ϵ_E is the detection efficiency at energy E , t is the counting live-time, g_d is the gamma ray yield per disintegration of specific nuclide for a transition of energy E and M_s the mass in kg of the measured sample. For more than one peak in the energy range analysis, the peak activities are averaged and the result is weighted average nuclide activity.

The total uncertainty (S_{tot}) and weighted systematic activity value is composed of counting statistic (S_{st}) and weighted systematic errors (S_{sys}) calculated by the following formula

$$S_{tot} = \sqrt{S_{st}^2 + \frac{1}{d} S_{sys}^2} \quad (3)$$

(Gyuk et al. 2017)

Results and Discussion

The result of radioactivity level in nine (9) soil samples from , Malali, Ungwar Rimi, and Ungwar Kanawa within Kaduna North local government area of Kaduna metropolis was measured by means of gamma-ray spectrometry with *Nal (TI)* detector to establish a data for activity concentration ^{226}Ra , ^{232}Th , and ^{40}K . Table 3 and 4, presents the results of background radiation reading and Gamma Ray spectrometer reading at the nine (9) different sites respectively.

Table 3 Background Radiation Reading of Kaduna North Local Government Area

S/NO	Sample ID	RDS 120 SERIAL NO. 990100 ($\mu\text{SV/hr}$)			MEAN OF EXPOSURE RATE ($\mu\text{SV/hr}$)	RDS 120 SERIAL NO. 210152 ($\mu\text{SV/hr}$)			MEAN OF EXPOSURE RATE ($\mu\text{SV/hr}$)	MEAN OF EXPOSURE RATE ($\mu\text{SV/hr}$)
		1	2	3		1	2	3		
1	UR1	0.12	0.11	0.13	0.12 ± 0.008	0.13	0.12	0.14	0.13 ± 0.008	0.13 ± 0.008
2	UR2	0.17	0.17	0.17	0.17 ± 0.006	0.15	0.14	0.17	0.15 ± 0.008	0.16 ± 0.006
3	UR3	0.14	0.13	0.15	0.14 ± 0.008	0.13	0.12	0.15	0.13 ± 0.008	0.14 ± 0.004
4	MA1	0.15	0.15	0.16	0.15 ± 0.006	0.15	0.15	0.14	0.15 ± 0.008	0.15 ± 0.007
5	MA2	0.11	0.11	0.11	0.11 ± 0.013	0.11	0.11	0.11	0.11 ± 0.008	0.11 ± 0.011
6	MA3	0.11	0.11	0.12	0.11 ± 0.010	0.12	0.12	0.12	0.12 ± 0.006	0.12 ± 0.008
7	UK1	0.11	0.11	0.11	0.11 ± 0.016	0.11	0.11	0.11	0.11 ± 0.008	0.11 ± 0.024
8	UK2	0.11	0.11	0.12	0.11 ± 0.008	0.11	0.11	0.11	0.11 ± 0.008	0.11 ± 0.008
9	UK3	0.11	0.11	0.12	0.11 ± 0.006	0.11	0.11	0.11	0.11 ± 0.010	0.11 ± 0.008

The highest activity concentration of ^{40}K , ^{226}Ra and ^{232}Th were found in soil collected from location UR1 (502.4883 Bqkg⁻¹), UK2 (74.6234 Bqkg⁻¹) and MA1 (195.0969 Bqkg⁻¹), respectively, where the mean activity of ^{40}K (192.4486 Bqkg⁻¹) is lower than the world

average of 420 Bqkg⁻¹ and the mean activity concentrations of ^{232}Th (96.8200 Bqkg⁻¹) is above the world average of 50 Bqkg⁻¹. ^{226}Ra have the lowest mean activity concentration of 45.2556 Bqkg⁻¹, is lower than the world average of 370 Bqkg⁻¹.

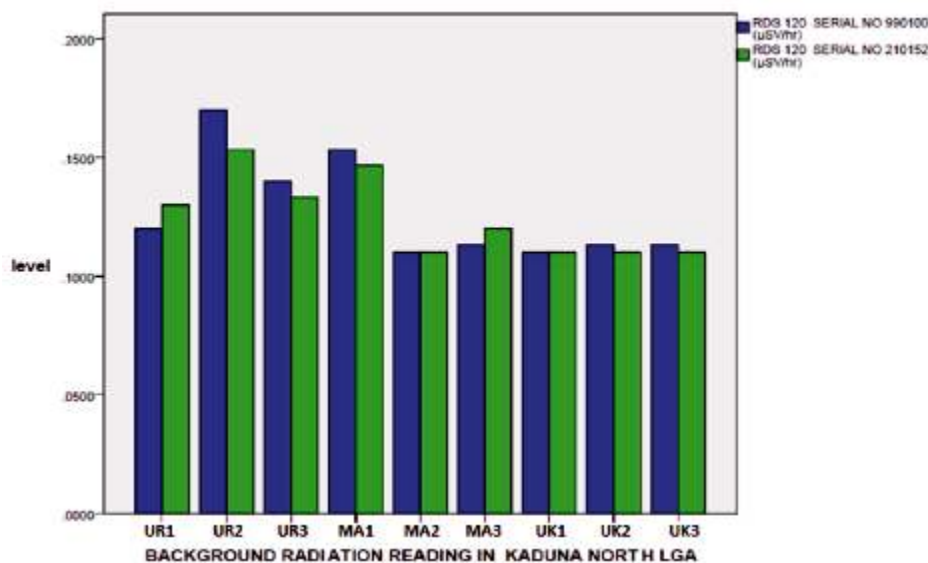


Fig. 2 Background radiation reading for Kaduna North Local Government Area

Figure 2 is the graphical representation of the result from background radiation readings and gamma spectrometry analysis obtained from soil samples in Kaduna North Local Government Area. Here UR (1-3), MA (1-3), and UK (1-3) represents Malali, Ungwar Rimi, and Ungwar Kanawa respectively, while the numbers 1, 2 and 3 are the three locations where the soil samples were taken for each of the

areas.

The chart figure 2 shows a background minimum reading at MA2 and UK1 while UR2 has the maximum background reading. The reading was obtained using two Rados portal survey meter (RDS 120), one has a serial number 990100 (mSv/hr), and second with serial number 210152 (mSv/hr).

Table 4 Gamma Ray Spectrometry Reading

S/N	Sample ID	K-40	Error ±	K-40	Error ±	Ra-226	Error ±	Ra-226	Error ±	Th-232	Error ±	Th-232	Error ±
		(CPS)	(CPS)	(Bqkg ⁻¹)	(Bqkg ⁻¹)	(CPS)	(CPS)	(Bqkg ⁻¹)	(Bqkg ⁻¹)	(CPS)	(CPS)	(Bqkg ⁻¹)	(Bqkg ⁻¹)
1	UR1	0.3231	0.0003	502.4883	0.4665	0.0531	0.0018	61.5295	2.0857	0.1125	0.007	128.2782	0.7982
2	UR2	0.0851	0.0032	132.3484	4.9757	0.0311	0.0028	36.0371	3.2445	0.0841	0.0021	95.8951	2.3945
3	UR3	0.1172	0.0029	182.2706	4.5101	0.0641	0.0011	74.2758	1.2746	0.0822	0.0031	93.7286	3.5348
4	MA1	0.0511	0.0004	79.4712	0.6221	0.0057	0.0062	6.6049	7.1842	0.1711	0.0009	195.0969	1.0262
5	MA2	0.0965	0.0029	150.0778	4.5101	0.0411	0.0003	47.6246	0.3476	0.0832	0.0035	94.8689	3.9909
6	MA3	0.1183	0.0003	183.9813	0.4665	0.0533	0.0006	61.7613	0.6952	0.0093	0.0011	10.6043	1.2543
7	UK1	0.0914	0.0018	142.1462	2.7994	0.0292	0.0030	33.8355	3.4762	0.0836	0.0023	95.3250	2.6226
8	UK2	0.1512	0.0036	235.1477	5.5983	0.0644	0.0032	74.6234	3.7080	0.0551	0.0043	62.8278	4.9031
9	UK3	0.0798	0.0007	124.1058	1.0885	0.0095	0.0029	11.0081	3.3604	0.0831	0.0020	94.7548	2.2805

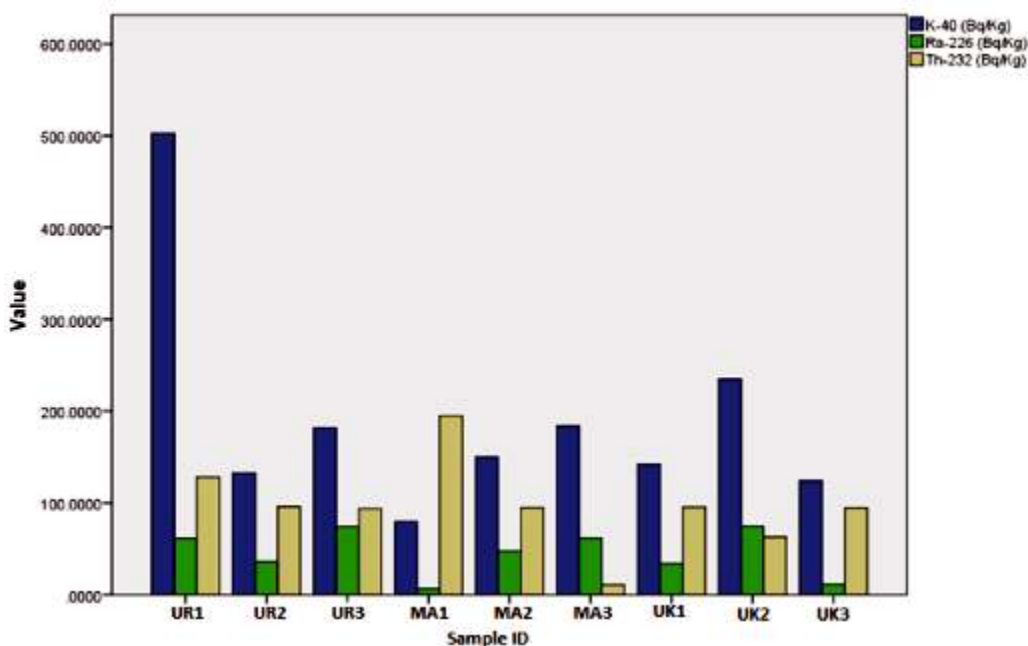


Fig 3 Result of Gamma Ray Spectrometry for ^{226}Ra , ^{232}Th , and ^{40}K done on twelve (12) soil Samples within Kaduna North L.G.A

Figure 3 shows the chart result obtained from Gamma spectrometry done in Centre for Energy Research and Training Zaria, on the soil samples taken from Kaduna North L.G.A. The results show that ^{40}K is more abundant among the three radio nuclides and is peaked at UR1 and is minimum at MA1. ^{232}Th is the second and it is peaked at MA1, and it is minimum at MA1. ^{226}Ra is the least among the three Radio nuclides and is also peaked at MA1 and the minimum is at MA3. Thus, Figures 2 & 3 shows that UR2 has the maximum background reading and it also shows that among the three radio nuclides ^{40}K is maximum.

Conclusion

Radioactivity levels of nine samples taken from three different locations within Kaduna North local Government area of Kaduna state, Nigeria has been measured by means of gamma-ray spectrometry with *Nal (TI)* detector to determine activity concentration of ^{40}K , ^{226}Ra and ^{232}Th .

Measured results indicate highest activity

concentration of ^{40}K , ^{226}Ra and ^{232}Th in collected soils from location UR1 (502.4883 Bqkg⁻¹), UK2 (74.6234 Bqkg⁻¹) and MA1 (195.0969 Bqkg⁻¹), respectively. The mean activity of ^{40}K (192.4486 Bqkg⁻¹), was found to be lower than the world average of 420 Bqkg⁻¹. Similarly, the mean activity concentrations of ^{232}Th (96.8200 Bqkg⁻¹) was found to be above the world average of 50 Bqkg⁻¹, while ^{226}Ra which has the lowest mean activity concentration of 45.2556 Bqkg⁻¹, was found to be lower than the world average of 370 Bqkg⁻¹.

Reference

- Ayodele, A. E., Arogunjo, A. M., Ajisafe, J. I. and Arije, O. T. (2017). Health Detriment Associated with Exposure to Natural Radioactivity from the Soil of Ondo and Ekiti States South Western, Nigeria. *Physical Science International Journal*, 14(4): 1-11.
- UNSCEAR (2000). United Nations Scientific Committee on the Effects of Atomic Radiation, Report to the General Assembly, with Scientific Annexes. I.

- McAulay, I. R. and Morgan, D. (1988) Natural radioactivity in soils in the republic of Ireland, *Radiation Protection Dosimetry*. 24(1-4): 47-49.
- Jibrin, N. N., Alausa S. K. and Farai, I. P. (2009). Radiological hazard indices due to activity concentrations of natural radionuclides in farm soils from two high background radiation areas in Nigeria. *International Journal of Low Radiation*. 6(2): 79-95.
- Alaamer, A. S. (2008). Assessment of human exposure to natural sources of radiation in soil of Riyadh, Saudi Arabia. *Turkish Journal Engineering and Environmental Science*, 32: 229–234.
- Boukenfouf W. and Boucenna A. (2011). The radioactivity measurements in soils and fertilizers using gamma spectrometry technique. *Journal of Environmental Radioactivity*, 102(4): 336-339.
- Ayodele, A. E., Arogunjo, A. M., Ajisafe, J. I. and Arije, O. T. (2017). Health Detriment Associated with Exposure to Natural Radioactivity from the Soil of Ondo and Ekiti States South Western, Nigeria. *Physical Science International Journal*, 14(4): 1-11.
- Ibrahim, U., Akpa, T. C. and Daniel, I. H. (2013). Assessment of Radioactivity Concentration in Soil of Some Mining Areas in Central Nasarawa State, Nigeria. *Science World Journal*, 8(2): 7-12.
- Gyuk, P. M., Habila, S. S., Dogara, M. D., Kure, N., Daniel, H. I. and Handan T. E. (2017). Determination of radioactivity levels in soil samples at Chikun environment of Kaduna metropolis using gamma ray spectrometry. *Science World Journal*, 12(2): 2-3.

Thermal Radiation Measurements at Agbada Flow and Metering Station, Igwuruta in Ikwerre Local Government Area of Rivers State, Nigeria.

Ogbonda, C.

Department of Physics, Ignatius Ajuru University of Education,
Rumuolumeni, Port Harcourt, Rivers State, Nigeria
Corresponding author's e-mail: clement.ogbonda@iaue.edu.ng

ABSTRACT

This study presents solar radiation measurement at Agbada flow and metering station using a simple jar and thermometer within 20 minutes' time interval. The radiation constants obtained during this study within the intervals of 50 m and 250 m are 2055.91 Wm^{-2} and 1956.86 Wm^{-2} . It was deduced that the duration of time is directly proportional to amount of solar radiation reaching the earth. A comparison between radiation constant of 1245.85 Wm^{-2} for Rivers State as reported by Torubeli in 1996 was made and the differences of Solar Radiation constants obtained for the heat effect are about 810.06 Wm^{-2} at 50 m and 711.01 Wm^{-2} at 250 m respectively. The radiation effect of about 810.06 Wm^{-2} and 711.01 Wm^{-2} is in excess, which means that the flow station is not habitable because of enormous heat. It was also observed that radiation of heat from other thermal sources like oil pump, compressors, generators oil pipe, etc contributed to the increased heat (high temperature) of the environment.

Keywords: solar constants, thermal radiation, Agbada flow station, radiation intensity, jar, and thermometer

Introduction

In recent times a great deal of research has been carried out on different aspects of environmental pollution in this country, however, very little appears to have been done in the area of thermal (heat) radiation. Yet, thermal radiation remains one very important pollutant of the environment. There are many sources of heat radiation, these includes, the sun, the flares, flames, fuel combustible machines, engines and sparks.

The sun's radiation (Solar radiation) is imposed on other sources when these other sources are directly in the open. The solar energy received at ground level, horizontally, varies according to latitude and season (Chineke 2002). Temperature is controlled by the amount, duration, and intensity of solar output which in turn is controlled mostly by the season and the position of the overhead sun in Nigeria. Extreme weather and climate events have been studied extensively in recent decades because of its significantly detrimental effects on society and natural ecosystems, of which temperature extremes are one of the most commonly examined due to (a) temperature records tend to be long and (b)

projections of temperature tend to be more robust (Schoof and Robeson 2016). Temperature extremes and their changes have been shown to influence daily mortality in Spain (Carmona *et al.* 2016), tendencies of accidents in building facilities and workers' accidents in Japan (Tamura and Tanaka 2016), injury risk from motor vehicle accidents in Maryland (Liu *et al.* 2016), wheat production systems in India (Aryal *et al.* 2016).

Temperature is so important because it influences Health, Agriculture, Evaporation, Transport, Rainfall, and Human comfort among others (Ogbonda 2014). Knowledge of the heat condition of an area has always been a fundamental parameter in the choice of sites for human settlement or activities. The variations of heat condition are due to many phenomena, some regular and predictable and others essentially random, like atmospheric impurities, clouds and so on. Solar radiation constant received directly from the sun in the tropics range between 1050 Wm^{-2} and 1450 Wm^{-2} ; while in colder regions of the earth the estimates range between 0 and 1024 Wm^{-2} in normal environment. Over the years, temperature in Nigeria is not static. Many

studies have shown that there has been a steady rise in temperature across the country. Audu in (2012) observed general increase in mean minimum temperature of 3°C per decade based on data for 40 years from Nigeria.

In this report, a study is carried out to estimate and determine thermal constants and intensity of radiation within the Agbada flow and Metering Station. Sources were not isolated because it would be practically impossible since the stations remained in normal operation as the study was carried out. However, it should be noted that the main sources of radiation in the stations apart from the sun, include the Flare, generator engines, pumps, compressors and pipes carrying crude. The attention is on the flare which incidentally remains a major source among all these. Thermal radiation measurement fall into two categories: measurement of radiant energy received from some source and the measurement of the radiation characteristics of the source or materials in the environment. Precisely, the work reported in this study is of the first category.

Theory of Radiation Measurement

Two laws are basically involved in radiation measurement. These are Kirchhoff's law which applies only on a spectral basis. It relates real radiation to black body radiation according to;

$$e = \frac{\int_0^\infty I(\lambda, T) d\lambda}{\int_0^\infty I_{bb}(\lambda, T) d\lambda} \quad (1)$$

Where e is total emissivity, I is intensity (gradient) of radiation, T is temperature in K , λ is spectral wavelength and bb refers to the blackbody. Consequently, the emissivity of an object is the ratio of the energy emitted with identical temperature by the object itself and the blackbody respectively.

$$e = \frac{e_{emitted}}{e_{bb}} \quad (2)$$

On the other hand the absorptivity ' a ' is defined as the ratio of absorbed energy to incident energy.

$$a = \frac{e_{absorbed}}{e_{incident}} \quad (3)$$

However, the spectra of luminous and non-luminous sources differ fundamentally resulting in great difference between absorptivity and emissivity

The second, law of radiation is the Stefan-Boltzmann's law. This states that in terms of emittance, the total radiation flux emitted by a real body is given by

$$H = S\epsilon T^4 \quad (4)$$

Where S is emissivity, S is Stefan's constant; T is absolute temperature (Ralf 1999).

Materials and Methods

Thermal radiation measurements can take various forms depending on the equipment used and the environment under consideration. One of the methods used within open environments is the use of radiometer in which thermal radiation is absorbed by a blackened surface of an insulated box with transparent windows. The temperature of the surface rises and is measured with a thermometer.

In this study we have adopted a similar method, with modifications in which we have used a black body absorber constructed from aluminum sheets and coated with black paint (see figure 1).

A hole was bore at the surface for insertion of the thermometer. The entire body was coated with antirust black paint for absorption of radiation.

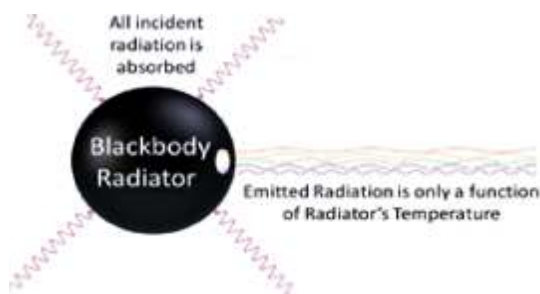


Fig 1 Blackbody radiator

Experimental Positioning

Everybody at any temperature above absolute zero **will** radiate to some extent, the intensity and frequency distribution of the radiation depending on the detailed structure of the

body. To begin analyzing heat radiation, we need to be specific about the body doing the radiating: *the simplest possible case is an idealized body which is a perfect absorber, and therefore also a perfect emitter.*

At Agbada flow and Metering Station, five blackbody absorbers were placed at distance 50 m from one another, positions as A, B, C, D, and E with A being 50 m from the gas flare, B = 100 m, C = 150 m D = 200 m and E = 50 m, all from the flare.

In each blackbody absorber, 200 cm³ of water was poured. Water is used, since it can absorb all radiation including infra-red. The absorber was placed about one meter above the ground to receive horizontal radiation from the sources. Another thermometer was placed near the absorber in open air, also at one meter above the ground, to read the ambient (or environmental) temperature at the particular site. The readings were taken at 20 minutes intervals.

Result and Discussion

The data obtained are presented in tables 1 to 5. The radiation constant was determined from the collected data by calculation based on the laws governing radiation and heat transfer. The temperatures of the blackbody absorber at different hours of the day were used to compute the radiation constant. For any particular time, the radiation constant was obtained as follows:

$$\text{Radiation constant} = \frac{(M_w C_w + M_a C_a) (Dq)}{A_a (DT)} \quad (6)$$

Where

Mass of water, M_w

Specific heat capacity of water, C_w

Mass of the black body absorber, M_a

Specific heat capacity of the material of absorber, C_a

Difference in Temperature, Dq ,

Surface area of black body absorber, A_a

Radiation Time, DT

The results presented show a gradual decrease of the radiation constant from near the flare to distances far away. At 50 m away from the flare we have obtained an average of 2055.91 Wm⁻² while at 250 m away the radiation is 1956.86 Wm⁻² but point D which is 200 m away showed higher average value of 1989.24 Wm⁻², this may be attributable to the heat generated by the pumps and compressors around this point within the flow station.

At a particular time of the day, (13:30pm), radiation at the different point attain peak values except at 150 m away from the station where the environmental temperature is peak at 12:30pm, see figure 2. The weather on the day of this measurement was very clear and the sun's contribution was enormous. From fig 2 we evaluate the radiation gradient (intensity) to be 0.70 Wm⁻³. This is the horizontal gradient of heat flux within the flow station for the period of this study, if we follow this trend, we will observe that at a distance of about 500 m the radiation or heat effect due to the flare shall disappear completely.

Solar radiation constant for Rivers state was reported by Torubeli (1996), as 1245.85 Wm⁻². If we assume this same level for 2019, the radiation constants obtained during this study within the intervals of 50 m and 250 m are 2055.91 Wm⁻² and 1956.86 Wm⁻². Comparing these with our data, the differences of solar radiation constants obtained for the heat effect are about 810.06 Wm⁻² at 50 m and 711.01 Wm⁻²

Table 1 Average thermal constant 2055.91 Wm^{-2} at 50m from the flow and metering station.

Hour of the day	Black body temperature	Environmental temperature in $^{\circ}\text{C}$	Radiation Constant in Wm^{-2}
6.30am	28.00 (Water)	32.00	-
6.50am	33.00	33.00	1889.82
7.10am	33.50	33.00	1893.2
7.30am	34.00	33.00	1893.2
8.10am	36.50	33.00	1910.9
8.30am	37.00	33.00	1913.2
9.30am	40.00	35.00	1933.9
9.50am	42.50	35.00	1950.9
10.50am	57.00	38.00	2049.3
11.10am	62.50	38.00	2086.6
12.10pm	74.50	40.50	2186
12.30pm	76.00	42.00	2178.2
13.10pm	81.00	43.00	2212.1
13.30pm	82.00	45.00	2218.9
14.10pm	78.00	45.00	2191.8
15.10pm	68.00	42.00	2123.9
15.30pm	64.00	42.00	2096.8
16.10pm	61.00	41.00	2062.9
17.10pm	59.00	39.00	2042.50
18.10pm	54.00	36.00	2028.9

Table 2 Average thermal constant 2055.91 Wm^{-2} at 100m from the flow and metering.

Hour of the day	Blackbody temperature	Environmental temperature in $^{\circ}\text{C}$	Radiation Constants in Wm^{-2}
6.30am	28.00 (Water)	32.00	-
6.50am	33.00	33.00	1889.82
7.10am	33.50	33.00	1893.2
7.30am	34.00	33.00	1893.2
8.10am	36.50	33.00	1910.9
8.30am	37.00	33.00	1913.2
9.30am	40.00	35.00	1933.9
9.50am	42.50	35.00	1950.9
10.50am	57.00	38.00	2049.3
11.10am	62.50	38.00	2086.6
12.10pm	74.50	40.50	2186
12.30pm	76.00	42.00	2178.2
13.10pm	81.00	43.00	2212.1
13.30pm	82.00	45.00	2218.9
14.10pm	78.00	45.00	2191.8
15.10pm	68.00	42.00	2123.9
15.30pm	64.00	42.00	2096.8
16.10pm	61.00	41.00	2062.9
17.10pm	59.00	39.00	2042.50
18.10pm	54.00	36.00	2028.9

Table 3 Average thermal constant 2002.91 Wm^{-2} at 150m from the flow and metering station.

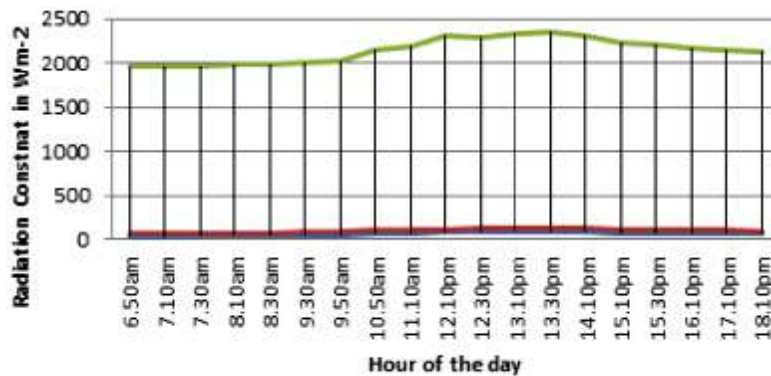
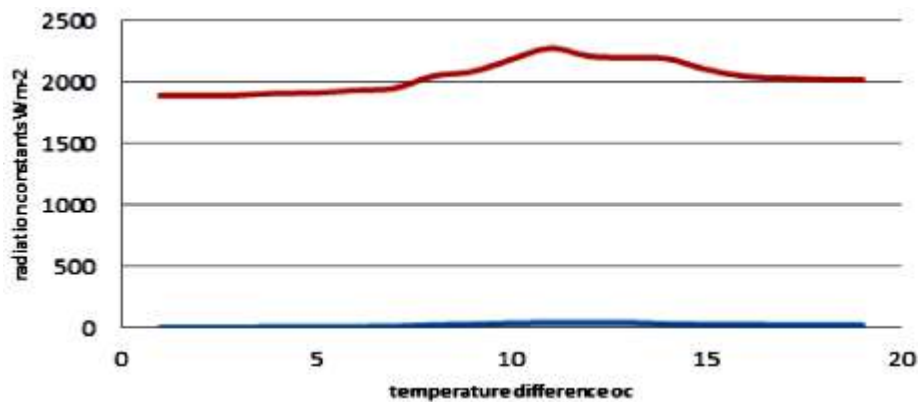
Hour of the day	Black body temperature	Environmental temperature in $^{\circ}\text{C}$	Radiation Constants in Wm^{-2}
6.30am	28.00 (Water)	32.00	-
6.50am	33.00	33.00	1889.82
7.10am	33.50	33.00	1893.2
7.30am	34.00	33.00	1893.2
8.10am	36.50	33.00	1910.9
8.30am	37.00	33.00	1913.2
9.30am	40.00	35.00	1933.9
9.50am	42.50	35.00	1950.9
10.50am	57.00	38.00	2049.3
11.10am	62.50	38.00	2086.6
12.10pm	74.50	40.50	2186
12.30pm	82.30	45.00	2278.2
13.10pm	81.00	43.00	2212.1
13.30pm	80.00	43.00	2200.9
14.10pm	70.00	42.00	2191.8
15.10pm	65.00	42.00	2103.9
15.30pm	64.00	42.00	2046.8
16.10pm	61.00	41.00	2032.9
17.10pm	59.00	39.00	2022.50
18.10pm	54.00	36.00	2018.9

Table 4 Average thermal constant 1989.24 Wm^{-2} at 200m from the flow and metering.

Hour of the day	Black body temperature	Environmental temperature in $^{\circ}\text{C}$	Radiation Constants in Wm^{-2}
6.30am	28.00 (Water)	32.00	-
6.50am	33.00	32.00	1700
7.10am	32.50	32.00	1750.2
7.30am	33.00	32.00	1750.2
8.10am	35.50	32.00	1810.9
8.30am	36.00	32.00	1845.2
9.30am	39.00	34.00	1870.5
9.50am	42.50	34.00	1900
10.50am	56.00	37.00	1950.3
11.10am	60.50	37.00	2000.6
12.10pm	70.50	41.50	2906
12.30pm	74.00	42.00	2128.2
13.10pm	80.00	43.00	2142.1
13.30pm	82.00	45.00	2180.6
14.10pm	77.00	44.00	2115.8
15.10pm	68.00	43.00	2100.9
15.30pm	64.00	42.00	2080.8
16.10pm	61.00	41.00	2000.9
17.10pm	59.00	39.00	1950.7
18.10pm	54.00	36.00	1938.9

Table 3 Average thermal constant 1956.86 Wm^{-2} at 250m from the flow and metering station.

Hour of the day	Black body temperature	Environmental temperature in $^{\circ}\text{C}$	Radiation Constants in Wm^{-2}
6.30am	28.00 (Water)	32.00	-
6.50am	33.00	34.00	1700
7.10am	33.50	34.00	1750.2
7.30am	34.00	34.00	1750.2
8.10am	36.50	34.00	1810.9
8.30am	37.00	34.00	1835.2
9.30am	40.00	35.00	1870.5
9.50am	42.50	36.00	1900
10.50am	57.00	40.00	1950.3
11.10am	62.50	42.00	2000.6
12.10pm	74.50	43.50	2086
12.30pm	76.00	44.00	2108.2
13.10pm	81.00	44.00	2142.1
13.30pm	82.00	45.00	2180.6
14.10pm	78.00	44.00	2115.8
15.10pm	68.00	42.00	2100.9
15.30pm	64.00	42.00	2020.8
16.10pm	61.00	41.00	2000.9
17.10pm	59.00	39.00	1950.7
18.10pm	54.00	36.00	1908.9

**Fig 2** Radiation constants versus hours of the day for 50 m away from flow station**Fig. 3** Radiation constants versus temperature difference ($^{\circ}\text{C}$) for 50m away from flow station

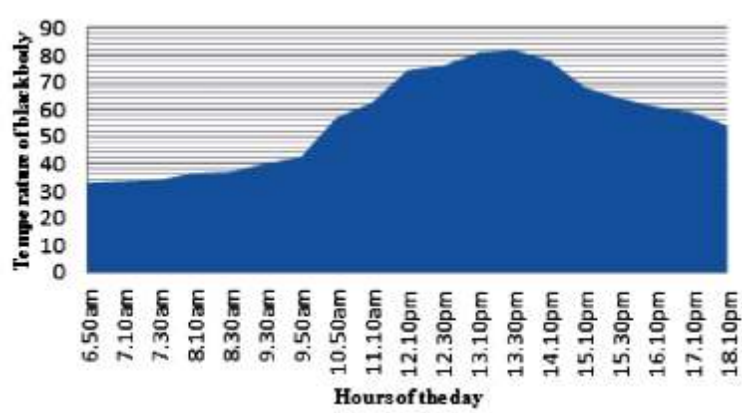
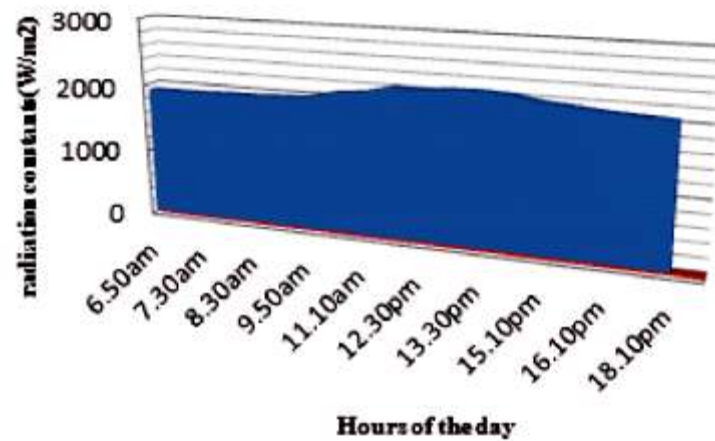
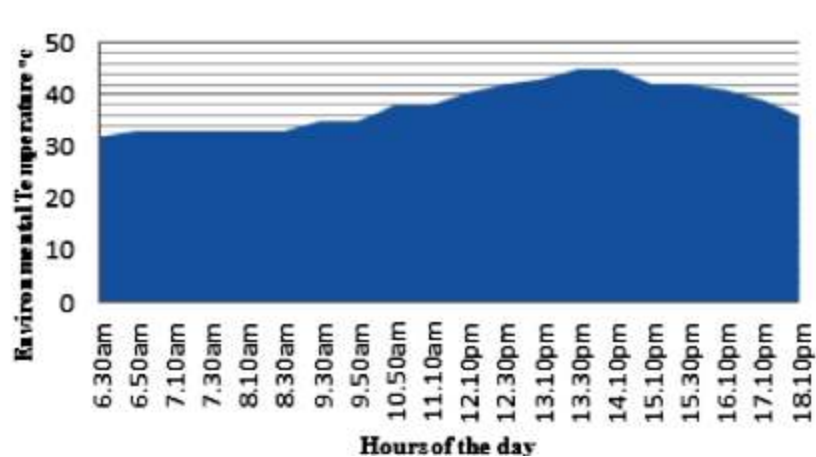


Fig. 4 Temperature of blackbody versus hours of the day

Fig.1 Radiation constant (Wm^{-2}) versus hours of the day for 100mFig. 5 Environmental temperature ($^{\circ}C$) versus Hours of the day 200m

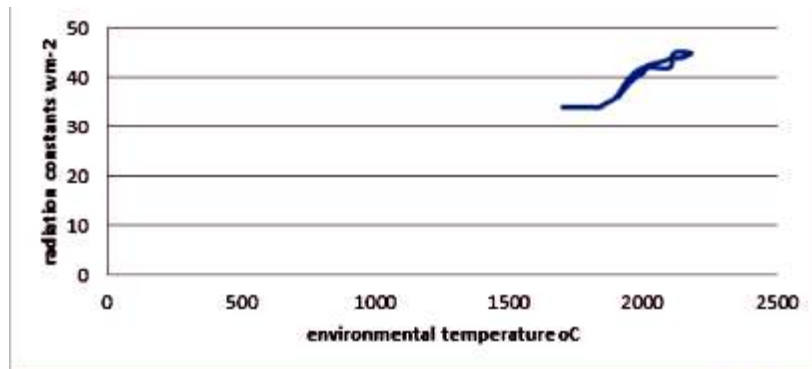


Fig. 6 Radiation Constants versus environmental temperature for 250 m

Conclusions

Estimation of the radiation spread for the Thermal Radiation Measurements at Agbada Flow and Metering station was investigated and presented. At the flow station, the presence of the flare contributed to the irradiance of the environment to 810.06 Wm^{-2} at 50 m away. Thermal Radiation Measurements at Agbada Flow and Metering station has the radiation level of about 561.11 Wm^{-2} . These are purely horizontal estimates and were recorded on a cloudless day. A complex study of the irradiance in these stations will involve a day-to-day observation and evaluation on all weather situations to be able to have very good data that isolates the sources and sites. We may wish to suggest that thermal constants of operational sites be determined before operation commences to truly establish the background situation.

References

- Chineke, T.C . (2002). A Robust Method of Evaluating the Solar Energy Potential of Data Sparse Site. *The physical scientist*, 1(1): 59-69.
- Schoof, J. T. and Robeson, S. M. (2016). Projecting Changes in Regional Temperature and Precipitation Extremes in the United States. *Weather Climate Extremes*, 11: 28–40.
- Carmona, R., Hansen, J. and Salo, M. (2016). Mortality Attributable to Extreme Temperatures in Spain: A Comparative Analysis by City. *Environ Int.*, 91: 22–28.
- Tamura, N. and Tanaka, T. (2016). Japan's Recent Tendencies of Accidents in Building Facilities and Workers' Accidents in the Environment of Extreme Temperature. *Procedia Engineering*, 146: 278–287.
- Liu, A., Weng, H. and Cox, S. (2016). Frequency of Extreme Weather Events and Increased Risk of Motor Vehicle Collision in Maryland. *Science Total Environment*, 580: 550
- Aryal, J. P., Balling, R. C, Skindlov, J. A. and Phillips, D. H. (2016). Conservation Agriculture-based Wheat Production Better Copes with Extreme Climate Events than Conventional Tillage-based Systems: A case of Untimely Excess Rainfall in Haryana, India. *Agricultural Ecosystem Environment*, 233: 325–335.
- Ogbonda, C. (2014). Estimate of direct solar radiation in Port Harcourt. *Journal of science and technology*, 9(1): 28–30.
- Audu, K. (2012). Climate Change, the Flooding and the Urban poor in Africa. *Environ. Urban*, 20(1): 187-205.
- Ralf, R. (1999). Thermal Physics, Cambridge, Cambridge Press.

Structural Evolution of Talcose Rocks in Kagara Area (Sheet 142 SE and Part of Sheet 142 SW) North Central, Nigeria

Ojo, A. A.¹, Tavershima, N.², Ismail, Y. A.³ and Oguntuase, M. A.⁴

¹Department of Geology, Faculty of Physical Science, Ahmadu Bello University, Zaria, Nigeria

⁴Science Laboratory Technology (Geology Option), Faculty of Science, Ekiti State University, **Nigeria**

Corresponding author's e-mail: adeoye.akintola@yahoo.com

ABSTRACT

This paper presents a study of the structural evolution of talcose in Kagara area north central Nigeria. The study area is part of the Kushaka schist belt of the Northern Nigeria Basement Complex. It lies within latitudes 10° 00'N and 10° 15'N and longitudes 6° 10'E and 6° 30'E, sheet 142 SE and part of Sheet 142 SW. The major rock units in the area are migmatitic gneiss, banded gneiss, granitic gneiss, meta-arkosic rock, amphibolite, talcose rock, phyllite, granodiorite, porphyritic granite, fine-medium grained granite, and pegmatite. Petrographical studies revealed that quartz, microcline, plagioclase and biotite constitute the major minerals present in the migmatitic gneiss, porphyritic granite, fine-medium grained granite, meta-arkosic rocks and pegmatite with epidote as the dominant accessory mineral. The talcose rock contains in addition to talc, appreciable amount of chlorite, magnesite, anthophyllite with magnesite and quartz forming the accessory minerals. The deformational textures of the study area were preserved in the talcose rock as most of the tectonism must have taken place at the time of the mineralization. The close association of ultramafic and related rocks with the fault structures suggest that they are crustal sutures of Pan-African collision. The sutures they serve as structural control for mineralization as the mineralizing solutions percolate and crystallize in them during ascent from the interior of the earth by the process of metamorphism in the study area.

Keyword: Tectonism, deformation, mineralization, basement complex, Kagara, North central Nigeria.

Introduction

The study area is bounded by latitudes 10° 00'N and 10° 15'N and longitudes 6° 10'E and 6° 30'E. It is a part of the Basement Complex of Nigeria and it is located towards the central

part of the N-S trending Kushaka Schist belts. The Kushaka belt occupies a belt of about 50 Km wide and stretches from Minna area up to Tsohon Birnin Gwari area in north-western Nigeria (Figure 1).

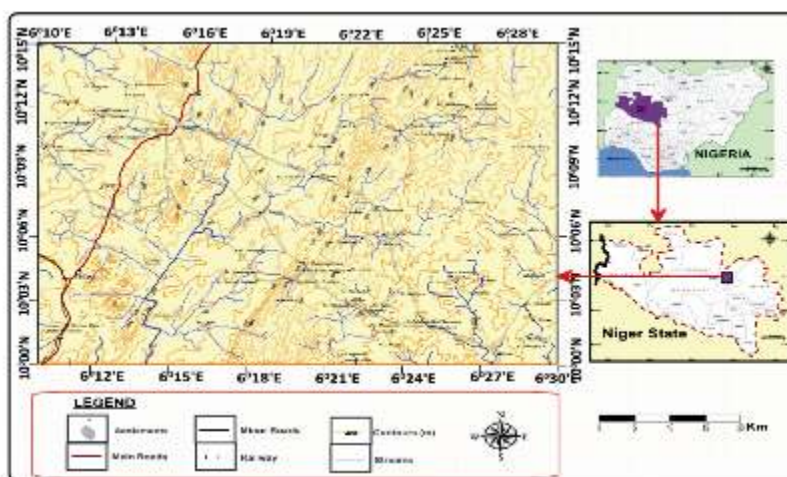


Fig. 1 Location map of the study area.

The Nigerian basement complex (Figure 2) consists of Precambrian gneisses and migmatitic rocks into which belts of N-S trending low to medium grade supracrustal rocks are infolded (Ajibade *et al* 1987). This supracrustal rocks consist of low to medium-grade metasediments of pelitic to semi-pelitic compositions, belonging to carbonates, psammitic rocks as well as mafic and ultramafic (talcose) rocks. These occur as lenticular to ovoid shaped bodies intercalated within the metasediments. Both basement and

supracrustal cover sequence that have suffered polyphase deformation and metamorphism and are intruded in some places by Pan- African granitoids. The occurrences of talcose rock in ultramafic rocks in Kagara area have previously been reported by Truswell and Cope, (1963); Elueze, (1982); Elueze and Dosunmu (1987); MSMD, (1997); RMRDC, (2010). Elueze (1983; 1986) were speculated on tectonic affinity of the amphibolites in the area.

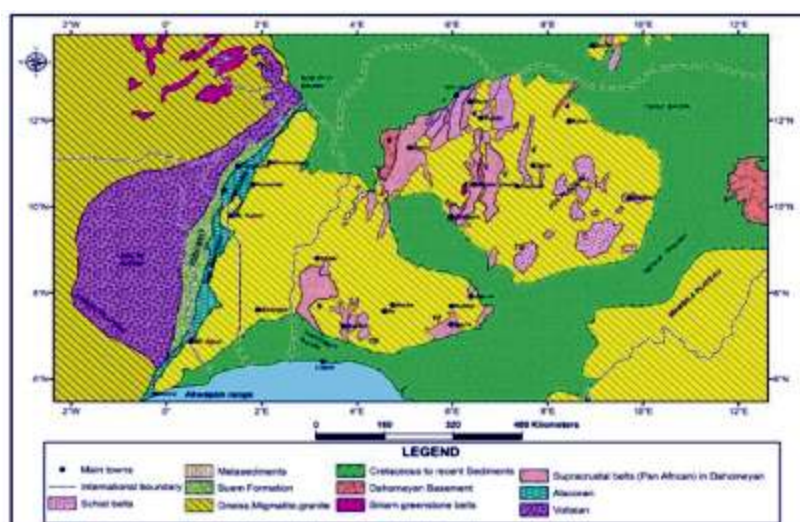


Fig. 2 Generalized geological map of Nigerian- Dahomeyan sub region: The Migmatite–Gneiss complex (mgc); Schist Belts (Sb); Older Granites (og), (after Woakes *et al*. 1987).

Other works done in the past were related to the geochemistry and general geology of the area without special preference to deposits like talcose occurring within the Kushaka schist belt (Ajibade 1982). Recently, geochemical studies by Ihaza *et al*. (2014) focused on appraisal of talcose bodies in the area with emphasis on its industrial application while Amoka (2000); Ogunbanjo and Amoka (2005; 2006) worked on decolourization of talcose rock from Kagara using magnetic separation and acid bleaching as route for colour enhancement; since strong colours are objectionable in most industrial applications, most of the talc deposits require bleaching before usage.

Apart from the aforementioned previous studies, no further work has been done on talcose deposits in this area. The aim of this paper is to undertake detailed field mapping, mineralogical investigations of the talcose rocks and host rocks in order to identify the structural elements features and its mineralization potential in Kagara area using remote sensing technique.

Materials and Methods

The methodology adopted in the execution of this research work consists of acquisitions and interpretation of satellite images using different remote sensing techniques; field study and laboratory analyses. The field study

involved geological mapping on a scale of 1:50 000 which was undertaken with topographic map, geologic hammer, compass - clinometers and Global positioning system (GPS). The laboratory work involved sample preparation, petrographic study.

The petrographic study was undertaken with the petrological microscope at petrographic laboratory, Department of Geology, Ahmadu Bello University, Zaria. Seven (7) samples of talcose rock and associated rocks were prepared for petrographic study.

Geological Setting

The study area belongs to the Nigerian Basement Complex, which forms part of the mobile belt (see figure 1) that lies between the Archean to Early Proterozoic West African and Congo Cratons (Kennedy 1964). The dominant N-S trending structures and extensive areas of igneous rejuvenation of this basement are attributed to the Pan-African Orogenic events (McCurry 1976; Van Breeman *et al.* 1977). The lithological framework, deformation and metamorphism of the basement rocks are established in the work of Ajibade (1976, 1980); Odeyemi (1988); Rahaman (1976, 1988); and Elueze

(1981). Olade and Elueze (1979) consider the schist belts to be fault-controlled rift-like structures. Grant (1978), Holt (1982) and Turner (1983), based on structural and lithological associations, suggest that there are different ages of sediments. However, Ajibade *et al.* (1979) disagree with this conclusion and show that both series contained identical deformational histories. McCurry (1989) observed that the main structural trends in especially northern Nigeria have been resolved into an early ENE to WSW trending moderately dipping foliation planes that have been transgressed by a more dominant deformation N-S steeply dipping structures. The structural relationships between the schist belts and the basement were considered by Truswell and Cope (1963) to be conformable metamorphic fronts and it was Ajibade *et al.* (1979) who first mapped a structural break.

Results and Discussion

Principal component analysis (pca) was used to display the iron-oxide and hydroxyl minerals in bright pixels, a negative image was obtained (Figures 3).

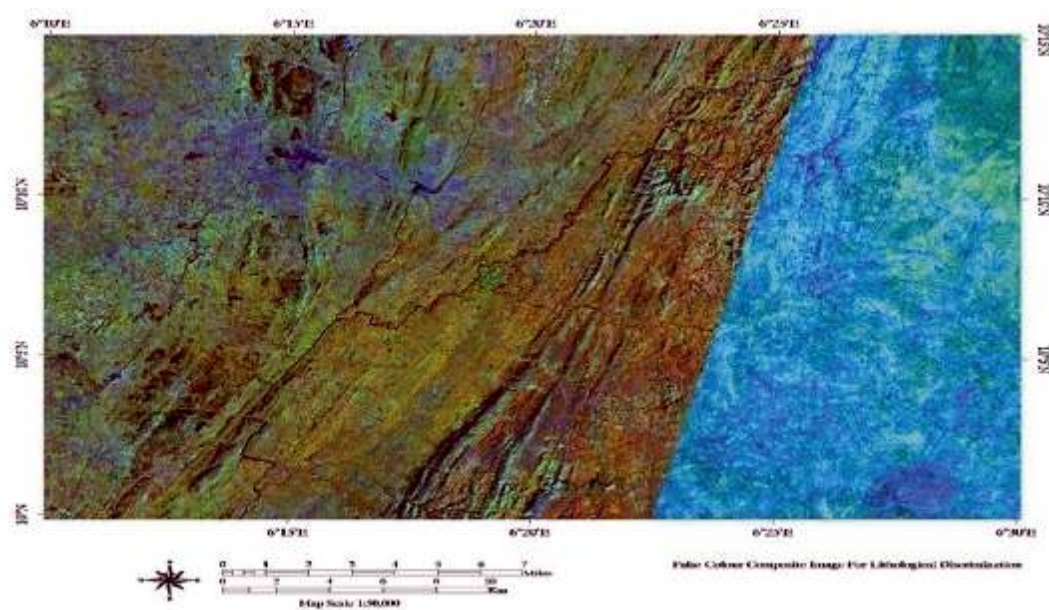


Fig. 3 False colour composite from principal component analysis of residue image 7:4:1 displaying areas of high alterations as blue.

In order to target highly altered areas, alteration threshold values for the different ratio images was calculated using the formula below,

$$\text{Threshold} = \text{Mean} (2 \times \text{Standard deviation}) \quad (1)$$

From this formula threshold values and basic statistics are applied in Table 1 and the following threshold values were obtained.

Table 1 Threshold values and basic statistics.

Ratio image	Minimum	Maximum	Mean	Std. Dev	Threshold
5/4	0.0	84.0	1.387689	1.979456	5.34661
3/1	0.0	24.5	0.865685	1.678983	4.223651

Using the threshold values, the highly altered areas were segregated and displayed on Figure 4.

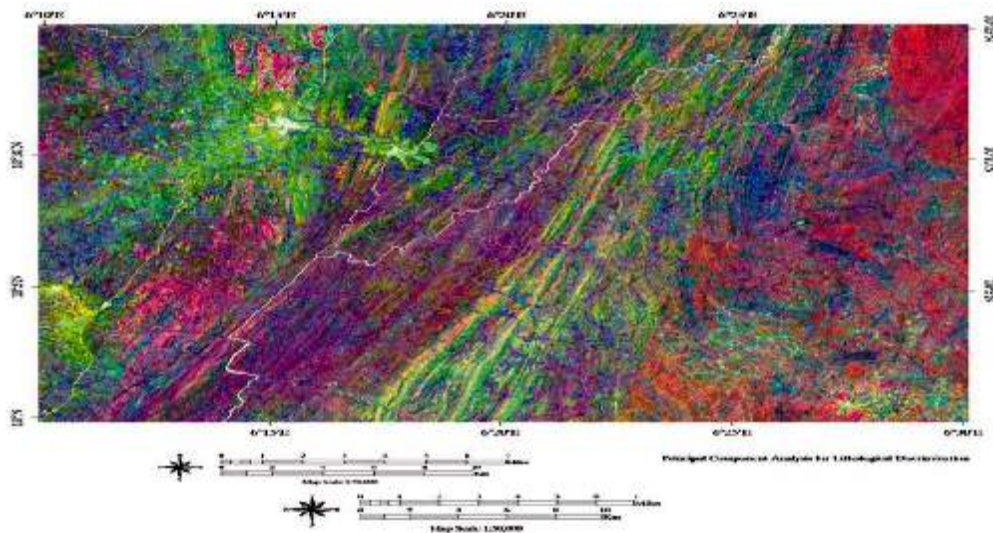


Fig. 4 Threshold image of Principal component analysis for lithological discrimination of the study area displaying granitic gneiss, talcose rock and hyllite as green; banded gneiss, granites, granodiorite as pink; migmatitic neiss, meta-arkosic rock as purple.

Geology of the Study Area

The major rock units in the area are migmatitic gneiss, banded gneiss, granitic gneiss, meta-arkosic rock, amphibolites, talcose rock, phyllite, granodiorite, porphyritic granite, fine-medium grained granite, and pegmatite through Remote Sensing technique (see Figure 3). Migmatitic-gneisses are extensive in the area, intruded by the Older Granites at the northern part truncating its massive extension from the western part of the area to the eastern. It constitutes well over 52% of the rock types in

the study area. The Older Granites in the study area are porphyritic and fine-medium grained granites. The porphyritic granites intruded the other rocks in the area especially in the southwestern axis and central part northwards, covering about 30% of the entire area while fine- medium grained granites cover 4% of the area notably in the northeast and toward the central part of the study area. The amphibolites and phyllites constitute about 8% of the rock types in the area. Outcrops of the amphibolites in are lenticular, texturally distinctive and well

oriented sub - parallel to the N-S foliated trend. The talcose rocks constitute about 6% of the rocks in the study area and occur in the northwestern part close to Kagara in Tsaunin Agwaru area in a ridge surrounded by amphibolites and the Older Granites. Outcrop of the talc occurs as lensoid bodies of moderate size and length. It extends to the south-western part having contacts with the migmatitic-gneisses and the Older Granites in an oval shaped outcrops of about 15 m above the surrounding ground surface. In the southern part of Kumunu, talcose rocks occurs as large inselbergs and massives exposures, and are bounded by the Older Granites and migmatitic gneiss in the western and eastern sides. The talcose rock truncates the linearly elongated north - south amphibolites bodies (Figure 5). The talcose bodies are largely extensive in Kagara area with different grade, colours, sizes, and textures. The colour of talc varies from grey, white to pale brown colour with a soapy feel when handled.

There are metamorphosed arkosic rocks mainly of sandstone containing at least 25 % of feldspar. This unit runs in N-S direction in the south-eastern part of the study area and also occurs in the north towards the east, though not as massive as in south-eastern part of the study area. The geological map of the study area is presented as (Figure 5).

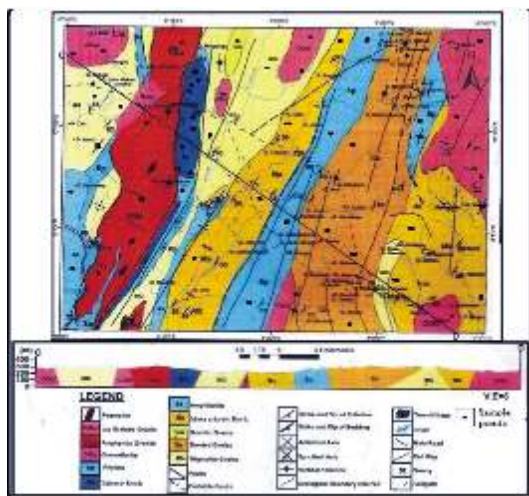


Fig. 5 Geological map of the Kagara area.

Petrography

Field observations were complimented by laboratory examination of selected hand specimens. Thin sections were prepared for all the rock types obtained from the field to describe the texture, mineralogy, alteration and deformation. Petrographical studies revealed that quartz, microcline, plagioclase and biotite constitute the major minerals present in the migmatitic gneiss, porphyritic granite, fine-medium grained granite, meta-arkosic rocks and pegmatite with epidote as the dominant accessory mineral. **Plate (I-IV).** The talcose rock contains in addition to talc, appreciable amount of chlorite, magnesite, anthophyllite with magnesite and quartz forming the accessory minerals.

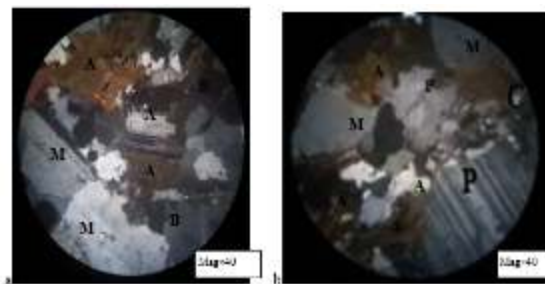


Plate I

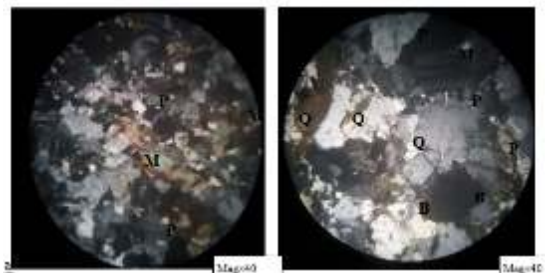


Plate II

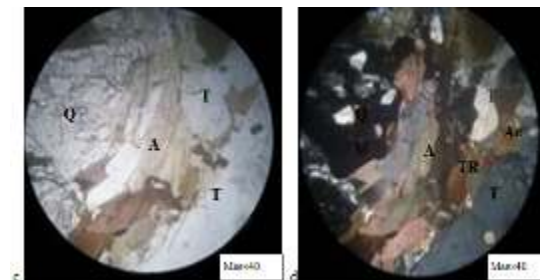


Plate III

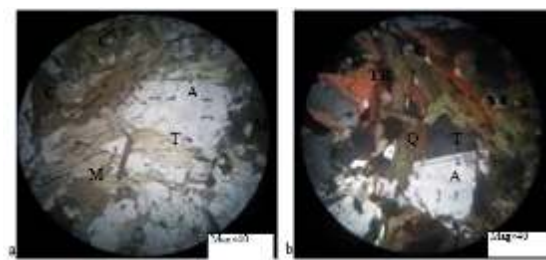
**Plate IV**

Plate I: Photomicrograph of amphibolites in (a) plane polarized light (PPL) and (b) crossed polarized light (XPL), (C) = Chlorite, Q = quartz, P = Plagioclase, A = Amphibole, B = Biotite, M = Muscovite and accessory minerals

Plate II: Photomicrograph of porphyritic granite under (a) plane polarized light (PPL)

and (b) crossed polarized light (XPL) P = Plagioclase, B = Biotite, M = Microcline and Q = quartz.

Plate III: Photomicrograph of talcose rock in (a) plane polarized light (PPL) and (b) crossed polarized light (XPL); (A) = Anthophyllite; (C) = Chlorite, (M) = Magnetite; Ac = Actinolite, Q = Quartz, (TR) = tremolite

Plate IV: Photomicrograph of talcose rock in (a) plane polarized light (PPL) and (b) crossed polarized light (XPL); (A) = Anthophyllite, (C) = Chlorite, (M) = Magnetite, Ac = Actinolite, Q = Quartz, (TR) = Tremolite.

Structures

The structures mapped and interpreted in the study area consist of those formed due to ductile deformation (foliations and lineations) and brittle deformation (joints and faults). The major structural trend is NE-SW with minor NW-SE.

Foliation

Foliation is common in banded and migmatitic gneisses in the study area. It occurs as simple banding of dimensionally oriented minerals. In the gneiss, foliation is defined by parallel alignment of alternating quartz and mafic minerals (Plate VI). The predominant trend observed is NE-SW with average dip of 40° NE.

Lineation

Lineation is common in migmatitic gneiss in the study area. Lineation in the rocks is displayed by the parallel crystal arrangement or preferred orientation of dark and light coloured minerals in migmatite. The dark coloured minerals are the ferromagnesian minerals (hornblende and biotite) while the light coloured minerals are the quartzofeldspathic minerals (quartz and feldspar) (Plate VII)



Plate VI A foliation on banded gneiss North of Gora displaying the trends in NE-SW



Plate VII Photograph of Lineations in migmatite around Madaka 10° 021 5011 N and Longitude 06° 271 5011 E).

Joint

These structures occur in all the rock types although very pronounced in the granites. The joint spacing was within the range of a few millimetres to 10 cm in areas where they occur as a joint set. In some places, they cross-cut the rocks horizontally while in others vertically which indicates complex tectonism. The general orientations of joints are E-W and

ENE-WSW thus suggesting dominant N-S or NNW-SSE directed stresses. Next to the dominant strike directions are N-S, NE-SW and minor NW-SE orientation joints. The strike direction of joint values recorded in the

field ranges from 10° – 35° . In some places, the joints have been filled with silica material probably quartz resulting in the cross cutting relationship which enables one to determine their order of formation (Plate VIII)

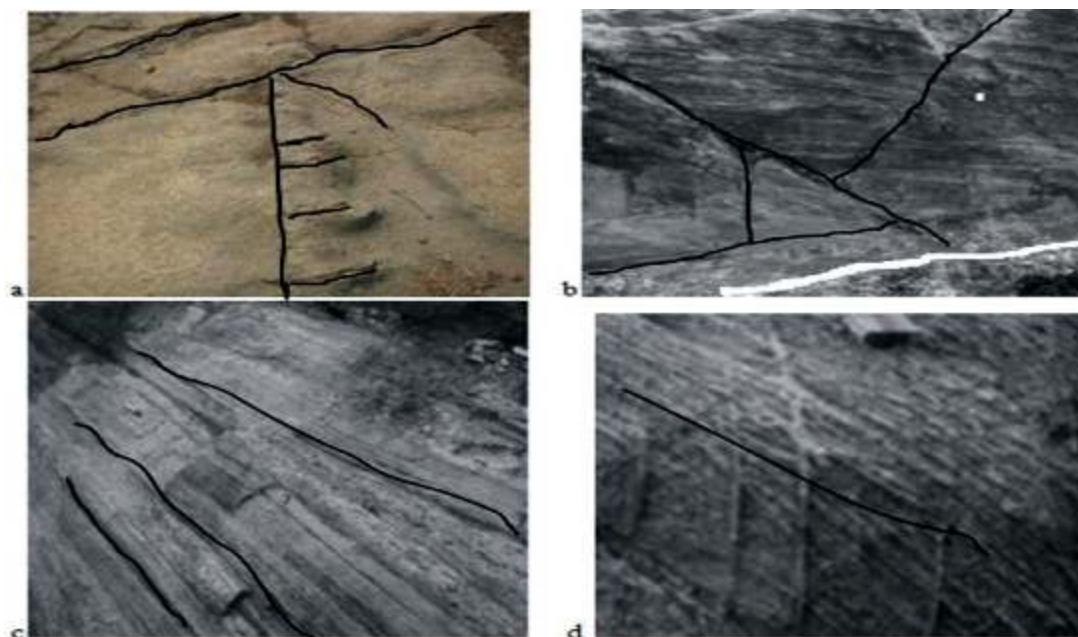


Plate VIII Photograph of joints in (a) granite displaying crosscutting relationship that provided a guide to the recognition of the two generation of joints on the outcrop South of Tegna- Ogu (b) Conjugate joints North of Supana (c) Joints running parallel to Pegmatite intrusions South of Dawaki (d) Joint run parallel to foliations North of Ogu

Faults

The faults in the study area are part of the major transcurrent fault system known in Nigerian Precambrian basement trending mostly in the NE-SW and NNE- SSW (Figure 4). Faults which are of regional extent have been mapped in the study area. Two northward-trending steeply dipping faults (sinistral) with more than hundreds of km displacement have been mapped by Cope and Truswell, (1963). These faults appear to have appreciable horizontal components of displacement in the study area, also normal faults with small displacements of the order of 5-25 cm were observed in the field (Plate IX).



Plate IX Photograph of a normal fault that occurred in the amphibolites at Tegna Ogu

Lineaments

Principal Component Analysis was applied to the six bands (1/5 and 7) of Landsat ETM image to compress the information into three bands (Figure 6). The prevalence of lineaments is an indication of high tectonic activity which

in turn may indicate a possibility of mineral deposition (Table 1) presented the statistics of the principal components (PCs) within the study area. This table show the anomaly of the Eigen values decreasing with variance in successive principal components. The first principal component contains 87.108 % of the total variance. The first three components contain 96.5% percent of the total variance within the whole volume of data of six bands details in Table (1) for Eigen values of Principal Component Analysis (PCA) give the lineaments map and rose diagram of the study area (Figures 6 and 7 respectively).

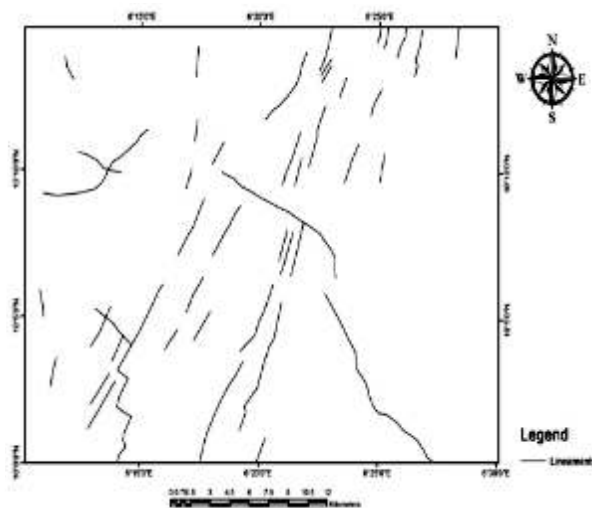


Figure 6: Lineaments map of the study area

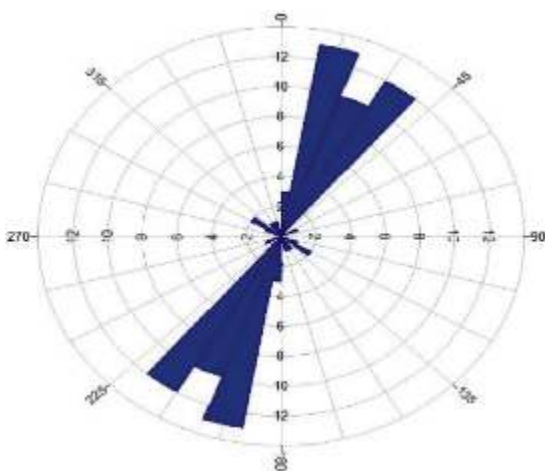


Fig. 7 The rose diagram for the Lineaments of the study area

Two major structural domains were identified from the lineament map. These are NE-SW and NW-SE with dominant orientation of lineament being NE-SW, suggestive of NW-SE tectonic (extensional forces), minor ENE-WSW and E-W orientation suggestive of shearing evidenced by conjugate joints sets were also recorded. Evidence from the lineament density map suggest that the NE and NW parts of the study area were highly dense while the SW and E-SE parts were less dense or near zero relative to lineament concentration. This same trend was earlier observed during the ground mapping by Ihaza *et al.* (2014). There is overlap between the minor NW-SE / ENE- WSW orientations in lineaments and joints. This implies that these fractures in both cases were produced by similar tectonic events while other orientations are product of dissimilar tectonic events / regimes.

Metamorphism and tectonic activity in the study area

The study area has been affected by dynamic metamorphism and this is largely reflected in the main phase of deformation of the rocks (Plate 1a). Fracturing is generally intense on amphibolite (Plate 1b). In thin section, it is commonly observed that the amphibolite has been altered to sequences of protomylonite and cataclastite with intensively transposive cataclastic fabrics (Plate 1b). The prevalent structures in the study area are laminations on which strong and penetrative stretching lineations is developed (Plate VII). Locally, near the margins of the granites at Dangwari, metamorphism and metasomatism have been superimposed on Banded gneiss.

The rocks in the study area are believed to be the result of the Pan-African deformation and accompanying regional metamorphism, migmatization, extensive granitization and gneissification which produced syntectonic granites and homogenous gneisses. Field observation reveal that the contact of the amphibolite with the surrounding rocks is marked by development of cataclastite which

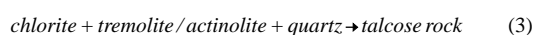
represent a major fracture zone with either joint or fault as the structural elements (Figure 5).

The foliation recorded on outcrop of gneiss is related to the metamorphic events which were observed as segregation of minerals into mafic and felsic bands. This event can be related to recrystallization of minerals during regional metamorphic episode. The foliation planes which were later folded into recumbent/asymmetrical folds by apparently E-W directed maximum stress is attributed to the process of regional metamorphism. The metamorphism in the study area is reflected through deformation that linked with recumbent folding of the dominant vein in NE-SW suggesting of a NW-SE directed minimum stress that result to sharp contact of the amphibolite and talcose rock (Plate X)



Plate X Recumbent fold in amphibolite with granitic material along the nose of the fold South of Gumna-Supana

The minerals in the study area are characterized with high pressures and variable temperature equations (2) and (3) below



The study area lies within the Kushaka belt that composed of low-grade deformed metasediment and metavolcanic that are intruded by granitoids whose metamorphism grades varies from low to middle amphibolites (Ajibade 1980; Danbatta 2001;

Fitches *et al* 1985). The presence of chlorite and tremolite are clear indication of greenschist facies. The greenschist facies comprises of rocks formed under low temperature (low grade) and as a result, greenish minerals predominate.

Conclusion

The presence of structures like faults and joints plays vital roles in formation of the constituent minerals of talcose rock. Two types of faults occur in the area. These are normal and reverse faults. In the normal faults, the hanging wall has moved down relative to the footwall, distorting the schistosity on the schist. Based on the sense of movement, it is a dip-slip fault as the movement or displacement is in the dip direction. Due to decrease in length of rock material along the fault plane, it is a constrictional fault because distance is lost; Note the downward movement of the hanging wall relative to the footwall and distortion of the schistosity in the rock (Plate VIII).

Field evidence shows that the rocks in the study area have more than one generation of joints and the orientation of these joints in the field does not follow any particular trends (directions), as they trend in all directions (Figure 6). Two dominant structural trends were identified from the lineament map namely: NE-SW and NW-SE (Figure 7). The minor ENE-WSW direction suggestive of shearing of conjugate joints. The multiple orientations support the hypothesis of polycyclic nature of the rock types in the study area. The shear forces produced these fractures were operative at different time in the history of the area. Talcose rock is formed very close to the major fault in the area (Figure 5).

The prevalence of lineaments is an indication of high tectonic activity in the study area. Tectonics play a major role in the genesis of a talc deposit. It enables hydrothermal fluids to penetrate the rock, creating a micro-permeability that facilitates reactions in the mass. The size and shape of talcose deposits in

the study area reflect the intensity of metamorphism. Pressure and deformations, both of which are concurrent with and subsequent to this transformation, determine the crystallinity of the talcose deposit. The extent of deformation in talcose rock from Kagara is expressed on occurrence and the magnitude of metamorphism and metamorphic structures of the area. Structures like foliations, joints and minor faults. The faults and other structures are believed to be due to Late Pan–Africa brittle deformation that occurred on a continental scale (Ball 1980). The close association of ultramafic and related rocks with the fault structures suggest that they are crustal sutures of Pan-African collision as earlier proposed by McCurry and Wright (1977), and Ajibade and Wright (1989).

The sutures they serve as structural control for mineralization as the mineralizing solutions percolate and crystallize in them during ascent from the interior of the earth. Also fractured rocks offer great prospect for groundwater. They are very important to engineers searching for groundwater since their presence enhances the development of good aquifers in fractured zones of the basement. In support of this is the regional deformation and faulting which produced fractures that served as conduit for easy ingress of solutions during the process of metamorphism in the study area. The deformational textures of the study area were preserved in the talcose rock as most of the tectonism must have taken place at the time of the mineralization.

Acknowledgements

The writers express their appreciation to Professor Saidu Baba for critical reading of the manuscript of the main work. We also wish to thank Professor. P.O. Ogunleye for much helpful criticism during the course of the work. Akintola wishes to acknowledge the co-operation of the many people involved in making available the specimens used in this investigation. Special thanks to Mr Yahaba Ibrahim for his assistance during mapping and

sampling at the mine. Dr O.O Akintola, Prof and Prof (Mrs) Sola Olopade are specially thanked for their financial assistance.

References

- Ajibade, A. C. (1976). Provisional classification of the Schists Belts of north-western Nigeria: In *Geology of Nigeria*, C. A. Kogbe Ed. *Elizabethan Publication Co.* Lagos; 85-90.
- Ajibade, A. C. (1980). Geotectonic evolution of the Zungeru Region Nigeria. Unpublished Ph.D. Thesis, University of Wales, Aberystwyth.
- Ajibade, A.C. (1982). The Origin of the Older Granites of Nigeria: Some evidence from the Zungeru region. *Journal of Mining and Geology*, 19; 223-230.
- Ajibade, A. C., Fitches, W. R. and Wright, J. B. (1979). The Zungeru mylonites, Nigeria: recognition of a major unit. *Rev de Geology, Geography*, 2; 359–363.
- Ajibade, A.C. and Wright, J.B (1989). The Togo-Benin–Nigeria shield evidence of crustal aggregation in the Pan-African belt, *Tectonophysics* 155; 125-129.
- Ajibade, A. C., Rahaman, M. A. and Woakes, M. (1987). Proterozoic Crusta Development in the Pan–African regime of Nigeria. In: *Proterozoic Lithospheric Evolution* (Kroner, A., Ed.), *American Geophysicists Union*, 17; 259–271.
- Amoka, I. S. (2000). Beneficiation of talcose rock from Kagara, North-Western Nigeria. Unpublished Master Technology Thesis, Federal University of Technology, Minna, Nigeria; 211.
- Ball, E. (1980). An example of very consistent brittle deformation over a wide intercontinental area: The Pan-African feature system national of the Tuareg and Nigerian shield. *Technophysics*, 61; 363-379.
- Danbatta, U. A. (2001). Rb-Sr Isochron Dating of Granitoids from the Kazaure Schist Belt North-western Nigeria. *Global Journal of Pure and Applied Science*, 8; 319-322
- Elueze, A. A. (1981). Petrographic studies of metabasic rocks and meta-ultramafites in

- relation to mineralization in Nigerian schist belts. *Journal of Mining and Geology*, 1; 31-37
- Elueze, A. A. (1982). Mineralogy and chemical nature of meta-ultramafics in Nigerian schist belts, Nigeria. *Journal of Mining and Geology*, 19; 21-29.
- Elueze, A. A. (1983). Dynamic Metamorphism and Oxidation of Amphibolites of Tegna Area, North-western Nigeria. *Precambrian Research*, 14; 379 – 388
- Elueze, A.A. (1986). Petrology and gold mineralization of the amphibolite belt, Ilesha area, South-western Nigeria. *Geologie en Mijnbouw*, 65; 189-195.
- Elueze, A. A. and Dosumu, O. O. (1987). Preliminary investigation of industrial properties of magnesite bearing rocks in Tungan Bako district, Tegna area North-western Nigeria, *Nigeria Journal of Science*, 21; 133-139.
- Fitches, W. R., Ajibade, A. C., Egbuniwe, I. G., Holt, R. and Wright, J. B. (1985). Late Proterozoic schist belts and plutonism in NW Nigeria, *Journal Geological Society of London*, 142; 319-337.
- Ihaza, C. A., Adekeye, J. I. D. and Omorinoye, O. A (2014). Appraisal of the Talc Bodies of Kagara Area, North-western Nigeria and their Industrial Potentials. *Centre point journal of science*; 151-171.
- Grant, N. K. (1978). Structural distinction between a metasedimentary cover and an underlying basement in the 600 my old Pan-African domain of North-western Nigeria. *Geological Society of America Bulletin* 89; 50–58.
- Holt, R. W. (1982). The Geotectonic Evolution of the Anka Belt in the Precambrian Basement Complex of NW. Nigeria. Unpublished Ph.D. Thesis, The Open University.
- Industrial Minerals (2000). Talc mineral Products, Processing emission factors, *Norway geological Tidsskr*, 54; 99-111.
- Kennedy, W. O. (1964) The structural differentiation of Africa in the Pan African (500m.y) tectonic episode: 8th Annual Resp. *Institute African Geology University of Leeds*; 48–49.
- McCurry, P. (1976). The geology of the Precambrian to Lower Palaeozoic rocks of northern Nigeria-a review. In: C.A.Kogbe (Editor), *Geology of Nigeria*. Elizabeth Publishing Cooperation. Lagos; 15-39.
- McCurry, P. (1989). A general review of the geology of the Precambrian to the Lower Pleozoic rocks Northern Nigeria, *Rock view international*, Nigeria; 13-35.
- McCurry, P. and Wright, J. B. (1977); Geochemistry of cal-alkaline Volcanics in Northwest Nigeria and possible Pan-African Suture Zone, *Earth planet science letters*; 90-96.
- MSMD (Ministry of Solid Minerals Development) (1997). An Inventory of solid minerals in Nigeria. Geological Survey of Nigeria Press; 59.
- Odeyemi, I. B. (1988). Lithostratigraphy and structural relationships of Upper Precambrian Metasediments in Igarra, South-western Nigeria. Esho Printers, Lagos, Nigeria. In: *Precambrian Geology of Nigeria* P.O. Oluyide (ed); 111-125.
- Ogunbanjo, M. I. and Amoka, I. S. (2005). Froth floatation studies on Kagara talc *Journal of Engineering, Technology and Industrial Applications*. 1; 66-71.
- Ogunbanjo, M. I. and Amoka, I. S. (2006). Decolourization of Kagara talc using Magnetic separation and acid bleaching. *Journal of Engineering Technology and Industrial Applications*. 2; 1-5
- Ogunbanjo, M. I., Amoka, I. S. and Mallo, J. S. (1999). Indigenous technology for mineral exploitation in Nigeria. *Nigerian Mining Journal*, 3 (1); 72-77.
- Olade, M. A. and Elueze, A. A. (1979). Petrochemistry of Ilesa amphibolites and Precambrian crustal evolution in the Pan African domain of South Western Nigeria. *Precambrian Research*, 88; 308–312.
- Rahaman, M.A. (1976). Review of the basement complex of Nigeria in: Kogbe, C.A. (ed) *Geology of Nigeria*. Elizabetha publishing Lagos, Nigeria; 514.

- Rahaman, M. A. (1988). Recent advances in the study of the basement complex of Nigeria. In Geological Survey of Nigeria (ed) *Precambrian Geology of Nigeria*; 11-43.
- RMRDC. (2010). Report of the Multi-disciplinary task Force on Non Metallic Raw Material Research and Development Councils, Abuja, 2010; 37-47.
- Truswell, J. F. and Cope, R. N. (1963). The geology of parts of Niger and Zaria provinces, Northern Nigeria, *Bulletin, Geological Survey of Nigeria*, 29; 1-104.
- Turner, D. C. (1983). Upper Proterozoic schist belts in the Nigerian sector of the Pan-African Province of West Africa. *Precambrian Research*, 21; 55-79.
- Van Breemen, O., Pidgeon, R. T. and Bowden, P. (1977). Age and isotopic studies of some Pan-African granites from north central Nigeria. *Precambrian Research*, 4; 307-319.
- Woakes, M., Ajibade C. A., Rahaman, M. A., (1987): Some metallogenic features of the Nigerian Basement, *Journal of Africa Science*. 5; 655-664

Integrated Geoelectrical and Geochemical Investigation to Characterize Hydrocarbon Contamination in Yenagoa Area, Bayelsa State, Nigeria

Tekena, Y. B.¹ and Marere, O.²

¹DICON Kakuri, Kaduna State, Nigeria

²School of Marine Technology, Burutu, Delta State, Nigeria

Corresponding author's e-mail: tbunonyo@gmail.com

ABSTRACT

The Vertical Resistivity Sounding (VES) with a modification faster and more detailed named Electrical Resistivity Tomography (ERT) method with electrodes used in environmental studies, aimed to characterize hydrocarbon contaminated plume in the Subsurface of Ikarama community, Bayelsa State. Geochemical analysis of borehole soil samples collected for Total Petroleum Hydrocarbon (TPH) concentration were used to assess the intensity and extent of contamination at an oil spill and unaffected site. From the result, resistivity values of 240-352 m, at pollutant depth of 17.3m imply that both the sub soil and groundwater at 3.62 m of VES 1 and 15.2 m of VES 2 may have been contaminated by the oil spill. Soils Total Petroleum Hydrocarbon (TPH) concentrations generally decrease from a maximum of 124mg/kg at 12 m profile 3at the time of investigation to a minimum of 89.9mg/kg at 6.76 m depth within the impacted zone and 25.8mg/kg at 3 m depth, a low concentration within unaffected zone. These values are much higher than the Department of Petroleum Resources (DPR) background value of 50 mg/kg for TPH in soils, thereby establishing high level of contamination for cases in Profile 2and 3. These geophysical methods show promise for application at sites of hydrocarbon contamination to help identify the extent of contamination.

Keywords: Geoelectrical, Geochemical, Contamination, Hydrocarbon.

Introduction

Commercial oil exploration which began in Nigeria in 1958 at Oloibiri present day Bayelsa State, has subjected the oil producing communities to environmental degradation leading to depletion of resources on which the livelihood of the people depends. In many countries, the development of the oil industry has been accompanied by the contamination of different areas of exploitation, transportation, refining and distribution. Soil and groundwater are usually contaminated during crude oil production, especially in Niger Delta regions of Nigeria. Some compounds of crude oil are carcinogenic and cultivated plant in the soil would absorb it and this is transferred to man through food chain.

Occurrence of oil spill on land has resulted in contamination of groundwater, loss of biodiversity, loss of farmlands and soil fertility, damage to human health and the socio-

economic environment. Geoelectrical imaging surveys are normally carried out with multi-electrode resistivity system. In this survey, adopting the Wenner technique, some electrodes were deployed in a straight line with constant spacing and connected to a multicore cable. A computer-controlled system is then used to select the active electrodes for each measurement. Therefore, to have a clearer picture of the subsurface and to map out the effect of the contamination on the structure of the subsoil, a 2-D geoelectrical resistivity survey was conducted. Electrical resistivity imaging has been a veritable tool in delineating bedrock depression, fracture, synclinal water accumulation zone and aquifer layer (Singh et al. 2006; Ayolabi et al. 2008).

Total petroleum hydrocarbon (TPH) is a mixture of hydrocarbons found in crude oil. Some of the chemicals found in TPH are hexane, benzene toluene, xylene, naphthalene, Agency for Toxic substances and Disease

Registry (ATSDR 1999). TPH may occur in soils in four different forms: dissolved in water, sorbed on solid particles, comprising the soil gas and, due to their limited solubility, forming an individual liquid phase, known as NAPL (non-aqueous phase liquid). NAPLs can generally be divided into two individual groups according to their specific gravity denser than water (dense DNAPLs e.g. tar) and less dense than water (light LNAPLs e.g. diesel). However, bacteria and microorganisms in the water may break down some of the TPH fractions. The objective of the study is to use ABEM SAS 1000 Terrameter with electrodes to delineate the vertical and lateral extent oil spillage arising from equipment failure migrated to the subsurface.

Geology and Geomorphology

The study area lies on Lat (5.24146° N– 5.00422° N) and Long (6.34265° E– 6.60972° E) in Yenagoa local Government area, Bayelsa State Nigeria as shown in Figure 1. The study area is bounded by Delta State to the west, Rivers State to the east, and the Gulf of Guinea to the Atlantic. The area, just like places along the Nigeria coastal zone experiences a tropical climate characterized by two distinct seasons the rainy season (April - Mid August, September to early November) and dry season (November till March) usually with sparse rainfall in-between (Ofoma *et al.* 2005). Rainfall in the area exhibits double maxima. The study area lies in the coastal Niger Delta sedimentary basin. The area survey is within the deltaic depositional environment of sensitive wet land, water ways and estuaries of the southern Nigeria.

Geologically, the area falls within the Niger Delta region of Nigeria which is underlain by three stratigraphic units: Akata, Agbada and Benin Formations (Short and Stauble 1967). The marine Akata Formation, Paleocene to Holocene in age, is composed of shales and occurs at the base of the delta sequence. It is overlain by the Agbada Formation which forms the hydrocarbon prospective unit in the Niger Delta and consists of an alternation of

sands, silts and clay in various proportions and thicknesses. It ranges from Eocene to Recent in age and has a thickness of more than 3000m (Doust and Omatsola 1990). The top of the stratigraphic sequence is occupied by the Benin Formation which is composed almost entirely of sand with intercalations of clay deposited in alluvial or upper coastal plain environments. It is probably Oligocene in age. It serves as the groundwater aquifer in the region.

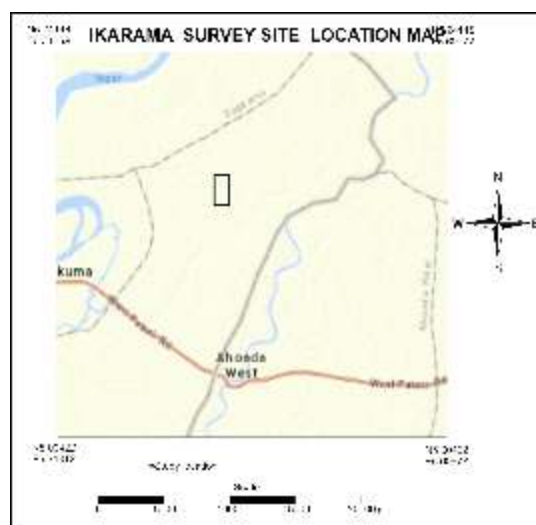


Fig.1 Ikarama survey site location map (Nigeria geological survey agency 2004)

Materials and Methods

The electrical resistivity data were acquired with an ABEM SAS (Signal Averaging System) model 1000 resistivity Earth meter (terrameter equipment) which consists of 25 electrodes, was used for the acquisition of Electrical Resistivity Tomography (ERT) data. The electrodes were driven into the ground surface at a spacing of 5m interval of spread length 120 m, to obtain the resistivity section; acquired data were processed by subjecting them to the inversion algorithm (RES2DINV) proposed by (Loke and Barker 1996). Four (4) 2D-ERT, Using Wenner array to view lateral changes ($n = 1- 6$, to increase the depth of investigation). Three (3) drills bore hole at 3m depth to the subsurface to acquire soil samples by using the hand auger at those location

predicted contaminated area from the geophysical survey interpreted result obtained from the study location. Two (2) 1D Vertical Electrical Sounding (VES), using Schlumberger array was used to investigate geoelectric characterization of subsurface and delineate depth (vertical section of subsurface lithology). The UV-Spectrophotometer was used to test for Total Petroleum Hydrocarbon (TPH) concentration, to confirm and quantify the presence of contamination in the study location. The Department of Petroleum Resources (DPR) in Nigeria regulatory standard limit of TPH is 50 mg/kg for soil, which was used to compare the analyzed concentration result. A value of apparent resistivity is calculated in each distance "AB" using equation 1.

$$\rho_a = k * DU / I \quad (1)$$

Where k is geometrical coefficient of the array:

U- potential difference (mV) registered between M and N electrodes.

I- electric current (mA) passed into ground through A and B electrodes.

ρ_a - Apparent resistivity (Ωm)

The geophysical technique was determination of contamination in the site, by analyzing soil samples for total petroleum hydrocarbon concentration both at the spill site and an unaffected area used as control. The drilled boreholes for collection of soil samples were strategically located to assess the contamination levels at the spill site and the unaffected surrounding. The existing borehole lithological logs were used for the description of the subsurface soils. It was analyzed in preference to total hydrocarbon content (THC) because its components are not easily

biodegradable and as such, persist in a medium for a long time, signifying contamination. This was used to correlate the electrical resistivity results.

Results

The data obtained from this study were initially interpreted using conventional Resistivity imaging and sounding. Based on this, a 1D and 2D imaging of subsurface lithology, estimates of layer resistivity, thickness and resistivity models were obtained, which serve as a starting point for computer assisted interpretation. The resistivity values to confirm resistivity obtained from the interpreted field data as show in table 1. The electrical resistivity curves showing true resistivity and thickness of layers is in figure 2 and 4, the geoelectric log is as shown in figure 3 and 5, geoelectrical drill log for correlating subsurface lithology in figure 6.0 while the geoelectric model obtained from the analyses field data are as shown in figure 7 - 10. The direction of flow of contamination is as shown in figure 11 – 12, while the co-ordinates of test points and total petroleum hydrocarbon (THP) Concentrations in soil samples is as shown in table 2. Profile 2 at 89.9mg/kg and Profile 3 at 124mg/kg detected high TPH concentration respectively while a control contamination zone of profile 1 at (48mg/kg) and 4 at (25.8mg/kg) detected low TPH concentration compare with the DPR regulatory standard limit. Hydrocarbon contamination may have extended to depths ranging from 2.5 - 17.6 m. The hydrocarbon contaminated clayey sand is characterized by relatively low layer resistivity values which are attributed to biodegradation of the crude oil.

Table 1 The values of resistivity after (Peck et al. 1974)

MATERIAL	RESISTIVITY (Ωm).
Clay and saturated silt	0-100
Sandy clay and wet silty sand	100-250
Clayey sand and saturated sand	250-500
Sand	500-1500
Gravel	1500-5000
Weathered rock	1000-2000

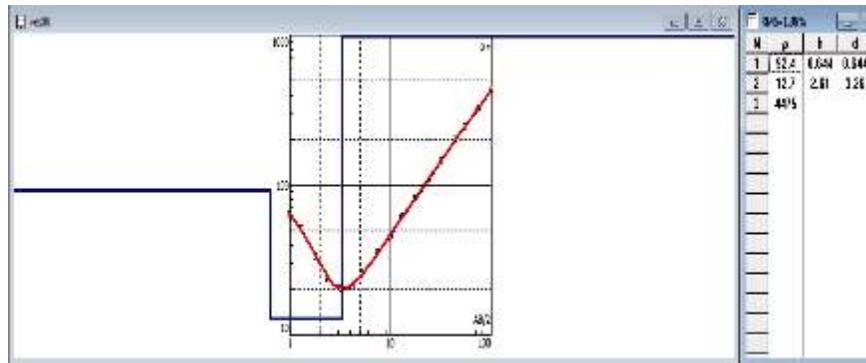


Fig. 2 Schlumberger Sounding Curve for VES 1

The second layer in inferred to be sand formation, likely unsaturated with water, as shown by high resistivity. This occurs at depth of 3.26m.

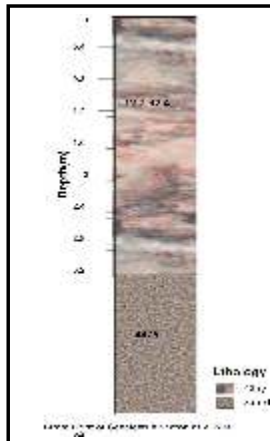


Fig. 3 Strater3 plot of Geoelectric section of VES 1 Model.

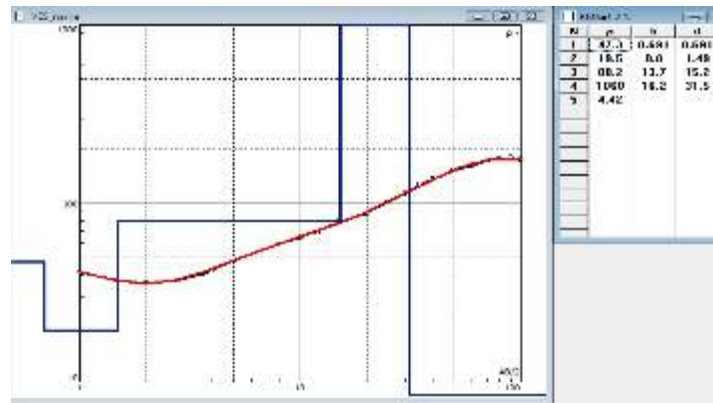


Fig. 4 Schlumberger Sounding Curve for VES 2

The second layer in inferred to be sand formation, likely saturated with water, and is underlain and overlain by clay. This is confined aquifer, occurs at depth of 15.2m and is 16.2m thick.

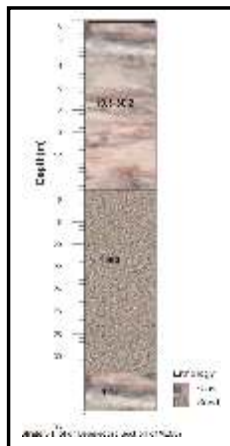


Fig. 5 Strater 3 plot of Geoelectric section of VES 2 Model.

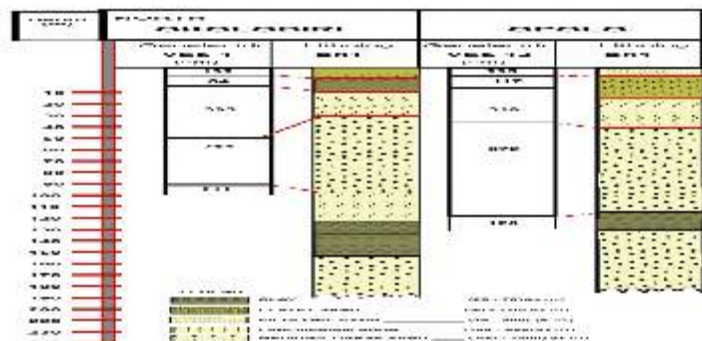


Fig. 6 Geological drill log for correlation (Bayelsa water board 2006)

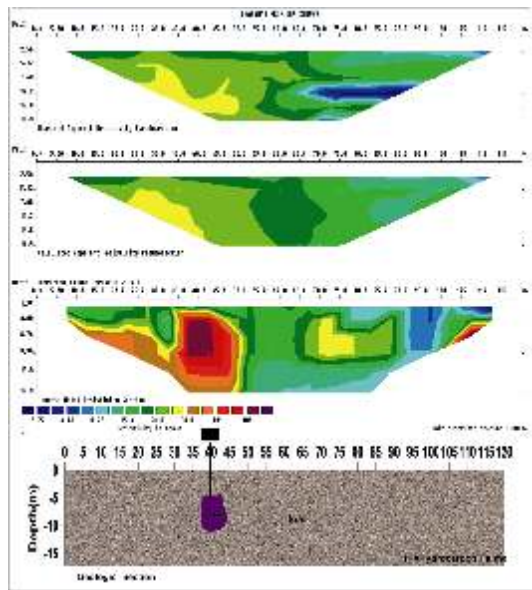


Fig. 7 Geoelectric Model of profile 4 with Plotted Geologic Section (control zone)

The anomaly (HP), purple color (350Wm) is located between the depths of 3.88 and 9.94m and laterally between 37.5 and 42.5m marks. From the lithology log, it appears to be located within the silty fine sand and clayey sand layers (up to 10m). From the reference resistivity table, silty fine sand likely is on the range 0 - 250Wm and clayey sand layer is on the 250 - 500Wm. Thus, resistivity greater than 250Wm in the silty fine sand and resistivity greater than 500Wm in the clayey sand likely indicate presence of hydrocarbon plume. The purple shade likely indicate residual phase hydrocarbon plume, probably a recent spill. Other color shades areas less than 100Wm likely indicates microbiologically cleaned-up area evidenced as highly conductive water within the plume area or locally concentrated clay material, and between 100 and 250Wm probably indicate cleaned-up area replaced by conductive water.

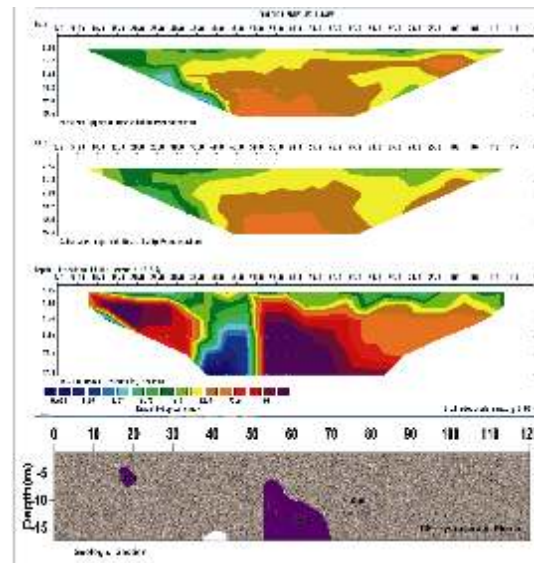


Fig. 8 Geoelectric Model of profile 6 with Plotted Geologic Section

Two anomalies (HP1 and HP2) of purple color (362Wm) are seen. The HP1 is located between the depths 2.5 and 6.76m and laterally between 10 and 20 m marks, and appears to be located within the silty fine sand (up to 6.76m). The HP2 located between the depths of 6.76 and 17.3m and laterally between 55 and 70m marks appear to be located within both the silty fine sand and clayey sand. From the reference resistivity table, silty fine sand is likely on the range 0 - 250Wm and clayey sand layer is on the 250 - 500Wm. Thus, resistivity greater than 250Wm in the silty fine sand and resistivity greater than 500Wm in the clayey sand expectedly indicate presence of hydrocarbon plume. The purple shade likely indicate residual phase hydrocarbon plume, probably a recent spill. Other color shades areas less than 100Wm likely indicates microbiologically cleaned-up area evidenced as highly conductive water within the plume area or locally concentrated clay material, and between 100 and 250Wm probably indicate cleaned-up area replaced by conductive water.

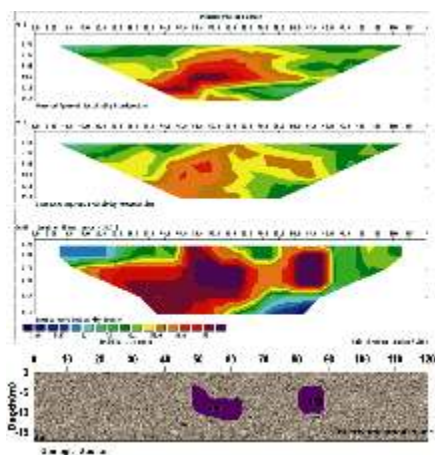


Fig. 9 Geoelectric Model of profile 8 with Plotted Geologic Section

Two anomalies (HP1 and HP2) of purple color (261Wm) are displayed. Both are located between the depths 3.88 and 12m and HP1 is laterally located between 50.0 and 62.5 m marks and the HP2 is laterally between 80.0 and 90.0m marks. These anomalies appear to be located within the silty fine sand and clayey sand (up to 10m). From the reference resistivity table, silty fine sand likely is on the range 0 - 250 $\Omega\cdot m$ and clayey sand layer is on the 250 - 500 $\Omega\cdot m$. Thus, resistivity greater than 250 $\Omega\cdot m$ in the silty fine sand and resistivity greater than 500 $\Omega\cdot m$ in the clayey sand likely indicate presence of hydrocarbon plume. The purple shade expectedly indicate residual phase hydrocarbon plume (most likely on the silty fine sand layer), probably a recent spill. Other color shades areas less than 100 $\Omega\cdot m$

likely indicates microbiologically cleaned-up area evidenced as highly conductive water within the plume area or locally concentrated clay material, and between 100 and 250 $\Omega\cdot m$ probably indicate cleaned-up area replaced by conductive water.

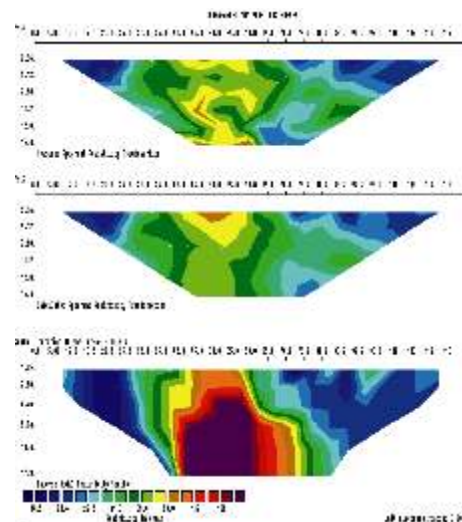


Fig. 10 Geoelectric Model of profile 13 (control measure zone)

The maximum resistivity indicated by purple color shade is 240 $\Omega\cdot m$, which less than maximum resistivity (250 $\Omega\cdot m$) infer for silty fine sand and maximum resistivity (500 $\Omega\cdot m$) infer for clayey sand. Therefore, this likely indicate the contaminated subsurface is microbiologically cleaned-up evidenced as highly conductive water within the plume area or locally concentrated clay material for those area less than 100 $\Omega\cdot m$.

Table 2 Co-ordinates of Test Points and THP Concentrations in Soil samples.

S/N	PROFILE	LATITUDE	LONGITUDE	ALTITUDE	DEPTH (m)	DRILL DEPTH (m)	LITHOLOGY	TPH (mg/kg)
1	PROFILE 1	05° 09' 20.43" N	06° 27' 03.29" E	16	4 - 9.94	3	Silty fine sand / clayey Sand	48
2	PROFILE 2	05° 09' 11.52" N	06° 27' 11.46" E	12.5	2.5 - 6.76	3	Silty fine Sand	89.9
3	PROFILE 3	05° 08' 57.95" N	06° 27' 23.37" E	19.5	3.88 - 12	3	Silty fine sand / clayey sand	124
4	PROFILE 4	04° 58' 06.99" N	06° 20' 33.65" E	42		3	Silty fine sand / clayey sand	25.8
5	DPR							50

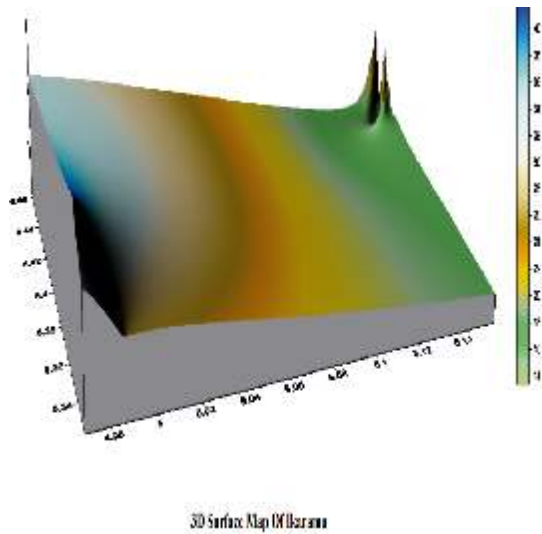
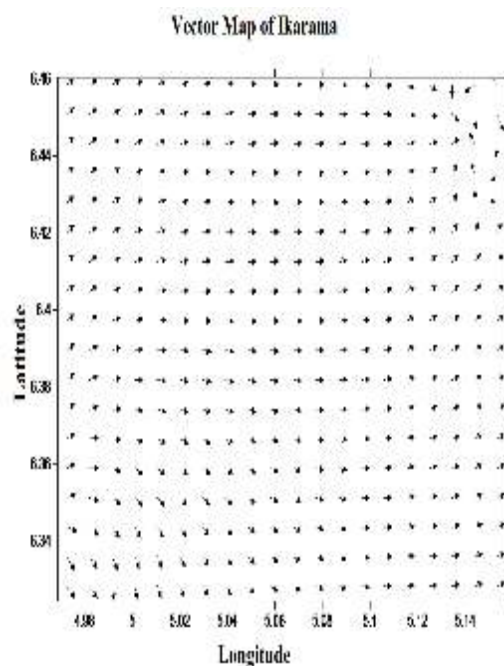


Fig. 11 3D Surface map of Ikarama showing flow direction (digital terrain model)



Discussion and Conclusion

Surface electrical resistivity surveys were conducted in Ikarama communities with the aim of providing valuable information on the hydrogeologic system of the aquifer and delineate the subsurface configuration of the area.

This research has provided reliable procedures

to detect electrically resistive hydrocarbon plume contaminants generated from crude oil spill and chemical flow direction of these materials into the surrounding soil. The efficiency of the resistivity sounding method with ERA instrument for the geoelectrical characterization of contaminated subsurface was confirmed, correlating the areas of pollution with zones of low resistivity. Range of resistivity values for different formations has been established using the interpreted geoelectric results and drilled borehole lithologs which help to understand the subsurface contamination depth ranges 2.5 – 17.6 m prevailing in the area. The groundwater occurs basically under unconfined condition at depths of about 3.26 m to about 15.2 m confined aquifer of the VES points.

In Profile 1, 2, 3 and 4 polluted zones and unaffected polluted zone as shown in table ii and their relations with the underground water flow were established. The pollution sources could be defined in the areas of minimal resistivity in figure 7.0 and 9.0 (zones of maximal contamination) and figure 10 area of unaffected contamination zone. From the general direction of the contamination flow in this study area of Ikarama, it was observed that plume will contaminant groundwater at depth range 2 – 17.6 m in the direction to the East, which was acknowledge from the evaluation of the subsurface of the earth using ERT, that aquifer are prone to pollutant in area closer to the plume direction which was agreeable with the surface topography of the area. Results generated from the electrical resistivity surveys, boring and soil hydrocarbon content determination show that the spill site is underlain by moderately permeable clayey sand which could slow plume flow in the subsurface. It is recommended that aquifer vulnerability studies should be carried out while groundwater monitoring should be conducted regularly in the area and there should be need for time lapse survey to monitor the subsurface migration rate or biodegradation process of the hydrocarbon plume. To manage and protect the groundwater

resources of the area, a risk based corrective action plan needs to be developed based on a conceptual model of the site to identify source pathway- receptor linkages for the contaminant.

Acknowledgment

The authors would like to thank sincerely Prof. F.O Ezomo for his immense intellectual contributing in the research work. The corporation of the Elders, Chiefs and Youths of the communities deserved special appreciation.

Reference

- Ayolabi, E. A., Folorunso, A. F and Ariyo, S. O. (2008). Resistivity imaging survey for Water Supply Tube wells in a Basement Complex, a case study of OOU main campus, Ago- Iwoye, Southwestern, Nigeria. *Proceedings of international symposium on Hydrogeology of Volcanic Rocks (SHID) Republic of Djibouti*: 67-71.
- ATSDR. Agency for Toxic substance and Disease Registry. (1999).
- Department of Petroleum Resources. (1991). Environmental guidelines and standards for the Petroleum Industry in Nigeria.
- Doust, H. and Omatsola, E. (1990). Niger Delta in Edwards, J. D and Santogrossi, P.A, Ed *divergent/passive margins basins AAPG memoir* 48; Tulsa, American association of petroleum geologists, 56:1975-1983.
- Loke, M. H. and Barker, R. D. (1996). Rapid Least squares Inversion of Apparent Resistivity Pseudo sections using a Quasi-Newton Method. *Geophysical Prospecting*, 44: 13-152.
- Nigeria Geological Survey Agency. (2004). Geological Map of Nigeria. NGSA, Abuja.
- Ofoma, A. E., Omologbe, D. A and Aigberua, P. (2005). Physiochemical Quality of Groundwater in parts of Port Harcourt city, Eastern Niger Delta, Nigeria. *Water Resources* 16: 18-24.
- Short, K. C. and Stauble, A. J. (1967). Outline of the Geology of Niger Delta. *AAPG bulletin*, 51 : 761 - 799 .
- Singh, N., Mulye, S. S. and Pant, G. B. (1992). *Some features of the arid area variations over India: 1871-1984. Pure and Applied Geophysics*, 138(1): 135-150.
- Peck, R. B., Hanson, W. E and Thornburn. (1974). T.H. Foundation Engineering Wiley, New York.
- Bayelsa State Water board. (2006).

Analysis of Weather Variables to Determine the Effect of Global Warming in Gusau Metropolis, Zamfara State, Nigeria.

Okoye, I. F.¹, Mainasara, H.² and Murana, K. A.³

^{1,2} Department of Physics, Federal University Gusau, Zamfara State Nigeria.

³Department of Geological Sciences, Federal University Gusau, Zamfara State Nigeria.

Corresponding author's e-mail: fitechfrank@gmail.com

ABSTRACT

Global warming and climate change refers to an increase in average global temperature. Natural events and human activities contribute to the increase in average global temperature daily. This research shows the changes occurred by the temperature which affects our environment and weather variables such as humidity, wind speed, atmospheric pressure and rainfall in Gusau metropolis by taking the daily average of the forty-eight (48) measurements recorded per day by the vantage pro 2 automatic weather machine in the space center Federal University Gusau. The forty-eight (48) measurement was converted to a single value per day and was later converted to a single value per month using Microsoft excel software. Statistical method was used to ascertain the effect of global warming using weather variables in Gusau metropolis Zamfara State Nigeria. Table of data and graphical result of weather variables; Temperature, Humidity, Wind speed, Atmospheric pressure, and Rainfall was presented and discussed. In all the result it was agreed that human activities like; farming, bush burning, deforestation and burning of fossil fuels contribute to increase in global warming in Gusau metropolis of Zamfara state, Nigeria. In conclusion global warming is on increase and can be control by moderating the human activities in Gusau metropolis of Zamfara State.

Keywords: Global warming, Climate, Temperature, Humidity, Atmospheric Pressure, Rainfall.

Introduction

Global warming and climate change refer to an increase in average global temperatures. With global warming increasing with the increase in temperature, ascertaining the effect of global warming and weather variables is very important for the purpose of recommending the best nature of the environment for human inhabitation. Natural events and human activities are believed to be main contributors to such increases in average global temperature. The climate change, caused by rising emission of carbon dioxide from vehicles, factories and power stations, will not only affects the atmospheric temperature of the sea but also will alter the geology of the earth. Emissions of carbon dioxide due to our fossil fuel consumption causes about 2°C to 6°C degree Celsius increase in the climate and the temperature variable within the year 2010, which is tremendous increases from our

current average temperature of 1.7°C as predicted by the inter-governmental panel of climate change (IPCC) (Bharat and Onkar 2012). This may cause huge changes to our civilization, both positive and negative, but the total impact on our society is currently very uncertain. Also global warming primarily is caused by increase in “greenhouse gases” such as carbon dioxide, methane, chlorofluorocarbons etc. These “Greenhouse gases” are the main components that increases the average surface temperature of the earth over the past one to two centuries as well as contributing to the increase in global warming (Michael 2009).

Similarly, Liu (1994) defined global warming is the ominous phenomenon of heating up the Earth's atmosphere by greenhouse gases (GHG) such as water vapor, carbon dioxide (CO₂), sulphur oxide (SO₂), nitrous oxide (NO₂), and chlorofluorocarbon (CFCs) etc. In

the normal levels, these gases maintain the atmospheric temperature and are the important reasons that life sustains on Earth. Regrettably, anthropogenic activities have made atmospheric emission levels of greenhouse gases (GHG) surpassing beyond the safety levels of 350 ppmv (Hansen 2008) and continues to increase the Earth's temperature at the range of 1.5-5.8°C (IPCC 2007). Currently, China, United States of America (USA), Russia, India, and Japan, respectively, are the five major contributors of global warming. Global warming leads to devastating consequences and forces the humans to face inevitable changes such as increase in sea level (up to 16 m), drastic changes in rainfalls etc. (Rohling 2007).

Greenhouse gases, present in the earth's atmosphere, are the gases that act as a protective barrier and filter harmful rays that enter into the atmosphere (www.ncdc.noaa.gov/monitoring-ref/faq/gng.php). Energy from the sunlight drives the earth's climate system and weather pattern which includes the heating of earth's surface. This heat is radiated back to the atmosphere which the atmospheric greenhouse gases (GHG) absorb and reduce the amount of heat that leaves earth (Reddy 2002). Water vapor, carbon dioxide (CO₂), methane, nitrous oxides are naturally occurring greenhouse gases (GHG) in the atmosphere (Campbell 2008). Other greenhouse gases (GHG) include chlorofluorocarbon, hydro fluorocarbons, per fluorocarbons as well as sulphur hexa fluoride which are artificially produced rising levels of greenhouse gases (GHG) causes imbalance between the concentrations of these atmospheric greenhouse gases (GHG) and the “sinks” places where the conversion of gases take place between the atmosphere and chemical compounds. Due to industrialization, the concentrations of these gases have increased beyond the threshold level. Among the aforementioned gases, water vapor contributes (35-75%) of greenhouse gases (GHG). Feedback warming of water vapor is a phenomenon by which concentrations of other

greenhouse gases (GHG) increase due to increasing concentrations of water vapor (Held 2000). Besides water vapor, although methane absorbs 21 times more heat than carbon dioxide (CO₂) and nitrous oxide traps 280 times more heat than a molecule of CO₂ (Allison 2009), the life of these gases are less in comparison to the amount of CO₂.

The aim of this research is to analyze weather variables to determine the effect of Global warming in Gusau Metropolis, Zamfara State, Nigeria. In this research work use is made of six months' data from May - October 2017 and May - October 2018 respectively which includes temperature, humidity, wind speed, atmospheric pressure and rainfall obtained from Federal University Gusau.

Methods of Carbon dioxide (CO₂) Sequestration

Carbon sequestration is the process of capturing carbon dioxide (CO₂) and other forms of carbon and storing them for long terms in order to control their concentration levels and thus reduce global warming (Sen 2012). Anthropogenic sequestration is a result of increasing anthropogenic emission of carbon dioxide (CO₂). Nature has been effective in handling its own emission better than the humans. Trees, oceans, earth and animals are all made “carbon based” by Nature and thus act as “carbon sinks” to balance the carbon levels. Human activities made this natural sequestration ineffective by emitting more carbon dioxide (CO₂) than the Nature itself can handle, thus increasing the need for artificial methods of sequestration such as abiotic and biotic sequestrations.

Abiotic Method

Abiotic sequestration is a method based on physical and chemical reactions for capturing and storing carbon without the help of biotic or living organisms. (Allison 2009). Abiotic method is of three types which are explained below:

a. Injection into Ocean

In this method, carbon dioxide (CO₂) is

injected deep into ocean. CO₂ from various sources are injected by the following methods:

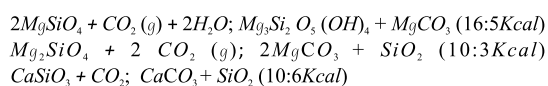
- I. Liquefied and injected below 1000 m at the ocean floor,
- II. Injection as a gas-water mixture at 500–1000m which sinks into the ocean,
- III. Discharges via long pipe from ships, and
- IV. Pumping into the ocean beds to form lakes of CO₂.

b. Geological Method

In this method, carbon dioxide (CO₂) is pumped into underground geological structures such as oil wells, coal mines, saline aquifers, etc. When injected into mines or oil wells, the gases gradually increase the yield of coal and oil, which has been proven beneficial for productivity. However, this method involves highly risky operating conditions and later consequence

c. Mineral Method:

In this method, scrubbing-the method of absorbing CO₂ by using a chemical solvent (amine or carbonate) is used to purify CO₂ and then injected into areas rich in magnesium, calcium, etc. The gas reacts with these elements mineral carbonation and forms minerals such as magnetite olivine, serpentine etc.



Biotic Method

Biotic method of sequestration involves living organisms such as plants and microbes. Bio mitigation or biological sequestration can be carried out by terrestrial plants and aquatic photosynthetic microorganisms. They are of the following types:

Terrestrial method

Carbon captured and stored by means of plants and trees is known as terrestrial carbon sequestration. Terrestrial carbon sequestration method can be subdivided as follows:

a. Forest ecosystems

This method makes use of forest vegetation to trap carbon and store it as lignin and other Polymeric carbon compounds. Plants and trees act as major carbon sinks since they reduce carbon effectively by means of their photosynthesis process. (Ruesch 2008). Gibbs, carbon dioxide information analysis center (CDIAC) in 2008 estimated that carbon storage of the total living vegetation worldwide amounts to an enormous 500 billion tons of carbon, which is around 60 times more than anthropogenic emissions. The current rate of carbon sequestration by forests is 1.7G 0.5 Pg C/yr annually, 40% of the total anthropogenic carbon is fixed photo synthetically by terrestrial plants. However, the slow growth rate is a major limiting factor for the terrestrial plants due to which they can account to only 3–6 % of the bio mitigation (Beiwang and Yangugi 2010). Afforestation includes various land management problems due to the ever growing, uneven increase in world population level. Besides their mitigation activity by photosynthesis, any intervention in this function of the plants leads to behavioral changes in plants which increase the risk of biodiversity problems (Armentan 1988); Greenhouse effect, sea level rise and coastal wetlands, United States (U.S) Environmental Protection Agency. Large scale plantation and forestation are followed by vulnerability to plugging maintenance costs, food security risks etc. Hence commercial use of terrestrial plants is currently not possible.

b. Wetlands Ecosystem

Wetlands have always played a major role in carbon sequestration. When compared to their other terrestrial counterparts, wetlands hold around 200 times or more amount of carbon. The huge wetlands of Amazon Forest are said to be saviors of Earth's ozone layer as they sequester around 200,000 tons of carbon dioxide (CO₂) annually (Hansen and Sato 2012). Even with this amount of significance in climatic effects, the wetlands still face problem such as land clearing for purposes such as agriculture, transport, housing, etc. due

to increasing food and housing demands, pollution due to various Eco hazard products usage and waste dumping near wetlands and other such activities due to which the rate of their sequestration is gradually decreasing.

c. Soil Ecosystem

Soil ecosystem is the method of carbon sequestration by improving the degraded soils and soil conservation practices (UNFAO). Soil ecosystems store carbon mainly by means of carbon assimilation by plants. Soil organic matter (SOM) a complex mixture of carbon compounds, consisting of decomposing plant and animal tissue, microbes (protozoa, nematodes, fungi, and bacteria), and humus is the primary way of soil carbon storage. It has been estimated that soils can sequester around 10% of the total anthropogenic carbon, particularly in India, which is estimated to be around 39 to 49 (44 ± 5) Tg C/y (Lal 2004). Erosion, desertification, land degradation, etc. lower soil carbon sequestration. Improved agricultural practices such as mulch farming, cover cropping, and crop rotation can increase soil carbon sequestration. Proper application of manures and fertilizers that affect carbon content in soil also help in reducing carbon emission from soils ecosystems. Although soil sequestration is a little cost expensive, it is worth practicing owing to the huge amount of carbon held within the ecosystem.

Ocean method

Phytoplankton photosynthesis also serves as a method of sequestering carbon. Intentional cultivation of these phytoplankton's in the ocean by means of providing Fe-rich resources is said to effectively reduce anthropogenic carbon emissions up to 45 Pg C/ Yr. However unnatural growth of this phytoplankton may produce unknown harmful effects to the entire ocean ecosystem.

Algae

An alternative and efficient way to sequester CO₂ (carbon dioxide) is bio sequestration by algae. Algae are simple unicellular to multi cellular microscopic organisms with both marine and freshwater habitats which have to their credit the photosynthetic ability. This

photosynthetic property along with their diverse habitat nature makes the algae a better option for bio mitigation of CO₂. Algae are classified into four main groups based on their size and metabolic characteristics into (i) macro algae, (ii) microalgae, (iii) alkalophilic (iv) halo tolerant algae. Microalgae are microscopic in nature and macroscopic algae are slightly larger in size while alkalophilic and halo tolerant microalgae have the ability to survive in highly saline conditions and alkaline conditions, respectively, with the help of their osmoregulatory functions.

The Ozone Layer

This is simply a layer in the stratosphere containing a relatively high concentration of Ozone. The earth's atmosphere is divided into several layers, and each layer plays an important role. The first region extending about 10km upwards from the earth's surface is called the troposphere. Many human activities like mountain climbing, gas as balloons and smaller aircrafts operate within this region. The next layer extending about 15 -60km is called the stratosphere from approximately 20 to 30 kilometers (12 to 19mi) above the earth's though the thickness varies seasonally and geographically. The Ozone layer protects the earth from the sun's UV Rays. If the Ozone layer is depleted by human action, the effects on the planet could be catastrophic (Michael 2005).

Ozone Depletion

Depletion of ozone layer has become a worrisome phenomenon to humanity in the recent time. The continuous existence of human race on the earth depends on how well we can protect the atmosphere and other properties e.g. oceans, seas, etc. from further degradation (Michael 2005). The quantity of ozone eaters that is ozone depleting compounds emitted into the atmosphere through human activities has been a source of concern to public health the accelerated thinning (ozone hole) of ozone layer at the poles and in other parts of the world should be viewed with all seriousness and be given a deserved attention (Annale *et al.* 2001). This is

because measurements undertaken since 1975 to date have shown that the concentration of stratospheric ozone is getting depleting at faster rate.

The Atmosphere

The sea of air in which people live is known as atmosphere. The atmosphere is made up of life sustaining gases such as oxygen, nitrogen, etc. It is divided into several spherical layers namely troposphere, stratosphere, mesosphere and so on (Michael 2005).

The Stratosphere

The stratosphere also known as the global sunscreen in the atmospheres second layer next to troposphere and it extends from about 17km to 48km above surface of the earth. Major component of this layer are the ozone and water vapor. The main function of the ozone layer is to prevent the harmful ultraviolet radiation of the sun from reaching the earth surface. Conservatively, about 99% Of the harmful UV Radiation from the sun is screened and filtered in the stratosphere by the ozone layer. This harmful UV Radiation consists of the three bands A, B and C. While ozone layer is able to absorb all the UV B and C Radiations, it's only able to screen small portion of the ultraviolet a radiation (Michael 2005).

Causes of Global Warming

Some of the major causes of global warming are as follows:

- I. Greenhouse effect and global warming occurred when CO₂ and other air pollutant and greenhouse gasses collected in the atmosphere absorbed sun light or solar radiation that has bounce off the earth's surface. Normally, this radiation will escape into space but these pollutants, which can last for centuries in the atmosphere, trap the heat and cause the planet to get hotter; this is known as greenhouse effect.
- II. Human Activities: - Human activity has obviously caused an imbalance equation in the natural cycle of the greenhouse effect and related processes. In Australia, for example,

land clearing and burning vegetation release millions of tons of CO₂ into the atmosphere every year. Scientific measurement over time reveals a clear correlation between CO₂ concentration in the atmosphere and global temperature. Research records also indicate that before the Industrial Revolution, the level of carbon dioxide in the atmosphere was 280 parts per million; today it is 380ppm (Matawa and Maton 2013).

Effects of Global Warming

The primary effects of global warming are listed as follows:

- I. Melting glaciers early, snowmelt, and drought will cause more dramatic water shortage and increase the rise of wildfires.
- II. Rising sea level will lead to coastal flooding
- III. Forests, farms and cities will face the troublesome new pests, heat waves, heavy downpour and increase flooding. All those factors damage the Agriculture and fisheries.
- IV. Allergies, asthmatic and infectious diseases outbreaks will become more common due to increase pollen producing ragweed, higher level of air pollution and of conditions favorable to pathogenic and mosquitoes.

Remedies of Global Warming

Carbon dioxide is the worst enemy of climate change. It's released when oil, coal, and other fossil fuels are burned for energy use in our day to day life (Electricity, Cars etc.). By using less of it, we can control, reduce the global warming and greenhouse effect which normally triggered climate change. Some other measures we employed to reduce the climatic challenges are:

- a. **Change Energy Usage:** Upgrade your heating and cooling systems and insulate your homes properly to make sure you aren't using energy in excess (Rio 1992). Since Energy usages contribute to increased levels of Carbon Dioxide (CO₂) into the atmosphere by reducing energy usage, you will reduce your personal carbon profile.
- b. **Update Buying Habits:** The way you shop is also a contributor to Global Warming (Rio 1992). Try to make purchases with

minimal packaging, and buy products that are designed to be efficient and long lasting. Keep track of your food wastage too; don't over purchase processed foods and the like.

c. Rethink Transportation: As it cuts down on emissions caused by oil and gasoline.

Measurement of Weather Variables.

Measurement of Temperature

Temperature: is the measure of the degree of hotness or coldness of a body or an object and it can be measured using an instrument called thermometer.

There are a wide variety of temperature measurement probes in use today depending on what you are trying to measure, how accurately you need to measure it, if you need to use it for control or just man monitoring, or if you can even touch what you are trying to monitor.

Measurement of Rainfall

An important theory on rain formation put forward by a Swedish meteorologist Bergeron in 1933 and strongly supported by findings in 1938 asserts that rainfall was, in effect, melted ice or snowflakes. The conflict with the theory lies in the fact that rain was also observed from clouds that did not extend up to freezing level. In some tropical countries like India and Nigeria a few observations have been made of rain from clouds, whose roofs were far below freezing levels (Hansen 2010). Air comprises water vapor. The quantity of water in a given mass of dry air is measured in grams of water per kilogram of dry air (g/kg). This is known as the mixing ratio. The quantity of moisture or water vapor in air is commonly called its relative humidity. Relative humidity is the percentage of the total water vapor the air can transform into a cloud is dependent upon its temperature (Joseph 2016). Cooler air can hold lesser water vapor than warmer air before becoming saturated. Hence, one method to saturate a measure of air fast is to cool it (Hansen and Sato 2012). Dew point is the temperature to which a measure of air must be cooled in order to become saturated. The various means by which water vapor is added

to the air are: daytime heating eventuating in evaporation of water from the surface of oceans and seas, smaller water bodies or wet lands; wind convergence into areas of upward motion; precipitation or virga falling from above; transpiration from plants; lifting air over mountains and cool or dry air moving over warmer water (Allison 2009). Water molecules start to condense on condensation nuclei such as ice, dust and salt in order to form clouds. Clouds are a group of visible tiny water and ice particles suspended above the earth's surface (Rio 1992). Rain is droplets of water that have condensed from water vapor in the atmosphere and then precipitated that is fall under gravity owing to its weight. Rain is one of the main constituents of the water cycle (Hansen 2010). It is responsible for depositing most of the fresh water on the earth. The chief maker of rain is moisture moving along three-dimensional zones of moisture and temperature contrasts known as weather fronts.

Measurement of Humidity

A hygrometer is an instrument used to measure relative humidity. Humidity is the measure of the amount of moisture in the air (<https://climate.ncsu.edu/edu/Instruments>). A sling psychrometer is a type of a hygrometer. A psychrometer uses two thermometers to measure relative humidity of the air; one measures the dry-bulb temperature and the other measures the wet-bulb temperature. (When you come out of your shower in the morning, your skin cools to the wet-bulb temperature and you feel a chill until the water evaporates.) The wet-bulb thermometer contains water in the base that evaporates and absorbs heat which decreases the temperature reading. To determine the relative humidity, the temperatures are taken from the dry-bulb thermometer and the temperature difference between the wet and dry bulb thermometers. From these measurements, a table is used to find the relative humidity at a certain location. A sling psychrometer is a common instrument used by meteorologists to determine the relative humidity. This instrument is swung around while being held. There are also a

variety of other humidity sensors which work automatically to measure the water content and relative humidity of the atmosphere. Some of the older hygrometers used sheaf of hair which increase in length as relative humidity increase.

Measurement of Wind

An anemometer is a type of weather instrument that is used to measure wind speed and wind direction in mile per hour. A common type of anemometer has three fixed cups fixed to a mobile shaft. as the wind blows faster the cup spin around faster. The actual speed of the wind shows up on a dial another type of anemometer which uses propeller instead of a cups to accomplish the same functions. The wind pushes the cups and causes the arms to rotate at a rate proportional to the wind speed. A windmill anemometer is a common instrument used at weather stations to obtain the wind speed. A wind vane is used as part of the anemometer to determine the wind's direction. As the wind flows over the windmill, the speed and direction of the wind can be measured with this instrument. Some scientific anemometers use the speed of sound to measure the wind speed more precisely in three dimensions. Wind direction is always given by where the wind is coming from, so that a west wind is blowing from the west and going towards the east.

Measurement of Atmospheric Pressure

Barometer is the common instrument used in weather station to measure atmospheric

pressure providing the measure in milli bar under most condition, high and rising pressure indicate sunny weather while low and falling pressure indicates approaching rain. The traditional aneroid barometer first appeared in the 1840s, the micrograph also measures air pressure but record its continuous measurement on paper.

Material and Method

Measurement of Data and Calculation

Two years data record was collected from space center Federal University Gusau Zamfara state Nigeria. The data was recorded forty-eight (48) times per day by vantage pro 2 automatic weather machine. The recorded values were summarized to a single value per day by finding the average of the forty (48) values for each day using mean summation method.

The daily (mean) of this data was summed up for each month and the monthly average calculated. This calculation is done by using mean summation formula.

The mean also known as the location parameter given by:

$$Mean = m = \frac{1}{N} \sum_{k=0}^n XK \quad (1)$$

Where N = Number of occurrence.

X = weather variable

K = 1, 2, 3, ..., n

Table 1 and 2 shows the weather variables summarized data from May to October 2017 and May to October 2018.

Table 1 Monthly Weather Variables Summarized Data for May-October 2018.

S/No	Variables	Time					
		May	June	July	August	September	October
1	Temperature	31.23	27.00	20.00	21.00	26.16	26.98
2	Humidity	53.34	71.00	63.64	50.00	82.57	65.56
3	Wind speed	0.39	0.35	0.17	0.018	0.06	0.03
4	Pressure	1008.95	1011.57	1010.52	1009.25	1011.50	1010.99
5	Rain fall	0.19	4.9	4.9	0.014	1.19	0.11

Table 2 Monthly Weather Variables Summarized Data for May-October 2017.

S/No	Variables	Time					
		May	June	July	August	September	October
1	Temperature	30.47	28.00	26.30	26.00	28.98	26.21
2	Humidity	56.79	74.72	81.91	83.31	82.67	55.78
3	Wind speed	0.50	0.34	0.25	0.15	0.14	0.42
4	Pressure	1009.55	1011.39	1013.20	1012.40	1012.16	1011.71
5	Rain fall	0.65	1.39	1.31	0.88	0.71	0.54

Results and Discussion

In Figure 1 and table 3 the average monthly temperature from May to October 2017 and from May to October 2018 was presented in table and bar chart graph form. The comparison of two years graph shows little difference in all the month that appears within the period of this research. The average monthly temperature of May 2018 is slightly higher than that of 2017. The average monthly temperature for the month of June, July, August, September and October 2017 is higher than average monthly temperature for month of June, July, August, September, and October 2018. Increase in temperature usually result to increase in global warming. From previous research, high temperature usually recorded as a result of bombardment of harmful toxic substances which emit carbon dioxide to the

environment. These activities of global warming and temperature increase usually affects agricultural products and humans and animal's life. As a result of increase in global warming and temperature, the year 2017 was characterized by high rate of heat waves, flood increase, unusually death of some of our agricultural products, and there was outbreak of diseases like meningitis etc. within Gusau, Zamfara State Nigeria as recorded in Federal Medical center (FMC) hospital Gusau, Zamfara state. All these factors would damage our environment, Agriculture products and fisheries there will be high level of air pollution and favorable conditions for pathogenic organisms.

Table 3 Showing Average Monthly Temperature.

Variables	Time					
	May	June	July	August	September	October
Temperature 2017	30.47	28.00	26.30	26.00	28.98	26.21
Temperature 2018	31.23	27.00	20.00	21.00	26.16	26.98

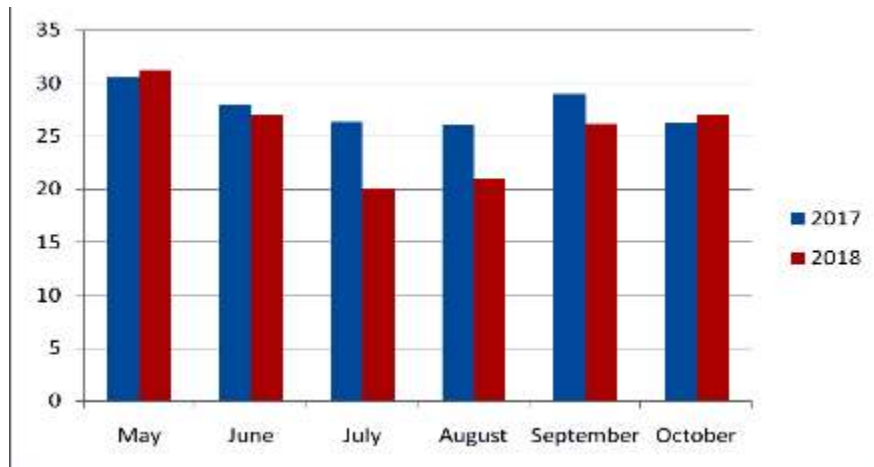


Fig. 1 Bar chart Showing Average Monthly Temperature from May-October 2017 and May-October 2018.

In figure 2 and table 4 the average monthly humidity from May to October 2017 and from May to October 2018 was presented in table and bar chart graph form. The comparison of two years graph shows little difference in all the month that appears within the period of this research. The average monthly humidity of September 2017 and 2018 is constant. The

average monthly humidity of May, June, July, and August 2017 is slightly higher than that of 2018. And also the average monthly humidity of the month of October 2017 is lower than average monthly humidity for the month of October 2018 which decrease in humidity usually result to an increase in temperature.

Table 4 Showing Average Monthly Humidity.

Variables	Time					
	May	June	July	August	September	October
Humidity 2017	56.79	74.72	81.91	83.31	82.67	55.78
Humidity 2018	53.34	71.00	63.64	50.00	82.57	65.56

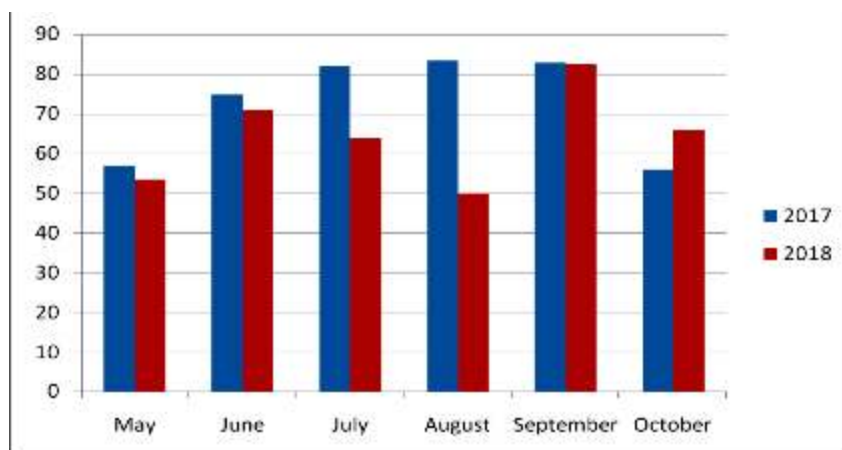


Fig. 2 Bar chart Showing Average Monthly Humidity from May-October 2017 and May-October 2018.

In figure 3 and table 5 the average monthly wind speed from May to October 2017 and from May to October 2018 was presented in table and bar chart graph form. The comparison of two years graph shows little difference in all the month that appears within the period of this research. The average

monthly wind speed of May, June, July, August and September 2017 is slightly higher than that 2018. Similarly the average monthly wind speed of October 2017 is higher than average monthly wind speed for the month October 2018. Increase in wind speed usually result to decrease in humidity.

Table 5 Showing Average Monthly Wind speed.

Variables	Time					
	May	June	July	August	September	October
Wind speed 2017	0.50	0.34	0.25	0.15	0.14	0.42
Wind speed 2018	0.39	0.35	0.17	0.018	0.06	0.03

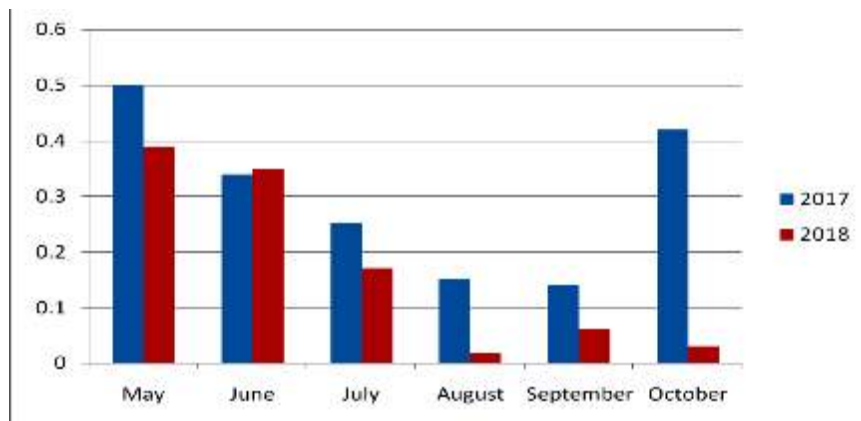


Fig. 3 Bar chart Showing Average Monthly Wind speed from May-October 2017 and May-October 2018.

In figure 4 and table 6 the average monthly atmospheric pressure from May to October 2017 and from May to October 2018 was presented in table and bar chart graph form. The comparison of two years graph shows little difference in all the month that appears within the period of this research. The average monthly atmospheric pressure for the month may, June, September and October 2017 is

slightly higher than average monthly atmospheric pressure for month of May, June, September, and October 2018. Similarly the average monthly atmospheric pressure for the month of July and August 2017 is higher than average monthly atmospheric pressure for the month of July and August 2018 where increase in pressure result to decrease in the amount of rainfall.

Table 6 Showing Average Monthly Atmospheric Pressure.

Variables	Time.					
	May	June	July	August	September	October
Atmospheric pressure 2017	1009.55	1011.39	1013.20	1012.44	1012.16	1011.71
Atmospheric pressure 2018	1008.95	1011.57	1010.52	1009.25	1011.50	1010.99

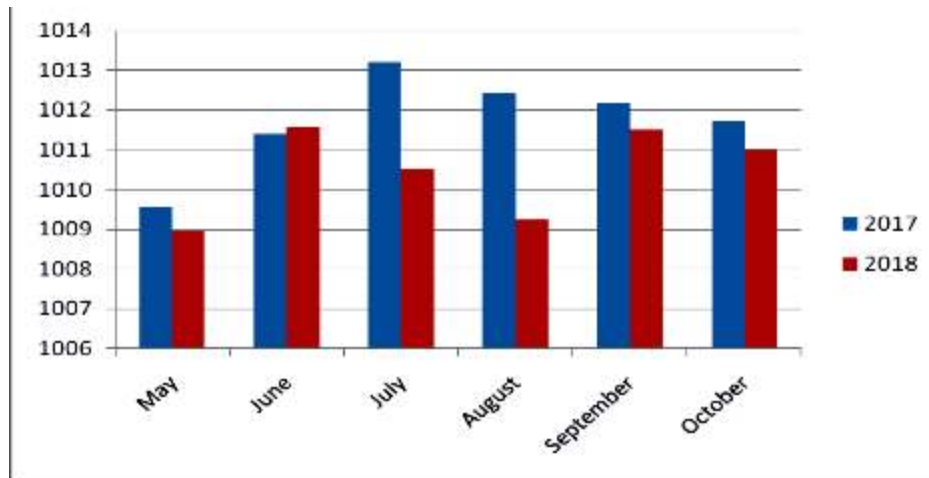


Fig. 4 Bar chart showing Average Monthly Atmospheric Pressure from May-October 2017 and May-October 2018.

In figure 5 and table 7 the average monthly rainfall from May to October 2017 and from May to October 2018 was presented in table and bar chart graph form. The comparison of two years graph shows little difference in all the month that appears within the period of this research. The average monthly rainfall of May, august, and October 2017 is slightly higher

than average monthly rainfall for the month of May, August and October 2018. The average monthly rainfall for the month of June, and July 2018 is higher than average monthly rainfall for the month of June and July 2017 where increase in the average monthly rainfall result to an unusual decrease in pressure.

Table 7 Showing Average Monthly Rainfall.

Variables	Time					
	May	June	July	August	September	October
Rainfall 2017	0.65	1.39	1.31	0.88	0.71	0.54
Rainfall 2018	0.19	4.9	4.9	0.014	0.19	0.11

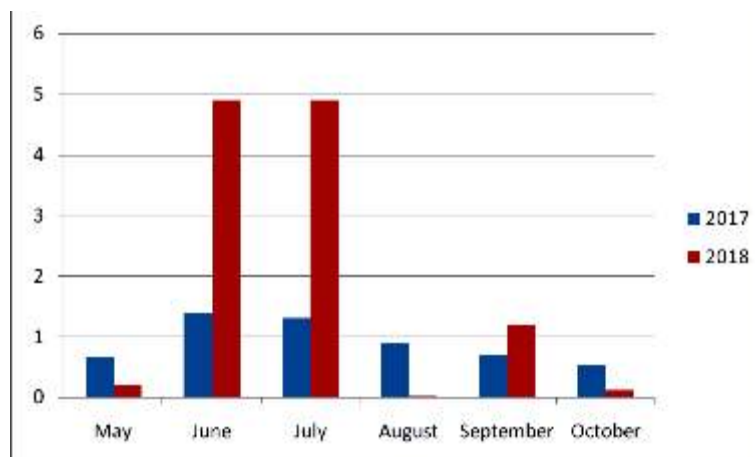


Fig. 5 Bar chart showing Average Monthly Rainfall from May-October 2017 and May-October 2018.

Conclusion

Global warming contributes to increase in some health challenges and gradually destroy our environment. This research was carried out to determine the effect of global warming using weather variables such as temperature, humidity, wind speed, atmospheric pressure and rainfall on environment. The research statistically analyzed the data obtained from Federal University Gusau space center. The data collected covers the weather of Gusau from May-October 2017 and May-October 2018. Measurements of temperature, humidity, wind speed, atmospheric pressure and rainfall were made by using Davis vantage pro 2 automatic machines, thermometer, hygrometer, anemometer, barometer and rain gauge, with results obtained indicating a gradual increase in temperature which obviously has a significant effect on the environment.

Reference

- Allen, F. and Rosselot, G. J. (1997). How Global is the solution global warming? *Economic modeling*, 20:93-117.
- Allison, I. (2009). The Copenhagen diagnosis updating the world on the latest climate Science. *Sydney: UNSW Climate Change Research*.
- Amentan, J. R. (1988). Global Surface Temperature Change. *Reviews of Geophysics* 48(4): RG400
- Annale, Y., Tord, K., Theo, D. K., and Teel, L. G. (2001). *Basic environmental health Oxford University Press New York*.
- Beiwang, G. and Yangugi, D. S. (2010). A global perspective on Last Glacial Maximum to Holocene climate change. *Quaternary Science Reviews* 29(15-16):1801-1816.
- Bharat, R. S. and Onkar, S. (2012). Study of impact of global warming on climate change: rise in sea level and disasters frequency. *Global warming - impacts and future perspective*, 2: 93-118.
- Campbell, K. O. (2008). Principle and practice of environmental health. *chapter 10* (121).
- Hansen, B. (2010). Global Surface Temperature Change. *Reviews of Geophysics*, 48 (4): RG4004.
- Hansen, J. and Sato. M. (2012). Paleoclimate Implications for Human-Made Climate Change. *Climate change inferences from paleoclimate and regional aspects*. Wien: Springer.
- Held, E. M. (2000). Do global warming and climate change represent a serious threat to our welfare and environment. *How scientists choose to fail or succeed*. 5: 101-109
- IPPC, Climate change fifth assessment report (2007): *The physical science basis summary for policy makers: 4*.
- Liu, H. (1994). Preventing global warming Starts at your home . <<https://www.welfarelabs.com/blog/preventing-global-warming-starts-at-your-home.php>> (01, Aug, 2018 22:35).
- Michael, K. O. (2005). Principle and practice of environmental health. *chapter 10*(121).
- Michael, K.O and Man, E. (2009). Do global warming and climate change. Represent a serious threat to our welfare and environment. *How scientists choose to fail or succeed*. 5: 101-109
- Matawal, D. S and Maton, D. J. (2013). Climate change and global warming impact and solution. *International journal of environmental science and development*, 4:61-62.
- N. A01. 2018. *Global temperatures*. U.K. Met Office. <http://www.metoffice.gov.uk/climatechange/guide/science/monitoring/global> (13, August, 2017 12:56).
- N.A. 2018. Global response to climate change. The Royal Society. <<https://royalsociety.org/policy/publications/2005/global-response-climate-change/>> (01, August, 2018 20:13).
- Reddy, H. (2002). Preventing global warming Starts at your home. <https://www.welfarelabs.com/blog/preventing-global-warming-starts-at-your-home.php> (01, August, 2018 22:35).
- Rio, D. J. (1992). Measuring and managing

weather variability protecting business from weather risk.

Meteoprotect, 5: 11.

Rohling, H. (2008). Preventing global warming Starts at your home.

<<https://www.welfarelabs.com/blog/preventing-global-warming-starts-at-your-home.php>> (01, August, 2018 22:35).

Ruesch, S. P. (2008). McGraw hill concise encyclopedia of science and technology.

McGraw-hill.

Sen, K. O. (2005). Principle and practice of environmental health. *chapter 10* (121).

Power Density Measurements for Associated Risk of Radio Frequency Radiation in Relation to Safety Limits for Human Exposure to EMF's in Zaria, Nigeria

Bello, I. A.¹, Sa'id, A.², Vatsa, M. A.³, Asuku, A.⁴ and Kure, N.⁵

^{1,2}Division of Agricultural Colleges, Ahmadu Bello University Zaria, Nigeria

^{1,3}Department of Physics Ahmadu Bello University, Zaria, Nigeria

⁴Center for Energy Research and Training, Ahmadu Bello University Zaria, Nigeria

⁵Department of Physics, Kaduna State University, Kaduna State, Nigeria

Corresponding author's e-mail: dbell1066@yahoo.com

ABSTRACT

Investigation of possible presence of radiofrequency (RF) radiations from mobile base stations was carried out within Sabon-Gari, Zaria, to estimate the maximum level of power density from radiofrequency radiations to which the members of the populace within specific radius from the base station are exposed to, in relation to the existing guidelines to human exposure. Power density S (Wm^{-2}) measurements were made at interval of 20 m to check the exposure level at public locations for 10 RF antenna sites starting from the foot of each base station to distance (radius) of 200m using TES-92 Electrosomog meter and the electric field strength E (Vm^{-1}) were calculated. The highest and lowest value obtained for measured average power density were 3229.82 mWm^{-2} and 1027.73 mWm^{-2} at a distance 20m and 200 m respectively, from the Base Stations (BS). Also, the highest mean electric field strength was $1137.943 \text{ E} (\text{Vm}^{-1})$ at distance 20 m, while the lowest mean electric field strength was $591.4135 \text{ E} (\text{Vm}^{-1})$ at 200m distance from the Base Station. The result of the study showed that the measured values were far less than the permissible exposure guideline values (ICNRP). Therefore, the amount of radio frequency radiation from selected base stations adhered to the international limits. RF emission from GSM base station may pose no health risk to members of the public within such vicinity.

Keywords: Telecommunication Antenna, Radio Frequency (RF), Power Density, Base Stations, EMF Exposure Limit

Introduction

Radiation is a form of energy that is constantly in motion and travelling at the speed of light through free space (Hoong 2003). The various forms of radiation known to man are arranged in a regular order termed as the "electromagnetic spectrum". Radio frequency radiation forms part of the electromagnetic spectrum; it has been found to be applicable in a variety of ways ranging from broadcasting to telecommunications and radar systems. The need to communicate with people far away has necessitated the development of various forms of technology in the field of telecommunications; consequently, there has been massive erection of telecommunication antennas in public places. The erection of

Global System for Mobile Communications (GSM) antennas in public places including residential areas has however become a source of concern to the members of the public. This is due to the suspected health effects that have been attributed to the radiofrequency radiation emitted by these antennas (Fawole 2011).

Radiofrequency radiation is a form of electromagnetic energy between 3 KHz-300 GHz (Habash 2008) in the electromagnetic spectrum. It is of great importance in wireless communication and it has the tendency of penetrating organic tissues, absorbed and may be converted into heat. The close proximity of Global System of Mobile Communication (GSM) base stations to public places leads to a high level of electromagnetic energy exposure

to the public. Exposure to RFR from mobile telephones is of a short-term, repeated nature at a relatively high intensity, whereas exposures to RFR emitted from cell mast is of long duration but at a very low intensity (Lai 1998). A study of radio frequency radiation was made to assess the exposure level from mobile phone base stations in Sabo-Gari Local Government Area, of Zaria, Kaduna state. The locations of the measurement were chosen based on the accessibility of the areas by the general public and places where the public used to spend their time. The measured values were then compared with the maximum permissible exposure set by the International Commission on Non-ionizing Protection (ICNRIP). This research discusses the findings of the study.

Quantification of RF Exposure

The International and national standards provide exposure limits in terms of power density S (Wm^{-2}) or in terms of electric field strength E (Vm^{-1}) and magnetic field strength H (Am^{-1}). The intensity (Power intensity) of radio frequency radiation in the environment is measured in units such as Wcm^{-2} or Wm^{-2} . At far Field where the radiation becomes a plane wave, the power density and electric field strengths are described by equation (1) below (Ozovehe et al. 2012).

$$E(Vm^{-1}) = \sqrt{S(Wm^{-2}) \times 377(\Omega)} \quad (1)$$

Where:

S = power density, E = Electric field strength (Ozovehe et al. 2012; Nwankwo et al. 2012)

Table1 below presents the permissible exposure limit of power density for workers and the general public.

Table 1 Permissible Exposure Guideline Values for

Exposure Characteristics	Power density (Wm^{-2})
Occupational exposure	50
General public exposure	10

Materials and Method

The research was carried out across Sabo Gari local government area, Zaria Kaduna state. The study area is located between latitude $11^{\circ}15'N$ and $11^{\circ}3'N$ of the equator and longitude $7^{\circ}30'E$ and $7^{\circ}45'E$ of the Greenwich meridian. Selected base stations were surveyed in the study area and coded BS1 to BS10 as shown in the Table 2 below.

All the base stations surveyed had at least 3 antennas on them with each antenna covering a sector of 120° . Thus, it was possible for measurement to be taken in any convenient direction within a particular sector. Measurements were taken at an interval of 20 m starting from the foot of each of the base station up till a distance of 200 m. The power density at each base station was measured with the aid of the TES-92 Electrosmog Meter. The Electric field strength was calculated using equation (1).

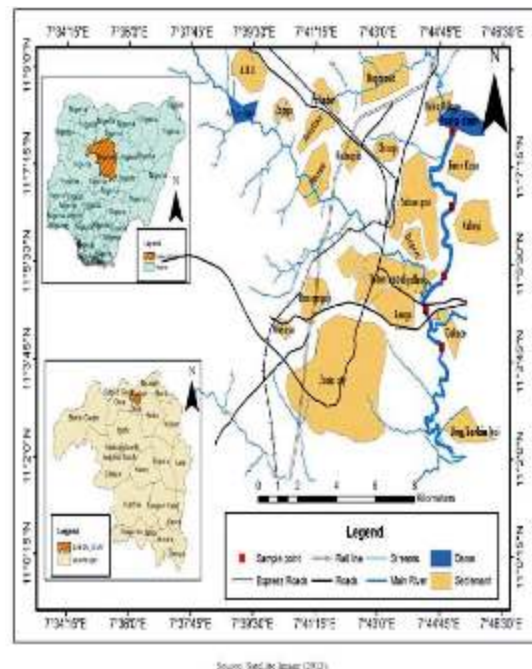


Fig. 1 Map of Sabon-Gari L.G.A in Zaria.

Table 2 Position surveyed of selected mobile station in Zaria.

Base Station	Location	Position
BS1	ABU (North Gate)	Lat. 11°09'12"N, Long. 07°41'28"E
BS2	Basawa	Lat. 11°09'03"N, Long. 07°41'11"E
BS3	Samaru (LEA Primary School)	Lat. 11°10'18"N, Long. 07°42'23"E
BS4	ABU (Area G Gate)	Lat. 11°10'25"N, Long. 07°42'20"E
BS5	Zango	Lat. 11°08'22"N, Long. 07°40'48"E
BS6	CERT	Lat. 11°09'18"N, Long. 07°38'16"E
BS7	Hanwa GRA	Lat. 11°08'09"N, Long. 07°39'28"E
BS8	Paladan (Angwa Fulani)	Lat. 11°08'19"N, Long. 07°38'37"E
BS9	ABUTH Tudun Wada	Lat. 11°07'22"N, Long. 07°33'24"E
BS10	Sabo Market	Lat. 11°09'22"N, Long. 07°36'04"E

Results

Measurement where carried out randomly at selected location at Sabon-Gari Local Government Area in Zaria, Kaduna State Nigeria. Table 3 summarizes the description of measurement level at each base station.

Table 3 Measured Power density of the Base Station (BS) at 20 m interval

Distance (m)	Power Density ($\mu W m^{-2}$)									
	BS1	BS2	BS3	BS4	BS5	BS6	BS7	BS8	BS9	BS10
20	370.8	1008	706.5	289.3	2827	1004	259.6	674	3031	1536
40	462.1	1343	1727	199.4	1445	1248	647	691.8	1235	1479
60	489.7	1154	1381	540.9	2964	1971	928.3	443.4	741.4	1753
80	934.6	519.3	1265	2192	5880	7018	744.5	4582	397.8	6053
100	2666	1203	222.1	1100	5934	1584	11560	703.7	581.4	6744
120	2225	1214	1911	1086	2552	3704	22.20	963.8	737.5	7051
140	803.2	1941	780.3	2334	4113	6162	4849	1396	708.9	10510
160	587.9	712.2	2181	1144	3756	6426	268.7	1137	2967	4952
180	638.9	501.2	2957	980.8	3462	3440	19790	280.1	346.6	2828
200	1223	702.6	3181	1509	2932	1231	48830	1314	355.9	3466

Table 4 Mean power density combined of all base station

Base Station	Distance (m)	Mean Power Density ($\mu W m^{-2}$)
BS1-10	20	3229.82
	40	2958.62
	60	2859.74
	80	2146.65
	100	2113.18
	120	1774.45
	140	1722.46
	160	1236.67
	180	1167.62
	200	1027.73

The highest and lowest value obtained for measured average power density were 3229.82 mWm^{-2} and 1027.73 mWm^{-2} at a distance 20 m and 200 m respectively, from the Base Station (BS) as shown

at Table 4. The power density decreases by the square of radial distance ($P_r / 4\pi R^2$) farther away from the reference base station.

Table 5 Mean electric field strength combined of all base station

Base Station	Distance(m)	Mean Electric Field Strength (Vm^{-1})
BS1-10	20	1137.943
	40	1024.055
	60	959.3141
	80	954.316
	100	932.107
	120	869.5842
	140	809.5583
	160	652.3551
	180	598.266
	200	591.4135

From Table 5, the highest mean electric field strength was $1137.943 \text{ (Vm}^{-1}\text{)}$ at distance 20 m, while the lowest mean electric field strength was $591.4135 \text{ (Vm}^{-1}\text{)}$ at 200 m distance from the Base Station. The electric field strength is seen to decrease farther away from the reference base station.

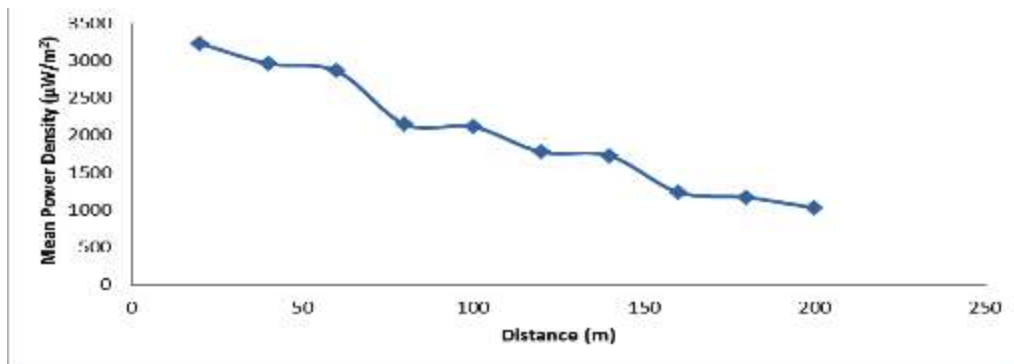


Fig. 2 Mean power density measured at 20 m Interval.

Figure 2 illustrate the power density decreases by the square of radial distance ($P_r / 4\pi R^2$) farther away from the reference base station. There were little fluctuations during measurement due to obstruction constituted by immobile structures.

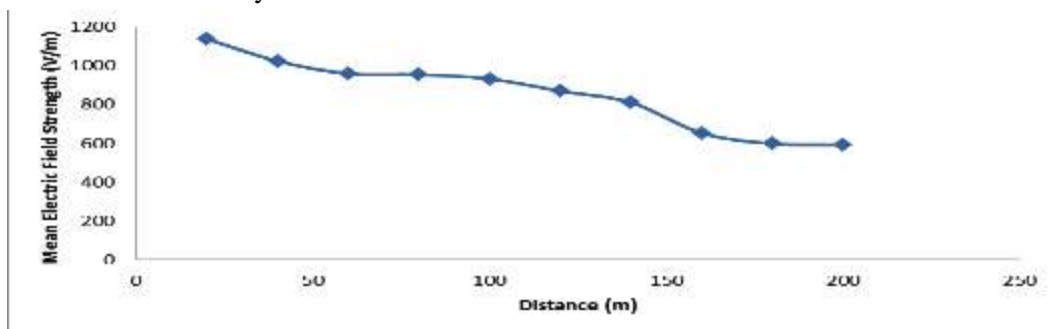


Fig. 3 Mean Electric Field Strength measurement at 20 m interval.

Similarly, figure 3 also illustrate the electric field strength decreasing farther away from the reference base station. Correspondingly, there were little fluctuations during measurement due to obstruction constituted by immobile structures.

Discussion

The highest value obtained for measured average power density was 3229.82 mWm^{-2} at a distance 20 m, from the Base Station (BS) shown at table 4 and figure 2. The highest value of electric field strength was 1137.943 Vm^{-1} , at distance 20 m from the base station shown at table 5 and figure 3.

The electric field strength and measured power density obtained the highest measurement at the same distance 20 m from the base station as shown in figure 2 and Figure 3 respectively, the lowest value of the electric field strength power density was at distance 200 m.

The power density and electric field strength decreases by the square of radial distance ($P_i / 4\pi R^2$) as we move farther away from the reference base station, however in figure (2 & 3), there was little fluctuation during measurement due to obstruction constituted by immobile structure (e.g. building) within the line sight of measurement, topography (or elevation) of the land area around reference base station with respect to radial distance away from the base station and wave interference from other sources of electromagnetic radiation around reference base station such as radio and TV antennas, receivers.

Conclusion

In general, the mean (average) power density and electric field strength of base station decreases as the radial distance (away from the base stations) were increased, also the radiation intensity varies from one mobile station to another (even at the same distance). The highest recorded exposure levels in all

location were below International Commission on Non Ionizing Radiation Protection (ICNRP) guideline. Therefore, RF exposure hazard index in Sabon-Gari L.G.A., of Zaria, was below the permitted RF exposure limit for the general public. Government should inert and enforce a law that ensure service providers adhere strictly to set guidelines for installation of mobile base station especially relating to their proximity to residential and official areas.

References

- Hoong, N. (2003). Radiation, Mobile Phones, Base Stations and your Health. Tam Lye Suan Millennia Comms, *Published for Malaysian Communications and Multimedia Commission*.
- Fawole, W. I. (2011). Estimation of Radiofrequency power density around GSM base stations in Northern Part of Lagos. Nigeria. *Unpublished M.Sc Project*.
- Habash, R. W. Y. (2008). Bio effects and Therapeutic Applications of Electromagnetic Energy London: CRC Press Taylor and Francis Group.
- Lai, H. (1998). Neurological Effects of Radiofrequency Electromagnetic Radiation. Paper presented at the "Workshop on possible Biological and Health Effects of RF Electromagnetic fields", Mobile Phone and Health Symposium. *University of Vienna, Vienna. Retrieved 22-04-2011 from <http://www.mapcruzin.com>*
- Ozovehe, A., Usman, A. U. and Hamdallah, A. (2015). Electromagnetic radiation exposure from cellular base station: a concern for public health. *Nigerian Journal of Technology*, 34(2): 355-358
- Nwankwo, V. U. J., Jibiri, N. N., Dada, S. S., Onugba, A. A., and Ushie, P. (2012). Assessment of Radio-Frequency radiation exposure level from selected mobile base stations (MBS) in Lokoja, Kogi State, Nigeria. *Physics.med-ph: 1-12*.

Mapping of Subsurface Geological Structures using Ground Magnetic and Electrical Resistivity Methods within Lead City University, Southwestern Nigeria

Adebo, B. A.¹, Layade, G. O.², Ilugbo, S. O.³, Hamzat, A. A.⁴ and Otoberise, H. K.⁵

^{1,4,5}Department of Physics, Lead City University Ibadan, Nigeria

²Department of Physics, Federal University of Agriculture Abeokuta, Nigeria

³Department of Applied Geophysics, Federal University of Technology Akure, Nigeria

Corresponding author's e-mail: adeboistalking@yahoo.com

ABSTRACT

Integrated geophysical methods involving ground magnetic and electrical resistivity methods were adopted in this study for the purpose of delineating subsurface geological structure within Lead City University, Ibadan, Nigeria. Four geophysical traverses were established; traverses one (1) and four (4) were established in east-west direction while traverses two (2) and three (3) in the south-north direction were occupied for Vertical Electrical Sounding (VES) and ten profile lines in east-west directions for ground magnetic method using Proton Precision Magnetometer and Omega Resistivity meter respectively. A total of thirty four points were acquired for VES in the study area. Magnetic method shows gradient of diagnostic structural changes interpreted in term of fractures and fault. The geoelectrical parameters determined from interpretation of the Vertical Electrical Sounding (VES) revealed that the area is underlain by four geoelectric layers corresponding to topsoil, weathered layer, fractured basement and fresh basement. The overburden thickness within study area is generally thin indicating that the basement is generally shallow. The integration of the results from the different geophysical techniques employed established effective correlation and relationship with allowance for speculations.

Keywords: Ground magnetic, Geoelectric sections, geological structures, Lithologies, Weak zone

Introduction

Geophysical techniques which can be taken with denser measurement spacing than direct sampling and involve much less costs, are potentially useful in characterizing building sites with adequate accuracy when large sites are to be studied (Adelusi et al. 2013). These methods are able to investigate and determine parameters and subsurface characteristics such as soil properties, bedrock depth and its topography below unconsolidated material, rock type, layer boundaries, water table depth and presence of weak zones and expansive clays (Ilugbo et al. 2018). Furthermore, these investigations provide information on inhomogeneities of the subsurface, presence of cavities, ancient relics and generally underground structures or bodies that have different physical properties from their

geological surroundings (Aubert 1984). Geophysical and geotechnical results could be combined to ascertain the in-situ properties of the subsurface. Engineering geophysics combined with geotechnical engineering focus on the behavior and performance of soils and rocks in the design and construction of civil, environmental and mining engineering structures. The two methods are often the most cost-effective and rapid means of obtaining subsurface information, especially when the area involved is large (Soupios 2007; Soupios et al. 2007; Oyedele and Bankole 2009). Surface magnetic and electrical resistivity geophysical field methods are widely used for groundwater, environmental and engineering studies of the Earth. These methods measure magnetic properties and electrical contrasts associated with earth materials. For instance, both magnetic and resistivity methods have

been successfully used in detection of mineshafts (Tsokas et al. 1998) and dam site investigations (Aina *et al.* 1996). These techniques are also important in delineating dipping formations and disruption in rocks units, structural trends, lithologic boundaries and contacts, faults, etc. within basement rocks (Olorunfemi *et al.* 1986). The basement rocks are often overlain by relatively flat-lying, sedimentary strata, which obscure the basement from direct view, but are largely transparent for geopotential fields. Due to conductive nature of deep weathering impacts and magnetization properties of the underlying basement rock, primarily migmatite-gneiss, both electrical and magnetic geophysical surveys are relevant in studying the subsurface characteristics and hydrogeological significance of aquifer types in this area. In the present study, combinations of surface geophysical investigation techniques utilizing Vertical Electrical Sounding (VES) and ground magnetic surveying are used to delineate subsurface geological fissures. The methods were employed to determine the subsurface electrical stratification, the presence of structures like weak zones and faults, contact between lithologic units and the depth to the possible basements and its undulation/morphology. The purpose of this work is to delineate the subsurface geological structure at a location in Lead City University, Ibadan, Nigeria using ground magnetic and electrical resistivity methods.

Description of the Study Area

The area investigated lies around Lead City University is located along the Ibadan-Lagos express way southwest Nigeria (Figure 1), located on 7, 21, 1.38 to 7, 22, 22.67 latitude and 3, 51, 38.59 to 3, 52, 43.98 longitude using geographics (WGS84). Major and minor road linkages characterize the study area. The topography of the area is generally flat and punctuated in some areas by hilly ridges and gentle steeps. Topographic elevations vary from about 320 to 390 m above sea level. It has an annual rainfall of between 1,100 mm and

1,300 mm (NSRMEA, 1994). The area enjoys a tropical climate with two distinct seasons comprising of rainy seasons (April to October) and Dry season (November to March). Mean monthly maximum temperature values from 30 °C to 35 °C which is recorded between April and May. While the mean minimum monthly temperature ranges between 17 °C to 21 °C in December and January.

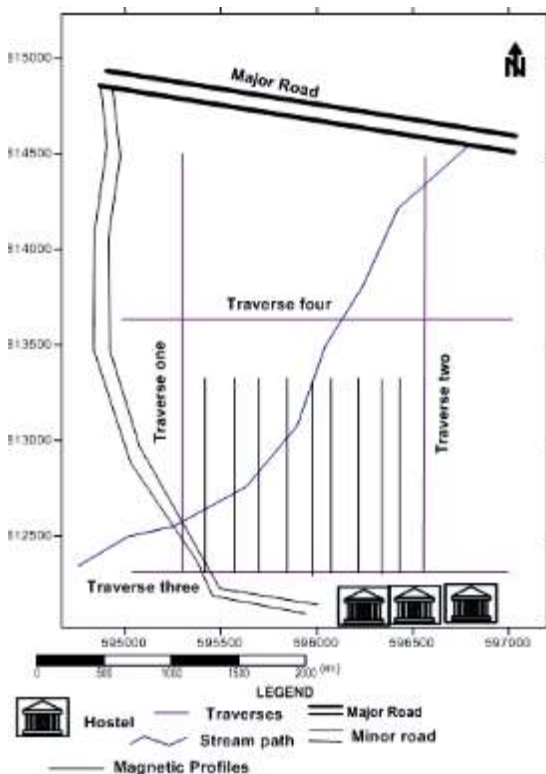


Fig. 1 Base Map of the Study Area

Geology of the Study Area

Regionally, the study area is concealed within the Southwestern Nigeria basement complex composing migmatite-gneiss complex, metaigneous rock such as pelitic schist, quartzite, amphibolites, charnockitic rocks, older granite and unmetamorphosed dolerite dykes. The rock sequence consists of basically weathered quartzite older granite. The basement complex rocks of Nigeria are made up of heterogeneous assemblages (Ramahan 1976). Lead City University, located along the

Ibadan-Lagos express way, forms part of the Western Nigeria basement environment. The basement complex is characterized by highly rugged terrain with rocks comprising mainly low permeable and less porous undifferentiated older granite, migmatite gneiss, quartzite and morphology granite gneiss with schist impregnation (Rahaman 1988). Due to conductive nature of deep weathering impacts and magnetization properties of the underlying basement rock, primarily migmatite-gneiss, both electrical and magnetic geophysical surveys are relevant in studying the subsurface characteristics and hydrogeological significance of aquifer types in this area.

Methods

The ground magnetic and Vertical Electrical Sounding (VES) technique was adopted in this work (Figure 2). The ground magnetic investigations were carried out using foot Geometrics 856 Proton Precision Magnetometer and Garmin Global Positioning System (GPS) navigational Equipment for real-time measurements. A base station was carefully selected and established near the study area where the magnetometer was used continuously to correct for diurnal variations of earth magnetic field and other sources of external origin. One magnetic measurement was taken per station while a total of 5 readings were taken at the base stations together with readings of the time. The mean of the magnetic measurements was adopted as the raw data for each observed stations. The acquired data was drift corrected. Corrected magnetic data was plotted against station positions using Microsoft Excel to produce the magnetic profiles along the traverses. Magnetic lows and magnetic highs were observed within the different stations to characterize the profiles. This method was used as a geophysical tool to map out the study area for basement structures.

Vertical electrical soundings (VES) were conducted within the study area using geophysical Omega resistivity meter.

Schlumberger array was employed with electrode separations (AB) ranging from 1 to 100 m. The VES points were made across the traverses adopted for the magnetic survey; the apparent resistivity values were calculated. The apparent resistivity measurements at each station were plotted against electrode spacing (AB/2) on bi-logarithmic graph sheets. The curves were inspected to determine the number and nature of the layering.

Partial curve matching was carried out for the quantitative interpretation of the curves. The results of the curve matching (layer resistivities and thicknesses) was fed into the computer as a starting model in an iterative forward modeling technique using RESIST version 1.0 (Vander Velpel 1988). From the interpretation results (layer resistivities and thicknesses), geoelectric sections along traverses was produced and correlated with the magnetic profiles for proper understanding of the subsurface structures.

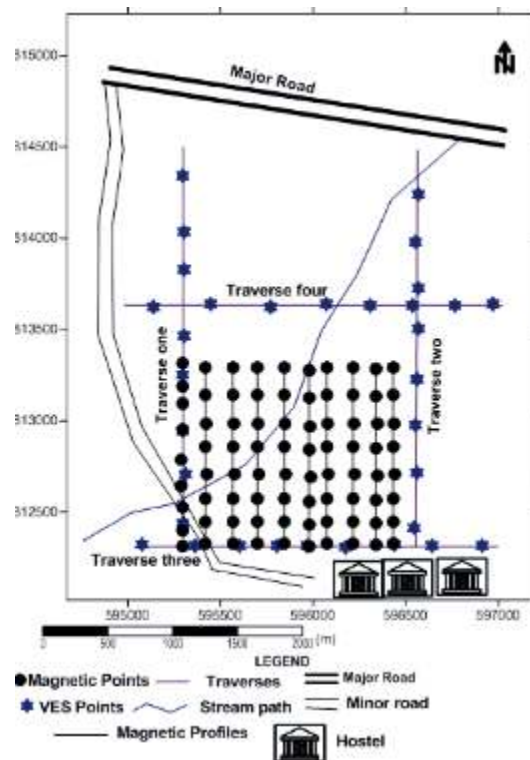


Fig. 2 Data Acquisition Map of the Study Area.

Results and Discussion

The results are presented as depth sounding curves, geoelectric sections and profiles. Each of the discussion of the results was done along each traverses for the methods employed in these research that is, along the Traverse one (1), Traverse two(2), Traverse three (3) and

Traverse four (4) respectively.

Vertical Electrical Sounding

The number of layers delineated by the curves varies between three and five layers. The VES curves are H, HA, A and HKH type as shown in Figure 3 (a-d) with the HA type predominating.

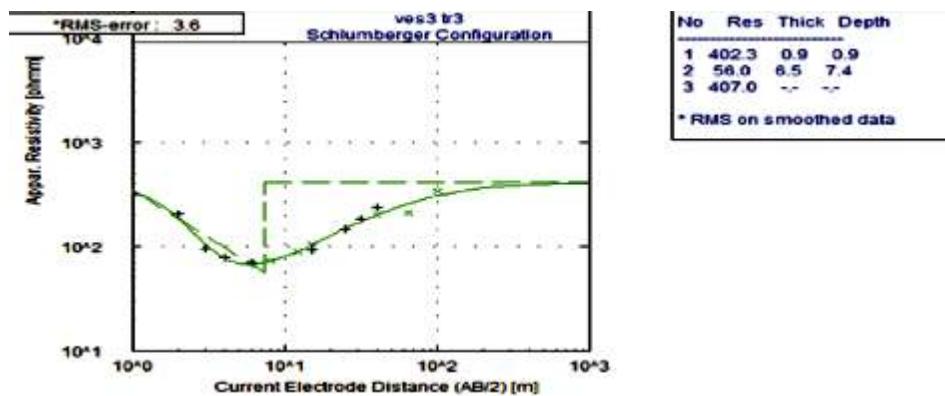


Fig. 3a Typical 'H' sounding curve

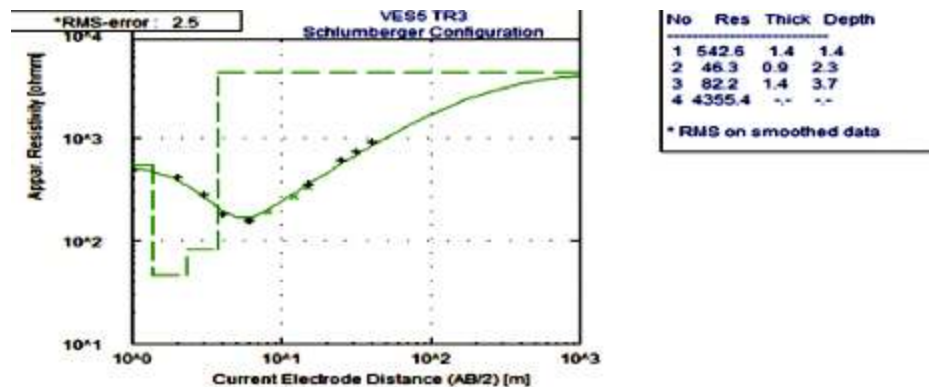


Fig. 3b Typical 'HA' sounding curve

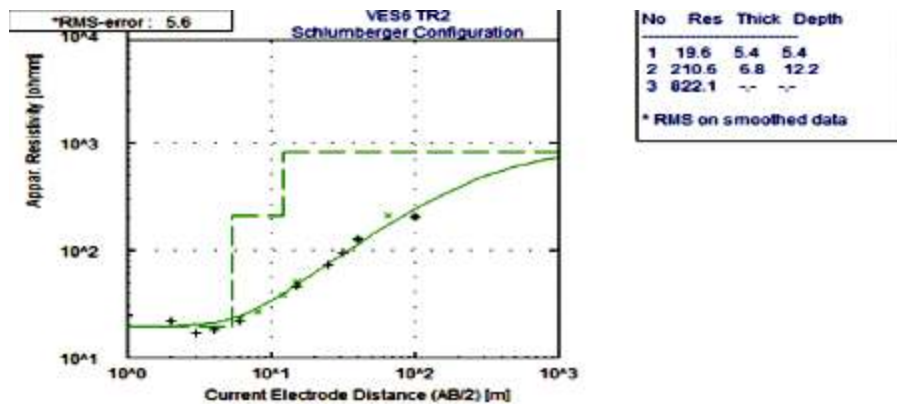


Fig. 3c Typical 'A' sounding curve

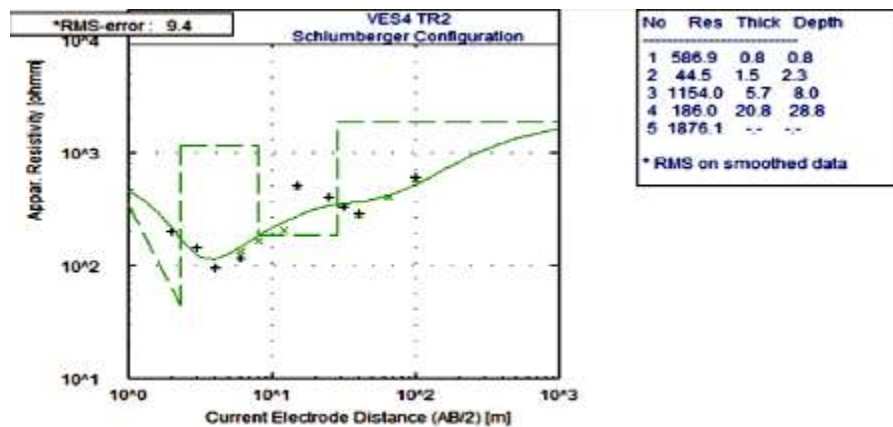


Fig. 3d Typical 'HKH' sounding curve

Geoelectric Sections

Four geoelectric sections were generated within the study area, and maximum of four geologic layers were delineated: the top soil, weathered layer, fractured basement and the fresh basement. The geoelectric section shows two dimensional or cross sectional impression of the subsurface. Topography of the bedrock along the profile can be seen from the sections. Bedrock depression and ridges are identifiable in the bedrock relief.

On traverse one the geoelectric section is composed of all the nine VES points on traverse one (Figure 4a). It is made up of four geoelectric layers namely; Topsoil, weathered layer, fractured basement and fresh basement. The topsoil comprises of clayey sand and sand with resistivity values ranging from 21 ohm-m to 437 ohm-m with thickness ranging from 0.8m to 1.5m. The weathered layer comprises of clay, sandy clay, clayey sand and sand with resistivity values ranging from 64 ohm-m to 594 ohm-m with thickness ranging from 2.3m to 25.9m. The fractured/fresh basement is characterized by resistivity values ranging from 8ohm-m to 4081ohm-m, the depth to the top of the bedrock ranges from 2.5m to 25.7m.

On traverse two the geoelectric section is composed of all the eight VES points on traverse two (Figure 4b). It is made up of four geoelectric layers; Topsoil, weathered layer, fractured basement and fresh basement. The topsoil comprises of clayey sand and sand with resistivity values ranging from 20 ohm-m to

878 ohm-m with thickness ranging from 0.5m to 5.4m. The weathered layer comprises of clay, sandy clay, clayey sand and sand with resistivity values ranges from 6 ohm-m to 197 ohm-m with thickness range of 2.3m to 29.0m. The fresh/fractured basement resistivity values range from 186 ohm-m to 1876 ohm-m, the depth to the top of the bedrock ranges from 10.3m to 59.9m.

On traverse three the geoelectric section is composed of all the nine VES points on traverse three (Figure 4c). It is made up of four geoelectric layers; Topsoil, weathered layer, fractured basement and fresh basement. The topsoil comprises of clayey sand and sand with resistivity values ranging from 84 ohm-m to 877 ohm-m with thickness ranging from 0.6m to 1.4m. The weathered layer comprises of clay, sandy clay, clayey sand and sand with resistivity values ranges from 2 ohm-m to 151 ohm-m with thickness range of 1.1m to 23m. The fresh/fractured basement resistivity values range from 246 ohm-m to 4355 ohm-m, the depth to the top of the bedrock ranges from 3.7m to 23m.

On traverse four the geoelectric section is composed of all the eight VES points on traverse four (Figure 4d). It is made up of four geoelectric layers; Topsoil, weathered layer, fractured basement and fresh basement. The topsoil comprises of clayey sand and sand with resistivity values ranging from 37 ohm-m to 515 ohm-m with thickness ranging from 0.5m to 1.2m. The weathered layer comprises of

clay, sandy clay, clayey sand and sand with resistivity values ranges from 11 ohm-m to 615 ohm-m with thickness range of 2.5m to 19.9m. The fresh/fractured basement resistivity values

range from 294 ohm-m to 1300 ohm-m, the depth to the top of the bedrock ranges from 2.4m to 19.9m.

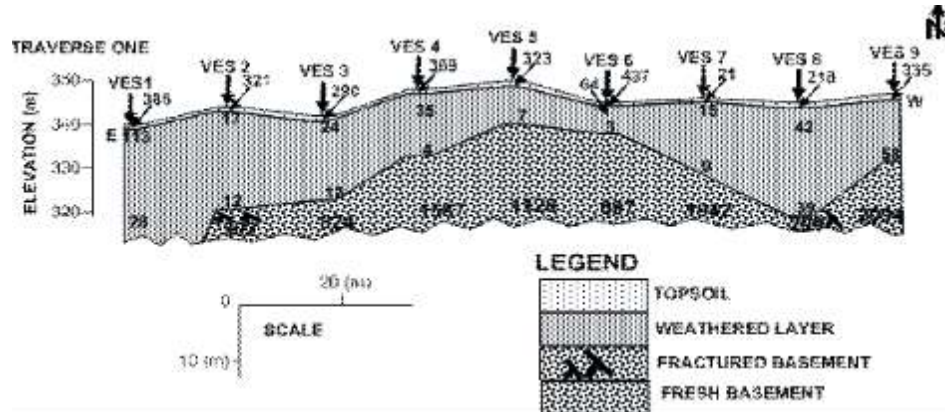


Fig. 4a Geoelectric section along traverse 1

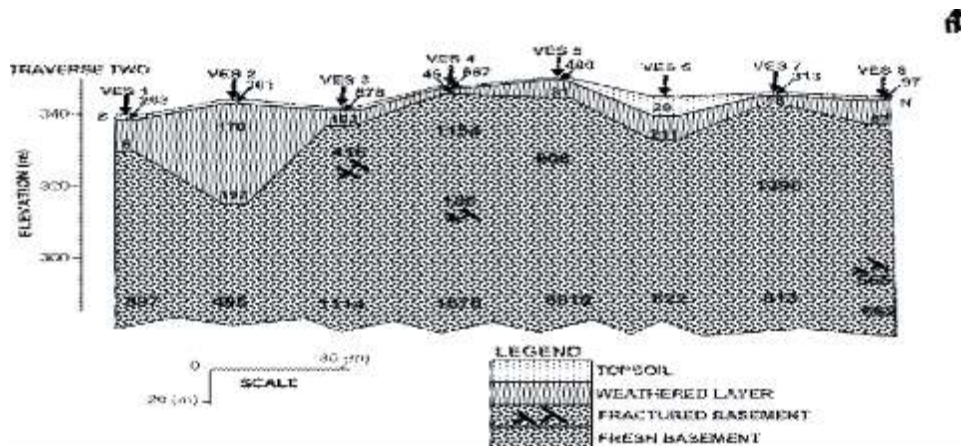


Fig. 4b Geoelectric section along traverse 2

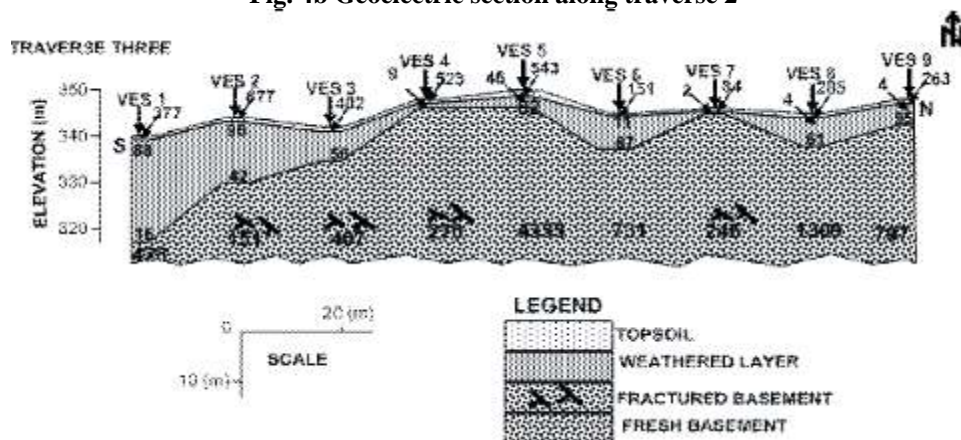


Fig. 4c Geoelectric section along traverse 3

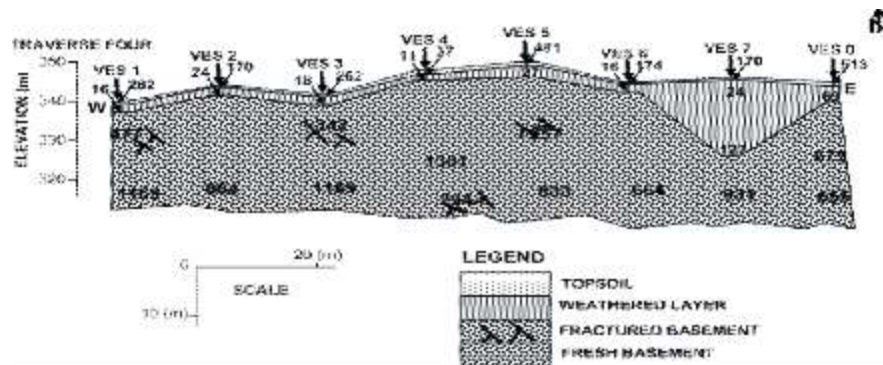


Fig. 4d Geoelectric section along traverse 4

Magnetic Profiles

The result of the geomagnetic data is presented as profiles (Figure 5a to Figure 5j) showing the variation in magnetic amplitude of the anomaly signature. The magnetic high is characterized by low amplitude and low intensity. Profile one, the magnetic intensity contrast observed between 33050nT and 33200nT at distance between 20 and 30m and between 33800nT and about 33900nT at distance ranging between 90 and 101m which are indicative of probable fracture zones.

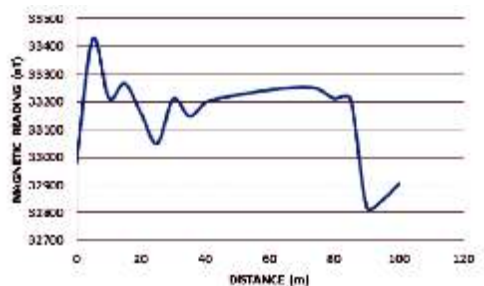


Fig. 5a Magnetic reading on profile 1

Profile two, the magnetic intensity contrast observed between 32200nT and 33200nT at distance between 20 and 24 m which are indicative of probable fracture zones.

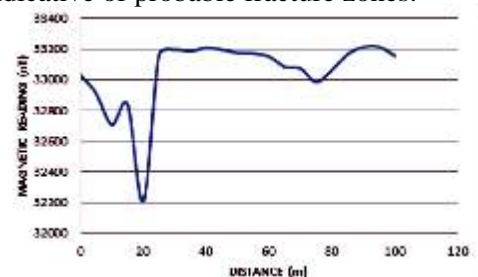


Fig. 5b Magnetic Reading on Profile two

Profile three, shows the magnetic intensity contrast observed between 32300nT and 33200nT at distance between 90 and 101m which are indicative of probable fracture zones.

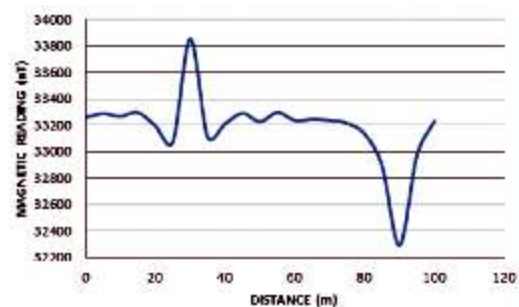


Fig. 5c Magnetic Reading on profile three

Profile four, the magnetic intensity contrast observed between 32400nT and 33700nT at distance between 10 and 30m which are indicative of probable fracture zones.

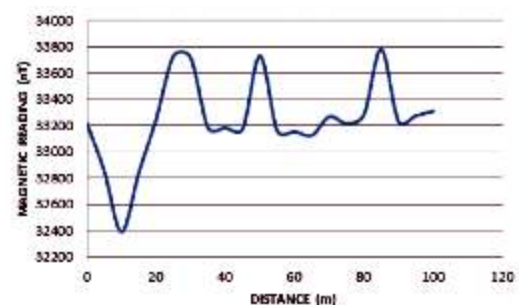


Fig. 5d Magnetic Reading on profile four

Profile five, the magnetic intensity contrast observed between 33110nT and 33300nT at distance between 22 and 31m which are indicative of probable fracture zones.

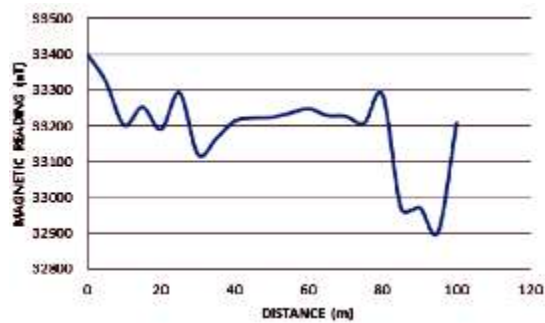


Fig. 5e Magnetic reading on profile five

Profile six, the magnetic intensity contrast observed between 32700nT and 33210nT at distance between 10 and 20m and between 32900nT and 33220nT at distance ranging between 70 and 78m which are indicative of probable fracture zones.

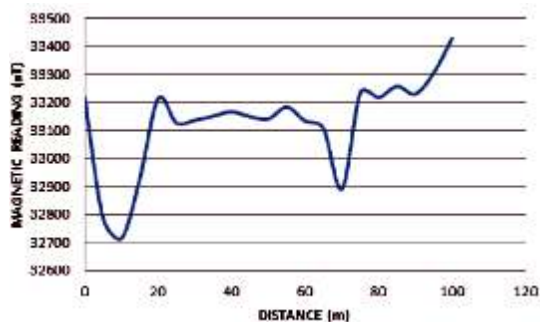


Fig. 5f Magnetic reading on profile six

Profile seven, the magnetic intensity contrast observed between 33050nT and 33280nT at distance between 38 and 80m which are indicative of probable fracture zones.

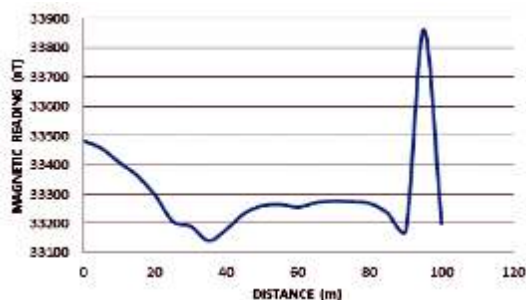


Fig. 5g Magnetic reading on profile seven

Profile eight, the magnetic intensity contrast observed between 330520nT and 33300nT at distance between 75 and 84m which are indicative of probable fracture zones.

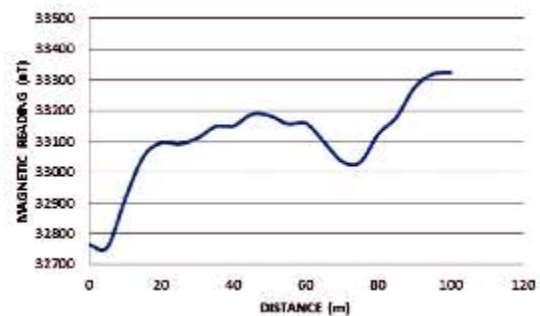


Fig. 5h Magnetic reading on profile eight

Profile nine, the magnetic intensity contrast observed between 33100nT and 33250nT at distance between 30 and 40m which are indicative of probable fracture zones.

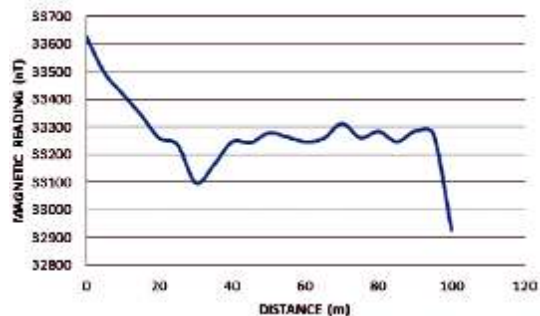


Fig. 5i Magnetic reading on profile nine

Profile ten, the magnetic intensity contrast observed between 33150nT and 33300nT at distance between 22 and 30m which are indicative of probable fracture zones.

The magnetic lows are indicative of depressed zones; the inflection points are indicative of geologic boundaries or contacts between two rock types, structural changes within the same rock type and the presence of lineaments such as network of joints, fractures and or faults.

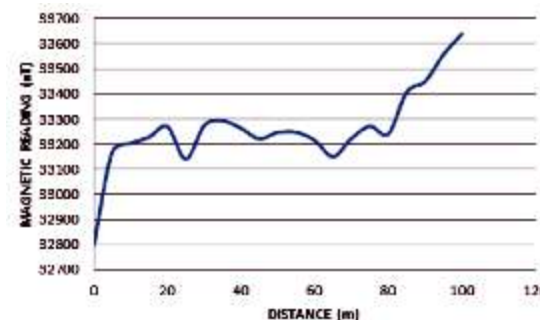


Fig. 5j Magnetic reading on profile ten

Comparison of Results

The magnetic intensity contrast observed at distance 20 to 30 m coincides with the depression observed on the geo-electric section at distance 140 m on traverse one. The magnetic intensity contrast observed at distance 30 to 40 m coincides with the depression observed on the geo-electric section at distance 140 m on traverse two. The magnetic intensity contrast observed at distance 60 to 78 m also coincides with the depression observed on the geo-electric section at distance 100 to 120 m on traverse three. These results reveal that the geophysical methods used for this study are complimentary. The magnetic intensity contrast observed at distance 80 to 90 m coincides with the depression observed on the geo-electric section at distance 80 to 140 m on traverse three. Based on the results of these study, future engineering construction should consider zones of possible geological structures in the design of the imposed structure as such zones are weak and can instigate failure in the proposed structure. However, groundwater development should concentrate along these zones delineated as they provide pathways and storage for groundwater accumulation.

Conclusion

Integrated geophysical methods involving Magnetic and Electrical resistivity methods have been adopted in this study for the purpose of delineating subsurface geological structures, at a location around Lead City University, Ibadan. Four geophysical traverse; traverse one (TR1) in the west – east and the other two traverses traverse 2 and traverse 3 in the south – north direction were occupied for Magnetic and the electrical methods, (Vertical Electrical Sounding (VES) using Proton Precision Magnetometer and Omega Resistivity meter respectively. A total of thirty four points were occupied for VES in the study area. The qualitative interpretation of the magnetic profiles revealed areas with changes in magnetic gradient

diagnostic of structural changes which were interpreted in form of fractures. The geoelectrical parameters determined from the interpretation of the Vertical Electrical Sounding (VES) revealed that the study is underlain by four geoelectric layers corresponding to the topsoil, weathered layer, fractured basement and fresh basement. The overburden within the study area is generally thin which indicates that the basement within the area is generally shallow.

The integration of the results from the geophysical techniques employed has been able to established effective correlation and relationship with allowance for speculations. Inferences from the methods have been able to corroborate one another to achieve the aim and objectives of this study.

References

- Adelusi, A. O., Akinlalu, A. A. and Nwachukwu, A. I. (2013). Integrated geophysical investigation for post construction studies of buildings around School of Science area, Federal University of Technology, Akure, Southwestern, Nigeria. *International Journal of Physical Sciences*, 8(15): 657-669.
- Aina, A., Olorunfemi, M. O. and Ojo, J.S. (1996). An integration of aeromagnetic and electrical resistivity methods in dam site investigation. *Geophysics*, 61(2): 349-356.
- Ilugbo, S. O., Adebiyi, A. D., Olaogun, S. O. and Egunjobi, T. (2018). Application of Electrical Resistivity Method in Site Characterization along Ado – Afao Road, Southwestern Nigeria, *Journal of Engineering Research and Reports*, 1(4):1-16.
- National Steel Raw Materials Exploration Agency, NSRMEA, (1994). Preliminary Report on Ajabanoko Iron Ore Deposit (Unpublished): 22.
- Olorunfemi, M. O., Ojo, J. S. and Akintunde, O. M. (1986). Hydrogeophysical evaluation of the groundwater potential of Akure metropolis, southwestern Nigeria, *Journal of Mineral Geology*, 35(2):207-228.
- Olorunfemi, M. O. and Olorunniwo, M. A.

- (1985). Geoelectric parameters and aquifer characteristics of some parts of Southwest Nigeria, *Geologia Applicata Indrogeologia*, 20: 99-109.
- Oyedele, K. F. and Bankole, O. O. (2009). Subsurface stratigraphic mapping using geophysics and its impact on urbanization development in Arepo area, Ogun state, Nigeria. *Science Journal* 2(2):31–45.
- Rahaman, M. A. (1988). Recent advances in the study of the basement complex of Nigeria. In Oluyide, P. O. (Coordinator), Precambrian Geology of Nigeria. *Geological Survey of Nigeria Publication: 11-43*
- Rahaman, M. A. (1976). Review of the basement of S.W. Nigeria Inc. Kogbe (Ed) Geology of Nigeria. Elizabethan press, Lagos: 4–58
- Souplos, P. (2007). Reconstructing former urban environments by combining geophysical electrical methods and geotechnical investigations. *Geophysics and Engineering*, 5:186–194.
- Souplos, P., Georgakopoulos, P., Papadopoulos, N., Saltas, V., Andreadakis, A., Vallianatos, F., Sarris, A. and Makris, J.P. (2007). Use of engineering geophysics to investigate a site for a building foundation. *Journal of Geophysics and Engineering* 4(1):94–103.
- Tsokas, G. N., Tsourlos, P. I., and Szymanski, J. E. (1998) Square array resistivity anomalies and inhomogeneity ratio calculated by the finite element method. *Geophysics*, 62, 426-435.
- Vander Velpen, B. P. A. (2004). RESIST Version 1.0. M.Sc. Research Project, ITC, Delft Netherland.

The Delineation of Mineralization and Hydrothermal Alteration Zones in Gitata Sheet 187, North Central Nigeria

Mam D. T.¹, Emmanuel E. U.², Abbass A. A.³ and Usman D. A.⁴

¹National Water Resources Institute, Mando Road Kaduna

^{2,3,4}Physics Department Federal University of Technology Minna

Corresponding author's e-mail: taweymam@gmail.com

ABSTRACT

This paper presents the delineation of potential mineralization and hydrothermal alteration zones within Gitata sheet (187) in north central Nigeria using airborne geophysical data. Aeromagnetic and aero radiometric data of high resolution covering the area were acquired and analyzed by mapping possible areas of mineralization, structures and hydrothermal alteration. The enhancement techniques applied to the data were the Analytic signal and Centre for Exploration Targeting (CET). The maps of radioelements and their ratios were used in the analysis. Structural analysis showed the dominant structural pattern within the study area to be NE-SW and NW-SE while the northwest and central portions of the study area were correlated with a strong analytic signal of 0.161 amplitude. Favorable mineralization zones were mapped from complex structural analyses and correlated with areas of high analytical signal within the northwest and central portion of the study area. Inspection of aero radiometric maps helped to delineate hydrothermal alteration zones that predominate in undifferentiated older granite, Migmatite and Gneiss followed by some occurrences within the porphyritic granites in the eastern part of the study area and the Pelitic schist/Muscovite having some occurrence of the hydrothermal zones delineated. Areas with strong analytic signal and complex structures are considered to be favorable for mineralization as mineralization fluids may have solidified in the structures and also alter the composition of the host and adjacent rocks.

Keywords: Mineralization, Hydrothermal Alteration, Complex Structural Analysis, Geomagnetic Declination

Introduction

The role of aeromagnetic method in mineral exploration varies from delineation of structures like faults, folds, contacts, shear zones and intrusions to automated detection of porphyry and favorable areas of ore deposits Elkhateeb and Ahmed (2018). These structures play important roles in the localization of mineralization. In comparison with other airborne geophysical methods, gamma-ray spectrometric method shows more success in mapping surface geology (Darnley *et al.* 1989). In addition, it is helpful in deducing some structures that may not be recognized through analyzing potential field methods. Also, this method is more useful and accurate in the identification of hydrothermal alteration zones and their detection. Shives *et al.* (1997) recommend the use of eTh/K ratio as the best

indicator of recognizing potassic alteration zones. Several studies have also been conducted for identifying alteration zones (Elkhateeb and Abdellatif, 2018; Feebrey *et al.* 1998; Irvine and Smith 1990; Morrell *et al.* 2011; Wemegah *et al.* 2015). As such, this work is aimed at delineating prospective mineralization and hydrothermal zones within Gitata (sheet 187) Nigeria.

Location and Topography of the Study Area

The area of study falls within two states and the federal capital territory. These are Kaduna and Nasarawa states (Figure 1). It is bounded by latitude 9° N to 9° 30' N and Longitude 7° 30' E to 8° E. The study area falls within the north central Nigerian basement complex and extend from south of Abuja to east of Ungwar Alura in the south and from Kwoi town to west of Kagarko in the north.

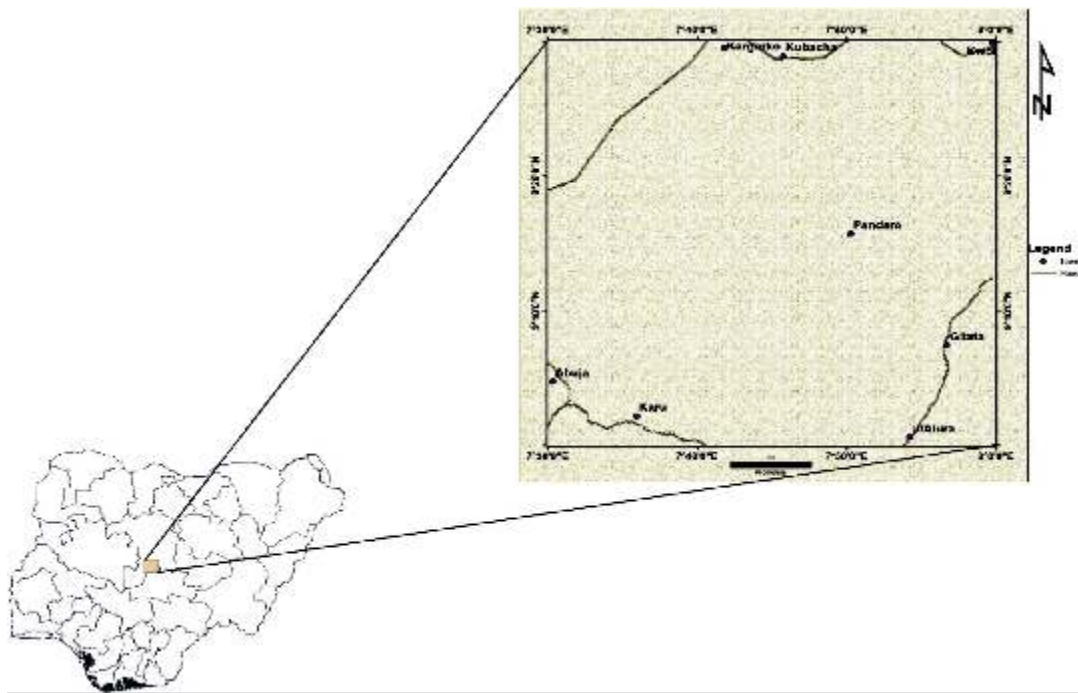


Fig. 1 Location of the study area

The topography of the area provided by Shuttle Radar Topography Mission (SRTM), ranges from 355.937 m for low elevated part of the area within the central portion of the study area down to the southern end (Figure 2) to areas having elevation above 772.317 m for highly elevated part of the map specifically around north-east across the northern part of the map to north-west toward the western end down to the south (Figure 2).

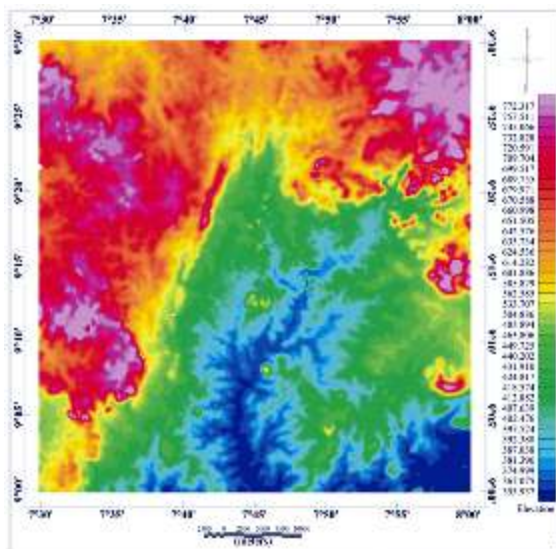


Fig. 2 SRTM Map of the Area with Topography Variation

Geology of the Study Area

The study area is underlain by the basement complex rocks (Figure 3) NGS, 2006. The basement complex rocks in the area are grouped into three, namely, the Migmatite-Gneiss Complex (MGC), the Schist Belt (Metasedimentary and Metavolcanic rocks), the Older Granites (Pan African granitoids). The Migmatite-gneiss complex is Neo-Proterozoic to Meso-Archean (542 Ma-3200 Ma) in age and composed of migmatites and gneisses. Migmatite is the most dominant and extensive rock type in the area occupying the central portion of the study area from south to the north (Figure 3). The older granites (or Pan-African granitoids) are Pan-African (600-200Ma) in age and consist mainly of undifferentiated older granites and gneiss occupying the south eastern part of the map and isolated occurrence of porphyritic granite.

Both the migmatites and gneisses were deformed and intruded by the older granites (or Pan-African granitoids) during the 600-200 Ma Pan-African episodes. Schists within the study area occupy the western portion of the

map (Figure 3), down to the south and other smaller occurrences of the Schists within the north, northeast, southeast, south and central portion of the map (Figure 3).

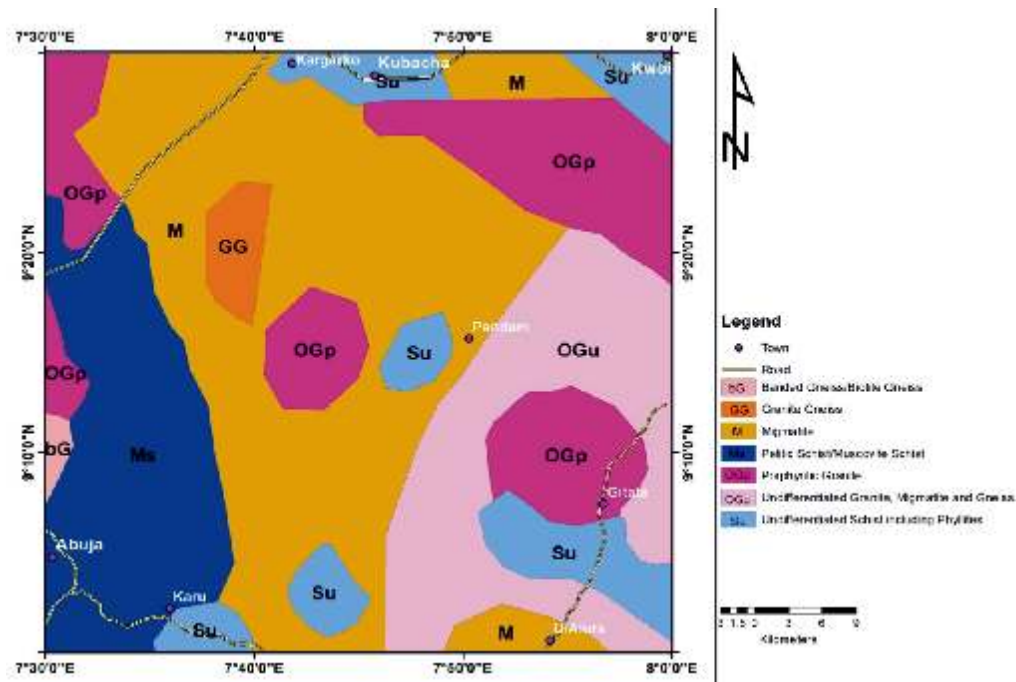


Fig. 3 Geologic Map of the Area

Materials and Methods

High-Resolution Aeromagnetic Data (HRAD) and airborne radiometric data (equivalent thorium and percentage potassium data) of part of central Nigeria were acquired from the Nigeria Geological Survey Agency (NGSA). The data covered an area of about 55 x 55 km² (bounded by latitudes 09° 00'-09° 30' N and longitudes 07° 30'- 08° 00' E). The aeromagnetic and radiometric surveys were carried out between 2005 and 2009 by Fugro Airborne Surveys for the NGSA. The data were recorded at an interval of 0.1 s (~7.5 m) for magnetic measurements and 1.0 s (~75 m) for radiometric measurements. The airborne surveys were flown in the NW-SE direction perpendicular to the major geological trends in the area, with flight line spacing of 500 m, terrain clearance of 80 m, and tie line spacing of 2000 m in NE-SW direction. Based on the

very short recording interval, lower survey flight height (80 m), and narrower flight line spacing, the resolution of the anomalies is immensely higher than the conventional high-altitude air borne surveys. All essential data corrections, including the removal of IGRF values, were done by Fugro Airborne Surveys. The maps were processed using the Oasis Montaj software version 8.4. The TMI was reduced to the equator, using magnetic inclination and declination of the centre point of the study area, so that anomalies observed would be directly positioned on their respective causative source bodies. Unwanted signals which include the regional fields were removed by upward continuing the Reduced-to-Equator (RTE) map to a height of 30 km, where the resultant grid was subtracted from the RTE grid to obtain the residual grid displays as map. Analytic Signal (AS) source

edge mapping technique was applied on the filtered residual data to delineate the magnetic source boundaries. The amplitude of analytic signal within the study area was achieved by calculating the square root of sum of squares of magnetic gradient in x, y and z directions using grid expression of Oasis Montaj. The CET grid analysis approach was employed in this study to identify linear features within the aeromagnetic data; then local structural complexity was analyzed using the spatial associations between adjacent linear features. Firstly, lineaments or structures were detected based on local texture (Holden *et al.* 2008). Then the spatial associations of the detected lineaments were analyzed to construct two maps corresponding to each of the structural complexity cases, namely a feature intersection contact occurrence density map and a feature orientation entropy map. These maps show the occurrence of these structural scenarios, which aided in manual prospectivity analysis. The radiometric data which comprise both the percentage potassium and equivalent thorium maps were displayed and ratio of the maps which is %K/eTh was obtained by the expression

$$\frac{\%K}{eTh} = \frac{\%K \text{ grid}}{eTh \text{ grid}} \quad (1)$$

using the grid and expression function of oasis Montaj version 8.4 which is very useful in the mapping of hydrothermal alteration zones. The structural map produced from the analysis of aeromagnetic data using CET were integrated with the hydrothermal alteration zones delineated from K/eTh map to produce a composite proposed geologic map of the area.

Analytic Signal Method

The analytic signal of total magnetic intensity data (TMI) has much less sensitivity to geomagnetic field inclination than the original TMI data and offers a way of analyzing low latitude magnetic fields without the RTP operator's concerns. Analytic signal is a common gradient enhancement which is related to the magnetic fields by the derivatives. Roest *et al.* (1992), showed that

the amplitude of the analytic signal can be determined from the three orthogonal gradients of the total magnetic field using the expression:

$$|A(X, Y)| = \sqrt{\left(\frac{\partial M}{\partial x}\right)^2 + \left(\frac{\partial M}{\partial y}\right)^2 + \left(\frac{\partial M}{\partial z}\right)^2} \quad (2)$$

where A (x, y) is the analytic signal amplitude at (x, y) and M is the magnetic anomaly observed at (x, y).

In the context of interpretation, this function is extremely interesting, in that it is completely independent of the direction of magnetization and the magnetic field of the earth. This means all bodies with the same geometry have the same analytic signal. The analytic signal shows maxima over the edges of the source body even if the magnetization direction is not vertical. Furthermore, since the peaks of analytic signal functions are symmetrical and occur directly over the edges of broad bodies and directly over the centers of narrow bodies, the analysis of analytic signal maps and images can, in theory, provide simple, easily understood indications of the geometry of the magnetic source, the half widths of these peaks can be linearly related to the depths, if the peak sources are vertical magnetic contacts (Roest *et al.* 1992). The analytic signal, although often more discontinuous than the simple horizontal gradient, has the property that it generates a maximum directly over discrete bodies as well as their edges. The width of a maximum, or ridge, is an indicator of depth of the contact, as long as the signal arising from a single contact can be resolved.

Centre for Exploration Targeting (CET)

Centre for Exploration Targeting (CET) is a suite of algorithms that provide enhancement, lineament detection and structural complexity analysis functionalities for potential field data (Core *et al.* 2009; Holden *et al.* 2008). This technique automatically delineates lineaments and identifies promising areas of ore deposits within the study area using total magnetic intensity (TMI) data through outlining regions of convergence and structural element

divergence using several statistical steps including textural analysis, lineament detection, vectorization and complexity analysis to generate contact occurrence. The contact occurrence areas show junction areas (point where two lineaments meet) and high linear density areas. These areas are favorable for hosting interest-bearing deposits and could be further explored (Geosoft 2012). Furthermore, CET grid method also enhances discontinuity zones in magnetic data and highlights critical magnetic intensity irregularities. Structures are founded in the data by finding several zones of texture in the restricted magnetic response before examining axes of symmetry. These axes are likely to detect straight abruption in magnetic intensity. Areas of magnetic discontinuity are often due to and exhibited by rock edges, elongated structures, and intrusions that are important to assuming the geological framework of an area (Kovesi 1991). Zones of magnetic discontinuity are expressed by the use of texture enhancement in the form of the skeletal structure. The output data defines each region of the discontinuity zones as skeletal line fragments which belong to each of them, showing the deviations within the structural characteristics clearly in the directions and offsets (Kovesi 1997).

This technique makes use of the following actions:

I. Texture Analysis Enhancement (Standard Deviation)-determines magnetic discontinuity related with regions of complicated textures. Standard deviation enables the local variation to be delineated in the data. This calculates the standard deviation of the data values within the local neighborhood at every point in the grid. Important features often show a high variability with respect to the background signal. For a window containing N cells with a mean value of μ , the cell's standard deviation of the cell values

$$S = \sqrt{\frac{1}{N} \sum_{i=1}^N (x_i - \mu)^2} \quad (3)$$

When interpreting the results, values which approximate zero indicate very little variation, whereas high values indicate large variation.

II. Phase Symmetry – Utilizes the texture enhancement results for distinguishing zones of lateral discontinuity.

III. Detection of Structures – Uses the results of phase symmetry to reduce the discontinuities including zones into line-like structures.

IV. Complex structural Analysis (Contact Occurrence Density and Orientation Entropy Maps)

The feature intersection density map is generated by a collection of selected intersections, which include crossings, junctions and corners of the identified line segments; first, by extending each line segment to infinity, all projected intersection points are determined from all pairs of line segments. Candidate contact points are the intersections of those extended line segments. Selection is determined for each candidate using the distance between the intersection point and their respective line segments, and the angle between the line segments. If a projected intersection point lies within a permissible separation distance of say 250 m on one or both of the line segments, then the point is selected as a candidate. Those candidate points will be further analyzed to remove line segment intersections of similar orientations. Using aeromagnetic data, a linear anomaly can appear as broken feature due to incomplete sampling of magnetic field variations in the magnetic field (Holden *et al.* 2012). These features that may belong to the same anomaly may exhibit similar orientations, and is filtered by a threshold angle deviation i.e. removal of candidate points from line segments with a deviation angle less than threshold. Figure 4 shows the processes of elimination for the candidate intersection.

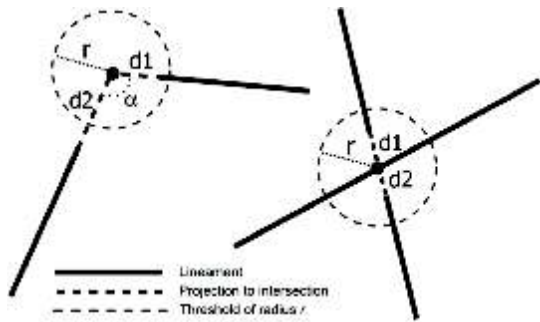


Fig. 4 Two example cases that qualify as valid intersection points. For the projected distances to the intersection d1 and d2, either d1 or d2, or both are less than the threshold distance of r . Also, in the first case, the angle α between the line segments also indicates that they are non-parallel (Holden *et al.* 2012).

The contact occurrence density map is constructed using the following processes.

Firstly, given the final collection of intersection points, each point contributes a Gaussian $G_i(x, y, \sigma)$ for a σ determined by the image resolution and scale of the local region being analysed for structural complexity. This causes areas with many valid intersection points to be supported by many Gaussian contributions. The resulting structural complexity heat map $H(x, y)$ is given by summing all Gaussians:

$$G_i(x, y) = \frac{1}{\sqrt{2\pi}\sigma} e^{-\left(\frac{(x-x_0)^2}{2\sigma^2} + \frac{(y-y_0)^2}{2\sigma^2}\right)} \quad (4)$$

$$H(x, y) = \sum_{i=0}^n G_i(x, y, \sigma) \quad (5)$$

Orientation entropy (diversity) map provides information about variability in feature orientations within a local neighborhood. As with the feature intersection density map, each identified texture ridge feature is represented as a collection of line segments.

These line segments are then used to calculate the orientation entropy (i.e., diversity) by measuring how many different orientations are represented by the line segments within each neighborhood. The range for all possible line

orientation (i.e., between 0° and 180°) is divided into a number of bins. For each line segment, the orientation is firstly quantized by determining the bin within which the orientation lies. Then for a given neighborhood, we measure the diversity of orientations of the line segments by determining how many different bins are represented within the neighborhood.

The traditional entropy measure (Parker 1997) was adapted to compute information for each pixel of the raw orientation diversity image, that is:

$$E = -\sum_{i=1}^n (p_i * \log(p_i)) \quad (6)$$

where n is the number of orientation bins, and p_i is the observed percentage of pixels with orientation i within the $r \times r$ neighborhood surrounding the pixel (x, y) , out of the total number of pixels corresponding to line segments. The size of the neighborhood controls the spatial extent to which the distribution of structures is examined. For example, given a pixel with a spatial resolution of 50 m, a square 60×60 pixel neighborhood represents a 3×3 km area. The appropriate choice of the window size depends on the spatial resolution of the data and the perceived size of the structures that are allowing movement of the mineralizing fluid. Finally, Gaussian smoothing is applied to the orientation diversity image to improve the visualization of the heat map (Holden *et al.* 2012).

Results and Discussions

The total magnetic intensity map (Figure 5a) reveals variation in magnetic signatures within the study area from south to north and from the east to west. The map (Figure 5a) is produced in different colors, pink to red and green to blue depicting positive anomaly (magnetic high) and negative anomaly (magnetic low). The magnetic intensity values within the area ranges from $32940.145 nT$ minimum to $33092.812 nT$ maximum with total number of 2,428,540 data points. The area is marked by both magnetic lows and high closures which could be attributed to the difference in the

lithology of the rocks within the study area and difference in the magnetic susceptibility of the rocks within the area, variation in depth to magnetic source within the study area and degree of strike. The magnetic high that occurs around south-eastern portion of the map coincided with the older granitoids (undifferentiated older Granite, Migmatite and

gneiss), undifferentiated schist with phyllites, porphyritic Granite and the Migmatite (Figure 3). The magnetic low that occurs around the north central portion of the study area coincided with the Migmatite, undifferentiated schist with phyllites, and the porphyritic Granite.

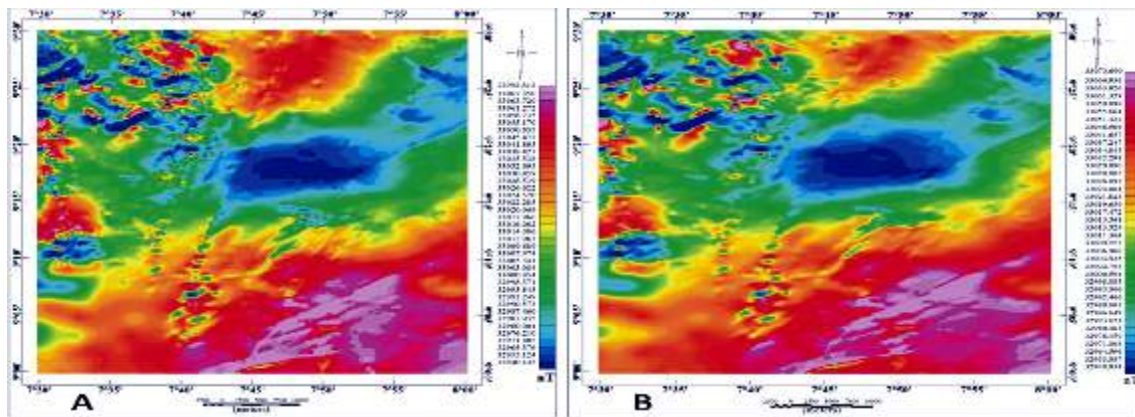


Fig. 5 (a) Total Magnetic Intensity and (b) Total Magnetic Intensity Reduced to Equator Maps

Also, around the north-western portion of the map, there is an observed occurrence of mixture of both magnetic low and high that could be attributed to the presence of deep-seated structures and possibly igneous intrusions.

To realign the anomalies and have their peaks symmetrically centered over their corresponding sources because the study area is very close to the equator. Total magnetic intensity grid of the study area was reduced to magnetic equator grid with geomagnetic inclination of -5.298 and geomagnetic declination of -1.995 of the central point of the study area to get the actual position of the magnetic anomalies without losing any geophysical meaning (Figure 5b). The RTE map (Figure 5B) when compared with the TMI (Figure 5a) map shows slight variation in their magnetic intensities. The RTE map have magnetic intensities that varies from 32938.934 nT minimum to 3307.690 nT maximum compared to TMI map where the magnetic intensity values within the area ranges from 32940.145 nT minimum to

33092.812 nT maximum. The total magnetic map reduced to equator (Figure 5b), when compared to the total magnetic intensity (TMI) (Figure 5a), the maps display similar anomaly in terms of anomalies trends, especially their symmetry, strike, extension, width, amplitude and gradients except for the magnetic low that occur within the north central portion of TMI map has now been reduced in size in the RTE map (Figure 5a and 5b). Also, the magnetic high that occurs just above this magnetic low within northern portion of TMI map has also been reduced in size in the RTE map (Figure 5a and 5b).

The Analytic Signal Map

The analytic signal map (Figure 6) accentuates the variation in the magnetization of the magnetic sources in the study area and highlights discontinuities and anomaly texture. These structures are observed around the North West and central portion of the area mostly trending NE-SW. The analytic signal amplitude maximizes over the edge of the magnetic structures as a result, the high magnetic anomalies zones are associated with

highly rich ferromagnesian-bearing rocks with minor felsic minerals (Telford *et al.*, 1990). Therefore, the AS map (Figure 6) has amplitudes that ranges from 0.002 m to > 1.61 m. The map could also be said to have exhibited three different magnetic zones in this area of study based on the amplitude of the anomalies within this area. Low to fairly low magnetic zone (LM) with amplitude ranges of 0.002 m to 0.014 m are areas

associated with highly weathered rocks and areas with thick cover of sediments. The moderate magnetic zone (MM) with amplitude 0.014 m to 0.047 m is associated with granite – gneiss as these rocks contain high ferromagnesian with low amount of felsic minerals. While the high magnetic zones with large amplitudes >0.047 could be attributed to freshly intruded rocks.

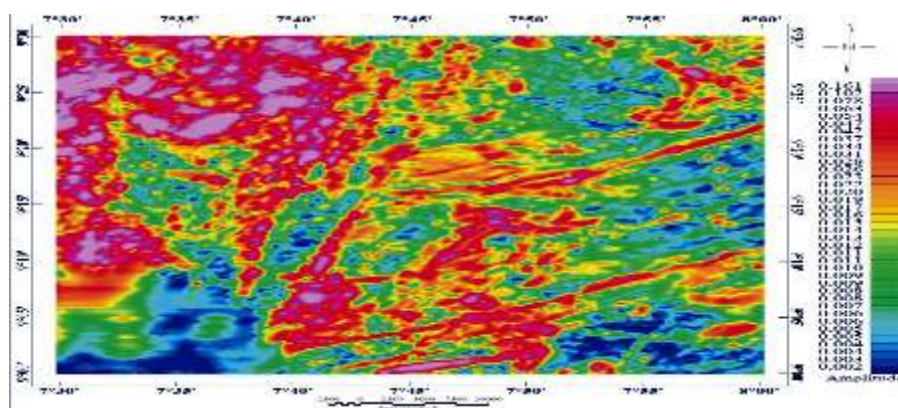


Fig. 6 Analytic Signal Map

Structural Complexity Analysis

The algorithm of the CET grid analysis was applied to the RTE map of the study area to produce the structural complexity maps which are standard deviation map, Vectorized structural map, contact occurrence density map and orientation entropy map.

The Standard Deviation Map

The standard deviation map of the study area (Figure 7a) indicates variation in the magnetic

intensity data of the study area. The pinkish colorations within the north western portion of the map indicate high variation where areas with deep blue coloration indicate low variation in the magnetic intensity across the area (Figure 7a). Within the western half of the map, structures are aligning predominantly in NE-SW direction while (Figure 7b) is a Vectorized structural map gotten from standard deviation map.

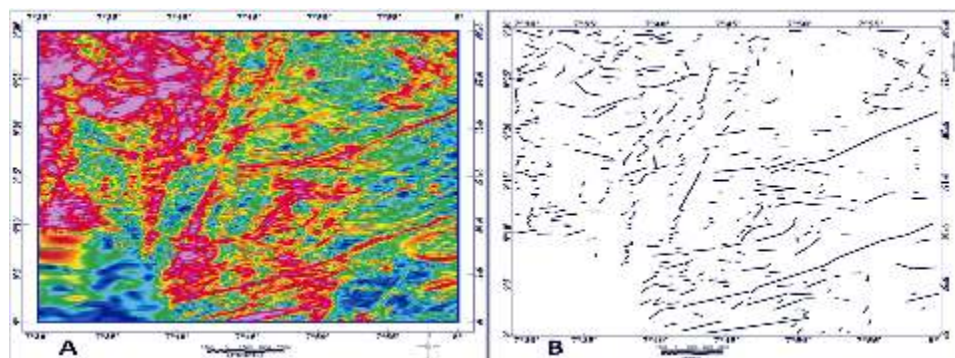


Fig. 7 (a) Standard Deviation and (b) vectorized Structural Maps

From the vectorized structural map (Figure 7b), it can be observed that the area is highly fractured especially the north eastern portion of the map compare to the standard deviation where the portion is having high magnetic intensity variation attributed to freshly intruded rocks within the area. The central portion of the map is also highly faulted down to the southern portion of the map (Figure 7b). Predominant structural trend based on the vectorized structural map of the area is NE-SW and NW-SE.

The Contact Occurrence Density and Orientation Entropy Maps

The contact occurrence density map of the

study area (Figure 8a) was derived from the vectorized structural map of the area (Figure 7b) and it displays the number of fault/shear intersection and splays, that is where the linear structures intercept or changes direction and from (Figure 8a) it is evident that our contacts as displayed in the map showed where the structures either changes direction or intercepted by another structure and historically, those areas where the linear structures intercept or change directions are areas with high prospect for mineralization (Geosoft 2012; Holden *et al.* 2008).

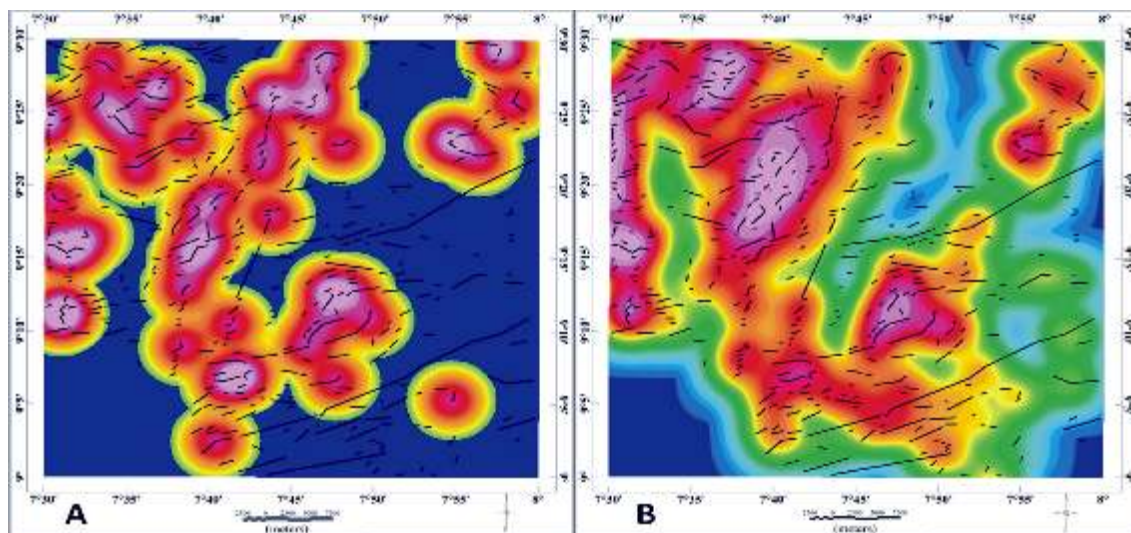


Fig. 8 (a) Contact Occurrence Density and (b) Orientation Entropy Maps

Also, the generated map of orientation entropy (Figure 8b) indicates high density zones of structural junctions or intersections. These are areas around the north eastern portion of the especially along the western edge and the central portion of the map (Figure 8b). These are areas presumed favorable for hosting deposits of interest which generally could be Gold, Pb-Zn mineralization, tin, iron ore, gemstone, Bismuth, Ilmenite and other minerals not discovered for now and could be further explored in more detail. It should be noted that this approach was originally designed to exploit a known deposits of

Archean Gold, but it may have some utility here since according to NGSA (2006), there is occurrence of Gold in some part of FCT with Lead-Zinc mineralization. The extrapolation from an Archean case to the current situation in current study area could be useful since some part of the FCT falls in the study area (Figure 1 and Figure 3), it may host some of these minerals.

Percentage Potassium (%K), and Equivalent Thorium (eTh) Maps

The potassium (%K), map (Figure 9a) shows different degrees of potassium concentrations ranging from 0.219 to 5.088 (%) that reflects

different lithological units and alterations in the area. Potassium radiation fundamentally comes from potash feldspars, which are mainly common in felsic igneous rocks (e.g. granite) and are low in mafic rocks (e.g. basalts and andesite) (Gunn *et al.* 1997b). Rock alterations can also result in high K concentrations (Wilford *et al.* 1997). A number of potassium anomalies are evident in the radiometric image (Figure 9a). The color blue corresponds with low K values whilst the pink corresponds with very high K values. The color red represents moderately high to high K values and the shades of orange to yellow color represent or are associated with moderately low K values. These pinkish colorations with very high K values within the eastern portion of the map are

attributed to the older granitoids (undifferentiated older granite and porphyritic granite. Also, figure 9b shows the eTh distribution map of the study area. The eTh distribution map has eTh concentration ranging from 6.189 to 36.159 ppm. For the purpose of this interpretation, the eTh concentration from the legend (figure 9b) in the study area will be relatively grouped as high (>22.304 ppm), corresponding mostly to the schist within north-eastern portion and Migmatite around the north with porphyritic granite around north-western portion of the map. While moderately high (13.925–22.304ppm), moderately low (8.392–13.925 ppm), and low (<8.392ppm) (figure 9b).

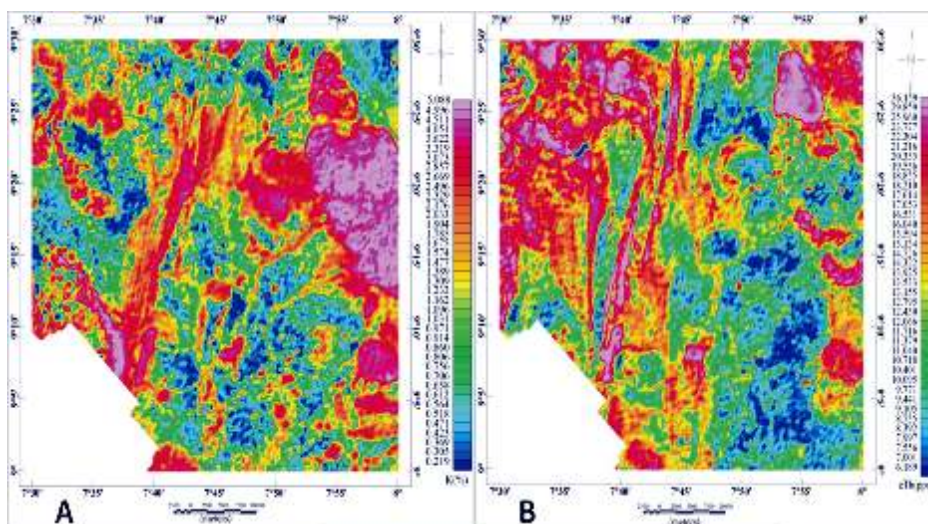


Fig. 9 (a) Percentage potassium and (b) equivalent thorium maps

Potassium/Thorium Ratio Map

Figure 10a displays K/eTh map and as potassium is more mobile than thorium, K/eTh ratio anomalies can be distinguished to areas of hydrothermal alteration which are characterized by K enrichment. However, depending on the fact that the ratio between potassium and thorium is rather constant in most rocks, typically varying from 0.17 to 0.2 K/Th in %/ppm (Hoover *et al.* 1992). Rocks with K/eTh ratios remarkably outside of this range have been named potassium or thorium specialized (Portnov 1987). So, the zones

characterized by the high K/eTh ratio values are the strong indicator of hydrothermal alteration. From the K/eTh ratio map (figure 10a) it is seen that the areas affected by the hydrothermal process is featured by pink color and have a high value about 0.385 of K/eTh ratio. These are areas associated with undifferentiated older Granite, Migmatite and gneiss with porphyritic granite in the east and some parts of Migmatite and pelitic schist/muscovite schist around southwestern portion of the map (figure 10b).

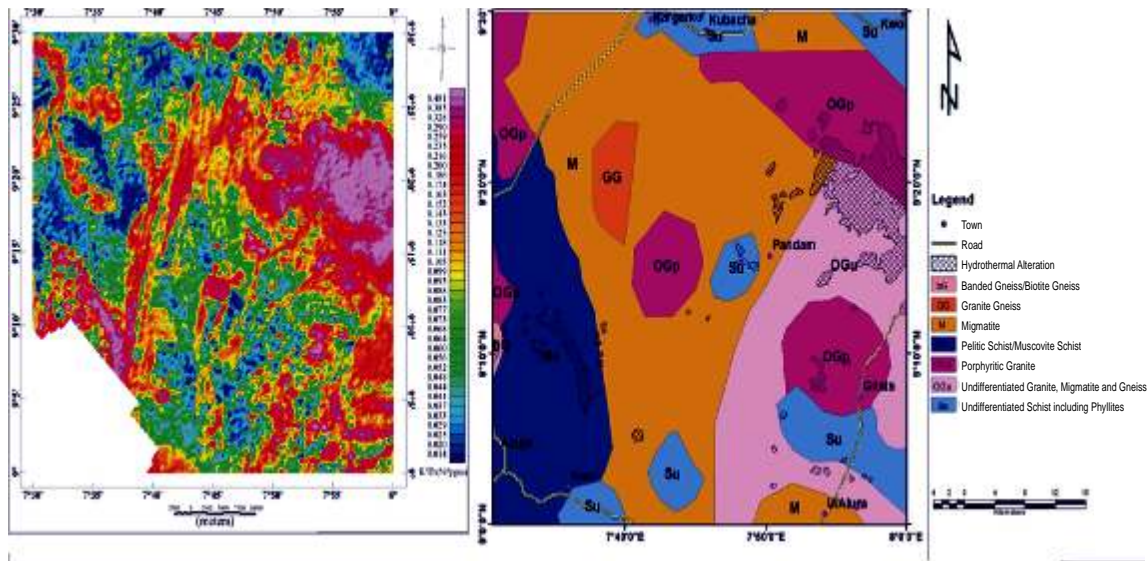


Fig. 10 (a) K/eTh and (b) hydrothermal Alteration Zones on Geologic map

Aeromagnetic and Aero Radiometric Data Integration

The results of aeromagnetic, aero radiometric data sets and geology were integrated to produce a composite map of the study area (figure 11). An inspection of this map showed some portions of the study that are highly faulted to be coincided with hydrothermal

alteration zone that is located within the area. Also, a number of hydrothermally altered zones are mapped from the K/eTh ratio map (figure 10b). Since these zones have one or more structures associations, they serve as channel pathways for migrating hydrothermal fluids that coincidentally reacted with rock formation which got altered subsequently.

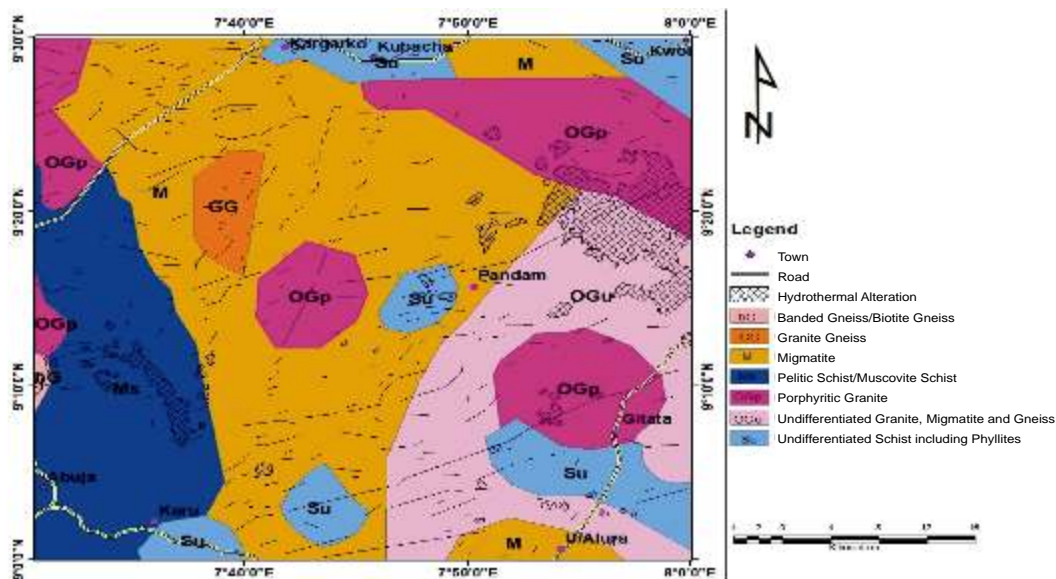


Fig. 11 Composite Proposed Geologic Map of the Area

Thus two kinds of mineralization source may have occurred within the area of study. These are

A. Mineralization based on the hydrothermal fluids that solidified within the existing structures in the older rocks in place veins that host several kinds of solid minerals.

B. The mineralization based on the effect of the hydrothermal fluids that changed the mineral constituents of the pre-existing rock by contact metamorphism thus resulting in different set of mineral within the rocks affected.

Conclusion

The use of aeromagnetic and aero radiometric data has aided in the mineralization and hydrothermal zones delineation within Gitata sheet 187. The analytic signal map of the area, (Figure 6) has revealed areas around north-western portions of the map to be of high magnetization with amplitude of 1.61 which has been attributed to freshly intruded rocks within this area. Also, structural complexity analysis of the CET has revealed the area to be to be highly faulted and dissected with structural trends majorly in NE-SW and NW-SE. The north-western edge of orientation entropy map (figure 8b), the central portion of the map is perceived to be favorable for mineralization as mineralization fluids must have find its way through structures within these areas. Analysis of aero radiometric map aided in delineation of hydrothermal alteration zones which are predominant within undifferentiated older Granite, Migmatite and gneiss with porphyritic granite in the east and some parts of Migmatite and pelitic schist/muscovite schist around southwestern portion of the map (figure 10b and figure 11). Potential field data (gravity and magnetic) are very important in mineral and structural studies. It is recommended that gravity data should also be used to ascertain the presence of the structures and mineralization zones mapped out using magnetic data, since electromagnetic method is very important in

mineral exploration, it can be used to show case the electromagnetic response of minerals within those areas delineated as prospective mineralization zones.

References

- Core, D., Buckingham, A., and Belfield, S. (2009). Detailed structural analysis of magnetic data done quickly and objectively, SGE Newsletter.
- Darnley, A. G. and Ford, K. L. (1989). Regional airborne gamma-ray surveys: a review, in *Proceedings of Exploration 87: Third Decennial International Conference on Geophysical and Geochemical Exploration for Minerals and Groundwater*, ed. Garland, G.D., Geological Survey of Canada. 3: 960.
- Elkhateeb, S. O., Ahmed, M. E., (2018). Interpretation of Aeromagnetic Data to Delineate Structural Complexity Zones and Porphyry Intrusions at Samr El Qaa Area, North Eastern Desert, Egypt. *International Journal of Novel Research in Civil Structural and Earth Sciences*, 5 (1): 1-9.
- Elkhateeb, S. O., and Abdellatif, M. A. G. (2018). Delineation potential gold mineralization zones in a part of Central Eastern Desert, Egypt using Airborne Magnetic and Radiometric data. *NRIAG Journal of Astronomy and Geophysics* 7: 361-376
- Feebrey, C. A., Hishida, H., Yoshioka, K. and Nakayama, K. (1998). Geophysical expression of low sulfidation epithermal Au-Ag deposits and exploration implications-examples from the Hokusatsu region of SW Kyushu. *Jpn. Resour. Geol.* 48: 75-86.
- Geosoft, (2012) Manual on how to carryout complex structural analysis of aeromagnetic data
- Gunn, P., Minty, B., and Milligan, P. (1997b). The Airborne Gamma-Ray Spectrometric Response over Arid Australian Terranes. In A. Gubins (Ed.), *Proceedings of Exploration 97: Fourth*

Decennial International Conference on Mineral Exploration, Australia: 733-740.

Holden, E. J., Dentith, M. and Kovesi, P. (2008). Towards the automatic analysis of regional aeromagnetic data to identify regions prospective for gold deposits. *Computers & Geosciences*, 34 (11): 1505-1513.

Holden, E. J., Jason C. W., Kovesi, P., Daniel, W., Dentith, M., and Bagas, L. (2012). Identifying structural complexity in aeromagnetic data: An image analysis approach to greenfields gold exploration, *Ore Geol. Rev.*

doi: 10.1016/j.oregeorev.2011.11.002

Hoover, D. B., Heran, W. D., and Hill, P. L., 1992. The geophysical expression of selected mineral deposit models.

U.S. Geological Survey Open-File report 92-557, 129p. Irvine, R.J., Smith, M.J., 1990. Geophysical exploration for epithermal gold deposits. *J. Geochem. Explor.* 36: 375-412.

Irvine, R. J., and Smith, M. J., (1990). Geophysical exploration for epithermal gold deposits. *J. Geochem. Explor.* 36: 375-412.

Kovesi, P. (1991). Image features from phase congruency", *Videre: Journal of Computer Vision Research, Summer*, 1(3), The MIT Press.

Kovesi, P. (1997). Symmetry and asymmetry from local phase, AI'97, Tenth Australian. Joint Conference on Artificial Intelligence. 2 -4.

Morrell, A. E., Locke, C. A., Cassidy, J. and Mauk, J. L. (2011). Geophysical characteristics of adularia-sericite epithermal gold-silver deposits in the Waihi-Waitekauri

region New Zealand. *Econ. Geol.*, 106: 1031-1041.

NGSA. (2006). *Geology and Structural Lineament Map of Nigeria*

Parker, J. R. (1997). *Algorithms for Image Processing and Computer Vision*. John Wiley & Sons Inc., USA: 417

Portnov, A. M. (1987). Specialization of rocks toward potassium and thorium in relation to mineralization. *Int. Geol. Rev.* 29: 326-344.

Roest, W., Verhoef, J. and Pilkington, M. (1992). Magnetic interpretation using 3-D analytic signal. *Geophysics*, 57: 116-125.

Shives, R. B. K., Charbonneau, B. K. and Ford, K. L. (1997). The detection of potassic alteration by gamma ray recognition of alteration related to mineralization, in: *Exploration 97, Fourth Decennial International Conference*. Mineral Exploration (Toronto, Canada): 345-353.

Telford, W. M., Geldart, L. P., Sherrieff, R. E. and Keys, D. A. (1990). *Applied geophysics*. Cambridge: Cambridge University Press: 860.

Wemegah, D. D., Preko, K., Noye, R. M., Boadi, B., Menyeh, A., Danuor, S. K., and Amenyoh, T. (2015). Geophysical interpretation of possible gold mineralization zones in Kyerano, South-Western Ghana using aeromagnetic and radiometric datasets. *J. Geoscience Environ. Prot.* 2015 (3): 67-82.

Wilford, J. R., Bierwirth, P. N., and Craig, M. A. (1997). Application of Airborne Gamma ray Spectrometry in Soil/Regolith Mapping and Applied Geomorphology. *AGSO Journal of Australian Geology and Geophysics*, 17(2): 201-216.

Numerical Solution of Variationally Iterated Burgers' Equation using Bivariate Pade Approximation Method

Peter, A.

Department of Mathematical Sciences,
Kaduna State University, Nigeria.
Corresponding author's e-mail: p.anthony@kasu.edu.ng

ABSTRACT

The numerical solution of Burgers' equation is considered in this paper. Multivariate Pade approximation is applied to the power series solution obtained from variational iteration method of the Cauchy problem. The paper combines certain unique properties of the variational method and Pade approximation to solve the Burgers' equation. Here, the Burgers' equation is pre-treated by the variational iteration method to obtain a series solution whose Pade approximant would be computed. The numerical results obtained using multivariate Pade approximation were compared with exact solution of the Burgers' problem. This paper presents numerical approximation for Burgers' equation in a rapid convergent rational series.

Keywords: Multivariate Pade Approximation, Burgers' equation, variational iteration.

Introduction

Many important mathematical models can be expressed in terms of partial differential equations (PDEs). Models of this type often arise from many areas of applications in engineering, physical sciences and population growth. Over the years, there is increasing research activities on numerically finding the solutions of these PDEs using different techniques. Some numerical methods were developed, using the Taylor series, two-dimensional differential transformation, three-dimensional differential transformation, Adomian decomposition and variational iteration method (Adomian 1984; Bildik and Konuralp 2006; Fatma 2003; Fatma 2004; Logan 1994; Zhou 1986).

This paper uses differential transform method to represent the Burger's equation given by:

$$\frac{\partial u}{\partial t} + u \frac{\partial u}{\partial x} - \frac{\partial^2 u}{\partial x^2} = 0, \quad 0 < x < 1, t > 0 \quad (1)$$

The Burgers' equation is an important model for turbulence in fluid dynamics. Equation (1) is a distinctive model because of its relevance in the study of nonlinear advection and viscous diffusion.

Burgers' equation is one of the most common

nonlinear time dependent partial differential equations (PDE) in fluid mechanics; this consists both of nonlinear propagation and diffusive effects. Like many PDEs Burgers' equation is found to describe various kinds of phenomena such as mathematical model of turbulence and the approximate theory of flow through a shock wave travelling in a viscous fluid (Zhou 1986). In literature, many numerical methods have been proposed and implemented for approximating solution of the Burgers' equation. Many authors like Pukhow (1986) have used various numerical techniques to solve Burgers' equation.

The Pade method of solving PDEs is a well-established method because of its added advantage of naturally increasing the domain of convergence of truncated power series. The solution of any differential equation could be directly expressed as a rational power series of the independent variable known as the Pade approximant. The Pade approximation deals with the construction of rational fraction with a numerator of degree N and denominator of degree M so that the Taylor series expansion agrees with the original function up to the term of order $N + M$. The obtained rational fraction is known as the Pade approximant of the original function. The coefficients of the

rational fraction representing the function under consideration are obtained by comparison with known coefficients of the Taylor expansion of the original function itself. This was done explicitly for the first time by Johann Heinrich Lambert (Mülhausen, now Mulhouse, 26 August 1728–Berlin, 25 September 1777), Lambert (1758), or by means of continued fractions as presented by Joseph–Louis Lagrange (Turin, 25 January 1736–Paris, 10 April 1813), Lagrange (1776).

A very lucid and elementary discussion of the variational iteration method appeared in He (1998). The variational iteration methods (He 1998; 1999; 2007; He and Wu 2007) is quite simple and possesses highly accurate results to the extent that exact solutions are sometimes realised. The method has been widely used to resolve nonlinear models. The main properties of this model lie in its flexibility to solve nonlinear systems accurately and conveniently.

This paper seeks to combine those unique properties of the variational method and Pade approximation to solve the Burgers' equation. The Burgers' equation is pre-treated by the variational iteration method to obtain a series solution whose Pade approximant would be computed. This paper is organized as follows: a brief introduction of our solution methods to create a platform for this particular work; relevant details of Pade and variational formulation, variational presentation of the Burgers' equation to give a framework for the Pade approximant computations and comparison of approximate solutions with the exact for the purpose of testing the efficacy of our model.

Preliminaries

Bivariate Pade Approximants

Pade approximants could be obtained in several different ways: one can solve the system defining equation explicitly and use their resulting determinant expressions; one could also set up the recursive *e – algorithm* or construct a continued fraction whose convergence lies on descending staircase of the

Pade table. A lot of properties of the univariate Pade approximant remains valid for the bivariate one under consideration; Cuyt and Wutack (1987) for more exposition.

Consider the following bivariate function:

$$f(x, y) = \sum_{i,j=0}^{\infty} c_{i,j} x^i y^j, \text{ about the origin.}$$

We know that a solution of the univariate Pade approximation problem $r[n/m]$ for

$$f(x) = \sum_{i=0}^{\infty} c_i x^i, \text{ is given by:}$$

$$p(x) = \frac{\sum_{i=0}^m c_i x^i \quad x \sum_{i=0}^{m-1} c_i x^i \quad \dots \quad x^n \sum_{i=0}^{m-n} c_i x^i}{\begin{vmatrix} C_{m+1} & C_m & \dots & C_{m+1-n} \\ \vdots & \vdots & \ddots & \vdots \\ C_{m+n} & C_{m+n-1} & \dots & C_m \end{vmatrix}}$$

and

$$q(x) = \frac{\begin{vmatrix} 1 & x & \dots & x^n \\ C_{m+1} & C_m & \dots & C_{m+1-n} \\ \vdots & \vdots & \ddots & \vdots \\ C_{m+n} & C_{m+n-1} & \dots & C_m \end{vmatrix}}{\begin{vmatrix} 1 & x & \dots & x^n \\ C_{m+1} & C_m & \dots & C_{m+1-n} \\ \vdots & \vdots & \ddots & \vdots \\ C_{m+n} & C_{m+n-1} & \dots & C_m \end{vmatrix}}$$

Let us now multiply the j^{th} row in $p(x)$ and $q(x)$ by x^{m+j-1} ($j=2, \dots, n+1$) and afterwards divide the j^{th} column in $p(x)$ and $q(x)$ by x^{j-1} ($j=2, \dots, n+1$). This results in a multiplication of numerator and denominator by x^{mn} . Having done this, we obtain:

$$\frac{p(x)}{q(x)} = \frac{\begin{vmatrix} \sum_{i=0}^m c_i x^i & x \sum_{i=0}^{m-1} c_i x^i & \dots & x^n \sum_{i=0}^{m-n} c_i x^i \\ C_{m+1} x^{m+1} & C_m x^m & \dots & C_{m+1-n} x^{m+1-n} \\ \vdots & \vdots & \ddots & \vdots \\ C_{m+n} x^{m+n} & C_{m+n-1} x^{m+n-1} & \dots & C_m x^m \end{vmatrix}}{\begin{vmatrix} 1 & 1 & \dots & 1 \\ C_{m+1} x^{m+1} & C_m x^m & \dots & C_{m+1-n} x^{m+1-n} \\ \vdots & \vdots & \ddots & \vdots \\ C_{m+n} x^{m+n} & C_{m+n-1} x^{m+n-1} & \dots & C_m x^m \end{vmatrix}}$$

If $D = \text{Det } D_{m,n} \neq 0$. This quotient of these determinants could be written in terms of their bivariate function $f(x, y)$. The sum $\sum_{i=0}^k c_i x^i$ is replaced by the k^{th} partial sum of the Taylor series development of $f(x, y)$ and the $c_k x^k$ by an expression that contains all the terms of degree k in $f(x, y)$. The bivariate term $c_{i,j} x^i y^j$ is said to be of degree $i+j$.

In this Pade approximation of our model, we are interested in finding the bivariate polynomials p and q such that the coefficients of $(fq-p)(x,y)$ diminishes.

The main idea here is to ensure that $f(x,y)$ is represented in rational form in a specified order:

$$f(x,y)_{[n/m]} = \sum_{i,j=0}^{\infty} c_{ij} x^i y^j = \frac{\sum_{i,j=0}^m p_{ij} x^i y^j}{\sum_{i,j=0}^n q_{ij} x^i y^j} \quad (2)$$

where $f(x,y)_{[n/m]}$ is the Pade approximant of $f(x,y)$ to order of $[n/m]$

This involves only computation of coefficients and rewriting the RHS of (16) with obtained coefficients. From (2) we compare coefficients and obtain the following equations as first step:

$$\begin{cases} c_0(x,y)B_0(x,y) = A_0(x,y) \\ c_1(x,y)B_0(x,y) + c_0(x,y)B_1(x,y) = A_1(x,y) \\ \vdots \\ c_m(x,y)B_n(x,y) + c_{m-1}(x,y)B_n(x,y) \dots c_{m-n}(x,y)B_n(x,y) = A_n(x,y) \end{cases} \quad (3)$$

and

$$\begin{cases} c_{m+1}(x,y)B_0(x,y) + \dots + c_{m+1-n}(x,y)B_n(x,y) = 0 \\ \vdots \\ c_{m+n}(x,y)B_0(x,y) + \dots + c_m(x,y)B_n(x,y) = 0 \end{cases} \quad (4)$$

where $c_k = 0$ when $k < 0$

We have:

$$p(x,y) = \sum_{k=0}^m A_k(x,y) \quad (5)$$

$$q(x,y) = \sum_{k=0}^n B_k(x,y) \quad (6)$$

Let us consider the homogeneous system for B_k , Taking

$$B_0(x,y) = \begin{vmatrix} c_m(x,y)B_1(x,y) & \dots & c_{m-n+1}(x,y)B_n(x,y) \\ \vdots & \ddots & \vdots \\ c_{m+n-1}(x,y)B_1(x,y) & \dots & c_m(x,y)B_n(x,y) \end{vmatrix} \quad (7)$$

Using Crammer's rule, we then solved and substituted into the equation defining $A_k(x,y)$. This gives exactly

$$p(x,y) = \begin{vmatrix} \sum_{i,j=0}^m c_{ij} x^i y^j & \sum_{i,j=0}^m c_{ij} x^i y^j & \dots & \sum_{i,j=0}^m c_{ij} x^i y^j \\ \sum_{i,j=m+1}^{\infty} c_{ij} x^i y^j & \sum_{i,j=m+1}^{\infty} c_{ij} x^i y^j & \dots & \sum_{i,j=m+1}^{\infty} c_{ij} x^i y^j \\ \vdots & \vdots & \ddots & \vdots \\ \sum_{i,j=m+n}^{\infty} c_{ij} x^i y^j & \sum_{i,j=m+n}^{\infty} c_{ij} x^i y^j & \dots & \sum_{i,j=m}^{\infty} c_{ij} x^i y^j \end{vmatrix} \quad (8)$$

$$p(x,y) = \begin{vmatrix} 1 & 1 & \dots & 1 \\ \sum_{i,j=m+1}^{\infty} c_{ij} x^i y^j & \sum_{i,j=m+1}^{\infty} c_{ij} x^i y^j & \dots & \sum_{i,j=m+1}^{\infty} c_{ij} x^i y^j \\ \vdots & \vdots & \ddots & \vdots \\ \sum_{i,j=m+n}^{\infty} c_{ij} x^i y^j & \sum_{i,j=m+n}^{\infty} c_{ij} x^i y^j & \dots & \sum_{i,j=m}^{\infty} c_{ij} x^i y^j \end{vmatrix} \quad (9)$$

It is easy to see that we can get (5) and (6) from (8) and (9).

Theorem: For every m and n a unique bivariate Pade approximant of order (m,n) for $f(x,y)$ exists (Cuyt 1987).

Variational Iteration Method

We provide here the following illustrations of basic variational methods due to Yao and Zhou (2010); there, references were made to He's variational iterations on various models. In particular, the following equation was studied:

$$u_t + au_x(x,t) = \phi(x) \text{ for } x \in \mathbb{R}, t > 0 \quad (10)$$

$$\phi(x,0) = x^2 \quad (11)$$

Equations (10-11) models so many physical phenomena, for example: when $a(x,t) = a$ is a constant, it represents the transport equation that is a useful model for the spread of epidemics like AIDS, movement of wind and a lot more in that class. If $a(x,t) = u$, it models the inviscid Burgers' equation i.e. a Burgers' equation with no viscosity. Inviscid Burgers' equation as above describes a one-dimensional stream of particles or fluids with zero viscosity. There are several iteration algorithms used to model many linear and nonlinear partial differential equation. Although, a lot of progress has been made in the use of variational methods but not very much has been achieved to obtain the Pade approximants of variational treated models of nonlinear PDEs. This paper is aimed at addressing this gap in order to achieve more accuracy for our model. In general, when solutions are presented in terms of their Taylor series, the radius of convergence remains an issue; however, when they are presented in rational form by their Pade approximants, we achieve convergence even for higher order terms. It is noteworthy that the variational iteration method presents solutions in terms of their Taylor series expansion, so it is liable to this limitation of very slow convergence rate. This, necessitates further refinements of their solutions in terms of their Pade approximants. From first principle, let us consider the basic variational methods for general nonlinear system:

$$Lu + Nu = \phi(x) \quad (12)$$

Where L and N represent linear and nonlinear operators respectively; $\phi(x)$ is a known analytic function.

$$u_{n+1}(x) = u_n(x) + \int_0^x \gamma \left\{ Lu(\xi) + Nu(\xi) - \phi(\xi) \right\} d\xi \quad (13)$$

Where γ is the Lagrange multiplier which could be identified through variational theory, and the references therein for more exposition. \bar{u} is a restricted variation denoted by $\delta \bar{u} = 0$. The initial guess $u_0(x)$ could be freely chosen from an unknown constant or be solved from the linear homogeneous equation $Lu = 0$.

The variational iteration method could solve any nonlinear partial differential equation accurately to a far extent so the solution converges quite well to the exact solution.

Application of Variational Iteration Methods to Inviscid Burgers' equation

Consider the equation:

$$u_t + uu_x = 0, x \in \mathbb{R} \text{ and } t > 0 \quad (14)$$

$$u_0(x) = x \in \mathbb{R} \quad (15)$$

From variational method (13) we write the following for (14):

$$u_{n+1}(x, t) = u_n(x, t) + \int_0^t \gamma \left\{ \frac{\partial u_n(x, \xi)}{\partial t} + u_n(x, \xi) \frac{\partial u_n(x, \xi)}{\partial x} - \phi(x) \right\} d\xi \quad (16)$$

Here, we do not need to solve the linear homogeneous system for our initial guess as we already have, for free, the initial condition $u_0(x) = x$ from (15); so the solution to (14) using variational iteration method yields the following:

$$\begin{aligned} u_0(x, t) &= x, \\ u_1(x, t) &= x - xt, \\ u_2(x, t) &= x - xt + t^2x - \frac{t^3x}{3}, \\ u_3(x, t) &= x - xt + t^2x - t^3x + \frac{t^4x}{3} - \frac{t^5x}{3} + \frac{t^6x}{9} - \frac{t^7x}{63}, \\ u_4(x, t) &= x - xt + t^2x - t^3x + t^3x - \frac{13t^4x}{15} + \frac{2t^5x}{3} - \frac{t^7x}{29} + \frac{71t^8x}{252} + \frac{86t^9x}{567} - \frac{22t^{10}x}{315} + \frac{5t^{11}x}{189} - \frac{t^{12}x}{126} + \frac{t^{13}x}{567} \\ &\quad - \frac{t^{14}x}{3969} + \frac{t^{15}x}{59535} \\ &\vdots \end{aligned}$$

$$u_n(x, t) = x - xt + t^2x - t^3x + t^4x - t^5x + \dots + (-1)^n t^n x + \dots \quad (17)$$

$$\text{Our solutions } u(x, t) = \lim_{n \rightarrow \infty} u_n(x, t) = \frac{x}{1-t}$$

Pade Approximation of the Variationally Iterated Inviscid Burgers' Equation

We recall equation (8) and write $u_4(x, t)$ of the variational iteration of inviscid Burgers' equation as the following one:

$$\begin{aligned} p(x, y) &= \begin{vmatrix} \sum_{i+j=0}^9 c_{ij} x^i t^j & \sum_{i+j=0}^8 c_{ij} x^i t^j & \sum_{i+j=0}^7 c_{ij} x^i t^j \\ \sum_{i+j=10}^9 c_{ij} x^i t^j & \sum_{i+j=9}^8 c_{ij} x^i t^j & \sum_{i+j=8}^7 c_{ij} x^i t^j \\ \sum_{i+j=11}^9 c_{ij} x^i t^j & \sum_{i+j=10}^8 c_{ij} x^i t^j & \sum_{i+j=9}^7 c_{ij} x^i t^j \end{vmatrix} \\ q(x, y) &= \begin{vmatrix} 1 & 1 & 1 \\ \sum_{i+j=10}^9 c_{ij} x^i t^j & \sum_{i+j=9}^8 c_{ij} x^i t^j & \sum_{i+j=8}^7 c_{ij} x^i t^j \\ \sum_{i+j=11}^9 c_{ij} x^i t^j & \sum_{i+j=10}^8 c_{ij} x^i t^j & \sum_{i+j=9}^7 c_{ij} x^i t^j \end{vmatrix} \end{aligned}$$

$$\sum_{i+j=0}^9 c_{ij} x^i t^j = x - xt + t^2x - t^3x + t^4x - \frac{13t^5x}{15} + \frac{2t^6x}{3} - \frac{t^7x}{29} + \frac{71t^8x}{252} = k_1$$

$$\sum_{i+j=0}^8 c_{ij} x^i t^j = x - xt + t^2x - t^3x + t^4x - \frac{13t^5x}{15} + \frac{2t^6x}{3} - \frac{t^7x}{29} = k_2$$

$$\sum_{i+j=0}^7 c_{ij} x^i t^j = x - xt + t^2x - t^3x + t^4x - \frac{13t^5x}{15} + \frac{2t^6x}{3} = k_3$$

$$\sum_{i+j=0}^6 c_{ij} x^i t^j = \frac{86t^9x}{567}, \sum_{i+j=0}^5 c_{ij} x^i t^j = \frac{71t^8x}{252}, \sum_{i+j=0}^4 c_{ij} x^i t^j = \frac{t^7x}{29},$$

$$\sum_{i+j=0}^3 c_{ij} x^i t^j = -\frac{22t^{10}x}{315}, \sum_{i+j=0}^2 c_{ij} x^i t^j = -\frac{86t^9x}{567}, \sum_{i+j=0}^1 c_{ij} x^i t^j = -\frac{71t^8x}{252}.$$

So,

$$p(x, t) = k_1 \{0.084611015542871\} t^{16} x^2 - k_2 \{0.040325646364690\} t^{17} x^2 + k_3 \{0.042682953382542\} t^{18} x^2$$

$$q(x, t) = \{0.084611015542871\} t^{16} x^2 - \{0.040325646364690\} t^{17} x^2 + \{0.042682953382542\} t^{18} x^2$$

$$\begin{aligned} &k_1 \{0.084611015542871\} t^{16} x^2 - k_2 \{0.040325646364690\} t^{17} x^2 + k_3 \{0.042682953382542\} t^{18} x^2 \\ r_{(9,2)} &= \frac{\{0.084611015542871\} t^{16} x^2 - \{0.040325646364690\} t^{17} x^2 + \{0.042682953382542\} t^{18} x^2}{12180(2482168t^2 + 30077064t + 55305585)} \end{aligned}$$

This yield

$$r_{(9,2)} = \frac{\left(197313169805t^8 + 194795648572t^7 + 161820668856t^6 - 247699921980t^5 + 337516192020t^4 - 337516192020t^3 + 337516192020t^2 - 307283385780t + 673622025300 \right) x}{12180(2482168t^2 + 30077064t + 55305585)}$$

Similarly, the following computations hold true:

$$r_{(11,2)} = \frac{\left(3332274t^{10} + 39785435t^9 + 280716390t^8 + 240748200t^7 - 221629716t^6 + 323269380t^5 - 323269380t^4 + 323269380t^3 - 195013980t^2 + 762297480t \right) x}{328860(390t^2 + 1725t + 2318)}$$

The following table is obtained based on the numerical result:

Table 1 Comparison of Pade Approximation with Exact Solution of Burgers' Equation

X	T	Exact Solution $u(x, t)$	$r_{(9,2)}$	$r_{(11,2)}$
0.001	0.001	0.0009990009990	0.0009990009992	0.0009990009989
0.002	0.002	0.001996007984	0.001996007984	0.001996007984
0.003	0.003	0.002991026919	0.002991026920	0.002991026919
0.004	0.004	0.003984063745	0.003984063745	0.003984063744
0.005	0.005	0.004975124378	0.004975124379	0.004975124378
0.006	0.006	0.005964214712	0.005964214713	0.005964214711
0.007	0.007	0.006951340616	0.006951340616	0.006951340616
0.008	0.008	0.007936507937	0.007936507936	0.007936507936
0.009	0.009	0.008919722498	0.008919722496	0.008919722499
0.01	0.01	0.009900990099	0.009900990099	0.009900990099

It could be seen from the table that the rational approximation of differentially transformed Burgers' equation is in agreement with the exact solution; above this, it provides a larger radius of convergence than the traditional power series approximation from where the exact solution has been obtained.

Conclusion

Rational series solution of Burgers' equation was constructed using multivariate Pade approximation. This approximation is effective to the extent that it maintains a rapid convergence to the exact solution of the Burgers' equation obtained from power series of variationally iterated Burgers' equation.

References

Adomian, G. (1984). Convergent series solution of nonlinear equations. *Journal of Computational and Applied Mathematics*; 11: 225–230.

Bildik, N, and Konuralp, A. (2006). Two-dimensional differential transform method, Adomian's decomposition method, and

variational iteration method for partial differential equations. *International Journal of Computer Mathematics*; 83(12): 973–987.

Cuyt, A. and Wuytack, L. (1987). *Nonlinear Methods in Numerical Analysis*. Elsevier: Amsterdam.

Fatma, A. (2003). On the two-dimensional differential transform method. *Applied Mathematics and Computation*; 143: 361–374.

Fatma, A. (2004). Solutions of the system of differential equations by differential transform method. *Applied Mathematics and Computation*; 147: 547–567.

He, J. H. (1998). Approximate analytical solution for seepage flow with fractional derivatives in porous media. *Comput. Methods Appl. Mech. Eng.* 167: 57-68.

He, J. H. (1999). Variational analytical methods- a kind of non-linear analytical techniques- some examples. *Int. Journal of nonlinear Mech.* 34: 699-708.

He, J. H. (2007). Variational iteration method- Some recent results and new interpretations. *Journal of Computational and Applied*

Mathematics 207:3-17.

He, J. H. and Wu, X. H. (2007). Variational iteration methods: new development and applications. *Journal of Computational and Applied Mathematics* 54: 881-894.

Lagrange, J. L. (1776). Sur l'usage des fractions continues dans le Calcul integral, Nouveaus Mem. Acad. Sci. Berlin; 7: 236-264.

Lambert, J. H. (1758). Observation Variae in Mathesin puram, *Acta Helvetica* 3: 128-158.

Logan, J. D. (1994). *An Introduction to Nonlinear Partial Differential Equations*. Wiley-Interscience: New York.

Pukhow, G. E (1986). *Differential Transformations and Mathematical Modelling of Physical Processes*. Naukova Dumka: Kiev.

Zhou J. K. (1986). *Differential Transform and its Applications for Electrical Circuits*. Huarjung University Press: Wuhan.

Spectral Analysis of Aeromagnetic Data showing Depths of Magnetic Sources of Kwoi within Jaba Local Government Area, Kaduna State, Nigeria

Magaji, S.¹, Afuwai, C. G.² and Aboh, H. O.³

¹Department of Science, Kaduna State College of Nursing,
Kafanchan Campus, Kaduna State, Nigeria

^{2,3}Department of Physics, Kaduna State University, Kaduna State, Nigeria
Corresponding author's e-mail: simonmagaji2012@gmail.com

ABSTRACT

A geophysical analysis of earth tremor using Aeromagnetic data of Jema'a NE sheet 188 was analyzed to study the subsurface structures in terms of depths of the magnetic sources of the study area. The study area is in Kwoi, Jaba local Government Area, located in the southern part of Kaduna State, Nigeria which lies between latitude 9°00' East and 9°30' East, and longitude 8°00' North and 8°30' North. *The results were delineated using spectral analysis*; these spectral depths were computed from measurements made on the widths and slopes of individual anomalies of the aeromagnetic profiles. The method is based on the principle that a magnetic field measured at the surface can be considered to be the integral of magnetic signatures from all depths. This statistical approach has been found to yield good estimates of mean depth to basement underlying Kwoi. The depth solution is calculated for the power spectrum derived from each grid sub-set and is located at the centre of the window. *The analysis suggests three source depths under the study area, the deeper source, of average depth of 4.05 km, the intermediate source, of average depth of 1.38 km and the shallower source, average depth of 0.33 km.*

Keywords: Geophysical Analysis, Spectral Analysis, Earth Tremor, Aeromagnetic Profiles

Introduction

The Earth covers a lot of natural resources that when investigated, could be of economic and scientific importance. Most economic minerals, oil, gas, and groundwater lie hidden beneath the earth surface and the presence and magnitude of these resources can be certain by geophysical investigations of the subsurface geologic structures in the area. Developments in Earth sciences and technology have made it easier to view the Earth's subsurface clearer without necessarily penetrating through it. This is done by studying the behavior and characteristics of the properties associated with the Earth's interior, using geophysical tools.

(Aina and Olarewaju 1991) state that Aeromagnetic method being a faster, economical and versatile geophysical tool may help reveal hidden and exposed both large and small scale geologic features. The main

advantage of this technique is that, it is quick and large areas which are not easy to access for ground surveys can be covered by this method effectively. A wide range of geophysical methods exist and for each, there is an operative physical property to which the method is sensitive. The type of physical property to which a method responds clearly determines its range of application. Several geophysical works have been carried out in some other areas like the basin using magnetic, electrical, gravity, seismic and other geophysical methods. For instance, Ofor et al. (2014) carried out a study of Pategi and Egbako areas of the lower Bida basin and revealed two prominent layers; with average values of 0.59km and 3.1km respectively. Megwara and Udensi (2014) also carried out structural analysis using aeromagnetic data over parts of southern Bida basin and the surrounding basement rocks and found the depth to be within the range of 0.01km to

0.51km with an average value of 0.128km. Ojo and Ajakaiye (1989) delineated the presence of a positive gravity residual centre in the basin. Udensi and Osazuwa (2004) estimated the average depth to basement to be 3.39km with a maximum depth of 4.5km. Ojo (1990) investigated a major east-west magnetic low whose deep seated structures dominate the southern part of the basin with depths to basement varying between 4.0km and 6.0km. Udensi (2001) identified the landward prolongation of St. Paul and Romanche fracture zones as lineaments passing through the northern and southern parts of Bida basin. In the spectral determination of depths to magnetic rocks in the Bida Basin, Udensi and Osazuwa (2004) were able to corroborate the interpretations of Ojo (1984) and Ojo and Ajakaiye (1989) that outlined the basin as being bounded by a system of linear faults. Olaniyan *et al.* (2012) used manual and automatic depth estimation methods to reveal depths ranging between 1km and 1.50km with some deep pockets around Mokwa, Kudu, Kotonkarfi, Auna, Akerre and Bida, ranging from 2.50km to 3.75km which could be reservoirs for hydrocarbon potentials. The depleting nature of the existing petroleum reserves and hence, the spectral depths are usually computed from measurements made on the widths and slopes of individual anomalies of the aeromagnetic profiles. The method is based on the principle that a magnetic field measured at the surface can be considered to be the integral of magnetic signatures from all depths. This statistical approach has been found to yield good estimates of mean depth to basement underlying a sedimentary basin (Udensi 2001). Spector and Grant (1970) developed the depth determination method which matches two dimensional power spectral calculated from gridded total magnetic intensity field data with corresponding energy spectral obtained from a theoretical model. A depth solution is calculated for the power spectrum derived from each grid sub-set and is located at the centre of the window. For the purpose of

analyzing aeromagnetic data, the ground is assumed to consist of a number of independent ensembles of rectangular, vertical sided parallelepiped with each ensemble characterized by a joint frequency distribution for the depth (h), length (b) and depth extent (t). In studying the characteristics of the residual magnetic field using statistical spectral methods, the data was transformed from the space to frequency domain and then the frequency characteristics analyzed.

The statistical spectral analysis of the residual field data was employed to determine the depths to the buried magnetic sources within the sub surface of the study area. Their model assumes that an uncorrelated distribution of magnetic sources exists at a number of depth intervals in a geologic column. The Fourier transform of the potential field due to a prismatic body has a broad spectrum whose peak location is a function of the depth to the top and bottom surfaces and whose amplitude is determined by its density or magnetization.

The aeromagnetic anomalies are patterns that are shaped very largely by the depths and volumes of the sources (Spector and Grant, 1970), and of course, their magnetization, mean depths to the sources can be determined by spectral analysis (Ruotoistenmaki 1983, 1987).

Nur, *et al.* (1994), obtained 1.6 to 5 km for deeper sources around the Middle Benue, while 0.06 m to 1.2 km was obtained for shallower magnetic sources. Nwogbo (1997), obtained 2 to 2.62 km for deeper source and 0.07 km to 0.63 km for shallower ones from spectral analysis of Upper Benue Trough; Udensi, *et al.*, (2003) obtained a maximum depth of 3.39 km at Nupe Basin; Nur, (2000) obtained depth range of 0.625 to 2.219 km for deeper source and an average of 0.414 km for shallow sources at the Upper Benue Trough; Nur, (2001). Spectral analysis and Hilbert transform of gravity data over the estimated a depth range of about 0.42 to 8.0 km around the southwest of the Chad Basin.

Spectral analysis of magnetic data is used extensively to derive the depth to certain

geological features such as magnetic basement. Ofoegbu (1985) stated that the depth factor invariably dominates the shape of the radially averaged power spectrum of the magnetic data. Depth estimation from potential field using power spectra requires a realistic assumption of the statistical properties of the source distributions.

Akpan and Yakubu (2010) observed the incidences of earthquake that occurred in Nigeria. Based on their findings several minor tremors were experienced in various parts of the country as recorded in the years 1933, 1933, 1939, 1964, 1984, 1990, 1994, 1997, 2000 and 2006 respectively. The strengths of these occurrences varied from III to IV according to the modified Mercalli intensity scale. In the midst of these occurrences, 1984, 1990, 1994 and 2000 were the only recorded events with a magnitude range from 4.3 to 4.5. Similarly, Chinwua (2013) in his work on earthquake resistance structure in Nigeria opined that the tremors experienced in the past years showed vividly an earthquake potential and seismicity in Nigeria. These further shows

that the tremors experienced over the years clearly indicated that Nigeria is not aseismic. This is because the persistent of tremors along the fault lines can lead to stress accretion and consequently its resultant effectual force could bring surface eruption. The place of study is Kwoi town in Jaba Local government area of Kaduna State experienced tremor in the recent times which led to destruction of buildings and breakages of rock. This paper intend to estimate the depth to magnetic sources by using spectral analysis of high resolution of aeromagnetic data aimed at finding out the cause of the tremors within the town under study.

Location and Geology of the study area

The study area is located in the southern part of Kaduna State, Nigeria which lies between longitudes $9^{\circ}00'$ North to $9^{\circ}30'$ North and between Latitude $8^{\circ}00'$ East to $9^{\circ}30'$ East, Figure 1. The area can be accessed through Kaduna – KachiaKeffi express Road at a distance of 192km, about 2hours 34minutes drive from Kaduna.

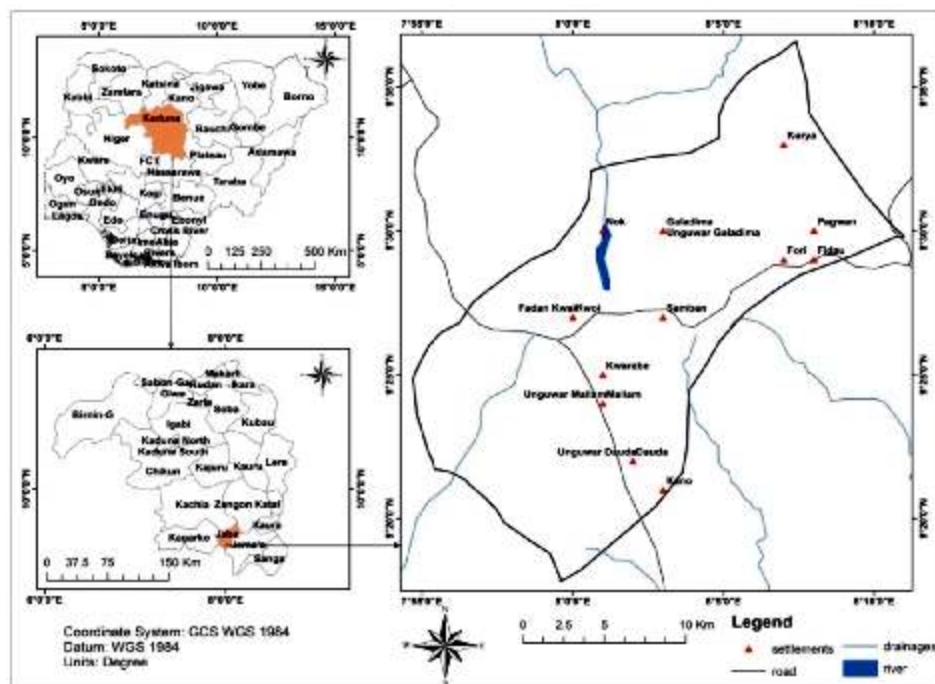


Figure 1: Showing the Location of Kwoi (Magaji, 2019)

The study area lies within the Basement Complex of Nigeria (Figure 2). The Basement Complex includes all rocks older than the late Proterozoic (McCurry 1976), and is composed mainly of gneisses, migmatite, granites and some extensive areas of schist, phyllites and quartzites (Preeze and Barber 1965; Baimba 1978). The basement complex rock of Kwoi area consists of migmatite-gneiss complex (older) and older granites. Minor dykes are found within these rocks (McCurry, 1975). Relicts' quartzite is also found in the basement complex occurring as an older metasediments. The older granite covers wide areas suite which include granites, grandiorites, syenites, diorites and gabbros. Contacts of the granitoids are often aligned N-S due the Pan – African orogeny (600 ± 150 M.Y.). Superficial deposits, which are the result of weathering and transportation of the rocks, occur as alluvium within river channels Aeolian soil and clay. Decomposed or weathered and /or fractured basement rocks are overlain by laterites, alluvium and sandy soils. The structure prevalent in the basement complex of Kaduna is not different from those of the Nigerian basement complex and this is defined by a network of faults and Dykes which have been deciphered by means of airborne geophysical survey and are rather simple. The Faults displayed a preferred orientation whose axis is generally NNE-SSW, similar to known joint direction N-S in Nigerian basement complex. The principal fracture of directions in the basement complex are trending N-S, NNE – SSW, NE – SW, NNW – SSE, NW – SE, and to a lesser extent E-W (Musilim and Ofoegbu 1983).

Nahikhare (1971) worked on the general geology of the study area and identified the dominant rocks as granites, migmatites and gneisses.

Okezie (1970) also identifies the general geology of the area under study to be underlain by rocks of basement complex of North central Nigeria, consisting of migmatites, granites gneisses, granites, newer

basalts, laterites, and alluvium. The migmatites exhibit a granoblastic texture and foliation characterizing with light and dark bands, visible minerals includes quartz, biotite and plagioclase. Granites gneisses are found scattered all over the study area isolated exposure lying low, they have pink color with foliation with quartz mineralization as vein. Minerals visible in hand specimen are notably quartz, feldspars (Nahikhare 1971).

Granites are the dominant rock unit in the study area and there are three types identified, namely: biotite granite, medium granite and biotite hornblende granite. Newer basalts occur as ridges in isolated exposures in the area, typical of tropical climatic belt. Alluvium stream channel contains deposit sand derived from the area as a result of weathered basement rocks (Okezie 1970).

Rahaman (1988) from the geological survey of some areas within southern Kaduna found out that the rocks of the areas consist mainly of vertically dipping hornblende and biotite gneisses of variable grain sizes and migmatites. He concluded that hornblende gneisses formed dissecting ridges generally along NW – SE which were litho – stratigraphically conform parallel to quartzitic ridges. Biotite displayed alteration rims and elongated sphene which occurred in accessory quantity.



Fig. 2 Kwoi is underlain by Basement Rocks (Obaje 2009 in Magaji 2015)

Methods

The magnetic method of exploration is governed by Coulomb's law which shows that the force between two magnetic poles P_1 and P_2 at a distance r apart is given by;

$$F = \frac{P_1 P_2}{\mu r^2} \quad (1)$$

We can also define the force per unit pole strength exerted by a magnetic monopole P_1 and P_2 . This is called magnetic field strength or magnetizing force H . Magnetic field strength is the quantity measured by the magnetometers (Telford et al. 1990). Thus

$$H = \frac{F}{P_2} = \frac{P_1}{\mu r^2} \quad (2)$$

Where, μ is magnetic permeability of the medium and it is a property of the material medium in which the two monopoles are situated.

Theory of Vertical Derivatives

Detection of the edges of geological structures from the analysis of potential field data is commonly performed. Vertical gradients of potential fields are a mainstay of the interpretation process, principally because they sharpen the response of geophysical features. This filtering method is effective in enhancing anomaly due to shallow sources; it narrows the width of anomalies and also Very effective in locating source bodies more accurately (Cooper and Cowan 2006).

Thus at the expense of deeper anomalies, it enhances near-surface features. The first vertical derivative (FVD) is given below:

$$FVD = \frac{\partial M}{\partial z} \quad (3)$$

Where M is the potential field anomaly, z is the unit vector along z direction. The vertical derivative was derivative was computed from

upward continued data. This is very important to this research as it will bring out the lineaments of interest more obvious.

The second vertical gradient can be calculated by exploiting Laplace's equation:

$$\frac{\partial^2 \phi}{\partial z^2} = -\frac{\partial^2 \phi}{\partial x^2} - \frac{\partial^2 \phi}{\partial y^2} \quad (4)$$

(Blakely 1995)

Second vertical derivative filters are used to enhance subtle anomalies while reducing regional trends. These filters are considered most useful for defining the edges of bodies and for amplifying fault trends. In mathematical terms, a vertical derivative can be shown to be a measure of the curvature of the potential field, while zero values (or contours) second vertical derivative contours defines the edge of the causative body. Thus, the second vertical derivative is in effect a measure of the curvature, i.e., the rate of change of non- linear magnetic gradients. The zero magnetic contours of the second vertical derivative often coincide with the lithologic boundaries (Blakely 1995).

Data Acquisition

One aeromagnetic map was acquired from the Nigerian Geological Survey Agency (NGSA), Abuja. The sheet is Jema'a (188). This aeromagnetic data was obtained as part of a nationwide aeromagnetic survey sponsored by the Geological survey of Nigeria. The data was acquired at a flight altitude of 80m along a series of NE – SW flight lines with a spacing of 500m. The sheet extend from Longitude 9°00' North to 9°30' North and between Latitude 8°00' East to 8°30' East, covering the study area and its environs.

Table 1 Spectral Depths of Deep, intermediate and shallow magnetic sources of Kwoi from 16 ensembles

S/N	X (m)	Y (m)	Deep M_d	Intermediate M_i	Shallow M_s	Z_d (Km)	Z_i (Km)	Z_s (Km)
1	1037500	432500	25.26	2.64	0.13	2.01	0.21	0.01
2	1025000	420000	12.69	12.69	1.38	1.02	1.01	0.11
3	1012500	407500	0.25	1.63	1.26	0.02	0.13	0.20
4	1007500	402500	12.57	0.38	0.13	1.00	0.03	0.01

Theory of Spectral Analysis

The theory of spectral analysis of energy spectrum considered a bottomless prism, for a spectrum peak at the zero wave number given by the expression:

$$f(w) = e^{h_0} \quad (5)$$

Where w is the angular wave number in radians/ground – unit and h is the depth to the top of the prism.

For a prism with top and bottom surface, the spectrum is:

$$f(w) = e^{-h_t^0} - e^{-h_b^0} \quad (6)$$

Where h_t and h_b are the depths to the top and bottom surface respectively. As the prism bottom moves closer to the observation point at surface, the peak moves to a higher wave number.

When considering a line that is long enough to include many sources, the log spectrum of this data can be used to determine the depth to the top of a statistical ensemble of sources using the relationship.

The energy spectrum according to Udensi (2001) is given by:

$$\text{Log}E(k) = 4\pi h k \quad (7)$$

Where h is the depth in ground – units and k is the wavenumber in *cycles / Km* – unit. The depth of an 'ensemble' of source can be determined by measuring the slope of the energy (power) spectrum and dividing by 4. A typical energy spectrum for magnetic data may exhibit three parts – a deep source component, a shallow source component and a noise component. The residual map of the study area was divided into sixteen (16) blocks of overlapping magnetic sections each with 25 Km^2 .

Method of Interpreting the Spectral Analysis Data

The divisions of residual data/map of spectral sections were filtered with Oasis montaj and the spectral energies were plotted against frequency (wavenumber). From the slopes of

the plots, the first and the second magnetic source depth was respectively estimated using the relations below:

$$Z_1 = -\frac{m_d}{4p} \quad (8)$$

$$Z_2 = -\frac{m_i}{4p} \quad (9)$$

$$Z_3 = -\frac{m_s}{4p} \quad (10)$$

Where m_2 and m_3 are slopes of the first, second and third segments of the plots while Z_1 , Z_2 and Z_3 are first, second and third depths respectively (Table 1). The coordinates of each spectral block were obtained by summing the values of the bounding latitude and longitude and averaging it. This was used in plotting the spectral energy against frequency as presented in figure 3.

Result and Discussion

In the course of the research work, there were several methods of qualitative and quantitative interpretation techniques employed, with the goal of meeting the research objectives in order to study the geological structures of Kwoi that might have been the cause of the earth tremor that occurred in 2016. The qualitative methods used for the purpose of this publication included the lineament of the study area and the spectral analysis deduced from residual map.

Lineaments

Lineaments are primarily the topographical features of geological formations, which can typically be of regional scope in linear curvilinear continuous or discontinuous over a whole distance. Lineament can be found in igneous, sedimentary and metamorphic rocks due to faults, joints, folds, contacts or other geological factors (McCurry 1970).

Ajakaiye et al. (1991) indicated that in the Nigerian continental landmass there are magnetic lineaments with definite characteristics trending NE.

Residual Field Map

The anomaly separation technique consists of the removal of regional fields from the observed measured field data in order to leave the irregular residual data. Figure 3 shows the residual map of the study area, which lies from -55.068891 to $44.020742nT$. The red colors, from 12.808400 to $25.294213nT$, blue colors,

from -55.068891 to $-17.435654nT$. The residual map revealed some subtle lineaments within the study area. This has anomalies of geological interest corresponding to wanted effect of high frequencies of the observed field which is usually subjected to further analysis and interpretation, hence, showing heterogeneous magnetic field.

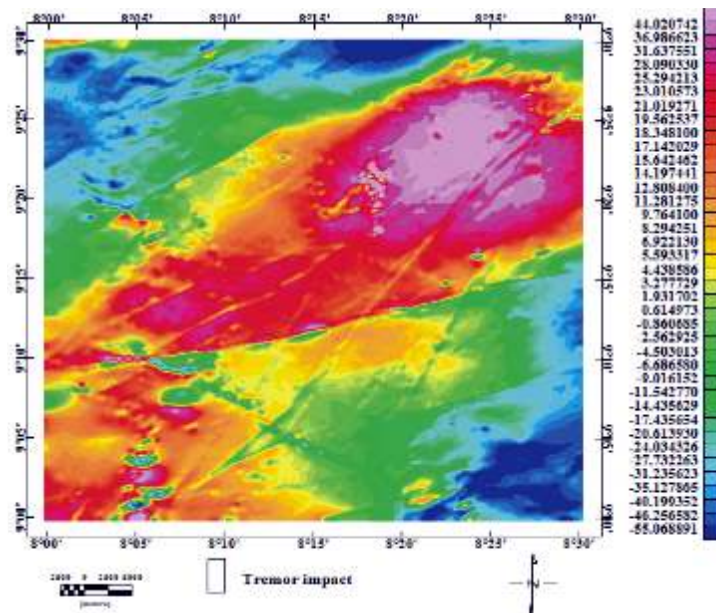


Fig. 3 Residual Map of the Study area

Spectral Analysis

The magnetic source depth determination through spectral analysis suggests three source depths under the study area as shown by the spectral graph in figure 4. These results also suggest the existence of the deeper source, the intermediate source and the shallower source. The first segment of the spectra represents the deeper magnetic source with an averaged depth of 4.05Km giving a statistical inference of 70.31%. The intermediate source is represented by the second segment of the spectra that is between the shallow and deeper precambian basement with pink color line average depth of 1.38 km and it is 23.96%. And the shallow source magnetic horizons represented by the third segment of the energy spectrum reflecting magnetic horizons source shallower than the basement and the intermediate, with blue color line average depth of 0.33 km and it is 5.73%.

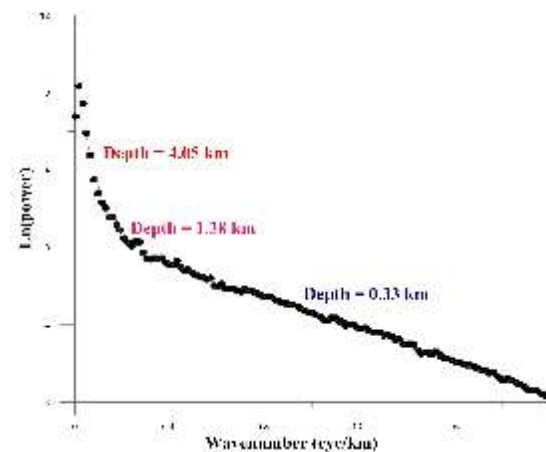


Fig.4 Spectral Analysis Graph of the Study Area

The thick sedimentary cover in the southern part and some areas in the northern part of the area correspond with the Middle Benue Trough and the thick sediments within the

calderas within the Jos Plateau ring complexes (Alkali and Kasidi 2015). It can also be explained best in terms of intrusive igneous bodies of variable depths existing within the area. The variable basement depths can be closely related to the tectonic and structural evolution of the area.

Conclusion

Aeromagnetic data (sheet 188 Jema'a NE) interpretation was obtained using a qualitative spectral depth analysis method that delineated the depths to magnetic sources within Kwoi Kaduna state, Nigeria which further confirmed the area of study consists of averagely three depths. These depths include 4.05Km, 1.38Km and 0.44Km are found to be equivalent to deep seated magnetic source, intermediate magnetic source and shallow magnetic source. For this reason, the spectral analysis has helped in mapping out the geologic structural depths of the magnetic sources and as such, relates to the tectonic and structural evolution in the study area.

References

- Akande, S.O., Ojo, O.J., Erdmann, B.D. and Hetenyi, M. (2005). Paleoenvironments, organic petrology and Rock-Eval studies on source rock facies of the Lower Maastrichtian Patti Formation, southern Bida Basin, Nigeria. *Journal of African Earth Sciences*, 41: 394–406.
- Ajakaiye, D.E., Hall, D.H. and Miller, T.W. (1983). *Interpretation of Aeromagnetic Data across the Central Crystalline Shield of Nigeria*. In: Kogbe, C.A. (Ed) *Geology of Nigeria*, Elizabeth Publication Company, Lagos, Nigeria: 81-92.
- Alkali S. C. and Kasidi S., (2015). Determination of Depth to Magnetic Sources Using Spectral Analysis of High Resolution Aeromagnetic Data over IBBI and Environs, Middle Benue Trough, North Central Nigeria, *International Journal of Science and Research (IJSR)*
- Baimba, A. B. (1978). Resistivity and Refraction Seismic methods for groundwater Exploration at Zango, Kaduna State. Unpublished M.Sc. Thesis: Department of Physics, Ahmadu Bello University, Zaria, Nigeria.
- Blakely, R. J. (1995). *Potential Theory in Gravity and Magnetic Applications*, Cambridge University Press, USA.
- Cooper, G. R. J., & Cowan, D. R. (2006). Enhancing potential field data using filters based on the local phase. *Computers & Geosciences*, 32(10):1585–1591. <https://doi.org/10.1016/j.cageo.2006.02.016>
- Megwara, J. U. and Udensi, E. E. (2014). Structural Analysis Using Aeromagnetic Data: Case Study of Parts of Southern Bida Basin, Nigeria and the Surrounding Basement Rocks. *Earth Science Research*, 3 (2): 27- 42
- McCurry, P. (1975). The Geology of Precambrian to Lower Paleozoic Rocks of Northern Nigeria, a Review in C.A.
- Muslin, I. and Ogoegbu, C. E. (1983). Geological Report on the Depth to water table in Kano State WRECA (Unpublished).
- Kogbe (Ed.) *Geology of Nigeria*, Elizabeth Publishing Co. Lagos: 15-39.
- McCurry, P. (1976): The Geology of the Precambrian to Lower Paleozoic rocks of Northwestern Nigeria. A review in Kogbe, C.A. (Ed), *Geology of Nigeria*. Elizabethan Publishing Company, Lagos, *Mid-America Earthquake Center, MAE Center Report No.07-02:15-39*.
- Nur, A. (2000). Analysis of aeromagnetic data over Yola arm of the Benue Trough, Nigeria. *Mining and Geol.* 36:77-84.
- Nur, A. (2001). Spectral analysis and Hilbert transform of gravity data over the south-west of the Chad Basin, Nigeria. *Journal of Mining and Geology*, 37: 155 - 161.
- Nur, A., Onuoha, K. M., and Ofoegbu, C.O. (1994). Spectral analysis of aeromagnetic data over the Middle Benue Trough. *Journal of Mining and Geology*, 30: 211– 217.
- Nwogbo, P.O. (1997). Mapping the shallow

- magnetic sources in the Upper Benue Basin in Nigeria from aeromagnetic Spectra, 4: 325-333.
- Obaje N. G. (2009). Geology and Mineral Resources of Nigeria, Lecture Notes in Earth Sciences. Springer Dordrecht Heidelberg, London New York: 221.
- Ofoegbu, C.O. (1985). Long wave magnetic anomaly and crustal structure underneath the Benue Trough and surrounding regions. *Nig. J. Min. and Geol.* 22: 45 - 50.
- Ofor, N. P., Adam, K. D. and Udensi, E. E. (2014). Spectral Analysis of the Residual Magnetic Anomalies over Pategi and Egbako Area of the Middle Niger Basin. Nigeria. *Journal of Natural Sciences Research*, 4(9): 44-50.
- Ojo, S. B. (1984). Middle Niger Basin revisited magnetic constraints on gravity interpretations. *A paper presented at the 20th Nigeria Mining and Geosciences Society Conference, Nsukka, Nigeria, Conference proceedings*: 52-53.
- Ojo, S. B. (1990). Origin of a major magnetic anomaly in the Middle Niger Basin, Nigeria. *Tectonophysics*, 85: 153 - 162. [dx.doi.org/10.1016/0040-1951\(90\)90410-A](https://doi.org/10.1016/0040-1951(90)90410-A)
- Ojo, S. B. and Ajakaiye, D. E. (1989). Preliminary interpretation of gravity measurements in the middle Niger Basin area, Nigeria. In: Kogbe, C.A. (Ed.), *Geology of Nigeria*, second ed. Elizabethan Publishing Co., Lagos: 347-358.
- Okezie, C. N., (1970). Interior report of geology of basement of 1:100,000 sheet 167 (Kafanchan) S. N. Unpublished
- G. S. N. Report: 1127
- Olaniyan, O., Abbah, U., Nwonye, N., Alich, A. and Udensi, E.E. (2012). Interpretation of Total Magnetic Intensity Field over Bida Basin. *Nigerian Geological Survey Agency. Occasional Paper No. 15*: 98.
- Preeze, J. W. and Barber, W. (1965). Distribution and chemical quality of groundwater in Northern Nigeria. *Geological Survey of Nigeria Bulletin No 36*: 60-63.
- Nahikhare, J. I. (1971). Geology of Western half of 1:100,000 sheet 188 (Jema'a). *Geology Survey of Nigeria Unpublished report. No. 1472*.
- Rahman, M. A. (1988). Recent Advances in the study of the Basement Complex of Nigeria in P. O. Oluyide (Coordinator), *Precambrian Geology of Nigeria. Geol. Survey Nigeria Publ.: 11-43*.
- Ruotoistenmäki, Y. T. (1983). Depth estimation from potential field data using the Fourier amplitude spectrum. *Geoexploration*, 21 (3): 191-201.
- Spector, A. and Grant, F. S. (1970). Statistical Models for interpreting aeromagnetic data. *Geophysics*, 35: 293-302.
- Telford, et al (1990). *Applied Geophysics*, Second (Ed.) Cambridge University Press, England.
- Udensi, E. E. and Osazuwa, I. B. (2004). Spectra determination of depths to magnetic rocks under the Nupe basin, Nigeria. *Nigeria Association of Petroleum Explorationists (NAPE) Bulletin* 17, 22-27.
- Udensi, E.E. (2001). Interpretation of the total magnetic field over the Nupe basin in West Central Nigeria using aeromagnetic data. Ph.D. thesis Dept. of Physics ABU, Zaria, Nigeria.
- Udensi, E.E. and Osazuwa, I. B. (2003). Spectral determination of the depths to the buried magnetic rocks under the Nupe Basin. *Nigerian Journal of Physics (NJP)*, 15 (1): 51 - 59.

Investigation of Gross Alpha and Beta radioactivity in Well Water in some parts of Makarfi Local Government Area, Kaduna State, Nigeria

Gazara, A. B.¹, Sadiq, U.², Rabi, N.³ and Abdulhadi, D.⁴

^{1,4}Department of Science Laboratory Technology, Nuhu Bamalli Polytechnic Zaria, Nigeria

^{2,3}Ahmadu Bello University Zaria, Nigeria

Corresponding author's email: abgazara@gmail.com

ABSTRACT

Nineteen samples of well water from nineteen different locations were taken from hand dug wells and bore holes from Makarfi Local Government Area of Kaduna state Nigeria. The total dissolved solids (TDS) were determined for the water samples. An aliquot of each sample was evaporated to dryness, based on the total dissolved solids (TDS) of the sample, and the residue counted for gross alpha and beta activity using the proportional counter. The results show that the counter has low background and good plateau, which were all reproducible, and the counting modes results also show that, the average alpha activity concentration in the well water samples is 12.87×10^{-4} Bq/L. The average beta activity concentration in the well water sample is 17.77×10^{-4} Bq/L. The overall results showed that both alpha activity and beta activity in the study area are far below the practical screening level of radioactivity in drinking water of 0.5 Bq/L for alpha and 1 Bq/L for beta, as recommended by CEC – FAO and WHO

Keywords: Radiation, Radioactivity, Alpha and Beta, Well Water, Activity Concentration.

Introduction

Water is an essential substance to man, animal and all that surrounds them. It has been in existence right from the origin of the universe itself. Water forms greater percentage of man and animal blood and tissue with about 75%.

Man uses water for many purposes in areas such as power generation, agriculture and above all for domestic purposes. Water for human consumption should be free from chemical, microbiological and radiological contaminations, but unfortunately in developing countries like Nigeria most people are not opportune to have access to such safe drinking water. In Makarfi local government area of Kaduna State people totally rely on the ground water sources comprising hand wells and borehole (deep and shallow). Tap water is mostly not provided, so most of the populace relies heavily on untreated ground water as their source of drinking water. Thus, it becomes necessary to investigate the radiological content of drinking water in the area through the response of gas free single

channel detector. This makes the ground water quality an area of increasing focus and importance so as to protect lives against the hazardous environmental effects, one of which is radionuclides in drinking water. Radioactivity in ground water was formerly limited to natural sources such as radon, radium, or uranium, but release from fertilizers, agrochemicals, medical and research facilities have added the dimension of man-made radioactivity finding its way into the drinking sources (Milvy and Conthern 1990).

Radioactivity in drinking water comes mainly from two sources: naturally occurring and artificially induced. Artificial radioactivity is usually found in surface water due to human activity while naturally occurring radioactivity comes from the bedrock. The natural radioactivity is mainly due to contamination as a result of leaching of minerals in the earth crust. Contamination in well water is mainly due to human activity in agriculture, medicine, and industry. This contamination may also

In this paper an investigation of Gross Alpha and Beta radioactivity in Well Water in some parts of Makarfi Local Government Area, Kaduna State, Nigeria is presented.

The proportional counters

The equipment used for the gross alpha and beta counting is a gas free single channel counter MPC 2000 Desktop Gross Alpha/Beta counter with 9^{1/4}” W x 11^{3/4}” H x 16^{3/4}” D. It has light weight of less than 35lbs with most options; easiest sample loading that is has no rotation latch, positive drawer lock and no sample drop through. It has multiple control options which include a keypad/console, programmable touch panel and a standard PC. The MPC 2000 has two detector options available. A2” active area, gas flow proportional detector is standard. This detector can be used with or without a user changeable ultra-thin entrance window. An optional non-gas flow detector is also available. It has low background of 0.05 CPM Alpha, 50 CPM Beta and lower background with optional shield

Other materials

Other materials used for the various experimental stages of this work include 2 liter polythene container to collect the water sample, conductivity meter in order to know the conductivity of the water sample, geographical positioning system (GPS) for measuring the geographical co-ordinates, stainless steel planchets, glass beakers Hot plate, weighing balance, also the following reagents were used namely Nitric acid, acetone, and Vinyl acetate.

Sampling Sites

The samples were collected at the Makarfi Local Government area, Kaduna State Nigeria. The area is situated at the northern part of Kaduna State. The geology of the area shows that the area fall into the biotite granite gneiss, porphyroblastic in part with subordinate magmatites (Webb 2016). Detail on the geology of sector is contained in the Geology map of Zaria area. However some portions of the study area fall in the region underlain by

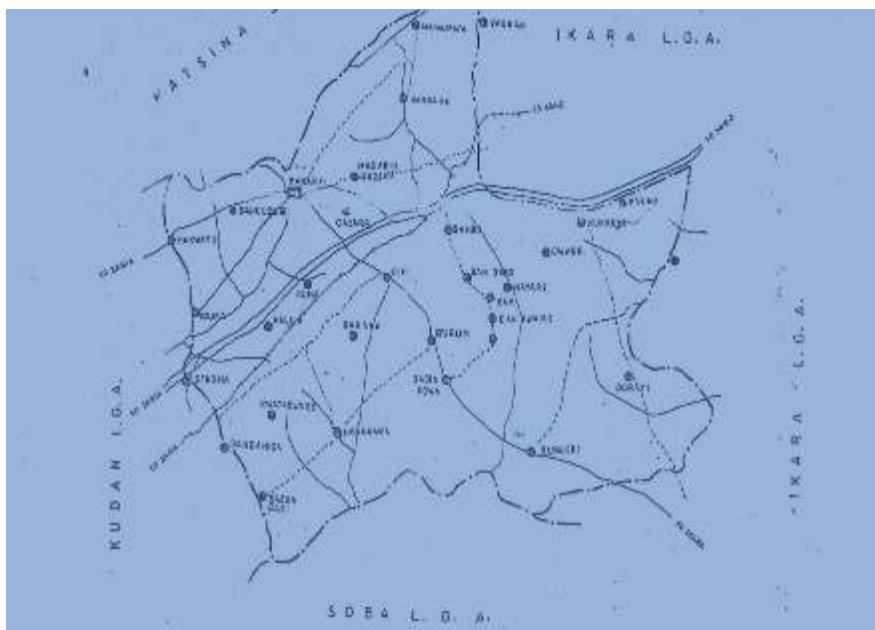


Fig. Map of the study area (Department of works Makarfi local government).

porphyroblastic hornblende granite, while the remaining, portion in underlain by fine medium grained biotite granite.

The geographical location will be determined by hand held GPS (Global positioning system). The area is comprised of a settlement of large populace, and the map of the study area is shown in Fig 1.

Sample collection and Preparation

A total of 19 samples were collected using the composite sampling method in the different villages around the local government area, namely Makarfi, D/Damisa, Tashan Yari, Gazara, Gangare, Gimi, Gubuchi, Mayere, Kunkumi, Gwanki, Dorayi, Durum, Nasarawa Doya, H/Tech, Tafida, Kunkumi, T/Musa, Kwatakwere, Hawan Maimashi. Samples were collected in clean 2 liters. Place in polyethene containers with tight covers. To avoid contamination, the boreholes were allowed to run so as to evacuate the existing water in the pipe before collection. The containers were also rinsed thoroughly with water. The specific conductivity of the water was measured on collection; the water sample was preserved with 20ml of concentrated HNO_3 per liter of water, in order to minimize the loss of radioactivity material from solution due to absorption. The acid would dissolve the radioactive materials already expected on the particulate materials in the sample. The sample was analyzed ten days after collection.

Determination of Total Solid

The total solid concentration in the samples was determined in order to know the appropriate volume of water to evaporate for each sample so as to avoid unnecessary sample thickness which may lead to self-absorption. The volume of water required is such that it can produce a mass of solid residue slightly in excess of 0.1 Amg (where A is the area of the planchet in mm^2). The volume of the sample that can give a solid residue slightly in excess of 71mg; the sample was prepared in accordance with the ISO 9696. Appropriate volumes of the samples that can produce a

mass of solid residue slightly in excess of 71mg were evaporated to near dryness using hot plates. The aliquots were transferred in planchets and a small quantity of acetone was added in order to reduce moisture. Also small amount of vinyl acetate was added to dry the sample in the planchets. The residues were taken for counting of gross alpha and beta activity using gas free single channel counter MPC 2000.

Counting Procedure

Plateau Test

The Plateau test together with the manufacturer's standard sources was used to verify the suitable voltages to be used for the different modes of counting and also to determine the efficiencies and detection limits of the detector.

Background Counting

In compliance with the ISO 9696 standard, clean empty planchets will be counted in order to determine the background radioactivity of the environment. We set the operational high voltage and allowed detector to run for 1800s-cycles. For five cycles by using the alpha only (1,550V), beta only (1,650V) and alpha and beta simultaneously (1,750V) modes. The background count rates were determined in counts per minute.

Counting

The counting equipment is automated. The procedure involves entering the present time, number of cycles and the counting (operational) voltage. Also the counter characteristics (efficiency and background count rate) volume of sample used and sample efficiency were entered. The sample efficiency was determined using equation shown below;

$$\text{Sample efficiency} = \frac{M_r}{0.1A} \quad (1)$$

Where M_r is the mass of residue in planchet got from sample preparation and $0.1A \text{mg}$ is the expected mass of the residue in the planchet. Where unit co-efficient is the multiplication coefficient making it possible to obtain the results expressed in the units used by the operator (e.g. in pc efficiency in %) (Knoll 1989).

Expression of Results

(a) Gross alpha counting

The high voltage for gross alpha counting was set at 1600V and samples were counted for 45 minutes in alpha only mode. Then the results were displayed as row counts; count rate (count/minutes). The count rate and the activity were calculated using the formula:

$$\text{Activity} = \frac{\text{Netcount}}{\text{D.E} \times \text{Samplevolume} \times 60} \quad (2)$$

Where D.E is the detector efficiency

Net count = Raw count - Background counting

(a) Gross Beta counting

The high voltage for gross beta counting was set at 1700V and samples were counted for 45 minutes in beta only mode. The count rate and the activity were calculated using the formula:

$$\text{Activity b} = \frac{\text{Netcount}}{\text{D.E} \times \text{Samplevolume} \times 60} \quad (3)$$

Where D.E is the detector efficiency

Net count = Raw count - Background counting

(Knoll 2000)

Contour distribution

The specific activities of radionuclide as well as the gross alpha and gross beta activity concentration were shown in contour distributions. This is aimed at finding out the areas of high distribution.

RESULTS AND DISCUSSION

The gas free single channel counter MPC 2000 used was initially calibrated using the manufacturer's standard Alpha and Beta

sources (Pu-239 and Sr-90 respectively). The calibration is aimed at obtaining the operational efficiency of the channel of the counter. After the calibration, the counter was then used to count the background radioactivity of the environment. The gross Alpha and Beta radioactivity counting modes applicable to the counter, whose respective voltages are 1,550 and 1650 volts, were then employed to count the prepared water samples collected from 15 different locations in Makarfi Local Government Area of Kaduna State.

Gross Alpha and Beta Radioactivity in Groundwater

Table 1 shows the gross alpha and beta activity concentration of the ground water of the selected locations obtained using alpha only and beta only measurement modes.

The result from the table 1 indicates an average alpha activity concentration in the wells water samples is $12.86 \times 10^{-4} \text{ Bq/L}$. The average beta activity concentration in the wells water sample $17.77 \times 10^{-4} \text{ Bq/L}$. The overall results shows that elevated areas of Alpha are $35.7 \times 10^{-4} \pm 2.64 \times 10^{-4} \text{ Bq/L}$ of Mayere W, and that of Beta are $51.8 \times 10^{-4} \pm 3.27 \times 10^{-4} \text{ Bq/L}$ of Mayere W, $36.4 \times 10^{-4} \pm 3.37 \times 10^{-4} \text{ Bq/L}$ of Gimi W, $34.8 \times 10^{-4} \pm 3.43 \times 10^{-4} \text{ Bq/L}$ of D/Damisa though both alpha activity and beta activity in the study area are far below the practical screening level of radioactivity in drinking water of 0.5 Bq/L for alpha and 1 Bq/L for beta, as recommended by CEC – FAO and WHO.

Table 1 Gross Alpha and Beta Activity Concentration of Groundwater from various locations in Makarfi L G A of Kaduna State

S/N	Location	Name	Activity Concentration	
			Alpha 10^{-4}Bq/L	Beta 10^{-4}Bq/L
1	N11°16'46.5" E008°04'24.6"	Derayi W	6.72±0.262	5.87±0.328
2	N11°14'20.2" E007°48'38.3"	H/Maimashi W	4.94±0.589	4.97±0.736
3	N11°21'32.7" E008°01'44.4"	Kunkumi W	7.21±1.42	20.5±1.74
4	N11°25'13.5" E007°56'31.5"	Gangare W	12.9±1.86	18.9±2.31
5	N11°21'51.8" E007°54'35.4"	Gazara W	24.8±1.36	24.1±1.72
6	N11°14'31.1" E008°01'18.5"	Gubuchi W	12.4±1.55	19.3±1.92
7	N11°19'23.0" E008°00'22.7"	Mavere W	35.7±2.64	51.8±3.27
8	N11°17'48.2" E007°57'30.7"	Durum W	16.1±1.35	28.9±1.66
9	N11°15'00.3" E007°54'16.2"	N/Doya W	6.82±1.04	10.2±1.28
10	N11°21'24.8" E007°53'23.6"	H/Tech W	7.72±0.83	3.87±1.05
11	N11°20'26.1" E008°01'38.4"	Gwanki W	11.9±1.52	11.3±1.89
12	N11°17'14.0" E007°51'43.9"	T/Musa W	5.21±0.69	11.3±0.85
13	N11°19'38.7" E007°56'02.3"	Cimi W	28.5±2.71	36.4±3.37
14	N11°18'08.1" E008°03'07.0"	Tafida W	2.70±0.41	6.93±0.49
15	N11°22'44.9" E007°52'34.4"	Makarfi W	7.24±0.81	7.82±1.01
16	N11°20'37.9" E007°54'38.5"	Tiyari W	8.24±0.99	17.0±1.22
17	N11°20'26.1" E008°01'38.4"	Gwanki W	5.16±0.47	7.14±0.58
18	N11°14'12.3" E007°50'30.8"	D/Damisa W	27.8±2.76	34.8±3.43
19	N11°15'13.5" E007°51'47.2"	K/Kware W	12.5±1.17	16.6±1.45

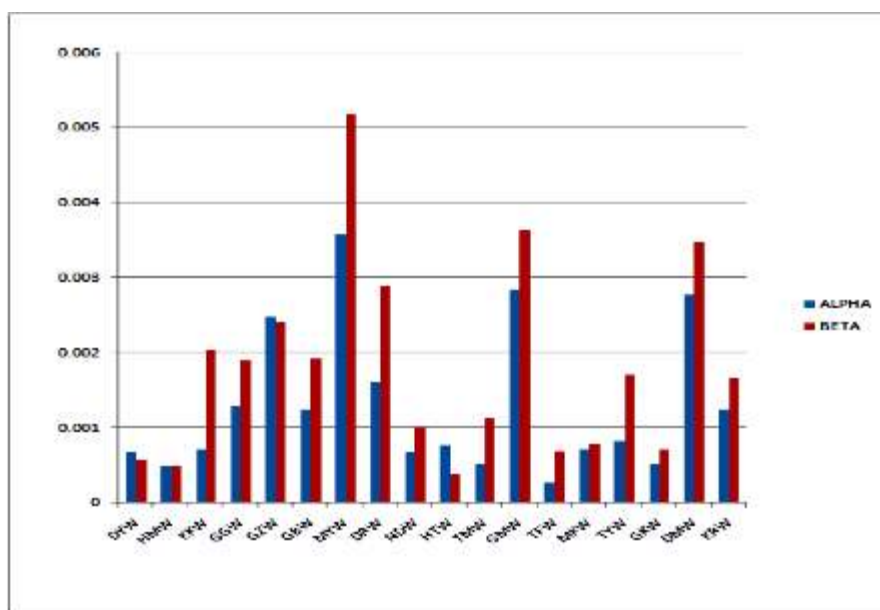


Fig. 2 Bar chart of the alpha and beta activity concentration of well water.

Alpha Activity Concentration

The histogram of the Gross Alpha Activity concentration in the area is presented in figure 3 below. The graph shows the pattern in which the activity concentration is distributed. The result shows the highest frequency distribution of 20 between 0.0005 to 0.0015 Bq/L and the

lowest frequency distribution of 1 between 0.0055 to 0.0065 Bq/L. The distribution is skewed towards the left. This shows a generally low alpha activity in the study area. Then the mean of the distribution is 0.001488 Bq/L and standard deviation is 0.001532.

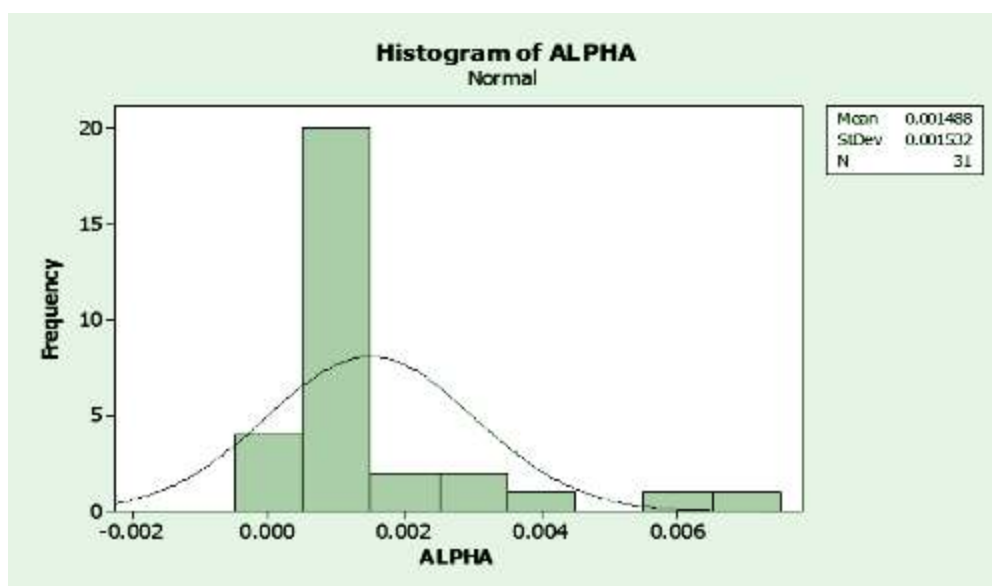


Fig. 3 Histogram of the Alpha Activity Concentration of the Study Area.

Figure 4 shows high alpha activity distribution of 0.005 - 0.0054 Bq/L and above at a narrow area bounded by latitude 11.4° – 11.5° and longitude 7.9° – 8.0° . The area includes Tashan Yari boreholes water samples. The areas bounded by latitude 11.0° – 11.6° and longitude 8.10° – 8.6° have low distribution of 0.0004 - 0.0008 Bq/L. The areas are the Nasarawan Doya boreholes water and Gwanki well water samples.

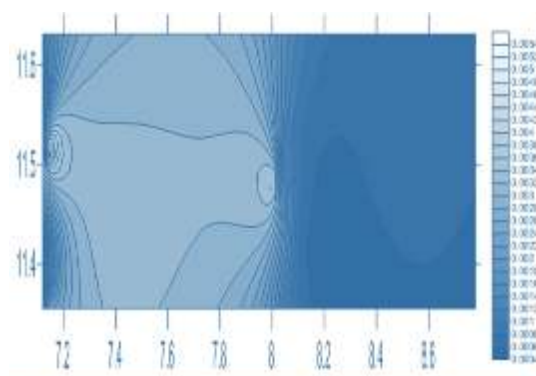


Fig. 4 Contour Plot of Gross Alpha Activity Concentration.

Beta Activity Concentration

The histogram of the Gross Beta Activity Concentration in the study area is presented in figure 5 below. The graph shows the pattern in which the activity concentration is distributed. The result shows the highest frequency

distribution of 7 between 0.001 Bq/L and 0.0015 Bq/L and the lowest frequency distribution of 1 between 0.0025 to 0.003 Bq/L . The distribution is skewed towards the left.

This shows a generally low beta activity in the study area. Then the mean of the distribution is 0.001724 Bq/L and standard deviation is 0.001153.

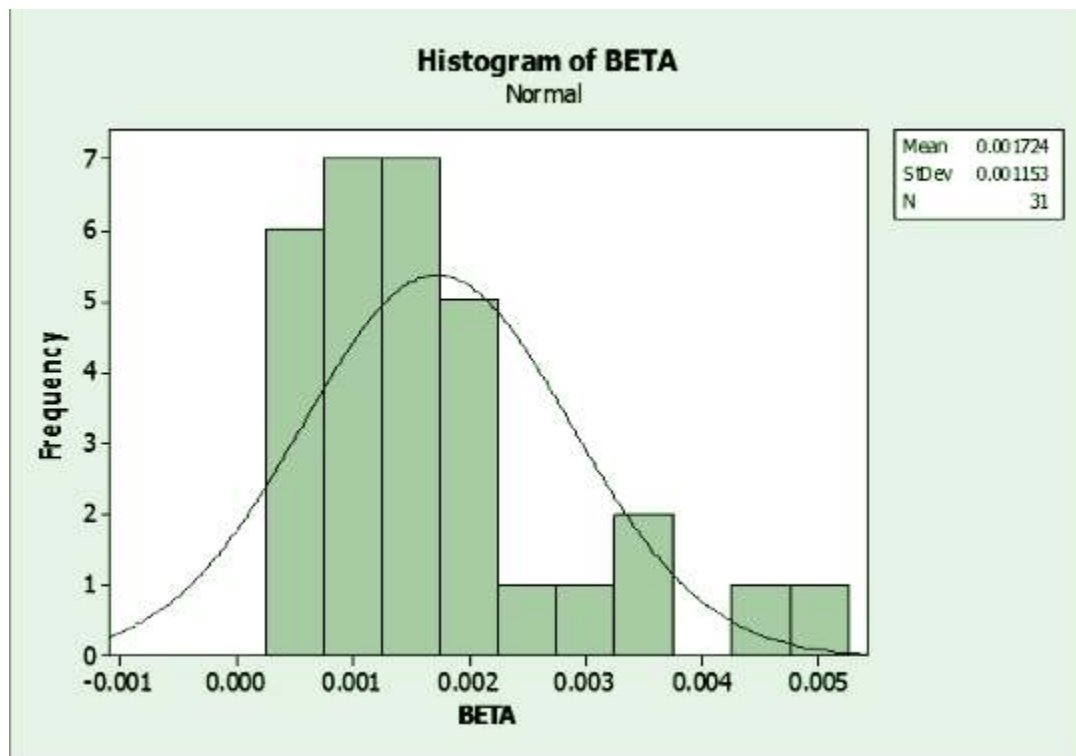


Fig. 5 Histogram of the beta activity concentration of the study area.

Figure 6 shows high beta activity distribution of 0.0052 Bq/L and above at a narrow area bounded by latitude 11.55° and longitude 8.4° . The area include Mayere well water sample. The areas bounded by latitude $11.4^\circ - 11.5^\circ$ and longitude $7.0^\circ - 7.3^\circ$ have low distribution of 0.0006 Bq/L . These well water samples are samples from Makarfi and Hawan Maimashi. Figure 6 is the contour map that shows the level concentration of the beta activity in the study area.

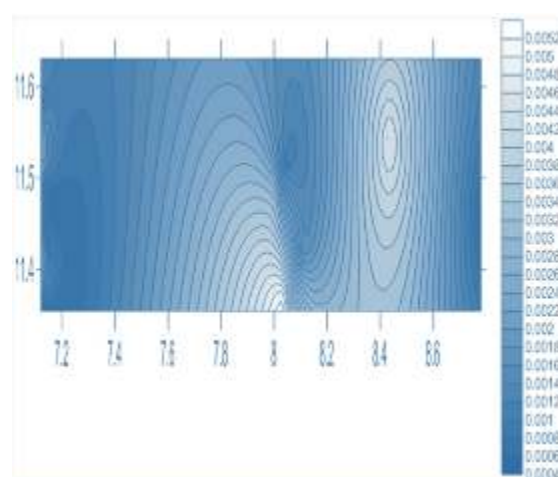


Fig. 6 Contour Plot of Beta Activity Concentration.

Comparison of alpha and beta activity between study area and other areas

From the results in Table 3 the alpha activity in the ground water of Makarfi local government area of Kaduna State Nigeria is about 14% of that in the ground water in Zaria, also the alpha activity in the ground water of Makarfi local government area of Kaduna State Nigeria is about 12.4% of that of River water of Kaduna, the alpha activity in the ground water of Makarfi Local Government Area of Kaduna State Nigeria is about 47% of that of ground water of Gwammaja, while the alpha activity in the ground water of Makarfi Local Government Area of Kaduna state Nigeria is about 54% of the alpha activity of ground water in Katsina, the alpha activity in the ground water of Makarfi Local Government Area of Kaduna State Nigeria is about 0.8% of that in the oil fields environment in Niger delta. The beta activity in ground water of Makarfi Local Government Area is about 0.89% of that of ground water Zaria, The beta activity in

ground water of Makarfi Local Government Area is about 0.68% of that of river water Kaduna. The beta activity in ground water of Makarfi Local Government Area is about 3.25% of that of ground water of Gwammaja, The beta activity in ground water of Makarfi Local Government Area is about 0.11% of that of ground water of Katsina, also the beta activity ground water of Makarfi Local Government Area of Kaduna state is about 0.03% of that of oil fields in Niger delta Nigeria. The results from the alpha and beta activity measurement of ground water in different places are far below the contamination limit of radioactivity in water as set by CEC-FAO and WHO that is 0.5 Bq/L for alpha and 1Bq/L for beta.

Result of alpha and beta activity measurements in ground water samples from other areas; and the results of the measurements from the wells and boreholes of Makarfi local government area as well as the WHO limits of alpha and beta activity in water is shown in the table below.

Table 1 Comparison of alpha and beta activity between study area and other areas.

Area	Alpha	Beta	Source
Ground Water of Zaria	0.021	0.312	Onoja (2004)
River Water of Kaduna	0.025	0.411	Nwoke (2006)
Ground Water of Gwammaja	0.0065	0.086	Tajuddeen (2006)
Ground Water of Katsina	1.19	2.54	Bashir et al (2006)
Oil fields environment Niger Delta	0.35	7.15	Ezekiel et al (2012)
Ground Water of Makarfi	0.0031	0.00274	This Work
WHO limit	1	0.5	Milvy and Cothorn(1990)

Conclusion

The gas free single channel counter MPC 2000 used for this research responded positively to the alpha and beta radioactivity. The counting modes employed gave Alpha efficiencies of 59.12% for Alpha. Similarly the beta efficiency obtained is 44.09% for beta. The Gross Alpha and Beta Activity concentrations in the water in the study area were found to range from, the average alpha

activity concentration in the wells water samples is 12.87×10^{-4} Bq/L. The average beta activity concentration in the wells water sample 17.77×10^{-4} Bq/L

It can be concluded that in comparatively high alpha and beta activity in wells water sample may be as a result of relationship between the water in the wells and total dissolved solids in the well due to the farming activity in the area where used of fertilizer.

This indicates the elevated areas of Alpha are $35.7 \times 10^{-4} \pm 2.64 \times 10^{-4} \text{ Bq/L}$, and that of Beta are $51.8 \times 10^{-4} \pm 3.27 \times 10^{-4} \text{ Bq/L}$ of Mayere W respectively, $36.4 \times 10^{-4} \pm 3.37 \times 10^{-4} \text{ Bq/L}$ of Gimi W, $34.8 \times 10^{-4} \pm 3.43 \times 10^{-4} \text{ Bq/L}$ of D/Damisa though both alpha activity and beta activity in the study area are far below the practical screening level of radioactivity in drinking water of 0.5 Bq/L for alpha and 1 Bq/L for beta, set by the International Commission for Radiological Protection (ICRP, 1991). The United States Environmental Protection Agency (USEPA 2000) and the World Health Organization (WHO 2003).

References

- Milvy, P. and Conthern, C. R. (1990). Scientific Background for Development of Regulations for radionuclides in Drinking water. Lewis Publishers Washington DC: 1 – 14.
- MPC2000 Desktop Gross Alfa/Beta Counter. Retrieved 2nd August, 2019 from
- Webb, P. K. (2016). Recent research on the Geology between Zaria and Kaduna. Savannah Vol.1.No.2
- Knoll G.F. (2000). Radiation Detection and Measurement, 4th edition, John and Willey and Sons Toronto, 161, 202 and 772
- Onoja, R. A., Akpa, T. C., Malam, S. P. and Ibeanu, I. G. E. (2004). Characteristics of the gross alpha/beta counter in the center for energy research and training. Zaria. Nig. J. Phys., 13-18.
- Nwoke, J. E. (2006). A survey of gross alpha and beta activity concentrations in groundwater from River Kaduna Nigeria. Radiation. Unpublished MSc thesis.
- Tajudeen H. V. (2006). Survey of Radioactivity in Wells and Boreholes from Gwammaja Area of Kano City. Unpublished MSc. thesis, Ahmadu Bello University, Zaria,
- Bashir Gide (2006) Muhammad, B. G., Jaafar, M. S. and Akpa, T. C. (2010). A survey of gross alpha and beta activity concentrations in groundwater from Katsina area of Northern Nigeria. Radiation. Protection. Dosimetry 142; 127-133.
- Ezekiel, A., Gregory, A. and Chadumoren, Y. (2012). Determination of Gross and Activity Concentration and Estimation of Adults and Infants Dose Intake in Surface and Ground Water of Ten Oil Fields Environment in Western Niger Delta of Nigeria. Journal of Applied Sciences and Environmental Management.
- International Commission on Radioactive Protection (ICRP). (1991) 1990 Recommendations of the International Commission on Radiological Protection. Publication 60. Annals of ICRP 21.
- United State Environmental and protection Agency (USEPA). (2000). National Primary Drinking Water Regulations. United State Environmental Protection Agency Report.
- World Health Organization (WHO). (2003). Guidelines for drinking water quality, Geneva, Report no: WHO/SDE/WSH 03.04.

Determination of the Concentration of Natural Radioactive Elements Present in Canned Tomato, Fish and Powdered Milk in Zaria, Nigeria

Gazara, A. B.¹, Yusuf, U.² and Abdulhadi, D.³

^{1,3}Department of Science Laboratory Technology, Nuhu Bamalli Polytechnic Zaria, Nigeria

²Federal University Gusau, Nigeria.

Corresponding author's email: abgazara@gmail.com

ABSTRACT

The concentration of natural radioactive element in three (3) samples of food packaging materials which are: canned tomato, canned fish and canned milk were determined using Sodium Iodide Detector (NaI). The samples were collected from different places in Zaria metropolis and were taken to centre for Energy Research and Training, Ahmadu Bello University, Zaria, for analysis. The activity concentration due to natural occurring radionuclide's of ^{40}K , ^{226}Ra and ^{232}Th for canned fish and canned tomato which are ^{40}K - 0.0187 Bq/Kg, ^{226}Ra - 0.028 Bq/Kg, ^{232}Th - 5.65 Bq/Kg¹ and ^{40}K - 0.0643 Bq/Kg ^{226}Ra - 0.005 Bq/Kg ^{232}Th - BDL (below detection limit) Bq/Kg were all below standard limit respectively. In the case of powdered milk, the activity concentration of natural occurring radioactive materials was found to be very high above the world average annual committed effective dose of 100.0 BqKg⁻¹ for ingestion of natural radionuclide's provided by UNSCEAR 2000 report and the activity concentration due to natural occurring radionuclide's for powdered milk was found to be 117.123 Bq/Kg, 12.46 Bq/Kg and 6.2910 Bq/Kg for ^{40}K , ^{226}Ra and ^{232}Th respectively. The results provides baseline values which may be useful in establishing rules and regulations relating to radiation protections as well as developing standards and guidelines for the use of canned food to the appropriate authorities.

Keywords: Sodium Iodide (NaI) Detector, Activity Concentration, Radionuclides, Canned Food, Packaging.

Introduction

Since the beginning of the atomic energy industry over 50 years ago, there has been an excellent record of safety in packaging food using nuclear materials. It is estimated that over four million packages containing radioactive material are transported from one country to another.

The use of radioactive materials sometimes gives rise to a lack of confidence in the safety standards in the processed food, with words such as radioactive, radioactivity, atomic, nuclear wastes etc. generating a lot of concern and fear in the minds of many people. Similarly, the use of atomic bomb, nuclear power plant accidents, and exaggerated hazards of cleanup at former nuclear weapons facilities have also created uneasiness in the

minds of the public. Modern society uses radioactive material to preserve foods, generate electric power, and for research, manufacturing, and a wide range of industries processes. In addition these materials are indispensable for medical diagnosing or therapy. These materials and any waste products are regularly transported from the industries to the final consumers which surely contain a certain concentration of radioactive materials which decay spontaneously into more stable forms emitting alpha, beta and gamma radioactive during the process.

In addition plants that are close to mining sites, nuclear power plants or industries that make use of radioactive materials also contain some concentration of radioactive materials (Jibrin et al 2007 and Zhuang et al 2009). These

radioactive materials get into our food not only through the process of packaging but also right from the planting activities through the soil, action of photosynthesis through the atmosphere that contains dose of radioactive materials, elements. As a result, the contaminated farm products that contains significance or small amount of radioactive element will be present during the food packaging process, as a result it will be observed that the concentration of radioactive elements present in that particular food packaging will be very high, i.e. in high concentration level that exceed the standard level estimated by World Health Organization (WHO), Food and Agriculture Organization (FAO) and International Atomic Energy Agency (IAEA) (Safety series 1996). Furthermore, the department of transportation act of 1966 does have a regulatory responsibility for safety in the transportation of all hazardous materials, including radioactive materials like food packaging materials. It also comprises of shipments by all modes of transportation in interstate or foreign commerce.

Further research on radioactivity and heavy metal concentration in foods can be seen in (Hassan et al 2017; Hernandez et al 2004; Jibiri and Okusanya 2008; McDonald 1999).

The paper is aimed at determining the concentration of natural radioactive elements present in Canned Tomato, Fish and Powdered Milk, from Zaria, Nigeria.

Materials

The material used for this research work is the Sodium Iodide (NaI) detector.

Working principle of NaI detector

The major principle for sensing and measuring radiations in survey instruments is based on the ionizations radiation produced when interacting in a gas filled detector. As described radiation passing through matter create ion pairs in a detector, these ions pairs are collected to form an electrical signal, either a current or a pulse, is then used to register the presence and amount of radiation. There are a number of different types of radiation detectors; each operating on this basic principle, but designed for specific purposes. Figure 1 presents a schematic diagram of the Sodium Iodide (NaI) detector used for this research.

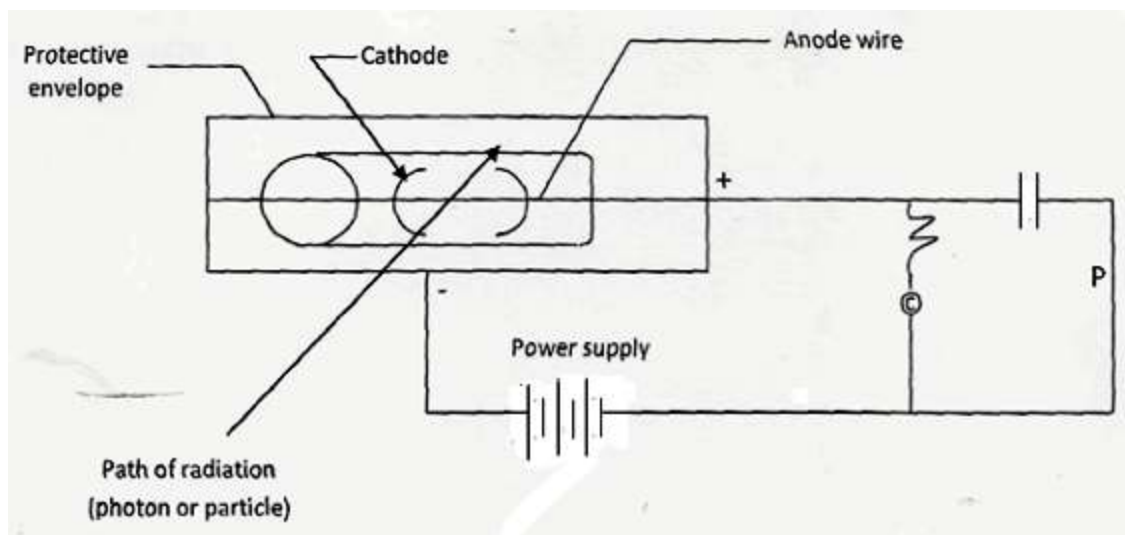


Fig. 1 Diagram of the Sodium Iodide (NaI) detector

The ionization produced in the gas converts neutral molecules to positive ions and electrons, within the sensitive volume. This volume is contained between charged electrodes, one positive, and the other negative. The charged species are collected at the electrodes of opposite sign. Either a photon (X or gamma ray), producing electrons along its path, or a particle (alpha or beta) producing secondary electrons, will create ions that will travel to the electrodes and be collected. A sufficient potential must be applied across the electrodes to prevent ion-recombination and make collection possible. As the ions are collected, a current will flow. This will be measured on a sensitive measuring circuit "c" shown in the diagram above. Alternatively, the current may be measured as a pulse by a pulse counter "p" from the collection of each primary particle.

Methods

Sample collection

The three (3) samples collected were canned fish, tomatoes and powdered milk. The samples were taken for analysis at Centre for energy research and training Ahmad Bello University Zaria for analysis.

Sample preparation

The samples (food packaging materials) are being dried properly at room (ambient) temperature (37° c) and crushed to fine powder so as to obtain uniformly homogeneous sample matrix. The samples are then filled into plastic

container of known weight. The weight of samples and the container is then measured using the weighing balance. The inner portion of the lid of the plastic container is being coated with Vaseline and then" the container sealed with the candle wax first followed by sealing with the masking tape (this is to trap the gaseous radio-nuclide radon (Rn) within the content and keep for circular equilibrium for a period of 24 days before the counting takes place). The weight of the sample is obtained by subtracting the weight of the empty container.

The samples were identified and the date of sealing is recorded to avoid sample loss. The sample is then kept for a period of 24 days at least for equilibration (the period for which all the radio nuclide is expected to have formed a saturated mixture) after which the sample can be counted for the gamma spectroscopy using the doped sodium iodide with thallium as detector to determine the low background level of naturally occurring radioactive materials (NORM) which are daughters of uranium (^{238}U), Thorium (^{232}Th) and potassium (^{40}K) from the energy-peak analysis, area under peak the that tells the level of NORMS can be evaluated.

Result and Discussion

The activity concentration for ^{226}Ra , ^{40}K and ^{232}Th respectively in three (3) different canned food materials (powdered milk, canned fish and canned tomato) was detected and presented in the table below.

Table 1 Activity concentration for ^{226}Ra , ^{40}K and ^{232}Th in canned powdered milk, fish and tomato respectively.

S/N	Sample	K-40	Error ±	K-40	Error ±	Ra226	Error ±	Ra226	Error ±	Th232	Error ±	Th-82	Error ±
	ID	CPS	CPS	Bq/kg	Bq/kg	CPS	CPS	Bq/kg	Bq/kg	CPS	CPS	Bq/kg	Bq/kg
1	Powdered milk	0.0753	0.0055	117.123	8.5268	0.0108	0.0029	12.467	3.356	0.0055	2.07	6.2910	0.240
2	Canned fish	0.0187	0.0046	0.0046	0.0186	0.0046	0.275	0.053	0.053	0.028	5.305	0.0057	1.72
3	Canned tomato	0.1286	0.0065	0.065	0.0643	0.0643	0.0032	0.0109	0.0032	0.005	BDL	BDL	BDL

CPS = Count per second

BDL = Below detection limit

Discussion

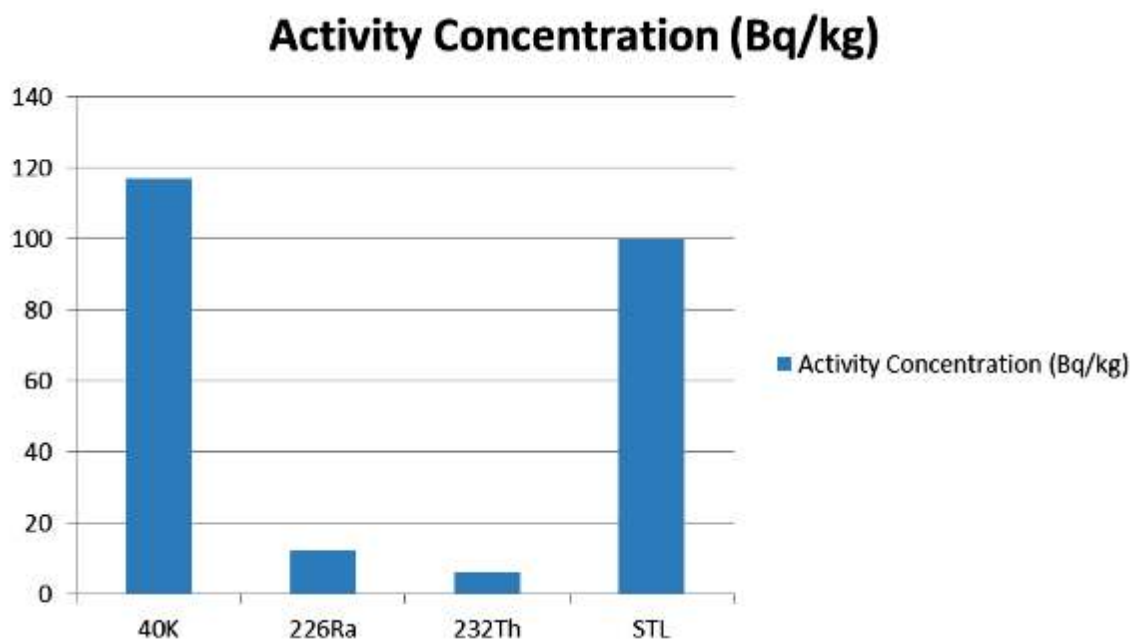
The activity concentration of canned food (powered milk) in (Bq/kg) ranges from 117.123, 12.467 and 6.2910 for ^{40}K , ^{226}Ra , and ^{232}Th respectively in powered milk the highest activity concentration of ^{40}K was recorded much among other radioactive materials. For

the activity concentration of ^{226}Ra and ^{232}Th have the lowest activity concentration of radioactivity. The activity concentration of the canned powdered milk is presented in table below together with the standard recommended limit reported by WHO, IAEA, ICRP etc.

Table 2 Activity concentrations and average annual committed effective dose limit of ^{40}K , ^{226}Ra , and ^{232}Th in the canned powdered milk.

S/N	Radioactive element	Powdered milk (Bq/kg)
1	^{40}K	117.1230
2	^{226}Ra	12.4670
3	^{232}Th	6.2910
4	STL	100.0000

The values were presented in the bar chart below.



The activity concentration of radioactive materials in canned powdered milk has value of radioactivity that is detectable and above the world standard value for baby food intake; therefore milk would be hazardous when used. The present of high activity of natural radioactive materials in powdered milk would be as a result of food contact material as the

food has direct contact with the food packaging materials that it can also be a source of radiation and chemical food contamination. The activity concentration of ^{40}K is high compared to ^{226}Ra and ^{232}Th due to it abundant in all part of organic constituents and in the atmosphere as natural radioactive material are

found everywhere in the atmosphere.

Canned fish

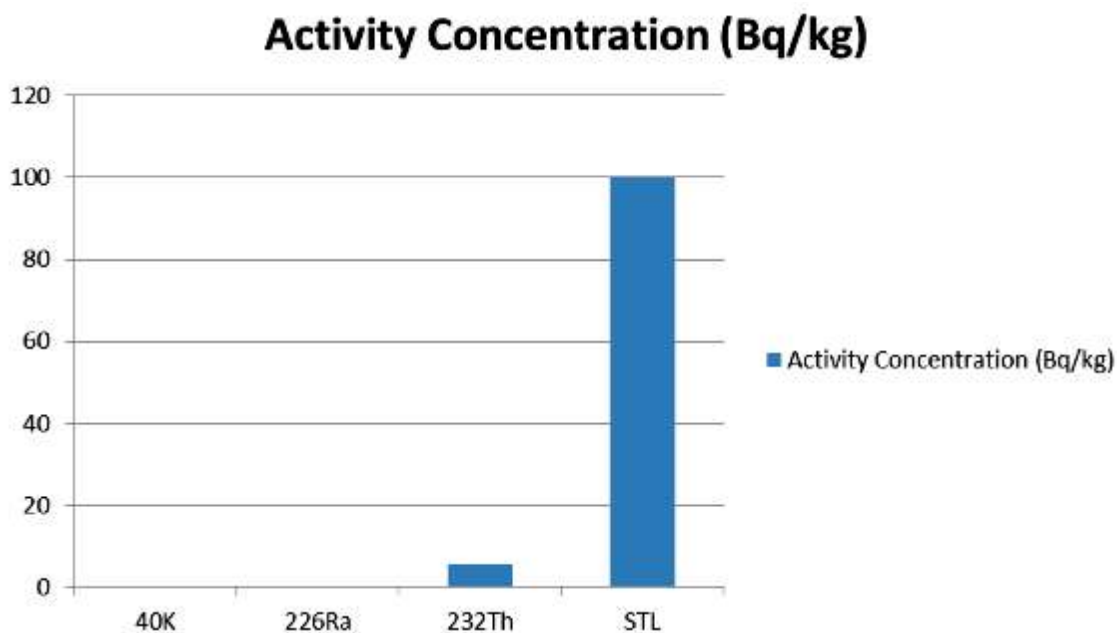
From the result obtained it shows that the activity concentration of natural occurring radioactive materials has low activity

concentrations for canned fish in ^{40}K and ^{226}Ra and slightly high in ^{232}Th . The activity concentration of canned fish is presented in the table below together with the standard recommended limit represented by WHO, FAO and ICRP.

Table 3 Activity concentration and average annual committed effective dose limit of ^{40}K , ^{226}Ra and ^{232}Th in canned fish.

S/N	Radioactive element	Canned fish (Bq/kg)
1	^{40}K	0.0186
2	^{226}Ra	0.028
3	^{232}Th	5.65
4	STL	100.00

The values were presented in the bar chart below



The low activity concentration may be as a result of good quality control during processing and packaging of the canned fish, therefore taking canned fish may not have any effects on human body.

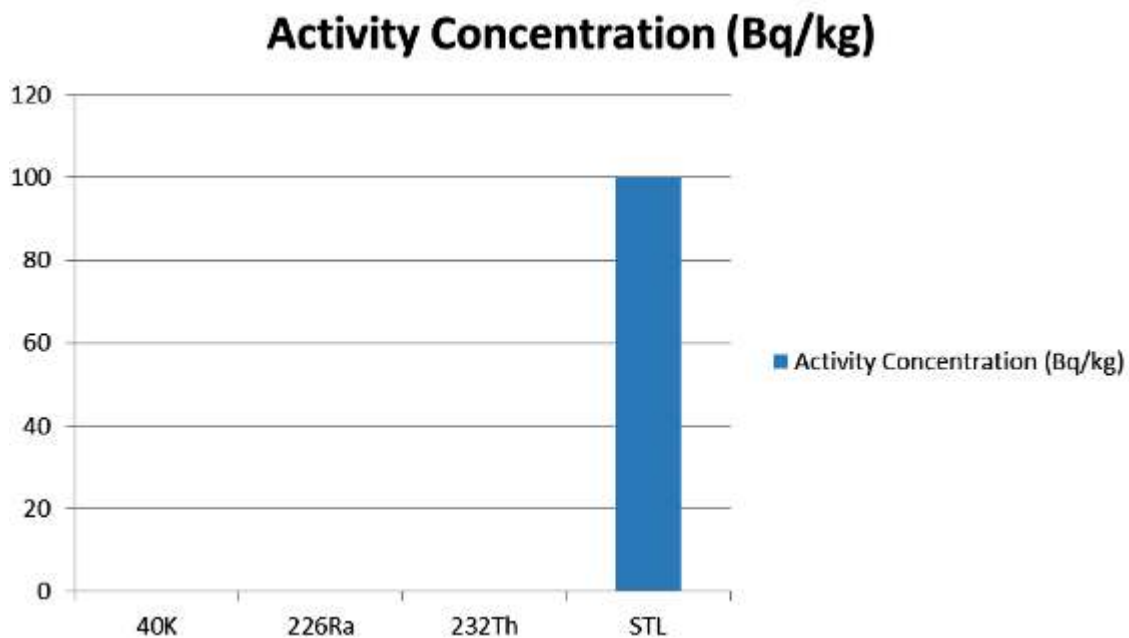
Canned tomato

The activity concentrations of canned tomato in (Bq/kg) are 0.0643, 0.005 and BDL in ^{40}K , ^{226}Ra and ^{232}Th respectively. The value obtained was compared with the standard value recommended by WHO, FOA and IAEA and found to be below the standard value.

Table 4 Activity concentration and average annual committed effective dose limit of ^{40}K , ^{226}Ra and ^{232}Th in the canned tomato.

S/N	Radioactive element	Canned tomato (Bq/kg)
1	^{40}K	0.0643
2	^{226}Ra	0.005
3	^{232}Th	BDL
4	STL	100.00

The values were presented in the bar chart below.



The activity concentration of natural occurring radioactive materials in canned tomato was found to very low compared to other two sample canned fish and powdered milk, this may also be as a result of good quality control during the packaging and processing of the canned tomato. As such it is safe and recommended for human consumption.

Conclusion

Natural radioactivity level of some canned food commonly used in Zaria metropolis were investigated using sodium iodide detector at the centre of energy research and training

Ahmadu Bello University, Zaria. The result obtained from these measurements showed that the activity concentration for ^{40}K , ^{226}Ra and ^{232}Th are low in canned tomato and canned fish compared with that of powdered milk. The ^{40}K which is present in all the three samples is still high in powdered milk, 117.123 Bq/kg compared to that in canned fish and canned tomato which are 0.0186 Bq/kg and 0.0463 Bq/kg respectively. Thus the radioactivity level of ^{40}K in powdered milk may be very hazardous to children and less hazardous to adult human, while canned fish and canned tomato are safe for consumption.

On the other hand, the high activity concentration of ^{40}K recorded in powdered milk can significantly aid in its therapeutic purpose in treating high blood pressure since patients with high blood pressure have low concentration of potassium in their blood stream.

References

- Jibrin, N. N., Farai, I. P. and Alausa, S. K. (2007). Estimation of annual effective dose due to natural radioactive elements in ingestion of foodstuffs in tin mining area of Jos-Plateau, Nigeria. *Journal of Environmental Radioactivity*, 94; 31-40
- Zhuang, P. B, McBride, m., Xia, H., Li, N. and Li, Z. (2009). Health risk from heavy metals via consumption of food crops in the vicinity of Daboshan mine, South China. *Science Total Environ*, 407; 1551-1561.
- Safety series No 115 (1996) International basic standard for radiation protection
- Hassan, A. A., Nada, F. K, Mahmood, S. K. and Ali, A. R. (2017). Hazard indices and age group parameters of powdered milk consumed in Iraq. *Higher Education Research*, 2 (5); 117-122
- Hernandez, F., Hernandez-Armas, J., Catalan, A., Fernandez-Aldecoa, J. C. and Landeras, M. I. (2004). Activity concentrations and mean annual effective doses of foodstuffs on the island of Tenerife, Spain. *Radiat Prot Dosimetry*, 111; 205-210.
- Jibiri, N. and Okusanya, A. (2008). Radionuclides contents in food products from domestic and imported sources in Nigeria. *Journal of radiological protection*, 28; 405-413
- McDonald, P. Jackson, D., Leonard, D. R. P. and McKay, K. (1999). An assessment of ^{210}Pb and ^{210}Po terrestrial foodstuffs from regions of potential technological advancement in England and Wales. *Journal of Environmental Radioactivity*, 43; 15-29.
- United National Scientific Committee on the effect of Atomic Radiation (UNSCEAR), (2000). Exposure from natural sources of radiation, United Nation New York; 81-86.
- World Health Organization (WHO). (1980). Wholesomeness of Irradiated Food. (Summary of the final draft of a joint FAO/IAEA/WHO expert committee.) Geneva: World Health Organization.
- World Health Organization (WHO). (1994). Safety and Nutritional Adequacy of Irradiated Food. Geneva: World Health Organization.

Time Effect On Temperature – Concentration Ratio on Electricity Generation using Saline Solar Pond

Ogbonda, C.

Department Of Physics, Ignatius Ajuru University of Education Rumuolumeni,
Port Harcourt, Rivers State

Corresponding author's email: clement.ogbonda@iaue.edu.ng

ABSTRACT

This study presents an experimental investigation on the potential of using a saline solar pond for the generation of electricity in Nigeria. A saline solar pond model is presented to simulate and optimize solar energy under the Nigerian climatic conditions to electric power. It was found that the solar pond can generate electricity to the power of 2kwh depending on the size of the pond, and other physical and chemical characteristics of the solar pond. It was observed that as time changes, the temperature of the solar pond changes, the heat generated in the solar pond to generator also changes. This change in temperature affects the salt concentration of the pond, hence a density gradient of water is established. This would produce a temperature gradient and heat accumulation in the lower depth of pond. The temperature may reach up to 70°C. Thus, the increase of thermal power produced from solar pond will increase electricity production.

Keywords: Saline Solar Pond; Time; Temperature; Thermoelectric; Electricity Generation.

Introduction

Nigeria is facing serious energy crisis at the moment. The natural gas reservoirs of the country are fast depleting due the flare and vandalisation, with the passage of time, the gap

between electricity consumption need and supply of the country is increasing every year as shown in the figure 1.

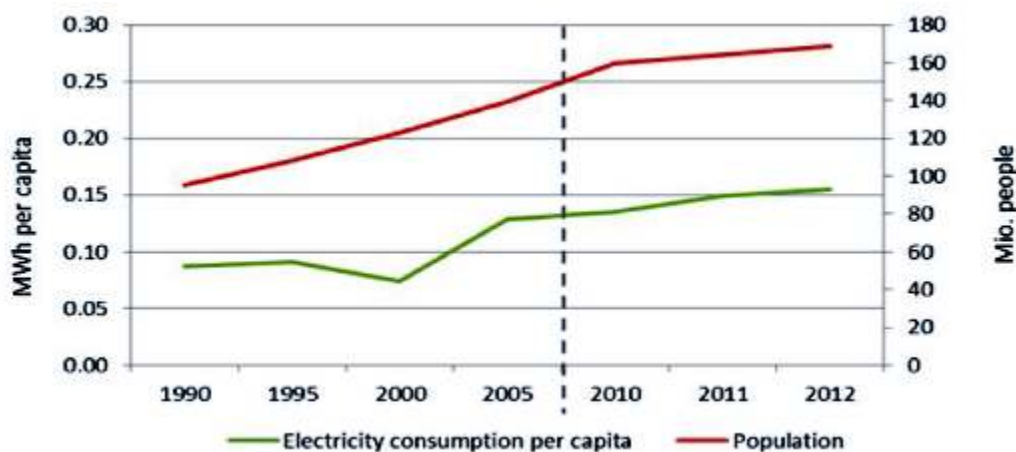


Fig.1 Rise In gap between Electricity Demand and the Supply in Nigeria (Nigerian Energy Support Programme 2015).

The alternative energy which is solar energy, such as Solar PV cells at large scale (~MW), are not yet competitive in the market due to their low efficiency and high cost. So there is a dire need for a reliable, pollution free and cost effective solution to the present energy crisis of the country. Solar thermal energy is one of the main source of clean energy which is abundantly available especially in country like Nigeria. The country receives about 22.06 MJ/m²/day and 15.23 MJ/m²/day of solar radiations on average (Adekunle et al 2015). One efficient way to trap this solar energy is solar pond technology. This solar pond technology, as compared with other methods of using solar thermal energy for power generation, is more efficient especially for the utilities where direct thermal energy is required such as for heating / drying purposes in many domestic and industrial processes. In all these processes where industrial need is of only the thermal energy and not the electricity, solar ponds can cheaply fulfill the industrial demand without the need of expensive conversion of solar energy into electricity generation. Thus increased efficiency in the use of solar energy can be ensured by skipping the inefficient step of first converting solar thermal energy into useful electricity and then using the expensive electricity, to produce hot water or hot air and cold air, for many domestic and industrial processes.

Ranjan et al.(2014) observed that the capacity of heat energy in solar ponds storage zone

available at about 50–100°C to power

desalination units even during cloudy days and off-sunshine hours, in their study of active solar distillation systems integrated with solar Ponds.

Bozkurt et al. (2012) studied heat storage performance investigation of integrated solar pond and collector system. Experimental studies were performed using 1, 2, 3 and 4 collectors integrated with solar pond. The

integrated solar pond efficiencies were determined experimentally and theoretically according to the number of collectors. Investigators have reported numerically, the prediction of the temperature and salinity profiles in the solar pond, as well as predict the stability of the solar ponds. A good report of this is given by Bardran et al (1995). Most of these investigations make use of a one dimensional model and use either finite elements or finite difference methods to solve such models (Panahi et al 1983).

Okujagu (1996) discussed the characteristic and stability of shallow saline pond. In this study the concentration of the pond was found to increase with depth, causing salt diffusion in opposite direction.

Alagao (1996) has proposed a one-dimensional mode to stimulate a closed cycle solar pond, by using both analytical and finite difference explicit models with a salt diffusivity varying linearly with the temperature.

Bechtel (1975) investigated a solar pond power plant using F-11 as the working fluid when the pond is 1 km². It was concluded that the cost of the solar pond power plant is five times larger than that of a conventional power plant of equal capacity.

Abbey et al (1998) modeled the effect of chemical reaction and heat transfer on characteristics of a rectangular solar pond. The stability of a solar pond depends on parameter as the Soret, Dufour, heat transfer and chemical reaction.

Xe *et al.* (1987) reported a methodology for the prediction of internal stability in solar ponds. Most works conducted on solar pond electrical power generation systems are associated with the analysis of the system on a certain cycle and working fluid. The most common cycle used is the Rankin cycle-base heat engine operating between the high and low temperatures of the pond (Tabor and Doron 1987).

Ogbonda (2015) presented a Numerical simulation of transient effect of the characteristics of a solar pond. Numerical

simulation were carried out, The model shows that time variation which resulted in the variation of solar intensity reaching the earth's surface has a tremendous effect on the characteristics parameter of the pond. The study shows that temperature and concentration increase with depth for a given time value and other parameters such as P_r , S_r , D_r , $N^2 Q_w$ and j_w respectively. The numerical computation reveals that the stability of the solar pond under transient conditions depends on parameters as Prandtl (p_r), number, Schmidt (S_c) numbers, the heat loss N^2 and the chemical reaction K_r^2 .

This study presents an investigation on the time effect on temperature – concentration ratio on electricity generation using saline solar pond.

Solar Pond

A solar pond is an artificial large body of water that collects and stores solar thermal energy. It is about 1 to 3 metres deep, and the bottom of the pond is usually painted black. The solar radiation landing on the surface of the pond penetrates the liquid and falls on the blackened bottom which is thereby heated. In the normal case, if the liquid is homogeneous, convection currents will be set up and the heated liquid, being lighter, will travel towards the surface and dissipate its heat to the atmosphere. In a solar pond these convection currents are prevented by having a density gradient of salt, the solution's density being highest at the bottom and lowest at the top. Typically a pond is composed of three zones as shown in Figure 2. The first zone is the Upper Convective Zone (UCZ), which is cold, close to the ambient temperature, and has low salt concentration (almost fresh water). The thickness of this surface layer varies from 0.1 to 0.4 m. The second zone is the Non-Convective Zone (NCZ) (or insulation layer), where the salt density increases with depth. The thickness of the NCZ ranges from 0.6 to 1.5 m. Hot water in the NCZ cannot rise because it has a greater salt content than the water above and is therefore denser. Similarly, cool water cannot fall because the water below it has a higher salt

content, therefore a greater density. Therefore, convection motions are hindered and heat transfer from the third hot zone, the Lower Convective Zone (LCZ) (or storage layer) to the cold UCZ can only happen through conduction. Given the fairly low conductivity of water, the NCZ layer acts as a transparent insulator, permitting solar radiation to be trapped in the hot bottom layer, from which useful heat is withdrawn. LCZ thickness depends on the temperature and the amount of the thermal energy to be stored (Angeli and Leonardi 2004; El-Sebaai et al 2011)

In this work a solar pond was filled with salty water of different concentrations to form three distinct zones. The first convective zone with a minimum salt concentration is called the upper convective zone (UCZ) and is situated on the top of the pond where the incident solar radiation is partially absorbed and the rest is transmitted to the zone below. The second convective zone is situated at the bottom of the solar pond and called lower convective zone (LCZ), which has a high temperature, and a maximum salt concentration. In this zone, solar radiation is absorbed and transformed to thermal energy. Therefore, it is an absorption and storage zone. These two zones are characterized by uniform concentration and separated by the important gradient zone called the non-convective zone which functions as a transparent insulator, permitting solar radiation to be trapped and stored in the bottom of the solar pond. In this zone, the salt concentration and the temperature increase with depth.

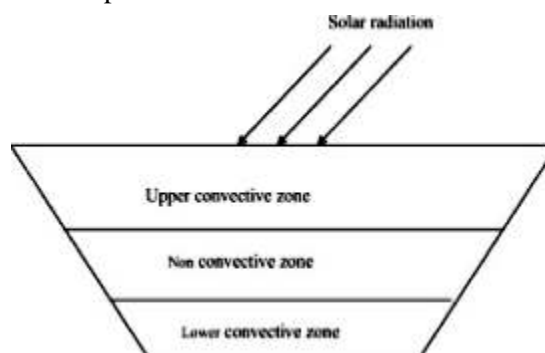


Fig. 2 Schematic of Solar Pond

Thus, when the solar energy is incident upon the solar pond, it is trapped in the hot bottom layers, called lower convective zone (LCZ) of the pond. To achieve heavier (increased density) water in the bottom of the pond, several organic or non organic material can be used. However, abundantly available table salt is more often added to LCZ (bottom most layers) of the pond to increase the density of water at the bottom. The salt concentration is gradually decreased in the preceding upper layers. The topmost upper layer, known as upper convective zone (UCZ) has the least concentration of salt to achieve a perfect solar pond containing several intermediate layers, known as non convective zone (NCZ) of water with gradually increasing density from the top to the bottom of the pond. The non convective zone of the solar pond is also the region when the convective force and current are zero. The surface of upper convective zone of the pond is the region which is usually exposed to the radiant energy from the sun.

It has been shown that solar energy from the sun is transmitted in the form of electromagnetic waves with distinct frequency and wave length. The amount of radiance energy from the sun falling on earth's surface per unit area per unit time is the radiant intensity. This according to Stefan depends on the fourth power of the absolute temperature

$$I \propto T^4$$

$$I = \sigma T^4 \quad (1)$$

Where σ is the Stefan Boltzmann constant

Experimental and theoretical studies in the literature, particularly those of Okujagu (1996) and Abbey et al (1998) have shown that the amount of energy which a solar pond can generate mostly depend on the temperature and concentration diffusion or transfer mechanism of the pond.

Experimentation

Thermoelectric Generator in remote areas, where the electric grid is not available, and the sun shines year round, combined power generation modules based on the small scale solar pond. Thermo Electric Generator is one

of the viable candidates for providing daily electricity demand in such areas. A Thermo Electric Generator has the advantage that it can operate from a low grade heat source such as waste heat energy. It is also attractive as a means of converting solar energy into electricity. The schematic diagram of the Thermo Electric Generator is shown in Figure 3. It consists of two dissimilar materials, n-type and p-type semiconductors, connected electrically in series and thermally in parallel. Heat is supplied at hot side at temperature Q_{qs} while the other end is maintained at a lower temperature Q_{cs} by a heat sink. As a result of the temperature difference, current (I) flow through an external load resistance R_{ex} . The power output depends on the temperature difference, the properties of the semiconductor materials and the external load resistance. Each thermoelectric element is assumed to be insulated, both electrically and thermally, from its surroundings, except at the junction to hot/cold reservoir contacts. The internal irreversibility for the Thermo Electric Generator is caused by Joule electrical resistive loss and heat conduction loss through the semiconductors between the hot and cold junctions. The Joule losses generate internal heat equal to $I^2 R_i$ where I (A) is electric current generated by thermoelectric generator, R_i () is total internal electrical resistance of the thermoelectric generator. Conduction heat loss is $k_{teg} (Q_{qs} - Q_{cs})$ where, k_{teg} [W/m.K] is thermal conductivity of thermoelectric generator. The external irreversibility is caused by finite rate heat transfers at the source and the sink (Randeep et al 2010; Rowe 1995). For a Thermo Electric Generator composed of n thermoelectric generating elements as shown in Figure 4, the following parameters can be calculated:

Rate of heat supply

$$H_{qs}^i = aIQ_{qs} - 0.5I^2R_i + K_{teg} (Q_{qs} - Q_{cs}) \quad (2)$$

Rate of removal

$$H_{cs}^i = aIQ_{cs} - 0.5I^2R_i + K_{teg} (Q_{qs} - Q_{cs}) \quad (3)$$

Output voltage

$$\text{Voltage} = a(Q_{qs} - Q_{cs}) - I^2R_i \quad (4)$$

Useful output voltage power

$$P = aI (Q_{qs} - Q_{cs}) - I^2 R_I \quad (5)$$

In above equations, $[V/K]$ is Seebeck coefficient for the thermocouple elements

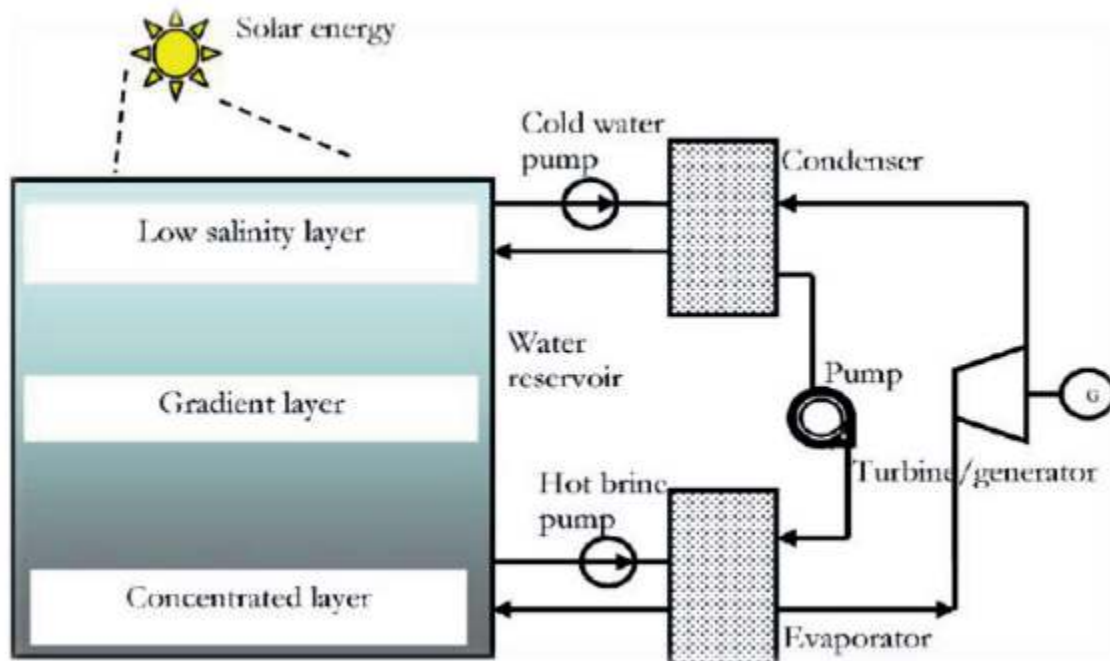


Fig. 3. The principle of a solar pond power plant (Tchanche et al 2011).

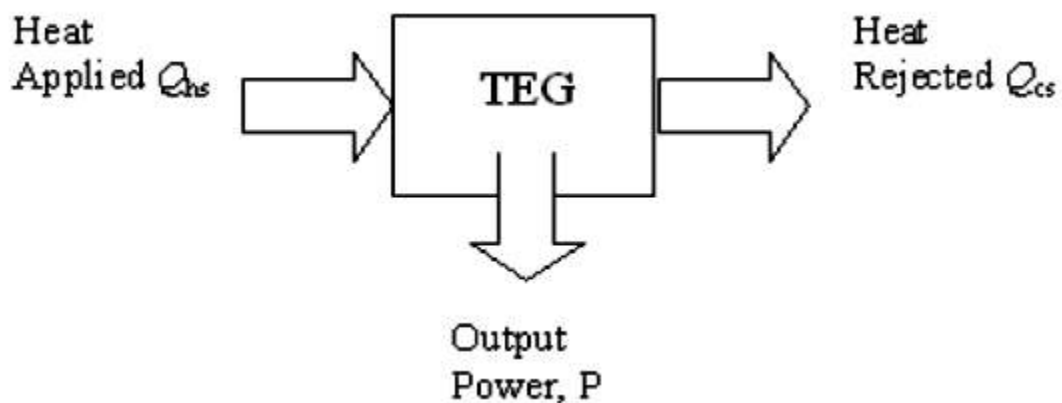


Fig.4 Block diagram of solar pond thermoelectric generator

Results and Discussions

This section present an experimental result of Time Effect on Temperature – Concentration ratio on electricity generation using Saline Solar Pond.

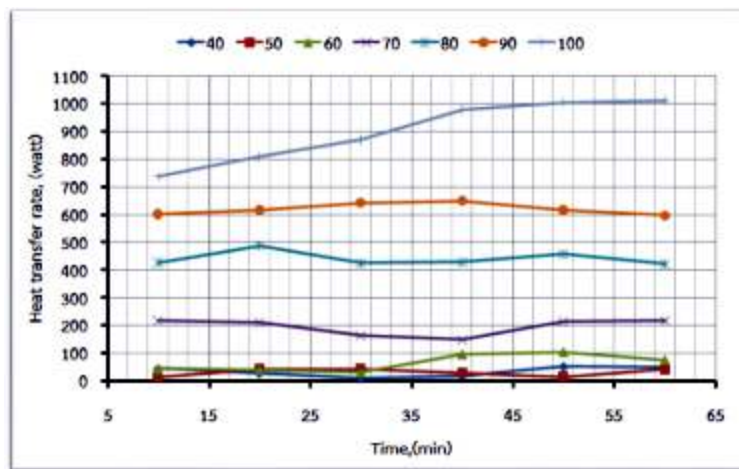


Fig.5. The distribution of temperature on the length of the heat pipe

Figure 5 showed the distribution of temperature along the steel pipe. To study its performance in transferring the heat, the pipe was divided into three parts; the evaporation area, the heat insulation area, and the condensation area with 0.40, 0.80, and 0.08 m. in diameter respectively. In the experiment, the flowing rate of cooling water was controlled at $1.34 \times 10^{-3} \text{ Kg/s}$. The temperature of cooling water at the condensation area was 10°C . The results showed that as time increases, the temperature at the evaporation area increases, heat transfer of the heat pipe increased accordingly as the evaporation area received much heat hence making the working fluid

inside the steel pipe change its status into steam moving to transfer more heat at the condensation area. When the temperature at the evaporation area increases, the temperature at the condensation area was similar to that of the evaporation area. When the temperature at the evaporation area was over 70°C , the rate of heat transfer decreased when compared to the increased temperature in the evaporation area. This was due to the insufficiency of working fluid moving to fill the evaporation section but was blocked by the vapor bubbles that were moving to cool the condensation area. In the experiment, the right temperature at the evaporation area had a good rate of heat exchange at 70°C .

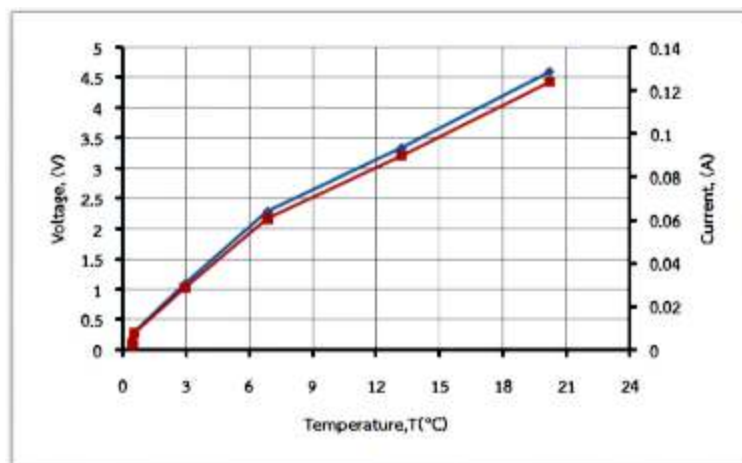


Fig. 6. The relation of temperature difference versus voltage and current

Figure 6 showed the transfer of the heat through the steel pipe. The transfer of heat at the condensation area was calculated by using Calorific by increasing the temperature at the evaporation section by 10 °C each time from 40 to 100 °C. As the temperature of the system increases, the heat to the thermo electric generator increases, resulting to power output. The figure further showed that increase in temperature leads to increase in voltage and current, the voltage and the electric current which were generated by the thermoelectric cells from the temperature difference between the hot and the cold sides. Which agrees with Ohms law, that $V \propto I$. The blue curve showed the voltage whereas the red curve showed the electric current. It could be seen that when the temperature difference between the two sides

was very vary, the thermoelectric cells would generate much voltage; for instance, the temperature difference at 20.1 °C could generate 4.6 Volts and 0.12 Ampere which was in accordance with equation 3. The rate of heat exchange changed according to heat values at the evaporation section. When the temperature at the evaporation increased, the heat transfer changed accordingly. At the beginning of experiment, the heat transfer slowly increased as the working fluid changed its status into steam to transfer heat at the condensation section. As time increased, the rate of heat exchange also increased and would become stable when the heat pipe got into its stable status. The results revealed that when the heat transfer became constant and consistent, the temperature at the evaporation section was at 90 °C.

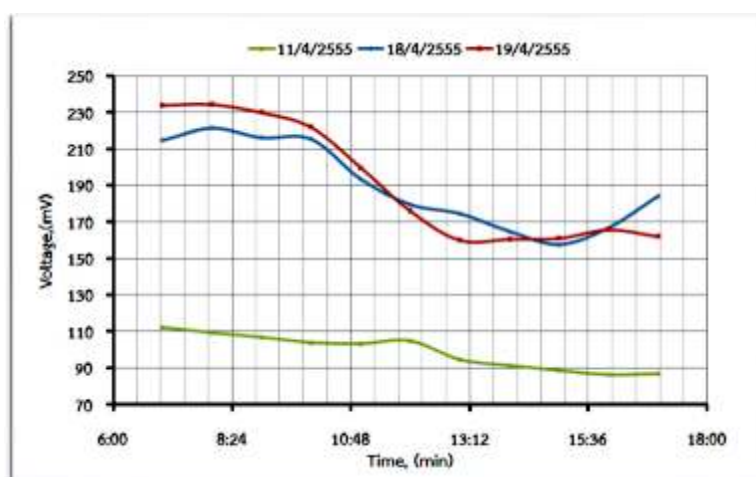


Fig.7. The relation between voltages generated by the thermoelectric cells versus time.

Figure 7 showed the relation between the voltage and the time. From this figure, it could be seen that the voltage generated by the thermoelectric cells changed according to the time and the temperature difference of the two sides of the heat pipe. The temperature on the hot side of the thermoelectric cells was dependent on the temperature of the under heat convection layer of the solar pond whereas the temperature on the cold side was dependent on the temperature of the upper heat convection layer of the solar pond. From the red and blue curves, it could be seen that at 07:00 hr, the

voltage generated increased and would decrease when the temperature in the upper heat convection layer increased and the voltage would increase when the temperature in the under heat convection layer increased at 15:00 hr.

Conclusion

Solar ponds are systems that can collect and store solar energy at low temperatures. High temperatures are undesirable because they negatively affect the gradient structure of the system. For this reason, the heat obtained in the

solar ponds can be either used directly or transferred to other systems as heat sources. The voltage generated by the thermoelectric cells is dependent on the temperature difference between the hot and the cold sides of the thermoelectric cells from the solar pond. When the difference very varies, the thermoelectric cells can generate much voltage. The temperature difference of the two sides is also dependent on the temperature of the under heat convection layer of the solar pond which acts as a heat source for the heat pipe, and the temperature at the upper heat convection acts also as a heat transfer for the thermoelectric cells, as demonstrated in the experiment at 08:00 hr where the highest voltage of 220 millivolts was generated and was slowly decreasing later as the temperature at the upper heat convection layer increased. The increase of heat produced from solar pond will increase electricity production; also increase in the flow rate will increase the electricity production.

References

- Nigerian Energy Support Programme (NESP). (2015). the Nigerian Energy Sector; an overview with a special emphasis on renewable energy, energy efficiency and rural electrification.
- Adekunle, A. O. Emmanuel, C. O., Ogungbenro, S. B. and Olugbenga, F. (2015). Analysis of Global Solar Irradiance over Climatic Zones in Nigeria for Solar Energy Applications. *Journal of Solar Energy* (35); 1 - 10.
- Ranjan, K. R. and Kaushik, S. C. (2014). Energy analysis of the active solar distillation systems integrated with solar ponds. *Clean Techn Environ Policy*, (16); 791–805.
- Bozkurt G. C. and Karakilcik, M. (2012). The Daily Performance of a Solar Pond Integrated with Solar Collectors. *Solar Energy*, (86); 1611-1620
- Badran, A. A., Jubran, B. A., Qasem, E. M. and Hamdan, M. A., (1995). Prediction of the temperature and salinity profiles in solar pond. *Journal Appl. Energy*, 63 (2); 167-177.
- Panahi, J. C., Batty, K. and Riley, J. P. (1983). An analysis of the non-convective solar pond. *Journal of Solar Energy Engineering, ASME Transactions*, 105; 369 - 376.
- Okujagu, C. (1996). Characteristics and stability of a shallow saline pond. *Nigerian journal of physics* 85; 11 - 14
- Alagoa F. B. (1996). Simulation of transient behavior of a closed cycle salt gradient solar pond. *Solar Energy* 5; 245 – 250.
- Bectel Corporation. (1975). Technical and economic assessment of the prospects for electrical power generation by use of solar ponds, Report to the U.S. Energy Research and Development Administration, Washington, D.C.; 1.1-6.3.
- Abbey, T. M, Ekine, A. S and Okonny, I. P. (1998). Effect of Chemical Reaction and heat transfer on the salt characteristic of a solar pond. *Proceeding of solar Energy Society of Nigeria* 1; 20
- Xe, H., Golding, P. and Nielsen, C. E. (1987). Prediction of internal stability in a salt gradient solar pond. *International Progress in Solar Ponds Conference, Cuenavaca, Mexico*.
- Doron, B. and Tabor H. Z., (1987). The Beit Haarava 5 MW solar pond power plant progress report. *International Progress in Solar Ponds Conference, Cuenavaca, Mexico*.
- Ogbonda, C. (2015). Numerical simulation of transient effect of the characteristics of a solar pond. *Reiko international journal of science and technology research*, 6(2A); 76 – 88.
- Angeli, C., Leonardi, E. and Maciocco, L. (2006). A computational study of salt diffusion and heat extraction in solar pond plants. *Solar Energy*, 80; 1498-1508.
- El-Sebaai, A. A., Aboul-enein, S., Ramadan, M. R. I. and Khallaf, A. M. (2011). Thermal performance of an active single basin solar still (ASBS) coupled to shallow solar pond (SSP). *Desalination*, (280); 183-190.
- Randeep, S., Sura, T. and Aliakba, A. (2010). Electric power generation from solar pond using combined thermosyphon and thermoelectric modules. *Mechanical and Manufacturing Engineering, RMIT University. Solar Energy*, 85; 371 -378.
- Rowe, D. M. (1995). *Handbook of Thermoelectric*, CRC Press.
- Tchanche, B. F. Lambrinos, G., Frangoudakis, A. and Papadakis, G. (2011). Low-grade heat conversion into power using organic Rankine cycles – A review of various applications. *Renewable and Sustainable Energy Reviews*, (15); 3963–3979.

Mixed Chalcogenides $\text{Bi}_2\text{Te}_{3-y}\text{Se}_y$ as high Performance Thermoelectric and Optical Material: A Review

Alhassan, S.

Department of Physics, Kaduna State University

Corresponding author's email: alhazikara@gmail.com

ABSTRACT

Mixed chalcogenides $\text{Bi}_2\text{Te}_{3-y}\text{Se}_y$ have been of recent investigation for applications in photovoltaic and thermoelectric devices. Due to their exceptional, thermal, and optoelectronic properties, thermoelectric devices based on such materials can be useful in a variety of technological applications. In this paper, a comprehensive review on the development of mixed chalcogenides compound for thermoelectric and optical applications, as well as theoretical simulations and experimental preparation, is presented.

Keywords: Ternaries mixed chalcogenide, thermoelectric properties, optical properties

Introduction

The earliest known transformed band material is the binary SnTe, which was found more than fifty years ago (Scanlon 1959). It has been observed that both the valence as well as conduction band edges in PbTe and SnTe occurred at the symmetry point in the BZ. It was assumed that both the valence and conduction bands of PbTe are specifically located L_6^+ and L_6^- states respectively, while it's vice versa in case of SbTe as shown in Figure 1. One can see that the sample of the alloy $\text{Pb}_x\text{Sn}_{1-x}\text{Te}$ initially decreases the energy gap as the two states L_6^+ and L_6^- states approach each other when the composition of Sn increases but closes at the middle composition at a points where the states turn out to be degenerate, and at the end the band gap revives, with the two states L_6^+ and L_6^- forming the conduction and valence band respectively (Dimmock et al 1966). In the early 1960s (Dimmock and Wright 1964; Dimmock et al 1966) calculated the band structure of both PbTe and SnTe. It was clearly observed that due to the relativistic effect in Pb and Sn clear reasons in the change of the energy gap within the composition of $\text{Pb}_x\text{Sn}_{1-x}\text{Te}$ alloy series can be understood qualitatively.

Similarly, the observed band inversion in $\text{Pb}_x\text{Sn}_{1-x}\text{Te}$ alloys takes place at the four corresponding valleys, given the even number of the surface states. Therefore, one can say it is a trivial or a weak topological insulator, which agreeing to what is known in the topological classification of TRS (Hasan and Kane 2010).

After the success of ternary $\text{Pb}_x\text{Sn}_{1-x}\text{Te}$, the focus for most researchers is currently on ternary chalcogenide from V-VI compounds. One of the earliest ternary mixed chalcogenides to be synthesized is $\text{Bi}_{30}\text{Se}_{(70-x)}\text{Te}_x$. The experimental study on the effects of VI/V ratio of electrical and thermoelectric properties of p -type $(\text{Bi}_{1-x}\text{Sb}_x)_2\text{Te}_3$ elaborated by metal-organic vapour deposition has also been reported (Das and Ganesan 1998).

This has made a necessity for both theoretical and experimental comparative study of the known binary combination Bi_2Te_3 , Sb_2Te_3 and $(\text{Bi}_x\text{Sb}_{1-x})_2\text{Te}_3$ (Nedelcu, et al. 2001). In most of the cases, the results of the theoretical study are found to be in good agreement with experimentally observed values (Bletskan 2006), with a better result from the ternary

chalcogenide system due to the difficulties concerning the binary compounds purity and stoichiometry.

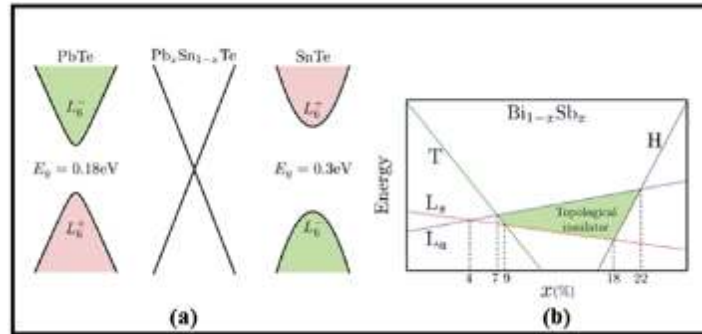


Fig. 1(a) Schematic representation of the valence and conduction bands for PbTe, for the composition at which the energy gap is zero and for SnTe, (b) Schematic representation of band energy evolution of Bi_{1-x}Sb_x as a function of x.

The Crystal Structure and Chemical Composition

By considering the subsequent contribution on predicting a High performance thermoelectric and optical material one can understand that mixed chalcogenides compound is commonly formed between group V and VI elements of the periodic table. They normally are observed in a quintuple layered structure, in which elements of group VI usually occupy the outmost and central (third) layer, while group V elements occupy the second layer in a primitive rhombohedral cell with the space group of $R\bar{3}m$ (No. 166) (Bennett and Rowe 1995; Wang et al 2011). For example, the structure of Bi₂Te₃ has a layer stack as the $-\text{Te}^{\text{I}}-\text{Bi}-\text{Te}^{\text{II}}-\text{Bi}-\text{Te}^{\text{I}}-$. The positions of the two group VI elements in the stack are not equivalent, but generally the stacking is similar to the FCC (Wang et al 2011), only with the different inter-layer distances. In particular, the distance between the neighbouring quintuple-layer is larger, making it easier to cleave with group VI elements. The bulk of these compounds also are formed as a hexagonal lattice with a number of atomic layers, which also provide the basis in the slab model for the thin film properties investigation. Thus, for the ternary combinations, they are commonly formed from the substitution of the central layer element in the binary ones (Menshchikova et al 2011; Wang and Johnson 2011). For example,

Table 1 shows the lattice parameters of Bi₂Se₃, and the crystal structure of these parameters as given in Figure 1.

Table 1 Lattice parameters for three Mixed chalcogenides samples (Bland and Basinski 1961; Nakajima 1963; Wang et al 2011)

Composition	a (Å)	c (Å)
Bi ₂ Se ₃	4.138	28.64
Bi ₂ Se ₂ Te	4.218	29.240
Bi ₂ Te ₂ Se	4.28	29.86

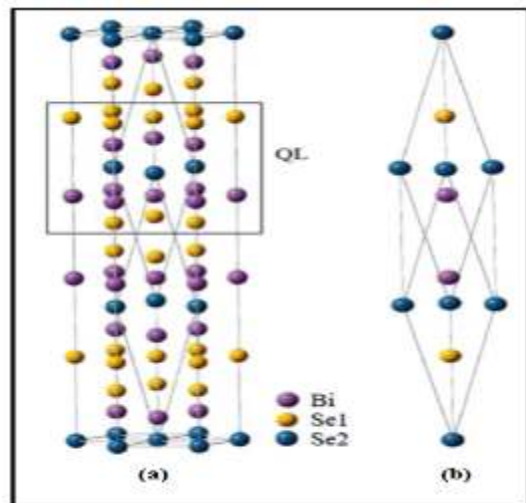


Fig.2 The crystal structure of binary Bi₂Se₃. (a) The rhombohedral crystal structure with hexagonal planes of Bi and Se stacked on top of each other along the z direction. A quintuple layer with Se1-Bi-Se2-Bi-Se1 is indicated by the black square. (b) Rhombohedral unit cell (LaForge et al 2010).

Most measurements of the band gap of this compound were carried out using DFT calculation, transport as well as optical experiments methods turned out to be around 0.25-0.35 eV.

In the case of the other binary compounds like bismuth telluride (Bi₂Te₃), the similarity in the chemical composition between Bi and Te leads to the defects of the antisite which has served as the initial source of carrier doping (*p* type) in Bi₂Se₃, therefore Bi and Se have a little ability to mix with one another, leading to the electron doping (*n* type) by extra charged selenium vacancies $V_{Se}^{\bullet\bullet}$ (Hor et al 2009). Indeed



The presence of donors can be compensated for instance by doping with Pb on the Bi site, as Pb has one electron less than Bi. However, this substitution does not form a *p* type material for Bi₂Se₃, probably because Pb is bipolar (Kim 2013). An additional ionic substitution along the Bi site can be obtained by substituting Ca, using the following reaction



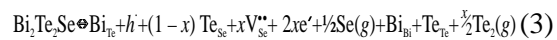
so that negative charge defect Ca_{Bi}' can be created due to the Ca substitution for Bi and a hole h^{\bullet} can be generated to replace the created electrons due to the Se vacancies.

For more than 50 years ternary compounds Bi₂(Te, Se)₃ have been investigated theoretically as well as experimentally due to their significant thermoelectric properties (Stordeur 1995). Normally little defect in density of either binary or ternary semiconductors leads to the large carrier density of about $\sim 10^{18-19} \text{ cm}^{-3}$, causing the bulk conductance to dominate over the surface one in case of the transport as well as optical properties measurements, therefore leading a difficulty in detecting the topological nature of those compounds.

Hence, one of the major targets of the recent condensed matter physics research about the investigation of this material was to succeed in obtaining a higher bulk carrier concentration crystal. More essentially, ternary Bi₂Te₂Se

have been observed as a heavy-doped *n* type material displaying a metallic character. The slight turning of the Te/Se ratio by changing the nominal composition at the present level (<15%) does not lead to semiconducting samples. On the other hand, reducing the Se starting concentration brings in higher resistance samples: this behaviour indicates that reducing Se starting concentration in Bi₂Te₂Se probably does not introduce the Se vacancies nature of Bi₂Se₃.

In contrast, Jia et al (2011) claim that many of Se deficiencies are filled by Te atoms, while the excess Bi atoms, that are present as a consequence occupy the sites left vacant by the displaced Te, leading finally to a *p* type doping. The proposed defect equilibrium for Bi₂Te₂Se that describes the *n* type carrier compensation mechanism is



In order to probe the electronic states of native and Ca-related defects, Bi₂Se₃ and Bi_{1.98}Ca_{0.02}Se₃ samples were studied in a cryogenic scanning tunnelling microscope (STM) at 4.2 K. The surface of the *p*-type crystals is fully stable in the STM experiments. One can identify various defects as well as the sign of their charge state which forms by the STM topographies, for both occupied and unoccupied states. The STM topographies of the native Bi₂Se₃ (001) surface are dominated by one type of defect, which appears as a bright triangular-shaped protrusion in the topography of empty states. Those defects are about 40 Å across on average but vary in size, indicating that they are in various layers beneath the surface. Since no other defects are observed, those defects are attributed to Se vacancies.

Thermoelectric Transport Properties of Mixed Chalcogenides: Previous Results

Recently, in the field of thermoelectric applications a well-known mixed chalcogenides compound that shows optimized *ZT* figures of approximate unity at ambient temperature is Bi₂Te₃. It is presently used primarily in different applications such as in photovoltaic (Raman et al 2017),

thermocouple (Zou et al 2002) and topological insulators (Zhang et al 2009).

Bi_2Te_3 exhibits the band inversion required for topologically insulating behaviour, but is inconvenient for studying topological insulator (TI). This is because of its small band gap and small defect formation energies, which indicate that for low bulk electrical conductivity prerequisite for observing the topologically protected surface states is difficult to attain. This is due to large bipolar conduction, in the lightly doped intrinsic regime and large band conduction (in the heavily doped extrinsic regime favoured by the low vacancy formation energies). This small band gap also presents a substantial hindrance to thermoelectric applications above room temperature, as bipolar conduction is highly destructive to thermoelectric performance.

$\text{Bi}_2\text{Te}_2\text{Se}$ has been observed with a structure closely related to that of Bi_2Te_3 . In particular, it has tetradymite type of rhombohedral crystal structure, consisting of $\text{Bi}_2\text{Te}_2\text{Se}$ layers stacked along the c -axis and separated by van der Waals gaps. These $\text{Bi}_2\text{Te}_2\text{Se}$ layers are the same as the Bi_2Te_3 layers comprising Bi_2Te_3 except that the central Te element is replaced by Se. Presumably this particular substitution is favoured by the fact that placing Se on this site which is more electronegative atom on the site with the metal coordination.

Recently, (Shi et al 2015) reported a result based on the above described method as summarized in Figure 3 of the thermoelectric transport properties of mixed chalcogenides both for the binary Bi_2Te_3 and ternary $\text{Bi}_2\text{Te}_2\text{Se}$ respectively.

Shi et al (2015) presented the calculated Seebeck coefficient for the two materials (Bi_2Te_3 and ternary $\text{Bi}_2\text{Te}_2\text{Se}$), at temperatures 300, 400 and 500 K (see Figure 3a). Because of the anisotropy behaviour of the ternary $\text{Bi}_2\text{Te}_2\text{Se}$, one can observe that the Seebeck coefficient as a function of carrier concentration is significantly larger for $\text{Bi}_2\text{Te}_2\text{Se}$ than for Bi_2Te_3 , for all given temperature ranges. This reflects the different electronic structure of these two materials, as

well as the larger calculated band gap of $\text{Bi}_2\text{Te}_2\text{Se}$. At all three temperatures, for p -type $\text{Bi}_2\text{Te}_2\text{Se}$ in a substantial range of carrier concentration the Seebeck coefficient is larger than $200 \mu\text{V/K}$. As observed, the Weidman-Franz relation essentially necessitates a Seebeck coefficient magnitude of $200 \mu\text{V/K}$ or greater for a high thermoelectric performance; it is worth saying within the limit of 300 Seebeck coefficient is optimally doped in case of binary Bi_2Te_3 . For n -type the thermo power of $\text{Bi}_2\text{Te}_2\text{Se}$ appears inferior to that of Bi_2Te_3 , even with the larger band gap, presumably due to the less anisotropy behaviour and hence less non-parabolic electronic structure. Therefore, one can only focus on p -type.

The benefits of $\text{Bi}_2\text{Te}_2\text{Se}$ relative to Bi_2Te_3 in the p -type Seebeck coefficient should *not* however, necessarily be taken as quantitative evidence for likely better, or even equal thermoelectric performance in $\text{Bi}_2\text{Te}_2\text{Se}$. For example, Figure 3 shows the plot of average electrical conductivity *versus* thermo power at 300 K. These results reveal that in the p -type region of Seebeck coefficient around $200 \mu\text{V/K}$, the two materials have virtually identical S^2/t , which would indicate comparable thermoelectric properties, if the scattering times are equal. The same behaviour is evident at 500 K. Note that in this comparison, Shi et al (2015) are *not* referring to the bottom portion of the graphs, where the Seebeck coefficient transits from positive to negative. This region is firmly within the bipolar regime, well below optimal doping, and for which thermoelectric performance is generally poor. Instead, we refer to the linear region adjacent to the bipolar regime, which is likely near where optimal performance would be found.

For further comparison, in Figure 3(c) Shi et al (2015) describe the calculated power factor $S^2\sigma/t$ (with respect to an average, unknown scattering time) at 300 K for both materials, for p -type and n -type, as a function of carrier concentration (carriers per unit cell). The plot shows comparable behaviour for p -type, consistent with the behaviour in Figures 3(a)

and 3(b), noting that shorter scattering times in $\text{Bi}_2\text{Te}_2\text{Se}$ may degrade the performance of this material relative to that of Bi_2Te_3 . For n -type

this result suggests, that performance of $\text{Bi}_2\text{Te}_2\text{Se}$ is significantly large than that of Bi_2Te_3 .

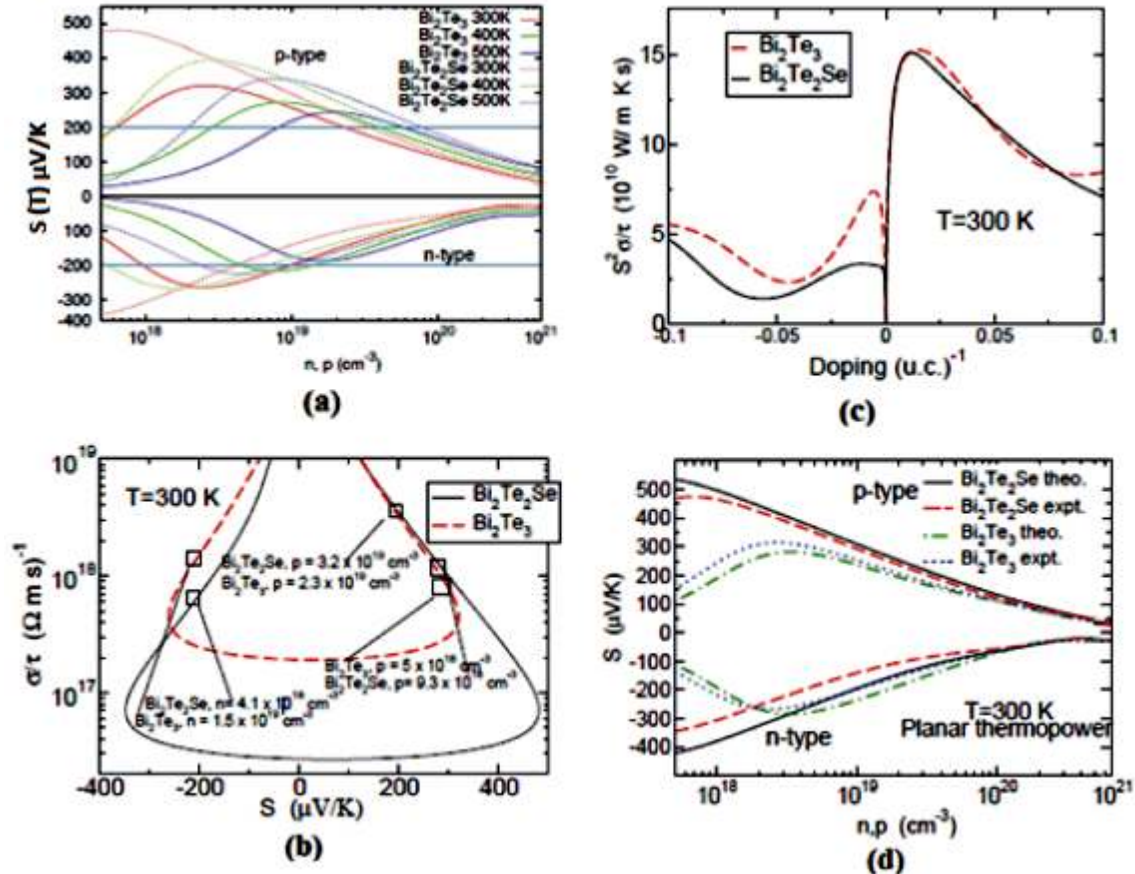


Fig. 3 Transport properties of mixed chalcogenides Bi_2Te_3 and $\text{Bi}_2\text{Te}_2\text{Se}$. (Shi et al 2015).

For the planar thermo-power at 300 K of p -type, the results depict a marginal decrease in Bi_2Te_3 thermo power, and equally marginal increase in $\text{Bi}_2\text{Te}_2\text{Se}$ thermo power; the main effect of the smaller theoretical lattice parameters is in fact an increase in the calculated band gap of $\text{Bi}_2\text{Te}_2\text{Se}$ of approximately 0.06 eV. This change, however, only affects the thermo power for $\text{Bi}_2\text{Te}_2\text{Se}$ at doping around 10^{18}cm^{-3} , far below optimal doping, so for the purposes of assessing thermoelectric performance the effects on p -type of the theoretical lattice parameters is essentially nil. With regards to n -type, the effects of the experimental lattice parameters are somewhat larger, but are of similar

magnitude (and the same sign) for both materials, so that on a comparative basis here for the effects are rather small.

Optical Properties: Previous Results of Mixed Chalcogenides Compound

A well-known binary compound Y_2X_3 ($\text{X}=\text{Te}, \text{Se}; \text{Y}=\text{Bi}, \text{Sb}$) and some of the observed ternary compound, have been studied using first principles by solving the Bethe-Salpeter equation (BSE) (which we have adopted in the case of the present research) for electrons and holes. In bulk materials, the BSE approach is known to fully describe the excitonic effects, which are completely omitted in case of TDLDA (Botti et al 2007). In a system such as clusters and TI material, the BSE approach is

anticipated to be more accurate than TDLDA due to the anisotropy in their structures, but well general comparisons of both methods have not been reported so far due to the difficulty of most numerical implementations of the BSE. One source of difficulty is the explicit evaluation of the dielectric function of the system. Initial theoretical applications use Fourier expansion of the static dielectric function, with dynamical effects included via semi-empirical models or ignored altogether (Giustino 2014). More recent studies employ generalized Plasmon-pole models in the description of dynamical screening.

Ö ü t et al. (2003) presented a fully computational method for the calculation of the static dielectric function in real space, leading to important simplifications compared to Fourier-expansion techniques.

Within both theoretical and experimental point of view, IR spectroscopy has proved to be a capable apparatus to test the elements of the charge transporters, since it permits one to study the electronic low energy excitations and their collaboration with different excitations of the material (for example, phonons). In this way on a basic level it permits one to uncover marks of the topological states, first on the grounds that they are touchy to the application of an electromagnetic field; furthermore, on the grounds that an attractive IR study can test the energy scattering as a capacity of the cyclotron reverberation (just as described in case of the theory using BSE), that characterized the Landau levels of the 2DEG in TIs.

Recently, Basov et al (2011) measured by FTIR (Fourier Transform Infrared) Spectroscopy the reflectivity and transmittance of the topological cover Bi₂Se₃, as a capacity of temperature (from 6 to 295K) and attractive field (from 0 to 8 T).

They discovered a narrowing of the Drude conductivity because of the diminished same molecule dispersing more an increment in the absorption edge because of direct electronic transition with bringing down of temperature. In the magnetic field perpendicular to the *c* -

pivot arrangement, Basov et al (2011) observed an upgrade of electronic absorption and a slight movement of the plasma edge to higher energies.

Bethe-Salpeter Equation (BSE) Optical Spectra Calculation

The electronic self-energy *S* is the major quantity concern in solving the Bethe-Salpeter equation when comes to the optical excitations (Rieger et al 1999) which can be evaluated from the first principles within the so called GW approximation GWA. This approach has been implemented in a different number of systems and at different levels of complexity. At its lowest level, the self-energy is schematically evaluated as

$$S_0 = G_0 W_0 \quad (4)$$

Where *G*₀ are the (DFT) Green's function and the screened Coulomb interaction is expressed as

$$W_0 = [1 - VP_0]^{-1} V \quad (5)$$

Where $V(r) = e^2/r$ is the Coulomb interaction potential following this and solving the actual BSE one can obtain the optical excitations from the singularities of the TDLDA polarizability in the frequency domain or by resolving the BSE numerical.

Following these (Zilong et al 2014) reported a linear and nonlinear optical infrared as the plasmonic properties of chalcogenides crystal of the Bi-Sb-Te-Se family. Figure 4 gives the summary of their results, where the authors observed that, both the transmittance as well as reflectance displays a sign of the optical band gap of about 0.3 eV. Band gap energy was determined by fitting the absorption coefficient with the expression $(\alpha h\nu) \sim (h\nu - E_g)$ for direct interband transitions. The temperature dependence of the energy band gap is found to follow the Varshni equation

$$E(T) = E_0 - \alpha T^2 / (T + \beta) \quad (6)$$

With fitting parameters *E*₀ = 0.316 eV, *a* = 0.000245 eV/K, and *b* = 58 eV, the corresponding optical band gap at room temperature is ~0.256 eV.

Photo induced reflectance *DR/R* spectra were

obtained by differential measurements with and without CW excitation at $\lambda = 532$ nm. Besides the strong differential signal at the band edge region, reflectance modulation both above (enhancement) and below (reduction)

the band gap energy is demonstrated throughout the mid-infrared region. This may be employed for broadband optical switching in reconfigurable plasmonic materials.

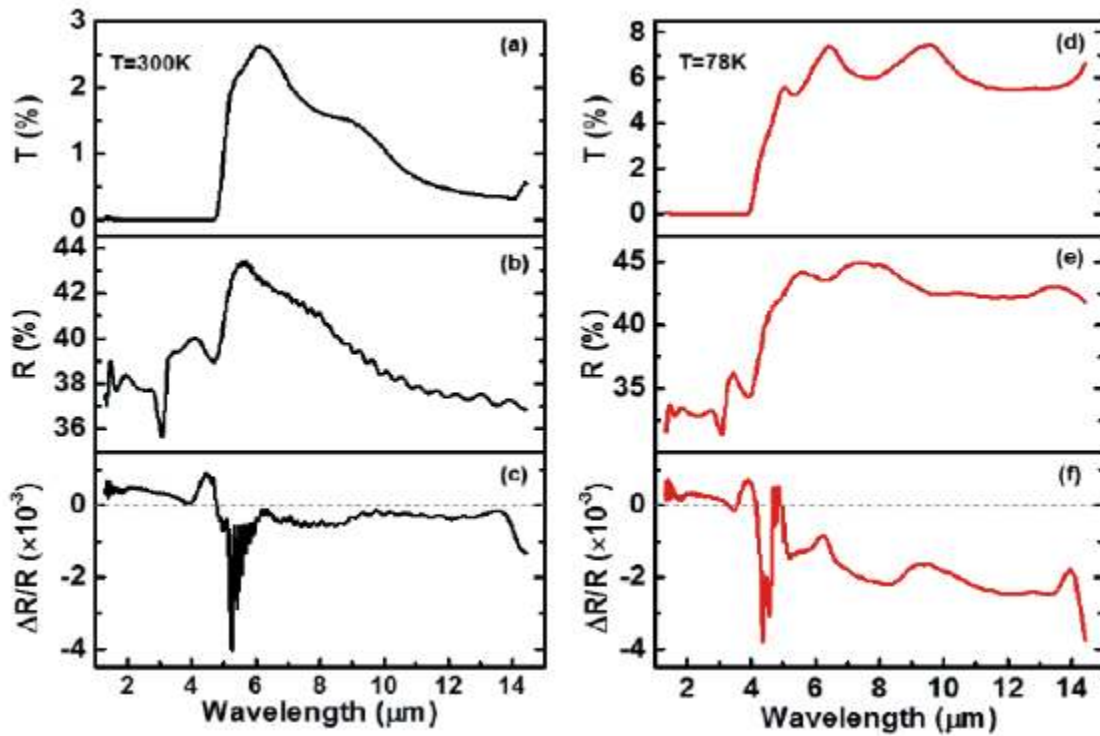


Fig. 4 Infrared transmittance (a), (d), reflectance (b), (e), and photo induced reflectance (c), (f) spectra of $\text{Bi}_{1.5}\text{Sb}_{0.5}\text{Te}_{1.8}\text{Se}_{1.2}$ measured at room temperature (left panels) and 78K (right panels) (Wang et al 2015).

Summary

In this review, the thermoelectric and optical properties of Bi_2Te_3 and $\text{Bi}_2\text{Te}_2\text{Se}$, were illustrated in detail. Moreover, the state-of-the-art of theoretical and experimental data were presented to elucidate the relation among various factors which determine the thermoelectric and optical properties of these materials. Although a tremendous progress has been achieved in the past few years, these properties still need to be improved for their practical application as thermoelectric and optical devices. Here, some major outlooks are presented to address this issue:

1. Both the thermoelectric performance and optical spectra of these materials are much

higher than those of conventional bulk thermoelectric materials. A precise chemical doping during the fabrication and the functionalization of Binaries Bi_2Te_3 to produced ternaries $\text{Bi}_2\text{Te}_2\text{Se}$ lead to a high ZT and optical spectra values.

2. It is of essential importance to achieve a superficial production of high-quality and accessible mixed chalcogenide material. This is currently an active research topic. Until now, many methods have been employed to fabricate the ternaries from the binaries materials, however, it is still challenging to manufacture such materials with a controlled structure via scale-up methods.

References

- Scanlon, W. W. (1959). Recent advances in the optical and electronic properties of PbS, PbSe, PbTe and their alloys. *Journal of Physics and Chemistry of Solids*, 8; 423-428.
- Dimmock, J. O., Melngailis, I. and Strauss, A. J. (1966). Band structure and laser action in Pb x Sn 1- x Te. *Physical Review Letters*, 16(26); 1193.
- Dimmock, J. O. and Wright, G. B. (1964). Band edge structure of PbS, PbSe, and PbTe. *Physical Review*, 135(3A), A821.
- Hasan, M. Z. and Kane, C. L. (2010). Colloquium: topological insulators. *Reviews of Modern Physics*, 82(4); 3045.
- Das, V. D. and Ganesan, P. G. (1998). Thickness and temperature effects on thermoelectric power and electrical resistivity of (Bi_{0.25}Sb_{0.75})₂Te₃ thin films. *Materials chemistry and physics*, 57(1); 57-66.
- Nedelcu, M., Sima, M., Visan, T., Pascu, T., Franga, I. and Craciunoiu, F. (2001, June). Bi/sub 2-x/Sb/sub x/Te/sub 3/thick thermoelectric films obtained by electrodeposition from hydrochloric acid solutions. In *Proceedings ICT2001. 20 International Conference on Thermoelectrics (Cat. No. 01TH8589)*. IEEE; 322-326.
- Bletskan, D. I. (2006). The growth mechanism of the layer-like and wire-like crystals aivbvi and aivb2 vi from gaseous phase. *Journal of Ovonic Research Vol*, 2(6); 137-145.
- Bennett, G. L. and Rowe, D. M. (1995). CRC Handbook of thermoelectrics. *CRC Press, New York*; 515-537.
- Wang, S., Xie, W., Li, H. and Tang, X. (2011). Enhanced performances of melt spun Bi₂(Te, Se)₃ for n-type thermoelectric legs. *Intermetallics*, 19(7); 1024-1031.
- Menshchikova, T. Y. V., Ereemeev, S. V., Koroteev, Y. M., Kuznetsov, V. M. and Chulkov, E. V. (2011). Ternary compounds based on binary topological insulators as an efficient way for modifying the Dirac cone. *Journal of Experimental and Theoretical Physics (JETP) letters*, 93(1); 15.
- Bland, J. A. and Basinski, S. J. (1961). The crystal structure of Bi₂Te₂Se. *Canadian Journal of Physics*, 39(7); 1040-1043.
- Nakajima, S. (1963). The crystal structure of Bi₂Te_{3-x}Se_x. *Journal of Physics and Chemistry of Solids*, 24(3); 479-485.
- LaForge, A. D., Frenzel, A., Pursley, B. C., Lin, T., Liu, X., Shi, J. and Basov, D. N. (2010). Optical characterization of Bi₂Se₃ in a magnetic field: Infrared evidence for magnetoelectric coupling in a topological insulator material. *Physical Review B*, 81(12); 125120.
- Hor, Y. S., Richardella, A., Roushan, P., Xia, Y., Checkelsky, J. G., Yazdani, A. and Cava, R. J. (2009). P-type Bi₂Se₃ for topological insulator and low-temperature thermoelectric applications. *Physical Review B*, 79(19); 195208.
- Kim, D. (2013). Thermoelectric properties of InSb- and CoSb₃-based compounds. Doctoral Dissertation Osaka University Knowledge Archive: OUKA
- Stordeur, M. (1995). Valence band structure and the thermoelectric figure-of-merit of (Bi_{1-x}Sb_x)₂Te₃ crystals. *CRC Handbook of Thermoelectrics*; 239.
- Jia, S., Ji, H., Climent-Pascual, E., Fuccillo, M. K., Charles, M. E., Xiong, J. and Cava, R. J. (2011). Low-carrier-concentration crystals of the topological insulator Bi₂Te₂Se. *Physical Review B*, 84(23), 235206.
- Shi, H., Parker, D., Du, M. H. and Singh, D. J. (2015). Connecting Thermoelectric Performance and Topological-Insulator Behavior: Bi₂Te₃ and Bi₂Te₂Se from First Principles. *Physical Review Applied*, 3(1); 014004.
- Botti, S., Schindlmayr, A., Del Sole, R. and Reining, L. (2007). Time-dependent density-functional theory for extended systems. *Reports on Progress in Physics*, 70(3); 357.
- Giustino, F. (2014). *Materials modelling using density functional theory: properties and predictions*. Oxford University Press.
- Ö ü t, S., Burdick, R., Saad, Y., and Chelikowsky, J. R. (2003). Ab initio calculations for large dielectric matrices of confined systems. *Physical review letters*, 90(12); 127401.
- Basov, D. N., Averitt, R. D., Van Der Marel, D., Dressel, M. and Haule, K. (2011). Electrodynamics of correlated electron materials. *Reviews of Modern Physics*, 83(2); 471.

A Review on Natural Pigments for Dye-Sensitized Solar Cells

Jude, O. O.¹, Dinesh, P.², Emmanuel, A.³ and Azubike, J. E.⁴

^{1,3}Department of Physics, Imo State University, Owerri, Imo State, Nigeria.

²Department of Physics, Sri Sai University, Palampur, Himachal Pradesh, India

⁴Department of Physics and Industrial Physics, Nnamdi Azikwe University, Awka, Nigeria

Corresponding author's email: kukuri2008@gmail.com

ABSTRACT

Dye-sensitized solar cells (DSSCs) are devices that convert light energy to electrical energy by imitating photosynthesis of plants. It is widely known as a low-cost and easy-assembly solar cell, in which both synthetic and natural dyes can be used as sensitizers for wide bandgap semiconductors. Most of the efficient DSSCs are sensitized with the dyes having ruthenium based complexes that have been shown to operate with power conversions up to 11% using nanoporous TiO₂ electrodes. In this article, we have reviewed the mechanism and recent developments in DSSCs. Simple methods of dye extraction from grasses was discussed and their viability as sensitizers for TiO₂ was shown. The natural pigments are used as alternatives to ruthenium based complexes. The photovoltaic performance of DSSCs fabricated with natural pigments was also presented. The authors have reviewed the basic design of DSSCs and sketched out the search for potential materials for more efficient and durable DSSCs.

Key words: Ruthenium, natural pigments, redox couples, dye sensitized solar cell

Introduction

Dye-sensitized solar cells (DSSCs) have been extensively studied for their reasonable photoelectric conversion efficiency, simple assemble technology, and potential low cost (Razykov *et al* 2011). Dye-sensitized solar cell, a device converting light energy to electrical energy by imitating photosynthesis of plants (Hagfelt *et al.* 1994; Gokilamani *et al* 2014; Arishi and Ozuomba 2018), was firstly developed by Gratzel's (Nazeeruddin *et al* 1993; Gokilamani *et al* 2014). DSSCs are devices that convert visible light into electricity based on the photosensitization of wide band-gap metal oxide semiconductor such as TiO₂, SnO₂ or ZnO (Hagfelt *et al* 1994; Razykov *et al* 2011). DSSCs have attracted a lot of interest towards development and improvement of new families of dyes and metal complexes (Gokilamani *et al* 2014). DSSCs are photo electrochemical in nature and have gained considerable academic and industrial interest (Nazeeruddin *et al* 1993). Most of the efficient DSSCs are sensitized with the dyes having ruthenium based complexes

that have been shown to operate with power conversions up to 11% using nanoporous TiO₂ electrodes (Nazeeruddin *et al* 1993; Gokilamani *et al* 2013; Evtushenko *et al* 2015; Liang *et al* 2018).

DSSC is composed of a dye-adsorbed wide band-gap semiconductor (example TiO₂) film formed on a transparent conductive oxide (TCO) substrate, the I₃/I redox electrolyte and the Pt counter electrode (Waita *et al.*, 2006; Wang *et al.*, 2010). F-doped SnO₂ (FTO) is usually used as the TCO material. In order to induce good contact between TiO₂ and electrolyte, TiO₂ film should have a mesoporous structure. TiO₂ acts as electrolyte acceptor and electron transport layer, while electrolyte acts as hole transport layer. The adsorbed dye molecules become excited under the irradiation of visible light and inject electrons into the conduction band of the semiconductor within pico- to femto-second (Waita *et al* 2006; Suri *et al* 2007; Sirimanne and Perera 2008). The photo-injected electrons

are collected at FTO via the porous TiO_2 network by diffusion process with rate of about micro- to mili-second. The oxidized dyes are regenerated by oxidation of iodide with nano-second time scale. Photo voltage is generally determined by the energy difference between the Fermi level of TiO_2 and redox potential of electrolyte (Suri *et al* 2007; Nandang *et al* 2017; Armendáriz *et al* 2020).

In DSSC, the dye-adsorbed TiO_2 film plays an important role because it serves as a pathway for photo-injected electrons. Figure 1 shows the cell structure and the principle of operation for the dye-sensitized solar cell (Kawakita 2010). The light incident on the transparent electrode (photo electrode) excites the dye in the cell from the ground state to an excited state, whereby an electron (e^-) is formed. The electron passes through TiO_2 to reach the transparent electrode, and flows into the external circuit. Meanwhile, the loss of electron in the dye is supplemented with iodine ions (3I^-) in the electrolyte. At this point, 3I^- are oxidized into iodine and then reduced to 3I^- by receiving an electron that is supplied from the counter electrode (Meng *et al* 2008). Such an electron transfer has been accounted for in terms of the energy level and electron transfer rate. The former provides the explanation that the energy level of the conduction band of titanium oxide and the redox level of iodine ions and iodine should be situated between the excited level and ground level of the dye molecules, so that electrons are moved by a phenomenon similar to that of water flowing from a high to low level. In the latter point of view, the main electron transfer proceeds preferentially because the electron transfer

rates in the respective reaction processes are more than 10 times higher than in the reverse reactions and sub reactions. If sunlight that had a higher energy than the difference between the ground level and excited level of the dye is supplied and converted into as much electricity as possible, the theoretical calculation of the energy conversion efficiency is 33 % (Kawakita 2010; Xiaodan *et al* 2017).

Preparation and development of synthetic dyes as sensitizers for DSSCs normally requires multistep procedures, which involves a variety of solvents and time-consuming purification processes, making synthetic dye production very expensive (Kumara *et al* 2013). Several studies have found the possibilities of using natural dyes as sensitizers for DSSC's (Sirimanne *et al* 2008; Okoli *et al* 2012; Kumara *et al* 2013). The use of natural dyes as sensitizers for DSSCs have several advantages over rare metal complexes and other synthetic dyes, in that they can easily be extracted from fruits, vegetables, and flowers with minimal chemical procedures, thus attracting a lot of interest in producing a low cost and yet easy to fabricate DSSCs as alternative to silicon photovoltaics (Kumara *et al* 2013). Natural pigments containing anthocyanins and carotenoids have shown overall solar energy efficiencies up to 1% (Kumara *et al* 2013).

In this work we present the features of dye-sensitized solar cells and review of potential materials. The basic device structure, operating principle and solar cell characteristics have been described. A simple method of extracting natural dyes from plants is presented in this article. We made a review of some recent works on using natural dyes as alternatives to the ruthenium complexes for dye-sensitized solar cells.

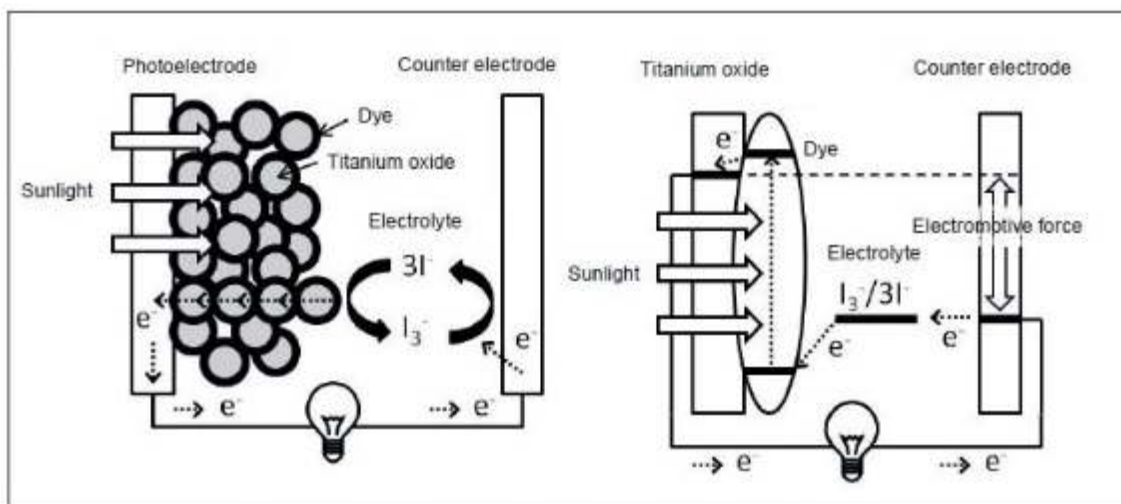


Fig.1 The structure (left) and principle of operation (right) of dye-sensitized solar cell (Kawakita 2010)

Dye-Sensitized Solar Cell Mechanism

Attention has been given to dye sensitized solar cells since the pioneering work of Michael Gratzel and O' Regan in 1991, as a great attention has been paid to dye as cheap, effective and environmentally benign candidates for a new generation solar power devices (Suri *et al* 2007; Arakawa *et al* 2009). Generally, a DSSC consists of an indium tin oxide (ITO), dye modified electrode, electrolyte and a counter electrode. When the DSSC is illuminated with sunlight, the dye absorbs the light and becomes excited. The absorption of light by the dye is followed by the injection of an electron from the excited state of the dye to the conduction band of the semiconductor. Simultaneously the oxidized dye is reduced by the electron donor in the electrolyte and returns to the ground state. The electrons in the conduction band of the semiconductor are collected at the counter electrode and flow through the external circuit, and through these processes, radiant energy is converted into electricity (Lenzmann and Kroon 2007).

Nanoparticle TiO_2 is typically used as the photo anode material (Adachi *et al* 2007; Suri *et al* 2007) made into a porous thick film by coating its colloidal paste onto a conductive glass substrate and sintering it at around 450°C (Waita *et al* 2006). Alternative wide band gap

metal oxide semiconductor such as ZnO and Nb_2O_5 have also exhibited decent performance when prepared into porous electrodes in the same manner (Suri *et al* 2007). Although various dye molecules have been investigated as photosensitizers in the last decade, ruthenium (Ru) complexes with carboxylated polypyridine ligand such as $\text{Ru}(\text{dcbpy})_2(\text{NCS})_2$ remains as one of the best sensitizers for TiO_2 (Waita *et al* 2006; Sirimanne and Perera 2008). In the case of the original Gratzel design, the cell has three primary parts. On the top is a transparent anode made of fluorine-doped tin oxide ($\text{SnO}_2:\text{F}$) (FTO) deposited on the back of a (typically glass) plate. On the back of the conductive plate is a thin layer of TiO_2 , which forms into a highly porous structure with an extremely high surface area. TiO_2 only absorbs a small fraction of the solar photons (those in the UV). The plate is then immersed in a mixture of a photosensitive ruthenium-polypyridine dye (also called molecular sensitizers) and a solvent. After soaking the film in the dye solution, a thin layer of the dye is left covalently bonded to the surface of the TiO_2 . A separate backing is made with a thin layer of the iodide electrolyte spread over a conductive sheet, typically platinum metal. The front and back parts are then joined and sealed together to prevent the electrolyte from

leaking.

Dye-sensitized solar cells operate differently from other types of solar cells in many ways with some remarkable analogies to the natural process of photosynthesis (Lenzmann and Kroon 2007). Various dye molecules like natural pigments, synthesized dyes, conjugated polymers, and so on (Sirimanne and Perera 2008) have been investigated as photo-sensitizers in the last decade, though Ruthenium complexes remain the best sensitizers for TiO_2 (Suri *et al* 2007).

The regenerative process

The regenerative process in the dye-sensitized solar cell consists of five steps:

- (i) At the beginning, the sensitizer absorbs a photon and an electron is transferred from its original state to a higher lying energy level. The sensitizer is in the excited state.
- (ii) Injection of the excited electron into the conduction band of the semiconductor occurs within a femtosecond timescale.
- (iii) The electron percolates through the porous TiO_2 layer to the conductive support and passes the external load to reach the counter electrode.
- (iv) The electron is then transferred to triiodide to yield iodide.
- (v) The iodide reduces the oxidized dye to its original state.

The device operates in a regenerative mode and cycles through these steps.

Solar cell efficiency factors

The energy conversion efficiency η of a solar cell is the percentage of power converted (from absorbed light to electrical energy) and collected, when a solar cell is connected to an electrical circuit.

$$\eta = \left(\frac{P_m}{P_{in}} \right) \quad (1)$$

P_m = Maximum power point

$$P_{in} = E \times A_c \quad (2)$$

where E = input light irradiance (W/m^2)

A_c = surface area of the solar cell (m^2)

This solar cell efficiency is calculated under standard test conditions (STC) i.e. temperature of 25°C and an irradiance of 1000 W/m^2 with an air mass 1.5 (AM 1.5) spectrum. These correspond to the irradiance and spectrum of sunlight incident on a clear day upon a sun facing 37° - tilted surface with the sun at an angle of 41.81° above the horizon. Under these conditions, a solar cell of 12% efficiency with a 100cm^2 (0.01m^2) surface area can be expected to produce approximately 1.2 watts of power.

Maximum-power point (pm)

A solar cell may operate over a wide range of voltages (V) and current (I). By increasing the resistive load on an irradiated cell continuously from zero (a short circuit) to a very high value (an open circuit) one can determine the maximum –power point, the point that maximizes $V \times I$; that is, the load for which the cell can deliver maximum electrical power at that level of irradiation. The output power is zero in both the short circuit and open circuit extremes. The maximum power point of a photovoltaic varies with incident illumination

Fill Factor (FF)

The fill factor of a solar cell is given by the maximum power point /actual power output ($V_{mp} \times I_{mp}$) versus the “dummy” power output ($V_{oc} \times I_{sc}$); where V_{oc} is the open circuit voltage and I_{sc} is the short circuit current. The fill factor measures the squareness of the I – V curve.

$$FF = \frac{P_m}{V_{oc} \times I_{sc}} = \frac{V_{mp} \times I_{mp}}{V_{oc} \times I_{sc}} \quad (3)$$

$$FF = \frac{\eta \times A_c \times E}{V_{oc} \times I_{sc}} \quad (4)$$

This is a key parameter in evaluating the performance of solar cells. Typical commercial solar cells have a fill factor above 0.70.

The fill factor is directly affected by the values of the cell series and shunt resistance. Increasing the shunt resistance and decreasing the series resistance will lead to higher fill factor, thus resulting in greater efficiency, and

pushing the cells output power closer towards its theoretical maximum.

Figure 2 below illustrates the I-V curves of both a high fill factor solar panel and a low fill factor panel. The lower fill factor panel

actually produces less power at its maximum power point compared to the higher fill factor panel. A buyer could easily be deceived in just testing the V_{oc} and I_{sc} for the panel's power measurement.

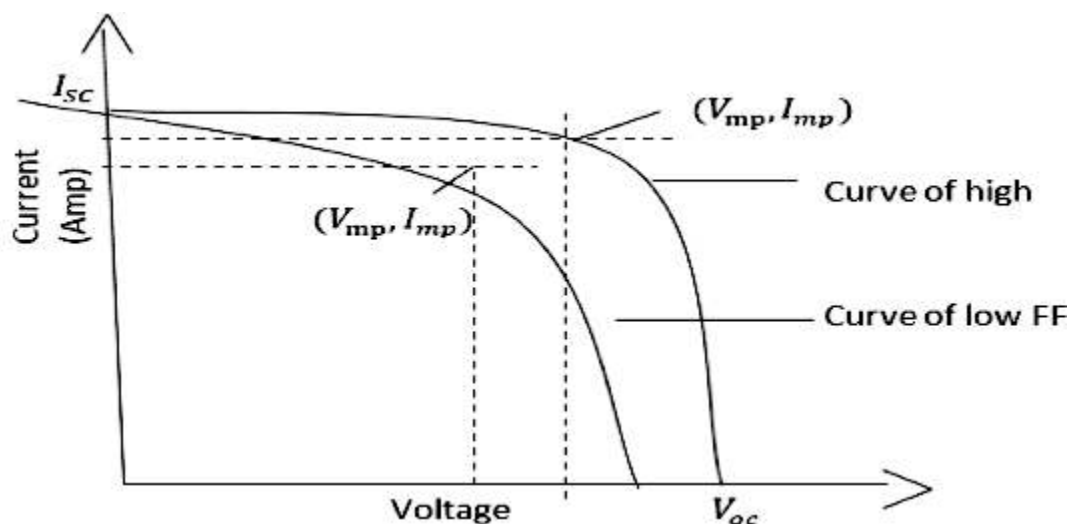


Fig. 2 Two solar cells with different fill factors but the same open circuit voltage and short circuit current

Evaluation of dye-sensitized solar cells

The equipments needed for evaluation of DSSCs include: light source (OHP, Halogen lamp, Xe lamp, etc.), Cables, Variable resistance (or switchable fixed resistances) and voltmeter. The experimental set-up is shown in Figure 3.

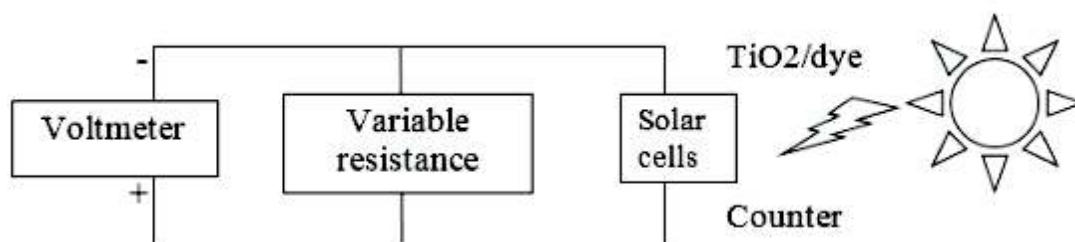


Fig.3 Simple circuit diagram for evaluation of photovoltaic parameters of DSSCs

The evaluation procedure is as follows:

(i) Shine the light from the side of TiO_2/dye electrode.

(Note; Light intensity has to be known in advance to calculate power conversion efficiency. It can be measured by a power meter or a calibrated photodiode).

(ii) Set the resistance at maximum value and record voltage.

(iii) Decrease the resistance and record voltage.

(iv) Repeat until the voltage reaches nearly zero and turn the light off.

(v) Calculate corresponding current at each recorded point.

$$I = \frac{V}{R} \quad (5)$$

(vi) Plot voltage (X-axis) vs current (Y-axis).

(vii) Plot voltage (X-axis) vs power (Y-axis) to find P_m .

(viii) Calculate fill-factor (FF)

(ix) Calculate power conversion efficiency (h)

Note that voltage recorded at zero resistance represents the open circuit voltage (V_{oc}). Also, if you set R to zero and replace the voltmeter with ammeter, you will be directly measuring the short circuit current (I_{sc}).

Light absorbing materials

All solar cells require a light absorbing material contained within the cell structure to absorb photons and generate electrons via the photovoltaic effect. It has been mentioned earlier in this chapter that materials used in solar cells tend to have the property of preferentially absorbing the wavelengths of solar light that reach the earth surface. There are many new alternatives to silicon photocells. Proprietary nano-particle silicon printing processes promise many of the photovoltaic features that conventional silicon can never achieve. It can be printed reel to reel on stainless steel or other high temperature substrates. However, most of the works on the next generation of photovoltaics are directed at printing onto low cost flexible polymer film and ultimately on common packaging materials. The main contenders are currently copper indium gallium selenide (CIGS), cadmium telluride (CdTe), dye-sensitized solar cell and organic photovoltaics.

Extraction of local dyes

The absorption spectrum of a semiconductor defines its possible uses (Sergio *et al* 2009). Various doping methods have been extensively utilized for modifying the electronic structures of photo-electrodes for dye-sensitized solar cells (Pawar and Nimbalkar 2012; Okoli, *et al* 2013). The present energy and environment crisis has stimulated the interest in exploring renewable energy sources. The central idea in DSSC fabrication is to separate the light absorption process from the charge collection process, mimicking natural light harvesting procedures in photosynthesis, by combining dye sensitizers with semiconductors. This enables the use of wide-bandgap but cheap oxide semiconductors such as TiO_2 . Early DSSC designs involved transition metal

coordinated compounds (e.g. ruthenium polypyridyl complexes) as sensitizers because of their strong visible absorption, long excitation lifetime, and efficient metal to ligand charge transfer (Meng *et al* 2008). Although highly effective, with current maximum efficiency of 11% (Adachi *et al* 2007; Meng *et al* 2008), the costly synthesis and undesired environmental impact of those prototypes call for cheaper, simpler, and safer dyes as alternatives. Natural pigments, including chlorophyll, carotene, and cyanin, are freely available in plant leaves, flowers, and fruits and fulfil these requirements (Meng *et al* 2008; Ozuomba *et al* 2011; Manmeeta *et al* 2012).

Meanwhile, the method of extracting the natural dyes is very simple. For dye extraction from grapes (*Vitis vinifera*), well cleaned grape fruits were mixed with 250 ml ethanol and were kept for 12 hours at room temperature. The residual parts were removed by filtration. The ethanol fraction was separated and few drops of concentrated HCl was added so that the solution became deep red colour (pH less than 1). This was directly used as dye solution for sensitizing TiO_2 electrodes (Gokilamani *et al* 2013). Also, Anthocyanin local dye was extracted from hibiscus sabdariffa which is an edible plant called zobo by Nigerians (Okoli *et al* 2012; Okoli *et al* 2013). Well cleaned leaves from hibiscus sabdariffa were properly blended and mixed with 90% ethanol. The resulting mixture was kept for 18 hours at room temperature. The residual parts were removed by filtration to obtain the anthocyanin natural pigment.

The Performance of DSSCS Fabricated with Local Dyes

In traditional photovoltaic cells, the semiconductor functions to simultaneously absorb visible light and mediate electrons. In contrast, DSSCs are not limited by the light harvesting ability of the semiconductor; in fact, most are optically transparent (Gratzel 2001). The sensitization of these semiconductors to visible light involves

interfacial electron transfer following selective excitation of a surface-bound molecular chromophore (Gratzel 2001). Such a photo induced charge-separation process is a key step for solar energy conversion. A typical DSSC contains five components: a transparent conducting oxide substrate, a monocrystalline network of a wide band gap semiconductor (usually TiO_2), a sensitizer, an electrolyte, and a counter electrode (Waita *et al* 2006; Suri *et al* 2007; Bryanvand *et al* 2012; Ozuomba and Ekpunobi 2013).

Titanium dioxide is a common wide band gap semiconductor that is used in many applications. TiO_2 can exist as an amorphous layer and also in three crystalline phases: rutile (tetragonal), anatase (tetragonal) and brookite (orthorhombic) (Mai *et al* 2009; Hasan *et al* 2010). TiO_2 displays excellent chemical stability and oxidation ability and can be considered as the most investigated material among metal oxides because it is used in a wide range of applications including photocatalysis and photovoltaics (Waita *et al* 2006; Phadke *et al* 2010; Khaleghi 2012). Titanium dioxide is characterized by the band gap of 3.0 eV (the

rutile phase) and 3.2 eV (the anatase phase) (Banerjee *et al* 2006; Mai *et al* 2009; Wang *et al* 2009; Khaleghi 2012) indicating that only a small fraction of the sun's energy (mainly ultraviolet region) will be utilized in solar energy conversion (Figure 4) (Reddy *et al* 2002; Ayieko *et al* 2012) and water splitting processes (Gratzel 2001; Wang *et al* 2009; Hasan *et al* 2010). TiO_2 is usually doped or sensitized to enable it absorb light beyond the ultraviolet region (Khaleghi, 2012; Ozuomba and Ekpunobi, 2013).

The absorption spectra for titania doped with natural pigments are shown in Figure 5 while the photovoltaic performance of DSSCs fabricated with the local dyes are shown in Figure 6. Chlorine dye was extracted from cynodon dactylon commonly called bahama grass while prophyrin dye was a local dye extracted from carica papaya leaves (Ozuomba *et al* 2011; Ozuomba and Ekpunobi, 2013). It was obvious from the absorption spectra that the local dyes actually narrowed the bandgap of titania leading to the absorbance of incident radiation beyond the ultraviolet region and, hence, a reasonable photovoltaic performance.

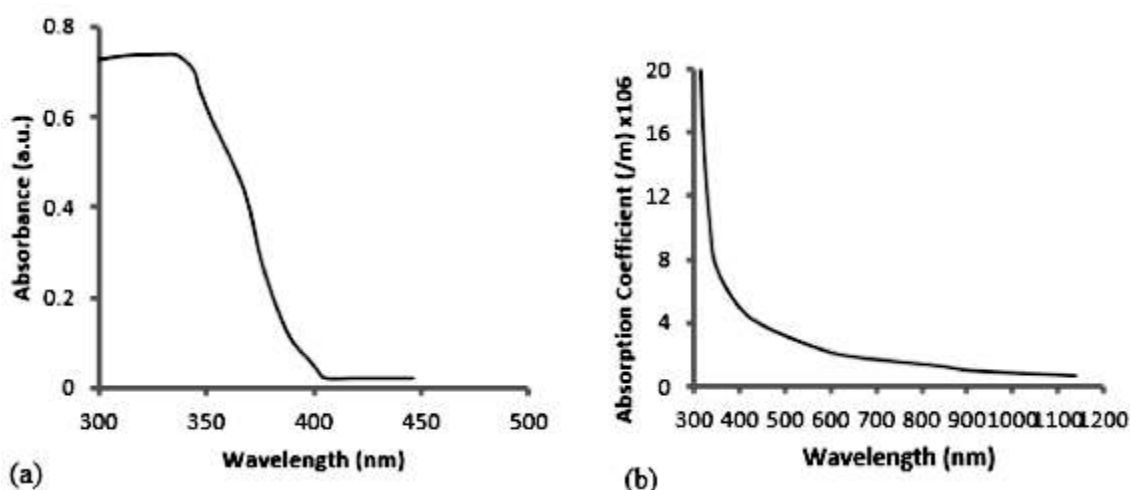


Fig. 4 (a) Diffused UV absorption spectrum of commercial polycrystalline titanium dioxide (Reddy *et al* 2002) and (b) Dependence of absorption coefficient on the wavelength of undoped titanium dioxide thin film of thickness 400 nm (Ayieko *et al* 2012).

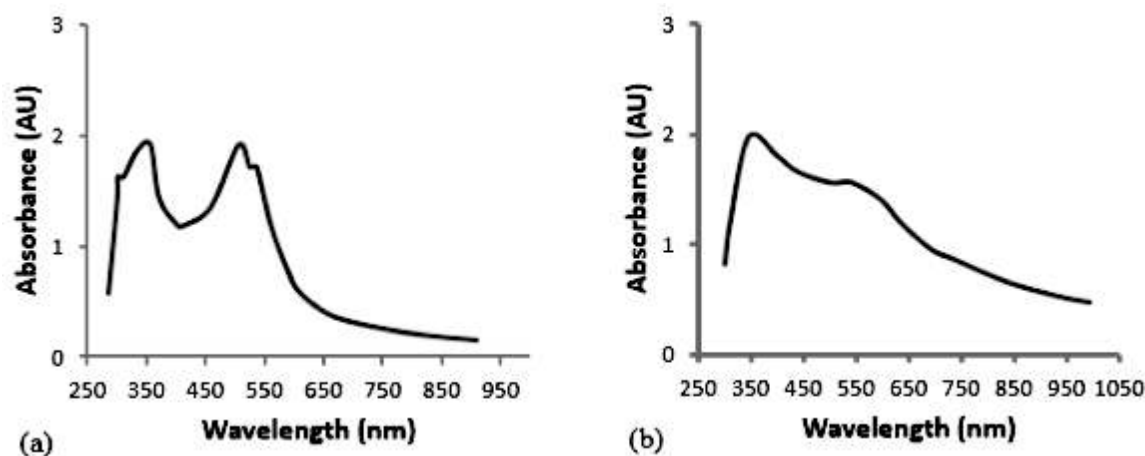


Fig. 5 (a) Optical absorption spectrum of chlorine-dyed nc-TiO₂, and (b) Optical absorption spectrum of prophyrin-dyed nc-TiO₂.

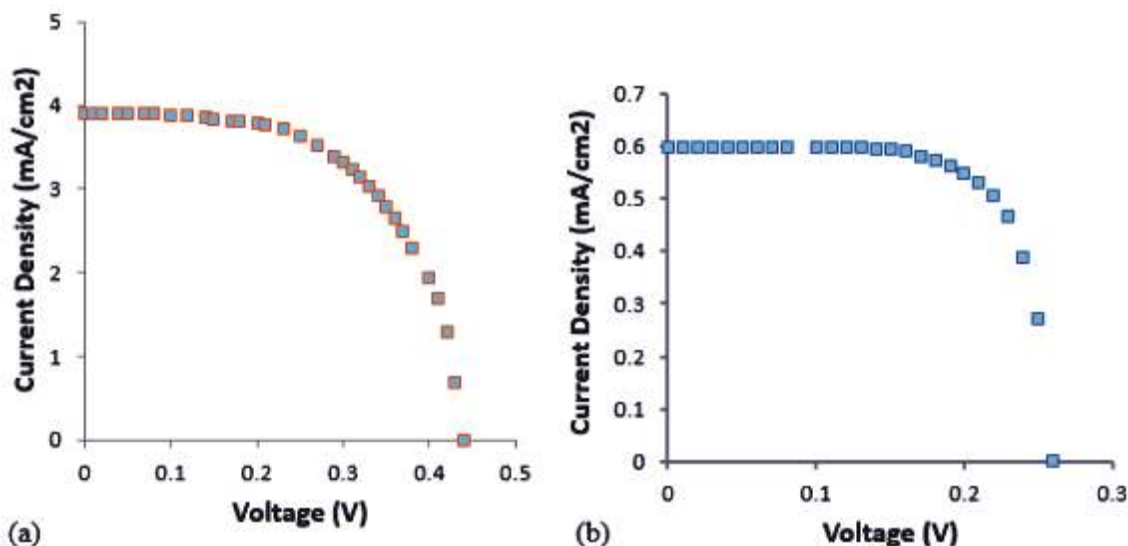


Fig. 6 (a) The I-V curve for solar cell sensitized with chlorine dye. The solar cell parameters were; open circuit voltage (0.44V), short circuit photocurrent (3.90mA/cm²), fill factor (0.587) and photoelectric conversion efficiency (1.008%) and (b) The I-V curve for solar cell sensitized with prophyrin dye. The solar cell parameters were; open circuit voltage (0.26V), short circuit photocurrent (0.6mA/cm²), fill factor (0.72) and photoelectric conversion efficiency (0.11%).

Potential Materials for Dye-Sensitized Solar Cells

Dye-sensitized solar cells (DSSCs) have been extensively studied for their reasonable photoelectric conversion efficiency, simple assemble technology, and potential low cost. The sensitization of wide-bandgap semiconductors, such as ZnO, by organic dyes was investigated by several research groups for photo electrochemical (PEC) processes.

Later on, the first use of a dye-sensitized TiO₂ particle and thin film in a PEC configuration was reported. The PEC approach to solar energy conversion then shifted toward the use of narrow-bandgap semiconductors (e.g., Si, GaAs, CdSe) in conjunction with electrolytes, the analogue of metal-semiconductor Schottky-barrier devices (Razykov *et al* 2011).

The use of new redox couples for enhanced performance

Although scientists have discovered several alternative redox couples that are less corrosive than iodide and whose potentials are more suited to achieving high open circuit voltage, solar cells containing such complexes typically have unacceptably high recombination rates and consequently poor performance (Hardin *et al* 2012). However, recent success using $\text{Co}^{2+}/\text{Co}^{3+}$ (Nusbaumer *et al* 2003), ferrocene, Fc/Fc^+ (Nusbaumer *et al* 2003), copper I/II (Nusbaumer *et al* 2003) and all-organic (Zhang *et al* 2008) electrolytes have resulted in more promising power-conversion efficiencies.

Dye-sensitized solar cells based on liquid electrolytes have reached efficiencies as high as 10% under Air Mass (AM) 1.5 (Nazeeruddin *et al.*, 1993). However, the use of liquid electrolyte has created difficulties in sealing and the long-term photochemical stability of the device (Papageorgiou 1997). To overcome these problems, researchers have attempted to replace the liquid electrolytes with solid or quasi-solid charge-transport materials (Nogueira 2001). Compared with other types of charge-transport materials, the gel electrolytes show higher ambient ionic conductivity (6-8 mS/cm) and better stability (Razykov *et al* 2011). Therefore, several types of gel electrolytes have already been used in quasi-solid-state DSSCs (Peng *et al* 2004; Stathatos *et al* 2004). Organic-inorganic nanocomposites such as gel electrolytes like sol-gel silica can modify liquid electrolytes, and higher overall energy conversion efficiencies have been achieved (Stathatos *et al* 2004).

Enhancing DSSC power conversion efficiencies

Unlike traditional inorganic solar cells, DSSCs require relatively large over-potentials to drive electron injection to titania and regenerate the oxidized dye, as shown in Figure 7 (Hardin *et al* 2012). This requirement results in significantly large loss-in-potential of more than 700 mV and defines the minimum bandgap of the sensitizing dye (and therefore the onset of light absorption). A plot of the maximum obtainable efficiency versus loss-in-potential and absorption onset is shown in Figure 8 (Stathatos *et al* 2004). Typically, a potential difference between the lowest unoccupied molecular orbital (LUMO) level of the dye and the conduction band of titania is required for fast electron injection (Hagfeldt and Gratzel 2000). The magnitude of the required offset has not been precisely determined but is likely to be around 100-150 mV (Koops *et al* 2009), which is much lower than the over-potential usually required to regenerate the dye. Regeneration of a ruthenium metal complex dye with the iodide/triiodide redox couple has a loss of around 600 mV, with over 300 mV of that being directly related to the reaction within the iodide electrolyte (Ardo and Meyer 2009; Boschloo and Hagfeldt 2009). It is estimated that the lowest loss-in-potential for the ruthenium complex/iodide system is 750 mV, which limits the maximum obtainable conversion efficiency to 13.8%, as shown in Figure 8 (Stathatos *et al* 2004).

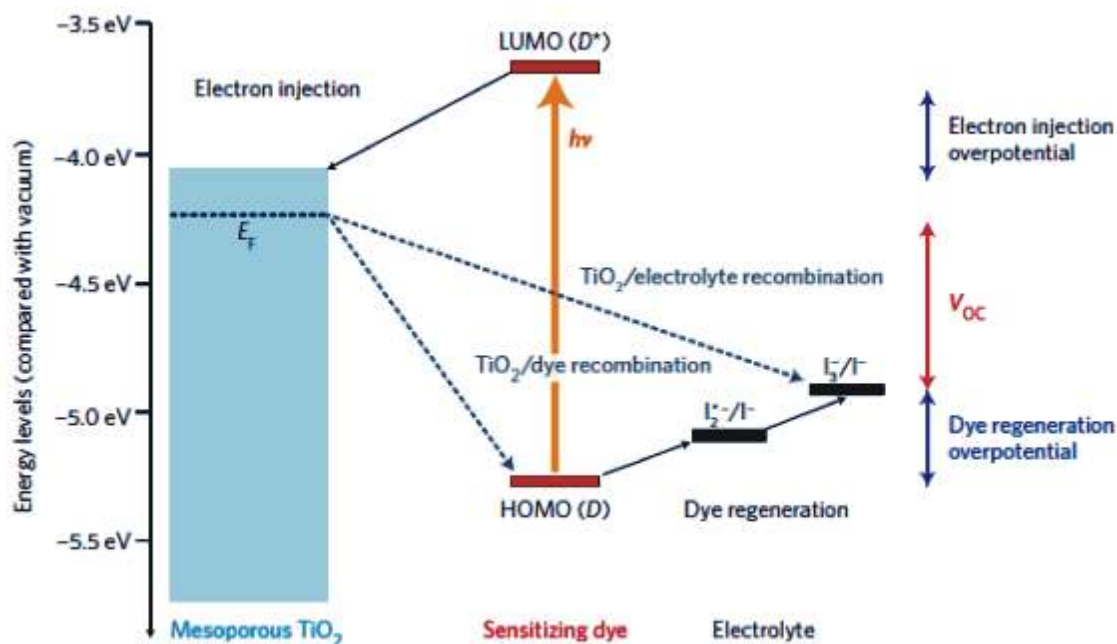


Fig. 7 Energy level and device operation of DSSCs. The sensitizing dye absorbs a photon (energy $h\nu$), the electron is injected into the conduction band of the metal oxide (titania) and travels to the front electrode (not shown). The oxidized dye is reduced by the electrolyte, which is regenerated at the counter-electrode (not shown) to complete the circuit. V_{oc} is determined by the Fermi level (E_F) of titania and the redox potential (I_3^-/I^-) of the electrolyte (Hardin *et al.* 2012).

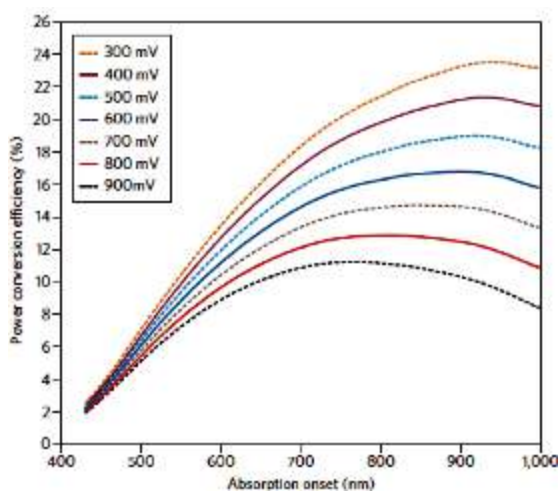


Fig. 8 Maximum obtainable power-conversion efficiencies versus absorption onset for various loss-in-potentials. The model assumes an external quantum efficiency of 90% with the rise from the onset of absorption occurring over a range of 50 nm and a constant fill factor of 0.75 (Snaith 2010).

There are two main ways in which the efficiency of a DSSC can be improved: extend the light-harvesting region into the near-infrared (NIR), and lowering the redox potential of the electrolyte to increase open circuit voltage. Using a dye that absorbs further into the NIR, while still managing to generate and collect the charge carriers efficiently, could increase the current by over 40%, as shown in Figure 8 (Hamann *et al* 2008; Koops *et al* 2009). Further increasing the power-conversion efficiency beyond 14% will require improved dyes and electrolytes with smaller over-potentials to efficiently transfer charge. Single-electron redox mediators based on cobalt and ferrocene complexes have two advantages over iodide (Hardin *et al* 2012). First, they do not require an intermediary step during regeneration and can therefore reduce the loss-in-potential. Second, unlike iodide, which does not have an ideal redox potential (0.35-0.40 eV over the normal hydrogen electrode), alternative electrolyte couples can

be tuned closer to the highest occupied molecular orbital (HOMO) level of the sensitized dye to obtain a higher open circuit voltage.

Co-Sensitization Strategy

The efficiency of all DSSCs can be greatly improved by reducing the energy gap of the dyes so that more light can be absorbed in the infrared region. However, finding one dye that absorbs strongly all the way from 350-940 nm is extremely difficult. Typically, the peak absorption coefficient and spectral width of a dye are inversely related to each other. The most promising technique for harvesting the whole spectrum is to use a combination of visible- and NIR-absorbing dyes.

The co-sensitization of ruthenium metal complex dyes was considered to be problematic because their low molar extinction coefficient required full monolayer coverage on the titania of relatively thick films to absorb all the incident red photons. However, organic dyes have significantly higher molar extinction coefficients than ruthenium metal complex dyes and thus require smaller surface areas, making it possible to co-sensitize thinner DSSC films without significantly reducing light-harvesting in any portion of the spectrum (Hardin *et al* 2012).

Conclusion

Generally, DSSCs are known for their reasonable photoelectric conversion efficiency, simple assemble technology, and potential low cost. An elaborate knowledge of the fundamental mechanism of dye-sensitized solar cells and the introduction of natural pigments for sensitization of the wide bandgap semiconductor electrode leads to a great progress in DSSCs in recent years. Some of the advantages of the natural pigments over ruthenium complex metal dyes are; low cost, simple method of extraction, readily available in different plants and higher molar extinction coefficients. There are many ways to improve the efficiency of DSSCs and scientists are

researching on new efficient materials and better device techniques. The progress made so far in identifying potential materials shows that commercialization of DSSCs will be achieved soon.

Acknowledgement

Physics Advanced Lab, Sheda Science and Technology Complex (SHESTCO), Sheda, Kwali, Abuja provided the enabling environment and the equipments for experimental work. One of the authors (J. O. O.) is grateful to Prof. Charles U. Okoroafor and Prof. T.C. Chineke for their unflinching support and continuous motivation.

References

- Adachi M., Jiu J. and Isoda S. (2007). Synthesis of morphology-controlled titania nanocrystals and application for dye-sensitized solar cells. *Current Nanoscience*, 3; 285-295.
- Arakawa H, Yamaguchi T, Okada K, Matsui K, Kitamura T, Tanabe N (2009). Highly durable dye-sensitized solar cells. *Fujikura Tech Rev.*, 2009; 55–59.
- Ardo, S., Meyer, G. J. (2009). Photo driven heterogeneous charge transfer with transition-metal compounds anchored to TiO₂ semiconductor surfaces. *Chem. Soc. Rev.*, 38; 115-164.
- Arishi, J. I. and Ozuomba, J. (2018). Analysis of Pure and Ag-Doped TiO₂ Thin Films Deposited by Field Assisted Spray Pyrolysis. *Chemical Science International Journal*, 24(4); 1-10.
- Armendáriz-Mireles, E.N., Caballero-Rico, F., Ramírez-de-León, J. (2010). Nano crystalline TiO₂ film with different additives for high performance dye sensitized solar cells. *Microsyst Technol.*
- Ayieko C. O., Musembi R. J., Waita, S.M., Aduda B. O. and Jain P. K. (2012). Structural and optical characterization of Nitrogen-doped TiO thin films deposited by spray pyrolysis on fluorine doped tin oxide (FTO) coated glass slides. *Int. J. Energy Engr.*, 2(3); 67-72.
- Banerjee S., Gopal, J., Murakedharan, P.,

- Tyagi, A. K. and Raj, B. (2006). Physics and chemistry of photocatalytic titanium dioxide: Visualization of bactericidal activity using atomic force microscopy. *Current Sci.*, 90; 1378-1383.
- Boschloo, G. and Hagfeldt, A. (2009). Characteristics of the Iodide/Triiodide Redox Mediator in Dye-Sensitized Solar Cells. *Acc. Chem. Res.* 42(11):1819-1826.
- Bryanvand, M. M., Kharat, A. N. and Fatholahi, L. (2012). Influence of nanostructured TiO film thickness on photo electrode structure and performance of flexible dye-sensitized solar cells *J. Nanostr.* 2; 327-332.
- Evtushenko, Y. M., Romashkin, S. V. Trofimov, N. S., and Chekhlova, T. K. (2015). Optical Properties of TiO₂ Thin Films. *Physics Procedia*, 73; 100-107.
- Gokilamani N., Muthukumarasamy, N., Thambidurai, M., Ranjitha, A., Velauthapillai, D., Senthil, T. S. and Balasundaraprabhu, R. (2013). Dye-sensitized solar cells with natural dye extracted from rose petals. *J. Mater. Sci. Mater. Electron* 24; 3394- 3402.
- Gokilamani, N., Muthukumarasamy, N., Thambidurai M., Ranjitha, A. and Velauthapillai, D. (2014). Grape pigment (malvidin-3-fructoside) as natural sensitizer for dye-sensitized solar cells. *Mater. Renew. Sustain. Energy*, 3(33).
- Gratzel, M. (2001). Photo electrochemical cells. *Nature*, 414; 338-344.
- Hagfeldt, A. and Gratzel, M. (2000). Molecular photovoltaics. *Acc. Chem.*, 33(5); 269-277.
- Hagfeldt, A., Didriksson, B., Palmqvist, T., Lindstrom, H., Sodegren, S., Rensmo, H. and Lindqvist, S. E. (1994). Dye-sensitized solar cells based on SnO₂ nanorod and surface treatment with Mg(II) film. *Sol. Energ. Mater. Sol Cells*, 31; 481-488.
- Hamann, T. W., Jensen, R. A., Martinson, A. B. F., Ryswyk, H. V. and Hupp, J. T. (2008). Advancing beyond current generation dye-sensitized solar cells. *Energ. Environ. Sci.*, 1; 66- 78.
- Hardin, B. E., Snaith, H. J. and McGehee, M. D. (2012). The renaissance of dye-sensitized solar cells, *Nature Photonics. Nature Photonics*, 6; 162-169.
- Hasan M. M., Haseeb, A. S., Saidur, R., Masjuki, H. H. and Hamdi, M. (2010). Influence of substrate and annealing temperatures on optical properties of RF-sputtered TiO thin film. *Optical Mat.*, 32; 690-695.
- Kawakita, J. (2010). Trends of Research and Development of Dye-Sensitized Solar Cells. *Sci. Tech. Trends*, 35; 71-82.
- Khaleghi S. (2012). Calculation of electronic and optical properties of doped titanium dioxide nanostructure. *J. Nanostr.*, 2; 157-161.
- Koops, S.E. O'Regan, B. and Barnes, J. R. (2009). Parameters Influencing the Efficiency of Electron Injection in Dye-Sensitized Solar Cells. *J. Am. Chem. Soc.* 2009, 131, 13; 4808-4818.
- Kumara, N. T. R. N., Ekanayake, P., Lim, A., Iskandar, M. and Ming, L. C. (2013). Study of the Enhancement of Cell Performance of Dye Sensitized Solar Cells Sensitized with *Nephelium lappaceum* (F: Sapindaceae). *J. Solar Energ. Engr.*, 135(3): 031014.
- Lenzmann, F. O., Kroon, J. M. (2007). Recent advances in dye-sensitized solar cells. *Adv. Opto-Elect (Recent Advances in Solar Cells)* 65073/1–65073/10.
- Liang, Y., Sun, S., Deng, T., Ding, H., Chen, W., and Chen, Y. (2018). The Preparation of TiO₂ Film by the Sol-Gel Method and Evaluation of Its Self-Cleaning Property. *Materials*, 11(3); 450.
- Mai, L., Huang, C., Wang, D., Zhang, Z. and Wang, Y. (2009). Effect of C doping on the structural and optical properties of sol-gel TiO thin films. *Appl. Surface Sci.*, 255; 9285-9289.
- Manmeeta, S. D., Dhiraj S., Sharma G. D. and Roy M. S. (2012). Improved performance of oxidized alizarin based quasi solid state dye sensitized solar cell by surface treatment. *Res. J. Chem. Sci.*, 2(2); 61-71.
- Meng, S., Ren, J. and Kaxiras, E. (2008). Natural dyes adsorbed on TiO nanowire for

- photovoltaic applications: Enhanced light absorption and ultrafast electron injection. *Nano Letters*, 8; 3266-3272.
- Nandang, M, Ifa, K. R., Laila, H., and Abdulloh, F. (2017). The effect of TiO₂ thin film thickness on self-cleaning glass properties. *Journal of Physics: Conference Series*, 853.
- Nazeeruddin, M. K., Kay, A., Rodicio, I., Humphry-Baker, R., Muller, E., Liska, P., Vlachopoulos, N. and Gratzel, M. (1993). Conversion of light to electricity by cis-X 2 b i s (2 , 2 ' - b i p y r i d y l - 4 , 4 ' - dicarboxylate) ruthenium(II) charge-transfer sensitizers (X = Cl-, Br-, I-, CN-, and SCN-) on nanocrystalline titanium dioxide electrodes. *J. Am. Chem. Soc.*, 115; 6382-6390.
- Nogueira, A. F., Marco, A., DePaoli, M. A., Montanari, I., Monkhouse, R., Nelson, J. and Durrant, J.R. (2001). Electron Transfer Dynamics in Dye Sensitized Nanocrystalline Solar Cells Using a Polymer Electrolyte. *J. Phys. Chem. B* 2001, 105(31); 7517-7524.
- Nusbaumer, H, Zakeeruddin, S. M, Moser, J. E. and Grätzel, M. (2003). An alternative efficient redox couple for the dye-sensitized solar cell system. *Chem Eur J*, 9; 3756–3763.
- Okoli, L. U., Ozuomba, J. O., Ekpunobi, A. J. and Ekwo, P. I. (2012). Anthocyanin-dyed TiO₂ Electrode and its Performance on Dye-sensitized Solar Cell. *Res. J. Rec. Sci.*, 1; 23.
- Okoli, L. U., Ozuomba, J. O., Ekpunobi, A. J. (2013). Influence of Local Dye on the Optical band-gap of Titanium Dioxide and its performance as a DSSC Material. *Res. J. Phys Sci.*, 1; 6-10.
- Ozuomba J. O., Ekpunobi A. J. and Ekwo P. I. (2011). The viability of prophyrin local dye in the fabrication of dye-sensitized solar cells. *Digest J. Nanomaterials and Biostructures*, 6(3); 1043-1051.
- Ozuomba J. O. and Ekpunobi A. J. (2013). Natural dyes adsorbed on nanocrystalline TiO for photovoltaic applications. *Der Chemica Sinica*, 4(3); 137-143.
- Papageorgiou, N., Maier, W., and Gratzel, M. (1997). An Iodine/Triiodide Reduction electro catalyst for Aqueous and Organic Media. *Journal of the Electrochemical Society*, 144; 876-883.
- Pawar, M. J. and Nimbalkar V. B. (2012). Synthesis and phenol degradation activity of Zn and Cr doped TiO₂ nanoparticles. *Res. J. Chem. Sci.*, 2(1); 32-37.
- Wang, P., Zakeeruddin, S. H. and Grätzel, M. (2004). Solidifying liquid electrolytes with fluorine polymer and silica nanoparticles for quasi-solid dye-sensitized solar cells. *Journal of Fluorine Chemistry*, 125(8); 1241-1245.
- Phadke, S., Sorge J. D., Hachtmann, S. and Birnie, D. P. (2010). Broad band optical characterization of sol-gel TiO thin film microstructure evolution with temperature. *Thin Solid Films*, 518; 5467-5470.
- Razykov, T. M. Ferekides, C. S., Morel, D., Stefanakos, E., Ullal, H. S. and Upadhyaya H. M. (2011). Solar photovoltaic electricity: Current status and future prospects. *Sol. Energ.*, 85; 1508-1602.
- Reddy, K., Manorama S. and Redd A. (2002). Bandgap studies on anatase titanium dioxide nanoparticles. *Mater. Chem. Phys.*, 78; 239-245.
- Sergio, V., Juan, M. M. and Gloria R. (2009). Study of the Bandgap of Synthesized Titanium Dioxide Nanoparticles Using the Sol-Gel Method and a Hydrothermal Treatment. *The Open Materials Science Journal*, 4; 9-14.
- Hattori, S., Wada, Y., Yanagida, S. and Fukuzumi, S. (2005). Blue Copper Model Complexes with Distorted Tetragonal Geometry Acting as Effective Electron-Transfer Mediators in Dye-Sensitized Solar Cells. *Journal of the American Chemical Society*, 127(26); 9648-9654.
- Sirimanne P. M. and Perera V. P. S. (2008). Progress in dye-sensitized solid state solar cells. *Phys. Stat. Sol.*, 245; 1828 -1833.

Table of Contents

Insight into the Kwoi Tremor of September 2016 and other Seismic Events in Nigeria – A Review Dogara, M. D. and Joseph, I. A.	1-11	The Delineation of Mineralization and Hydrothermal Alteration Zones in Gitata Sheet 187, North Central Nigeria Mam D. T., Emmanuel E. U., Abbass A. A. and Usman D. A.	74-86
Determination of Radioactivity Levels of ^{222}Ra , ^{40}K and ^{232}Th using Gamma Ray Spectrometry within Kaduna North Local Government Area of Kaduna State, Nigeria. Sarki, S. H, Kassimu, A. A., Daniel. H. I. and Kure, N.	12-18	Numerical Solution of Variationally Iterated Burgers' Equation using Bivariate Pade Approximation Method Peter, A.	87-92
Thermal Radiation Measurements at Agbada Flow and Metering Station, Igwuruta in Ikwerre Local Government Area of Rivers State, Nigeria. Ogbonda, C.	19-26	Spectral Analysis of Aeromagnetic Data showing Depths of Magnetic Sources of Kwoi within Jaba Local Government Area, Kaduna State, Nigeria Magaji, S., Afuwai, C. G. and Aboh, H. O.	93-101
Structural Evolution of Talcose Rocks in Kagara Area (Sheet 142 SE and Part of Sheet 142 SW) North Central, Nigeria. Ojo, A. A., Tavershima, N., Ismail, Y. A. and Oguntuase, M. A.	27-38	Investigation of Gross Alpha and Beta radioactivity in Well Water in some parts of Makarfi Local Government Area, Kaduna State, Nigeria Gazara, A. B., Sadiq, U., Rabi, N. and Abdulhadi, D.	102-110
Integrated Geoelectrical and Geochemical Investigation to Characterize Hydrocarbon Contamination in Yenagoa Area, Bayelsa State, Nigeria. Tekena, Y. B. and Marere, O.	39-45	Determination of the Concentration of Natural Radioactive Elements Present in Canned Tomato, Fish and Powdered Milk in Zaria, Nigeria Gazara, A. B.¹, Yusuf, U.² and Abdulhadi, D.	111-117
Analysis of Weather Variables to Determine the Effect of Global Warming in Gusau Metropolis, Zamfara State, Nigeria. Okoye, I. F., Mainasara, H. and Murana, K. A.	46-58	Time Effect On Temperature – Concentration Ratio on Electricity Generation using Saline Solar Pond Ogbonda, C.	118-125
Power Density Measurements for Associated Risk of Radio Frequency Radiation in Relation to Safety Limits for Human Exposure to EMF's in Zaria, Nigeria. Bello, I. A., Sa'id, A., Vatsa, M. A., Asuku, A. and Kure, N.	59-63	Mixed Chalcogenides $\text{Bi}_2\text{Te}_{3-y}\text{Se}_y$ as high Performance Thermoelectric and Optical Material: A Review Alhassan, S.	126-133
Mapping of Subsurface Geological Structures using Ground Magnetic and Electrical Resistivity Methods within Lead City University, Southwestern Nigeria. Adebo, B. A., Layade, G. O., Ilugbo, S. O., Hamzat, A. A. and Ootobrise, H. K.	64-73	A Review on Natural Pigments for Dye-Sensitized Solar Cells Jude, O. O., Dinesh, P., Emmanuel, A. and Azubike, J. E.	134-146